Multicarrier Communication over Fast Fading Mobile Channels : Interference Analysis, Equalization, and Channel Estimation

Ahmad Hamdan

THÈSE

Pour obtenir le grade de

DOCTEUR DE L'UNIVERSITÉ GRENOBLE ALPES

École doctorale : EEATS - Electronique, Electrotechnique, Automatique, Traitement du Signal (EEATS)
Spécialité : Signal Image Parole Télécoms
Unité de recherche : Grenoble Images Parole Signal Automatique

Communication Multiporteuse sur des Canaux Mobiles à Evanouissement Rapide : Analyse de l'Interférence, Egalisation et Estimation de Canal

Multicarrier Communication over Fast Fading Mobile Channels: Interference Analysis, Equalization, and Channel Estimation

Présentée par :

Ahmad HAMDAN

Direction de thèse :

Laurent ROS PROFESSEUR DES UNIVERSITES, Université Grenoble Alpes	Directeur de thèse
Hussein HIJAZI Libanese International University (LIU)	Co-encadrant de thèse
Cyrille SICLET MAITRE DE CONFERENCES, UNIVERSITE GRENOBLE ALPES	Co-encadrant de thèse
Ali AL-GHOUWAYEL Libanese International University (LIU)	Co-encadrant de thèse

Rapporteurs :

Joumana FARAH-FRANCIS
PROFESSEUR, Université Libanaise
Damien ROQUE
PROFESSEUR DES UNIVERSITES, ISAE - SUPAERO

Thèse soutenue publiquement le **2 mars 2023**, devant le jury composé de :

Joumana FARAH-FRANCIS PROFESSEUR, Université Libanaise	Rapporteure
Damien ROQUE PROFESSEUR DES UNIVERSITES, ISAE - SUPAERO	Rapporteur
Jean-Marc BROSSIER PROFESSEUR DES UNIVERSITES, GRENOBLE INP	Président
Jean-Baptiste DORE INGENIEUR DOCTEUR, CEA CENTRE DE GRENOBLE	Examinateur
Eric-Pierre SIMON MAITRE DE CONFERENCES HDR, UNIVERSITE DE LILLE	Examinateur

UNIVERSITÉ GRENOBLE ALPES

THESIS

for obtaining the grade of

DOCTOR OF THE UNIVERSITY OF GRENOBLE ALPS

Specialty : **Signal, Image, Parole, Télécom (SIPT)**

Presented by
Ahmad HAMDAN

Thesis directed by **Laurent Ros (Professor, Grenoble-INP)** and co-supervised by **Cyrille Siclet** (Associate Professor, Université Grenoble Alpes), **Hussein HIJAZI** (Associate Professor, Lebanese International University), and **Ali Chamas AL GHOUWAYEL** (EFREI Paris, Panthéon Assas Université)

prepared within the
Grenoble Images Parole Signal Automatique (GIPSA) Lab
in the **école doctorale Électronique, Électrotechnique, Automatique, Traitement du Signal (ED EEATS)**

Fast Fading Mobile Communication with Multicarrier Modulation: Interference Analysis, Equalization, and Channel Estimation

Thesis publicly defended on **March 2nd, 2023**,
in front of a jury composed of:

Joumana FARAH-FRANCIS
Professor, Lebanese University, Reviewer
Damien ROQUE
Professor, ISAE-SUPAERO Toulouse, Reviewer
Jean-Marc BROSSIER
Professor, Grenoble-INP, Examiner, President of the jury
Jean-Baptiste DORE
Research engineer, CEA-LETI Grenoble, Examiner
Eric-Pierre SIMON
Associate Professor, University of Lille, Examiner

For my parents,
my wife May ♡,
and my son Abbas

Thanks

This work took place at the Lebanese International University (LIU), Beirut Lebanon, in the Computer and Communication Engineering department, and Grenoble, Image, Parole, Signale, Automatique (GIPSA) laboratory, Grenoble France, in the Image and Signal department, started in October 2019.

I would like to sincerely thank my thesis director Prof. Laurent Ros (GIPSA), and my co-supervisors PhD. Hussein Hijazi (LIU), PhD. Cyrille Siclet (GIPSA), and PhD. Ali Al-Ghouwayel(EFREI-Paris, previously with LIU) for their support and assistance, inside and outside the scientific area. Their enthusiasm and their enriching remarks allowed me to develop this thesis. More importantly, not only being supporter and guiders at the scientific level, but at the personal level making them supervisors and friends.

I am particularly grateful to Prof. Jérôme MARS, director of GIPSA-lab, for welcoming me to their lab.

I would like to thank Mr. Jean-Marc BROSSIER, professor at the ENSIMAG Grenoble, for giving me the honor of him chairing the jury, as well as Ms. Joumana FARAH-FRANCIS, professor at Lebanese University, Roumieh, Lebanon, and Mr. Damien ROQUE, professor at ISAE-Supaero Toulouse, for having reported this work in an extremely detailed and constructive manner. Thanks also to Mr. Jean-Baptiste DORE, research engineer at CEA-LETI Grenoble, and Mr. Eric-Pierre SIMON, associate professor at University of Lille, for reviewing this work.

Thanks to all the colleagues of the GIPSA-lab and in particular to the group of PhD students, for their welcome and help.

Finally, thank you to my loved ones, family and friends, who also participated in their own way in the completion of this thesis. Thanks especially to my parents, my precious wife, May, and my son, Abbas, for having endured it all.

Contents

List of Figures

List of Tables

Table of Acronyms

$\mathcal{F}$	Fourier Transform
ADSL	Asymmetric Digital Subscriber Line
AWGN	Additive White Gaussian Noise
BEM	Basis Expantion Model
BER	Bit Error Rate
BFDM	Bi-orthogonal Frequency Division Multiplexing
CDMA	Code Division Multiple Access
CP	Cyclic-Prefix
CP-OFDM	Cyclic-Prefix Orthogonal Frequency Division Multiplexing
CSI	Channel State Information
DAB	Digital Audio Broadcasting
DDC	Digital Down Converter
DDS	Direct Digital Synthesizer
DFT	Discrete Fourier Transform
DVB	Digital Vidio Broadcasting
EPA	Extended Pedestrian A model
ETU	Extended Typical Urban model
EVA	Extended Vehicular A model
FBMC	Filter-Bank Multi-Carrier
FBMC-OQAM	Filter-Bank Multi-Carrier with Offset Quadrature Amplitude Modulation
FDM	Frequency Division Multiplexing
FFT	Fast Fourier Transform
FIR	Finite Impulse Response
Gauss	Gaussian
GFDM	Generalized Frequency Division Multiplexing
GMSK	Gaussian Minimum Shift Keying
GSM	Global System for Mobile
GSM-450	GSM 450MHz frequency band

ICI	Inter-Carrier Interference
IDFT	Inverse Discrete Fourier Transform
IEEE	Institute of Electrical and Electronics Engineers
IFFT	Inverse Fast Fourier Transform
ISCI	Inter-Symbol and Inter-Carrier Interference
ISI	Inter-Symbol Interference
LoS	Line of Sight
LS	Least Square
LTE	Long-Term Evolution
MC	Multi-Carrier
MCM	Matched Channel Multiplier
MIMO	Multiple-Input Multiple-Output
ML	Maximum Likelihood
MMSE	Minimum Mean Square Error
MSE	Mean Squared Error
NLoS	No Line of Sight
OBE	Out of Band Energy
OFDM	Orthogonal Frequency Division Multiplexing
PDP	Power Delay Profile
PPN	Polyphase Network
PSD	Power Spectral Density
QAM	Quadrature Amplitude Modulation
Rect	Rectangular
RF	Radio Frequency
RRC	Root Raised Cosine
SAGE	Space-Alternating Generalized Expectation-maximization
SIR	Signal to Interference Ratio
SIS	Successive Interference Suppression
SNR	Signal to Noise Ratio
SP	Single Path Channel
SVD	Singular Value Decomposition
TFL	Time-Frequency Localized

WCP-OFDM	Weighted Cyclic-Prefix Orthogonal Frequency Division Multiplexing
WiFi	IEEE 802.11
WSS	Wide Sense Stationary
WSSUS	Wide Sense Stationary Uncorrelated Scatterers
ZF	Zero-Forcing

Introduction

Communication technologies have been advancing in an extreme rate in the recent decades. Despite the tremendous advancement in such technologies, the demand of the increase in the amount of services and quality of service provided by such technologies is increasing at a faster rate. This demand pushed the research community and the technology providers to have an extraordinary improvement in the communication technologies in the last decade. One of the most active parts of such technologies is the wireless communication industry, where higher data-rates and efficiency, and more reliability, use-cases, and services are now considered to be mandatory. This was mainly observable by the technological advancement between the 4^{th} Generation of mobile communication (4G) and its 5^{th} Generation (5G). In the next few years, as we look forward to the 6^{th} Generation of mobile communication (6G), an even larger leap forward is required in order to satisfy the increase in demand and services. Among all the complications that such requirements raise, such systems will require covering scenarios where a receiver needs to efficiently and reliably receive a signal while moving, and possibly when in rapid motion. In addition to that, and due to having the radio spectrum already occupied by active services, higher carrier frequencies will be employed to support that wide variety of services, especially when wide bandwidth is required. These problems make mobile systems susceptible to high Doppler spread, or what is commonly known as fast varying channels, beside the already existing problems like multipath propagation.

Most modern communication systems are using multi-carrier systems due to their various benefits. The 4^{th} and the 5^{th} generations of mobile communication are using Cyclic-Prefix Orthogonal Frequency Division Multiplexing (CP-OFDM), and it is expected that the 6^{th} generation will be using multi-carrier modulation too. However, it is not clear which variant of multi-carrier modulation would be preferred for such systems. Following the complications mentioned above, this work tries to analyze the properties of pulse shaped oversampled multi-carrier systems in presence of high Doppler spread mainly in terms of interference. It is well known that high Doppler spread will lead to inter-carrier interference in multi-carrier systems. However, we try to analyze in more details the properties of such interference for several pulse shaped multi-carrier systems. Following such properties, we also deal with the problem of channel equalization and channel estimation for multi-carrier systems operating over fast varying mobile channels which are considered quite challenging using the existing technology.

In this manuscript, we deal with these problems by first presenting the background, context, and 'tools' required to develop this analysis. We then analyze in details the interference problem in the considered environment. Later we provide solutions for the equalization problem, and finally for the channel estimation problem. At the end of chapter 1, we provide detailed presentation of the content and objectives of this work.

Chapter 1

General Context and Background: Radio Mobile Channels, Multicarrier Systems, and Channel Estimation and Equalization

Contents

As mentioned in the introduction, this work targets to analyze and improve the Multi-Carrier (MC) transmission over varying channels. To provide this, in this chapter, we discuss the details of the background and context of this work. We describe the properties of a mobile communication channel in section 1.1 and its model, provide an overview of MC systems, and have a quick look on channel impact, estimation, and equalization for such systems.

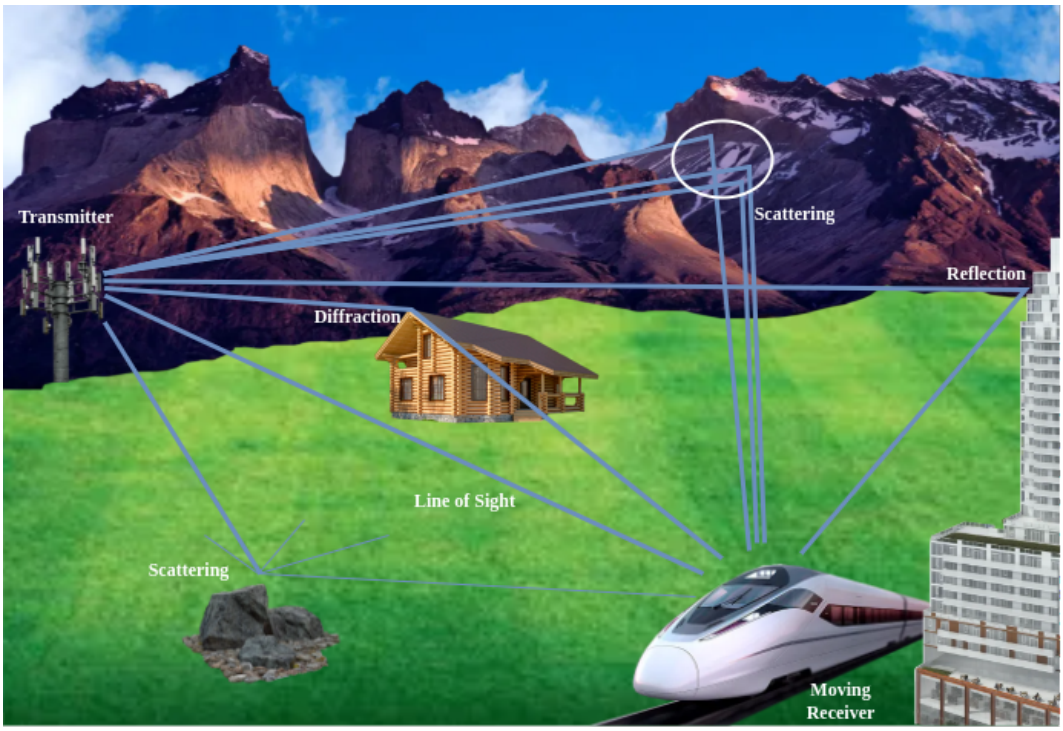

Figure 1.1: Typical scenario of mobile communication channel.

1.1 Radio Mobile Channels

1.1.1 Characteristics of the radio mobile channels

The transmission of information over the radio channel in wireless communication systems is carried out either from a base station to an end-user (downlink) or from an end-user to the base station (uplink). By default, we consider the downlink. In wireless communication, the propagation conditions are variable and depend on the environment [Aul79]. Figure 1.1 shows an example of a typical radio propagation scenario from the base station to the mobile. The propagation mechanisms that occur in mobile communication, and that are shown in this figure, are:

- reflection: it occurs when an electromagnetic wave encounters smooth surfaces of very large dimensions compared to its wavelength λ [Ric51]. For instance, the surfaces of buildings and walls.
- diffraction: may occur when a relatively thick and sharp obstacle obstructs the electromagnetic wave between the transmitter and the receiver. Depending on the size of the obstacle and the wavelength λ, the wave might bend around the edge [LD76].
- scattering: signifies the phenomenon when the energy of the wave is dispersed in many directions. This occurs when the wave encounters an obstacle whose thickness is of

the order of its wavelength, such as street lamps and traffic lights for Global System for Mobile (GSM) frequencies, and glass windows and cups for IEEE 802.11 (WiFi). Another scattering scenario occurs when the wave hits a "rough" surface or a very large number of surfaces close to each other, leading to many reflections and diffractions which aggregate into a scattering effect.

- delay: as the paths the signal took might have different lengths, the signal received through each path will have different time of arrival. This difference in time of arrival is often referred to as the "delay spread" as a quantity or "frequency selectivity" as an underlying impact [DiT52].

- time variation due to motion: different beams of the received signal arrives at the receiver after passing through different environments each arriving from a different angle. While the receiver is in motion, this leads to a variation in the "value" of the channel relative to the path the signal followed [Lee66]. This means that different paths of the channel will encounter different variations. This channel variation is often referred to as the "Doppler" effect or the Doppler spread due to its underlying impact.

The transmitted signal is affected by the propagation losses due to distance, attenuation induced by the obstacles it passes by and the confusion caused by the existence of multiple paths. Therefore, the received signal is a combination of several paths whose amplitudes, phase shifts, variation and delays differ. Consequently, the mobile radio channel is often a fluctuating multipath channel. This fluctuation refers to the change in the amplitude and phase of the signal over a short period of time. Any movement of the mobile receiver will then generate amplitude and phase variation in the total received signal, especially when multiple paths arrive at very close times. Statistically, these fluctuations are generally characterized by a Rician or Rayleigh fading [PS08]. The first generally corresponds to the rural environment, when there is direct Line of Sight (LoS). The second corresponds to the urban environment, when there is No Line of Sight (NLoS). Although "most" of the analysis in this work is valid for any channel model, we focus on the more common urban environment modeled by Rayleigh fading. In the next section, we provide the mathematical model of this physical channel.

1.1.2 Mathematical model of the physical mobile channel

In the previous section, we discussed how the nature of the environment and the movement of the receiver would result in receiving multiple copies of the transmitted signal, each having different fluctuations. In this section, we pin down this problem mathematically assuming the more common urban environment and provide its relative (well known) mathematical model. We assume that the signal $s(t)$ is being transmitted to then arrive at the receiver taking several paths. It is possible that multiple paths can have very close delays because of having some scattering near the receiver. We assume that in such cases, the paths aggregate into a single "macro-path" and treated as a single path. The total number of macro-paths or simply paths the signal propagated through is denoted by $\mathcal{L}$. Following the discussion in section 1.1, each path will have a different delay and fluctuation function/attenuation. We describe the d^{th}

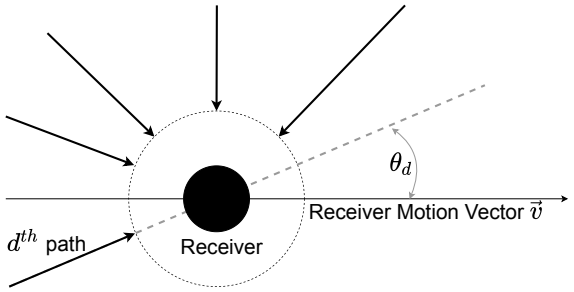

Figure 1.2: Schematic of multiple paths arriving at a moving receiver.

path delay by $\tau_d(t)$ and attenuation by $h_d(t)$. As the transmission time is usually measured in μs or even ns, we can assume that the receiver is moving in a fixed direction with a constant speed modeled as vector $\vec{v}$ whose amplitude is v and direction is $\vec{v}/v$. The signal observed at the receiver is illustrated accordingly in figure 1.2. From this figure, it is clear that if the receiver is moving by $\vec{v}$, the change in the distance of path d would be affected by its propagation having the magnitude $v\cos(\theta_d)$ with θ_d the angle between the motion vector $\vec{v}$ and the direction of the d^{th} path. Consequently, the impact of motion by $\vec{v}$ after a time Δt on the delay τ_d is directly the distance divided by the speed of the electromagnetic waves c, which can be described as follows:

$$\tau_d(t+\Delta t) = \tau_d(t) + \frac{v}{c}\cos(\theta_d)\,\Delta t. \tag{1.1}$$

For a linear relation between $\tau_d(t)$, the delay, and $\psi_d(t)$, the phase of $h_d(t)$, the impact of the time difference Δt on the phase $\psi_d(t)$ is:

$$\psi_d(t+\Delta t) = \psi_d(t) - 2\pi\frac{v}{c}f_c\cos(\theta_d)\,\Delta t, = \psi_d(t) - 2\pi F_d\cos(\theta_d)\,\Delta t, \tag{1.2}$$

with f_c the carrier frequency of the real Radio Frequency (RF) signal of $s_r(t)$ and the Doppler frequency:

$$F_d = \frac{v}{c}f_c, \tag{1.3}$$

where the real RF signal of $s_r(t)$ is the transmitted real version of the complex baseband signal $s(t)$ of bandwidth B such that:

$$s_r(t) = \mathcal{R}\left\{s(t)e^{j2\pi f_c t}\right\} \tag{1.4}$$

Notice that the delay $\tau_d(t)$ and the phase $\psi_d(t)$ will be constant if the receiver is static. In addition to that, over a realistic duration Δt (e.g. frame duration), the delay variation $(\tau_d(t+\Delta t) - \tau_d(t) = \frac{v}{c}\cos(\theta_d)\,\Delta t)$ is negligible compared to the resolution time $1/B$ since $\frac{v}{c} \ll 1$. On the other hand, the phase $\psi_d(t)$ can vary due to the possibility of having a relatively high F_d especially for high carrier frequencies f_c. In other words, the phase $\psi_d(t)$, has a variation of $\psi_d(t+\Delta t) - \psi_d(t) = -2\pi\frac{v}{c}f_c\cos(\theta_d)\,\Delta t$, which can be considerable. Therefore, it is safe to replace $\tau_d(t)$ by a constant τ_d, but $\psi_d(t)$ might be critically variable in function of

t. The complex baseband received signal $r(t)$ can then be described by:

$$r(t) = \sum_{d=1}^{\mathcal{L}} h_d(t)s(t-\tau_d) + \omega(t), \tag{1.5}$$

where $\omega(t)$ is additive complex circular white Gaussian noise. The time-variant impulse response of the channel can consequently be defined as:

$$h(t,\tau) = \sum_{d=1}^{\mathcal{L}} h_d(t)\delta(\tau-\tau_d). \tag{1.6}$$

Although τ_d is safely assumed to be constant over transmission time, this is not the case for $h_d(t)$ which needs to be analyzed. A classical approach commonly used for modeling $h_d(t)$ that has proved to be practical is the Wide Sense Stationary Uncorrelated Scatterers (WSSUS) model [Bel63]. By this approach, the channel properties can be modeled in terms of the time-frequency auto-correlation function $R_H(\Delta t, \Delta f)$ such that:

$$R_H(\Delta t, \Delta f) = \mathrm{E}\left\{H(t,f)H^*(t-\Delta t, f-\Delta f)\right\}, \tag{1.7}$$

where $\mathrm{E}\{\}$ is the expectation operator, $()^*$ is the complex conjugate operator, and $H(t,f)$ is the Fourier Transform ($\mathcal{F}$) of $h(t,\tau)$ in the delay dimension τ such that:

$$H(t,f) = \mathcal{F}_\tau\left\{h(t,\tau)\right\}. \tag{1.8}$$

The just defined time-frequency auto-correlation function $R_H(\Delta t, \Delta f)$, following the WSSUS model, depends only on the difference (Δ) in time and frequency, as the reader can notice. Note that the 'frequency' being discussed here is the 'steady frequency', obtained by applying Fourier Transform with respect to the delay dimension τ, in contrast to the 'Doppler frequency' dimension obtained by applying Fourier Transform with respect to the time dimension t. This function includes a lot of information about the channel and its impact on the communication process, which we analyze in the next two sections.

1.1.3 Delay spread and frequency selective channels

In the previous section, we have shown the model of the mobile channel including multipath propagation delays and channel variation. In this section, we analyze the impact of multipath propagation delay on the communication channel. One trivial impact of multipath propagation is the possibility that two signals transmitted at two different time slots might unintentionally overlap due to having different delays, or what is know as "delay spread". We define this delay spread as:

$$\mathcal{T} = \max_d\left\{\tau_d\right\} - \min_d\left\{\tau_d\right\}. \tag{1.9}$$

Notice that a single path channel will have equal max and min, and consequently $\mathcal{T} = 0$ (or practically $\mathcal{T} \ll 1/B$). In this section, we focus on the frequency domain impact of delay spread. It can be seen from equation (1.8) that the autocorrelation function from equation (1.7)

Table 1.1: Standard GSM PDP

d	1	2	3	4	5	6
$\tau_d(\mu s)$	0	0.2	0.5	1.6	2.3	5
$\sigma^2_{\alpha_d}$	-7.219	-4.219	-6.219	-10.219	-12.219	-14.219

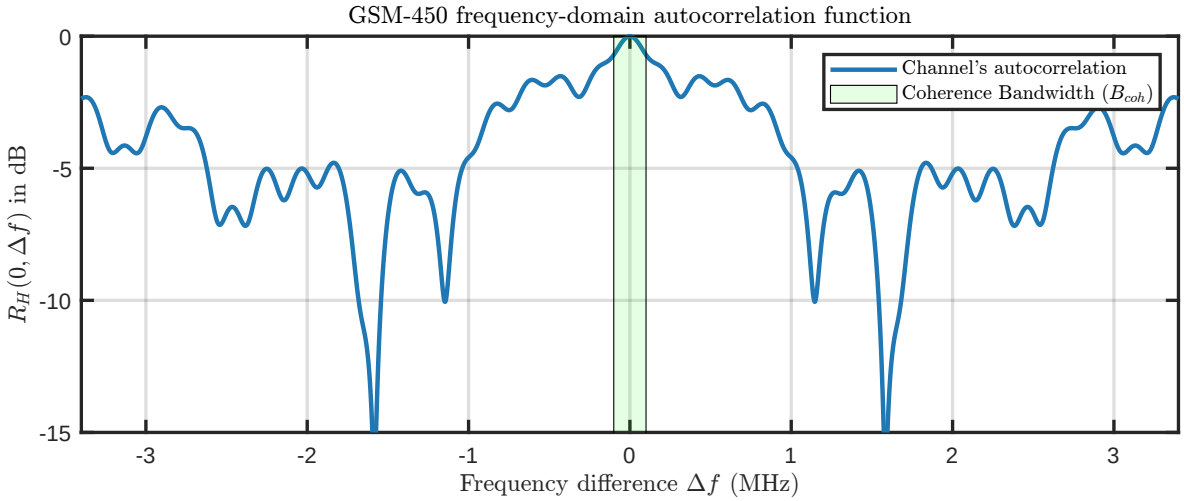

Figure 1.3: GSM-450 frequency-domain autocorrelation function and coherence bandwidth considering the standard GSM delay profile.

is affected by the delays through the relative frequency response of those delays. Although this work targets advanced and general techniques, we consider in this section a GSM example system as it works well for illustrating the impact of multipath propagation on communication channel. The standard power and delay of each path, known as Power Delay Profile (PDP), assumed for GSM [TS93] systems is presented in table 1.1. It can be seen from this table that the assumed delay spread of GSM is $\mathcal{T} = 5\mu$s. As mentioned before, the delay spread has an important part of its impact observed in the frequency domain, which is the effect that we are focusing on. This effect is often referred to as "frequency selectivity" and is measured by the coherence bandwidth (B_{coh}) property approximated by:

$$B_{coh} \approx 1/\mathcal{T}. \tag{1.10}$$

Using this definition and the values of table 1.1, we have the GSM coherence bandwidth $B_{coh} \approx 1/5\mu s = 0.2$MHz. To interpret the significance of the coherence bandwidth, we analyze the channel's frequency-domain autocorrelation when considering GSM 450MHz frequency band (GSM-450), which have the narrowest GSM downlink bandwidth being 6.8MHz. Figure 1.3 shows the GSM-450 coherence bandwidth by plotting $R_H(0, \Delta f)$ considering the standard GSM delay profile. Note that $\Delta t = 0$ is considered since we focus only on the delay spread and relative frequency selectivity in this section. It can be seen from the shaded area that within this bandwidth, the frequency response of the channel is highly correlated. On the other hand, when going beyond this B_{coh}, the correlation starts to vary significantly, where it becomes nearly uncorrelated for some frequencies. Consequently, if only a part the channel

occupying bandwidth narrower than B_{coh}, it will face what is called "flat" channel, while using the whole bandwidth will suffer from what is called "frequency selective" channel. Equivalently, when we have $B \ll B_{coh}$, the channel is a flat fading channel, otherwise, it will be a frequency selective channel. This effect is the reason why multi-path channels are often referred to as frequency selective channels, which is a property of wireless channels. A property specific to wireless "mobile" communication channels is the channel variation and the underlying Doppler spread that is examined in the next section.

1.1.4 Rayleigh fading channels and the doppler spread

In this section, we focus on the more important channel effect for this work which is the channel variation. This effect is of the main interest of this work since it is related to the motion of the receiver, as discussed in sections 1.1.1 and 1.1.2. $R_H(\Delta t, \Delta f)$ introduced in equation (1.7) includes two dimensions:

- Δf, which corresponds to the correlation in the static frequency-domain, is affected by the delay spread, and reflects the coherence bandwidth (B_{coh}) as discussed in section 1.1.3,
- and Δt, which corresponds to the correlation in the time-domain, is affected by the channel variation and reflects the coherence time (T_{coh}) and its underlying Doppler spread, as will be discussed through this section.

The coherence time (T_{coh}) mentioned above can be described as the minimum time shift needed to have an uncorrelated channel. When considering a channel correlation function that fluctuates with the decaying average, this can be seen as the span of the "main lobe" of the correlation function. The T_{coh} can be approximated by:

$$T_{coh} = \frac{1}{F_d}. \tag{1.11}$$

Although none of these definitions of T_{coh} is exact, they all provide similar values as a quantification of how long the channel can be considered invariant. As mentioned in section 1.1.1, the variation in a NLoS environment, such as the one we consider, is usually modeled by Rayleigh fading. In addition to that, we consider the WSSUS assumption which states that the scatterers are uncorrelated, or equivalently, the multiple paths (where some are the so-called macro-paths) are uncorrelated. For the $\mathcal{L}$ paths considered, we define the variance of d^{th} channel response $h_d(t)$ as σ_d^2. Following what was just stated, the properties of the channel variation can be defined as follows:

- the real and imaginary parts of $h_d(t)$ are uncorrelated and Gaussian distributed,
- the absolute amplitude of the channel $\rho_d(t) = |h_d(t)|$ follows the Rayleigh distribution

described by:

$$p\left(\rho_d\right) = \begin{cases} \frac{\rho_d}{\sigma_d^2} e^{-\frac{\rho_d}{\sigma_d^2}} & \text{if } \rho_d \geq 0 \\ 0 & \text{otherwise} \end{cases}, \tag{1.12}$$

- and the phase of channel $\psi_d(t) = \angle h_d(t)$ is uniformly distributed in $[0\ 2\pi[$, where $\angle$ is the argument operator.

The just listed properties define the fluctuation of the channel at an instant t. Added to those, another important property is the autocorrelation function in time-domain $R_H\left(\Delta t, 0\right)$. Notice that, contrary to section 1.1.3, $\Delta f = 0$ since we are interested in analyzing the channel variation and then the correlation in the time dimension. This (normalized) autocorrelation function is defined and calculated in an isotropic environment by [Cla68] to be:

$$R_H\left(\Delta t, 0\right) = J_0\left(2\pi F_d \Delta t\right), \tag{1.13}$$

having F_d proportional to the receiver's movement speed and signal's carrier frequency as in equation (1.3), and J_0 the Bessel function of the first kind and order 0. Note that $R_H(\Delta t, 0)$ is the same for all the uncorrelated paths of the received signal, where (if not to be normalized) the only difference will be the scaling by the power of the path (σ_d^2). The function $J_0\left(2\pi F_d \Delta t\right)$ is a fluctuating function that has its fluctuation rate controlled by F_d. As a result, an increase in F_d would result in a "faster" fluctuation in $J_0\left(2\pi F_d \Delta t\right)$, consequently causing $R_H\left(\Delta t, 0\right)$ to arrive at an uncorrelated state at an earlier time difference. This earlier de-correlation signifies narrowing the coherence time, which aligns with the definition of T_{coh} in equation (1.11) as it is inversely proportional to F_d. Taking into account the definition of F_d in equation (1.3), it is proportional to the carrier frequency f_c and the receiver movement speed v. Although the key reason for the channel variation is the motion of the receiver, the carrier frequency f_c has much more impact on the Doppler frequency F_d as it can take a wider range of values. For instance, if we consider a classical GSM receiver operating at 450 MHz in an extremely fast train moving at 600 km/h (world record is 574.8 km/h held by SNCF near Metz in the east of France), we will have $F_d \approx 250$ Hz. On the other hand, if we consider a signal transmitted over a carrier frequency $f_c = 3$ THz, which is a frequency that will be used in 6G systems, and received by a pedestrian "walking" at 9 km/h (2.5 m/s), we will have a 100 times higher Doppler frequency reaching $F_d \approx 25$ kHz. The coherence time resulting from this Doppler frequency is $T_{coh} \approx 1/F_d \approx 40\mu s$. The relevant autocorrelation function in the time-domain and the coherence time are shown in figure 1.4. This reflects a direct view to the variation of the channel in the time-domain. This coherence time is usually compared to the symbol time T_s as a ratio. If we consider this example to be compared with the standard 4G symbol duration $T_s = 66.7\mu s$, we will have $\frac{T_s}{T_{coh}} = 1.667$. This ratio is more commonly referred to as $F_d T_s = \frac{T_s}{T_{coh}}$, naming it as "normalized Doppler spread". To put that into comparison, we grab the reader's attention that $F_d T_s \geq 0.1$ is usually considered as a relatively fast-varying channel. Another impact of this phenomenon is better analyzed in the frequency domain. Specifically, as the channel variation is multiplication by some variable function in the time-domain, it results in convolution by the frequency response of this function in the frequency-domain, or what is also referenced as Doppler frequency-domain due to having this effect because of

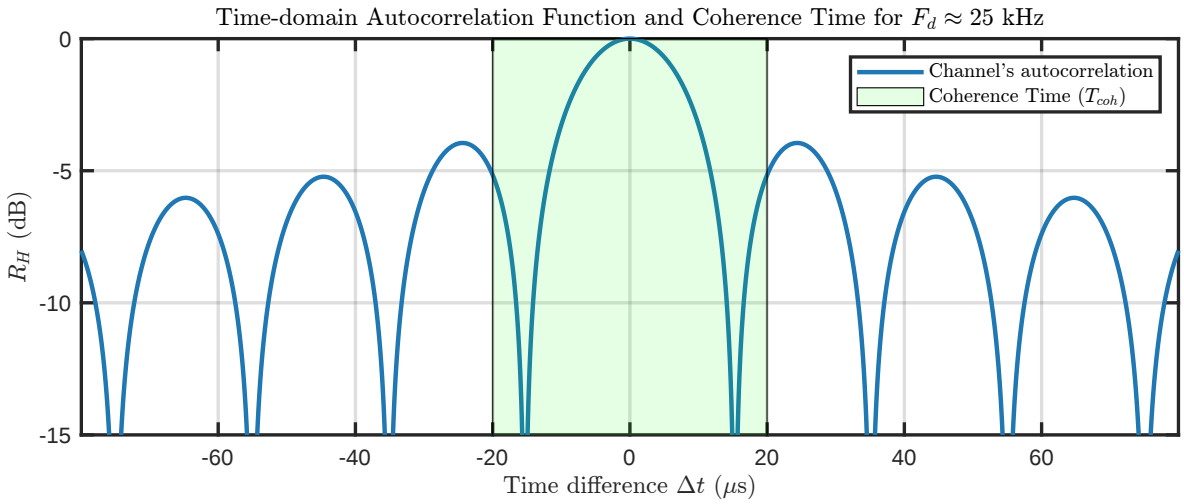

Figure 1.4: Time-domain Autocorrelation Function $R_H(\Delta t, 0)$ and Coherence Time T_{coh} for $v = 9$ km/s and $f_c = 3$ THz.

motion. As the convolution operator is a spreading operator, this effect is called Doppler spread. The Doppler spread resulting from a single realization of a channel can be obtained by obtaining the frequency response of this realization, as just mentioned. However, this is not generalized. A generalization of this spread can be obtained by calculating the Power Spectral Density (PSD) of the channel $S_H(f)$ by applying the Fourier Transform to the time-domain autocorrelation function $R_H(\Delta t, 0)$. As we investigate the Doppler spread effect, we neglect for the moment the multipath propagation and consider a normalized channel by setting $\sigma_d^2 = 1$. This will lead to the PSD being defined (in [Cla68]) by:

$$S_H(f) = \begin{cases} \frac{1}{\pi F_d \sqrt{1-(\frac{f}{F_d})^2}} & \text{if } |f| < F_d \\ 0 & \text{otherwise} \end{cases}. \tag{1.14}$$

The PSD resulting from this definition, plotted in figure 1.5 for the previous example of $F_d \approx 25$ kHz, is often referred to as Jakes' spectrum or U-spectrum due to its bowl shape. This effect has a lot of impact on the communication system especially in MC systems. To measure this impact, we may compare the amount of spreading to the signal bandwidth B by calculating the ratio $\frac{F_d}{B}$. Again, to put this into comparison with the 4G specification, knowing that usually $T_s = 1/B$, the value $\frac{F_d}{B} = F_d T_s = 1.667$. This shows how critical the spreading is as it means that the bandwidth of the signal is spreading in each direction by 166.7% of the initial bandwidth leading to a total bandwidth of $4.334B$. Note that even if a lower value of $F_d T_s$ is to be considered (e.g. $F_d T_s = 0.1$), it will not have such a dramatic impact on channel bandwidth enlargement. However, it will still result in strong degradation of performance due to the variation over multiple samples in time. Such effects are looked into extensively in this work including the impact on Inter-Carrier Interference (ICI), Inter-Symbol Interference (ISI), estimation, and equalization. The just discussed model considers continuous time and frequency domains. However, as the system to be implemented is digital, we need to consider the equivalent impact in discrete-time. This is looked at in the next section.

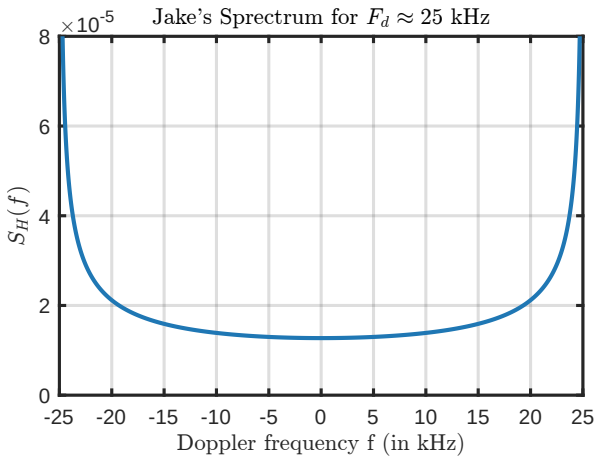

Figure 1.5: Doppler spread Jake's spectrum for $v = 9$ km/s and $f_c = 3$ THz.

1.1.5 Equivalent discrete-time channel

In the previous sections, we have looked into the details and properties of the continuous-time channel in mobile environments. In this section, we discuss the transfer from continuous-time to discrete-time. Normally, any digital receiver includes Digital Down Converter (DDC) within the first stages of the processing of the received signal. This is preceded by analog filtering and sampling, and can be preceded by analog down converter. The down-conversion performed includes passing through the following blocks:

1. Direct Digital Synthesizer (DDS): which generates digital cos and -sin signals at the carrier frequency (or intermediate frequency) to be multiplied by the real received signal to obtain two versions of it:
   (a) the one generated by the cos containing the real (I) component of the equivalent complex signal at the baseband,
   (b) and the one generated by the sin containing the imaginary (Q) component of the equivalent complex signal at the baseband,
2. Low-Pass Filter: to obtain the baseband signal of its input (I for the signal obtained by cos and Q for the other),
3. and Down-sampler: which reduces the sample rate of the low-pass filter output.

The receiver might perform also multiple layers of low-pass filtering/down-sampling for optimization purposes. However, this still has the same behavior of having a single equivalent filter and a single down-sampler to the final rate. A generic block diagram of a DDC is shown in figure 1.6. Normally, we have the low-pass filter "flat" in the baseband and have a negligible response for unneeded frequencies. The final sampling rate after downsampling is normally equal to (or slightly larger than) the (single side) bandwidth of the signal of interest [PS08]. We assume that the low-pass filter frequency response is unitary (1) at frequencies of interest,

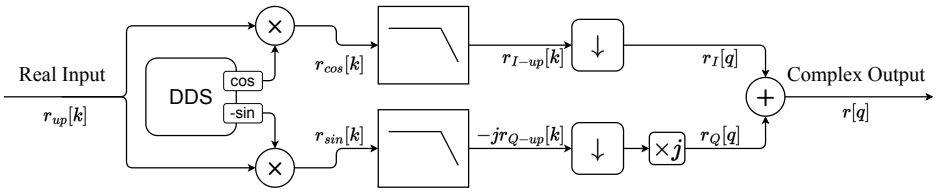

Figure 1.6: IQ-receiver DDC block diagram.

in addition to being flat. At first sight, it might seem that this is enough to assume that an extremely short impulse received at the input of the DDC is observed as a single impulse at the output. However, this is true only when the impulse is perfectly aligned with the final sampling time. Otherwise, the impulse would produce values on every tap within the support range of the down conversion filter $\mathcal{G}$. Following the just discussed steps and the block diagram in figure 1.6, we have the sampled real input $r_{up}[k]$ as:

$$r_{up}[k] = r_r(kT_{up}) = \sum_{d=1}^{\mathcal{L}} h_r\left(kT_{up}, \tau_d\right) s_r(kT_{up} - \tau_d) + \omega_r(kT_{up}), \tag{1.15}$$

where T_{up} is the sampling time before the down conversion, $k \in \mathbb{K}$, r_r is the real-valued received signal, h_r is the real-valued channel, s_r is the real-valued transmitted signal, and ω_r is the real-valued Gaussian noise. The input of the two (identical) low-pass filters $\mathcal{G}$ will then be:

$$r_{cos}[k] = r_{up}[k]cos(2\pi f_c k T_{up}) \quad \& \quad r_{sin}[k] = -r_{up}[k]sin(2\pi f_c k T_{up}). \tag{1.16}$$

Then, after filtering, we have:

$$r_{I-up}[k] = r_{cos}[k] * \mathcal{G}[k] = \sum_p r_{cos}[k-p]\mathcal{G}[p]. \tag{1.17}$$

The downsampling by a ratio R_D will then lead to:

$$r_I[q] = r_{I-up}[k = qR_D] = \sum_p r_{cos}[qR_D - p]\mathcal{G}[p]. \tag{1.18}$$

Similarly for r_{sin} with an imaginary unit multiplication we get:

$$r_Q[q] = j\sum_p r_{sin}[qR_D - p]\mathcal{G}[p]. \tag{1.19}$$

Summing together, we finally obtain:

$$r[q] = \sum_p \left(r_{cos} + jr_{sin}\right)[qR_D - p]\mathcal{G}[p]. \tag{1.20}$$

However, following the assumption that $\mathcal{G}$ is flat in the baseband and perfectly isolates it by approximately removing all the residuals beyond the band of interest, the amount $(r_{cos} - jr_{sin})$ is equivalent to r_c the complex version of r_{up} with the I component of s existing in the real

part and the Q component of s existing in the imaginary part. This leads to:

$$\begin{aligned} r[q] &= \sum_{p} r_c[qR_D - p]\mathcal{G}[p] \\ &= \sum_{p}\sum_{d=1}^{\mathcal{L}} \mathcal{G}[p]\left(h_d\left((qR_D - p)T_{up}\right) s((qR_D - p)T_{up} - \tau_d) + \omega((qR_D - p)T_{up})\right) \\ &= \sum_{p}\sum_{d=1}^{\mathcal{L}} \mathcal{G}[p] h_d\left((qR_D - p)T_{up}\right) s((qR_D - p)T_{up} - \tau_d)) + \omega[q], \end{aligned} \tag{1.21}$$

where h_d is the equivalent complex gain of the d^{th} path of h_r, s is the complex equivalent of s_r, and $w[q]$ is the complex circular baseband Gaussian noise. Finally, this results in having:

$$r[q] = \sum_{l=0}^{L-1} h[q,l]s[q-l] + \omega[q], \tag{1.22}$$

where L is the equivalent discrete-time channel maximum number of paths such that

$$L = \left\lceil \frac{\mathcal{T} + \text{support}(\mathcal{G})}{T_{sa}} \right\rceil \tag{1.23}$$

for sampling time $T_{sa} = R_D T_{up}$, $s[q]$ is the complex down-sampled equivalent of $s(t)$ similar to the relation between $r[q]$ and $r(t)$, and $h[q,l]$ is the complex equivalent discrete-time channel obtained by:

$$h[q,l] = \sum_{d=1}^{\mathcal{L}} \mathcal{G}\left[lR_D - \frac{\tau_d}{T_{up}}\right] h_d\left((q-l)R_D T_{up} + \tau_d\right), \tag{1.24}$$

all obtained by having $p = lR_D - \frac{\tau_d}{T_{up}}$. Note that this assumes that $\frac{\tau_d}{T_{up}}$ is an integer. Although this assumption is not strictly true, it is practical and normally considered as it facilitates the problem formulation. In addition to that, resolution of identifying two very close delays is $1/B_{up} = 2T_{up}$. This means that the difference in a time of a fraction of T_{up} is not resolvable even if physically exists. Therefore, if this assumption is not considered, it will lead to one of two situations:

1. there are multiple paths that are unresolved and acts like a single "macro-path",

2. this analysis will propagate to the analog filter and obtain a similar equation with negligible additional shift.

Consequently, we will assume that this assumption holds. From now on in this document, we consider the received discrete signal in equation (1.22). Notice that the properties discussed in sections 1.1.3 and 1.1.4 are similar for the equivalent channel. In the next section, we present the principles of MC systems, discuss some of the most important MC systems, and introduce the MC system that we consider for this work.

1.2 Multicarrier Systems

1.2.1 History and principles

Classical communication systems, both analog and digital, started to use single-carrier systems for modulation by default. However, the idea of transmitting over multiple carriers has always been there, mainly for multiplexing reasons. One of the first reasons why multi-channel communication was used for is broadcasting of television channels by transmitting audio and video over different carrier frequencies, and then each color channel of the video on a different carrier frequency [Har61]. Another form of multi-channel communication considered for digital communication was by discriminating the channels using pseudorandom codes instead of carrier frequencies. This idea was first introduced in a military context for secret and interference-robust transmission [Age35]. It was later extended toward civil use by benefiting from the ability of having different devices transmitting over the same bandwidth through using orthogonal codes [Sch82]. This was the heart of the evolution towards the radio interface of the third generation (3G) of mobile communication through Code Division Multiple Access (CDMA) [Car+97]. In parallel to this development of a code-based multi-channel communication, work in different types of channels for multi-channel communication was still advancing. On the other hand, some researchers have considered the modeling and analysis of multi-channel communication independent of what type of channel is adopted [KG70], while other researchers were still working on using multiple carrier frequencies for the multi-channel communication [Cha66]. The development of this carrier-based sub-channels work done by Robert W. Chang, which was later registered in a patent [Cha70], appeared in parallel to the rise of Fast Fourier Transform (FFT) [CT65], making Multi-Carrier (MC) transmission an efficient candidate for multi-channel communication. This type of transmission is being used in the fourth generation (4G) and fifth generation (5G), and will be used in the sixth generation (6G) mobile communication networks. In the next section, we introduce some of the most common MC systems based on the work introduced by Chang.

1.2.2 Orthogonal multicarrier systems

In this section, we briefly look at the orthogonal MC system introduced by Chang [Cha66] and discuss some of the most commonly used and studied derivatives of this system. As the name might suggest, such systems are based on the transmission of different symbols on different subcarriers such that these transmitted sub-signals are kept orthogonal to each other. To describe such systems mathematically, we first define the following: M is the number of subcarriers, N is the interval – in samples – between two consecutive MC symbols such that for a sample duration T_{sa}, the MC symbol duration (interval) is $T_s = NT_{sa}$, K is the time span of a pulse shape in terms of MC symbols (number of pulse shape samples/N) such that KN is an integer, and (equivalently) $K-1$ is the overlapping factor, bold face lowercase and uppercase letters correspond to vectors and matrices respectively, $()^*$, $()^H$, and $()^{-1}$ are the conjugate, conjugate transpose, and inverse operators respectively, and $\langle(),()\rangle$ is the inner product operator defined by $\langle \boldsymbol{x}, \boldsymbol{y} \rangle = \sum_k x[k]y^*[k]$. As pulse shapes have a defined length of

KN, the prototype transmitting pulse shape $g[k]$ and the prototype receiving pulse shape $\tilde{g}[k]$ are supported for $k \in [0; KN-1]$, and $g[k] = \tilde{g}[k] = 0$ otherwise. In multi-channel systems, for constellation symbol $c_{m,n}$ to be transmitted over the sub-channel m and the symbol n, we have the q^{th} sample of the transmitted signal $s_{m,n}$:

$$s_{m,n}[q] = g_{m,n}[q]c_{m,n}, \tag{1.25}$$

where $g_{m,n}$ is the transmitting pulse shape for the m^{th} channel and n^{th} symbol. Consequently, the complex baseband transmitted signal s is simple the aggregate over all symbols and sub-channels such that:

$$s[q] = \sum_{n} \sum_{m} s_{m,n}[q]. \tag{1.26}$$

At the receiver, if not considering equalization (or when equalization is done at different stage), for a received signal r, the extracted constellation symbol $\hat{c}_{m,n}$ at the m^{th} sub-channel of the n^{th} symbol is obtained by:

$$\hat{c}_{m,n} = \sum_{q} \tilde{g}^{*}_{m,n}[q]r[q], \tag{1.27}$$

where $\tilde{g}_{m,n}$ is the receiving pulse shape for the m^{th} channel and n^{th} symbol. The just-stated simple transmitting and receiving concept applies to general multi-channel communication system, and equally to specific variants of it by specifying the nature of the channel (e.g. code, sub-carrier, etc.). The main concept behind it is to transmit multiple symbols at the same time on different sub-channels while maintaining orthogonality to each others. As the definitions of $g_{m,n}$ and $\tilde{g}_{m,n}$ control the behavior of such systems, this orthogonality is achieved by having:

$$\left\langle \boldsymbol{g}_{m,n}, \tilde{\boldsymbol{g}}_{m',n'} \right\rangle \approx \begin{cases} \text{Const}, & \text{if } m = m' \text{ and } n = n' \\ 0 & \text{otherwise.} \end{cases} \tag{1.28}$$

If the just defined constraint is not satisfied, a part of the alphabet $c_{m,n}$ transmitted using $g_{m,n}$ over sub-channel m and symbol n may appear on a different (undesired) sub-channel m' and symbol n' leading to ambiguity at the receiver. In the next section, we discuss the most famous and commonly used orthogonal MC, which is Orthogonal Frequency Division Multiplexing (OFDM).

1.2.2.1 Orthogonal frequency division multiplexing

OFDM might be considered the reason of the wide interest in MC systems. Its various benefits made it the waveform for many standards, such as Digital Audio Broadcasting (DAB), Digital Vidio Broadcasting (DVB) and Asymmetric Digital Subscriber Line (ADSL) standards and WiFi. It was first introduced in [Cha66] and later registered in a patent [Cha70]. The orthogonality constraint of equation (1.28), in addition to transmitting at full spectrum density, was achieved by Chang in [Cha70] through:

1. setting the receiving and transmitting pulse shapes to Rectangular (Rect) pulses,

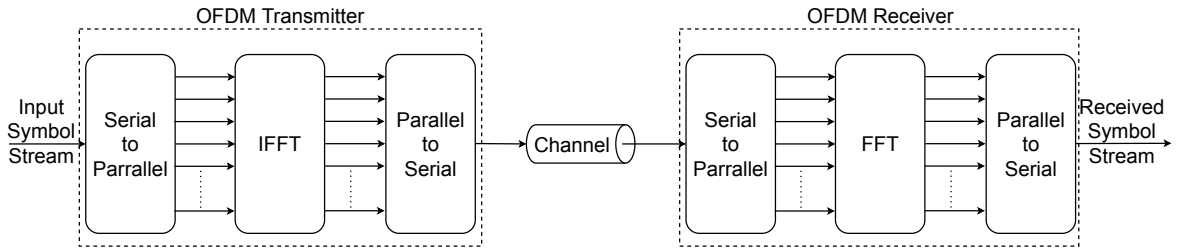

Figure 1.7: Classical FFT-based OFDM transceiver block diagram.

2. using M different subcarriers equally separated from each others by subcarrier frequency $F_s = \frac{B}{M}$ for total bandwidth B,

3. and using a pulse duration equaling the symbol time $T_s = \frac{1}{F_s}$, which means there will be no overlapping between consecutive pulses.

In the discrete-time representation, this is equivalent to setting:

$$g_{m,n}[q] = \tilde{g}_{m,n}[q] = \begin{cases} \frac{1}{\sqrt{M}} e^{j2\pi \frac{qm}{M}} & nN \leq q < (n+1)N \\ 0 & \text{otherwise,} \end{cases} \tag{1.29}$$

while having $N = M$, m in the integer range $[0 \;\; M-1]$, and $\frac{1}{\sqrt{M}}$ as a power normalization factor. As the reader may have noticed, this definition perfectly matches the constraint of equation (1.28), not only approximates it. This type of multiplexing has even gained much more attention, since its definition of pulse shape is exactly the definition of a single point Inverse Discrete Fourier Transform (IDFT). This allowed efficient implementation of a bank of orthogonal pulses using Discrete Fourier Transform (DFT) [WE71], or specifically FFT [CT65] as shown in figure 1.7. Such implementation reduces the complexity from $\mathrm{O}(M^2)$ to $\mathrm{O}(M \log(M))$. Through this design, every M symbols are (parallely) distributed over M subcarriers resulting in a serial output of N complex samples. Note that for such a system, we have $N = M$ and $K = 1$. Although this design was revolutionary in communication engineering, it was not the variant used for most systems using OFDM. In the next section, we discuss the most widely used variant of OFDM: Cyclic-Prefix Orthogonal Frequency Division Multiplexing (CP-OFDM).

1.2.2.2 Cyclic-prefix orthogonal frequency division multiplexing

CP-OFDM [SWG97] is the most used variant of OFDM obtained by the insertion of Cyclic-Prefix (CP). This is done by "oversampling" the OFDM symbols ($N > M$) through copying the last $(N - M)$ samples of the classical OFDM symbol to be transmitted just before it, as sketched in figure 1.8. The receiver side simply "drops" the CP and takes only the last M samples. The intention behind this system is to protect against multi-path propagation assuming that the CP duration is greater than the delay spread $\mathcal{T}$. For the classical OFDM discussed in section 1.2.2.1, multipath propagation will lead to many impairments, including

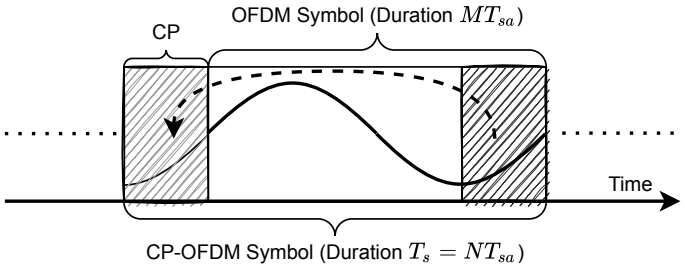

Figure 1.8: CP-OFDM symbol structure sketch.

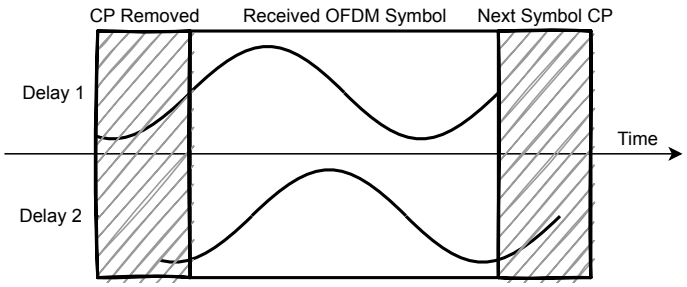

Figure 1.9: An example for a CP-OFDM represented as a single sinusoid received with two different delays.

the following:

1. the symbols will overlap with each others due to the delay spread leading to ISI unless sufficient guard interval is used,
2. the delayed versions of the received symbols will have their last part dropped out by the receiver causing a shorter received pulse which, consequently, have its subcarriers not orthogonal to each others and though causing ICI.

If the assumption of $(N - M)T_{sa} > \mathcal{T}$ holds, inserted CP will cause the part lost at the end of the symbol due to the receiving duration to be cyclically restored at the beginning of the symbol. Since a Rect pulse is considered for OFDM, this cyclic restoration will align the delayed version of the symbol with the first arriving version with a simple phase shift. Figure 1.9 shows a simplified example of this advantage of CP. The sketch represents the OFDM symbol as a simple sinusoid to simplify the analysis. It can be seen through this figure that for the first delay, the added CP is removed and the original OFDM symbol is restored without any change. However, the main interest is around the further delayed version. It can be seen that due to CP, the second copy of the symbol is still represented as a complete sinusoid but only with a phase shift. The residual part of the CP is still removed while removing the CP of the first received version of the symbol. Consequently, being able to observe the full period(s) of the sinusoids (observing an integer multiple of the period), which allows maintaining inter-carrier orthogonality. Note that the last part of the delayed OFDM symbol will not interfere with the next symbol as it will be removed by the CP removal of the

next symbol. This introduces the second benefit of CP-OFDM which is having the CP acting as a guard interval between symbols. These benefits comes at the cost of transmitting additional signal that is not used in symbol detection where a pulse of length NT_{sa} is transmitted, while the receivers crops it to the duration MT_{sa}. Note how following this analysis and discussion, the CP-OFDM can be related to the definition of the MC systems in section 1.2.2 by setting $N > M$ for CP length $N - M$, $K = 1$,

$$g_{m,n}[q] = \begin{cases} \frac{1}{\sqrt{M}} e^{j2\pi \frac{qm}{M}} & nN \leq q < (n+1)N \\ 0 & \text{otherwise,} \end{cases} \tag{1.30}$$

and

$$\tilde{g}_{m,n}[q] = \begin{cases} \frac{1}{\sqrt{M}} e^{j2\pi \frac{qm}{M}} & nN + (N-M) \leq q < (n+1)N \\ 0 & \text{otherwise.} \end{cases} \tag{1.31}$$

Note that these definitions of $g_{m,n}[q]$ and $\tilde{g}_{m,n}[q]$ introduces phase shift between if the transmitter and the receiver need to be implemented directly using Inverse Fast Fourier Transform (IFFT) and FFT. This shift is removed by having both multiplied by $e^{j2\pi \frac{(M-N)m}{M}}$, but we provide the values as in equations (1.30) and (1.31) for simplicity. This advantage of CP-OFDM is obtained by relaxing the pulse duration constraint allowing the transmission of oversampled OFDM symbols through appending a CP. In the next section, we will discuss the Filter-Bank Multi-Carrier (FBMC) which can also be seen as an extension of OFDM through relaxing a different constraint.

1.2.2.3 Filter-bank multicarrier

Another MC system that is considered as a flagship of wireless communication is FBMC, which is in fact as old as OFDM. More precisely, OFDM is a special case of FBMC, where they were initially the same work [Cha66] before OFDM took its known shape [Cha70]. However, FBMC gained much more interest in the last decade to overcome some of the limitations of OFDM [FB11]. It relaxes the constraint of having Rect as the system's pulse shape and allows any convenient pulse shape design:

$$g_{m,n}[q] = \tilde{g}_{m,n}[q] = g[q - nN] e^{j2\pi \frac{qm}{M}}, \tag{1.32}$$

where g is the prototype pulse to be selected. This allows to overcome some constraints of OFDM based on the pulse shape that can be selected relative to the constraint to deal with. Arguably, the most important OFDM limitation that FBMC overcomes is in the multiple-access uplink scenario. For OFDM, this requires almost perfect synchronization among all the devices to avoid breaking the orthogonality among allocated channels, while FBMC does not have this constraint [FB11]. In addition to that, FBMC systems can still be implemented using FFT [ADFR19] through what is known as Polyphase Network (PPN) as will be shown in section 1.2.3.1.

1.2.2.4 Bi-orthogonal frequency division multiplexing

Another MC system is the Bi-orthogonal Frequency Division Multiplexing (BFDM). This variant of MC relaxed the requirement that the transmitting pulse shape g and the receiving pulse shape $\tilde{g}$ are matched (performs correlation using $\tilde{g} = g$). For BFDM, it is sufficient to have g and $\tilde{g}$ satisfying the biorthogonality condition of equation (1.28), but not necessarily matched, or what is called '*biorthogonal*' [SS00]. This variant is often considered along with oversampled MC systems [SSP02] by setting $N > M$. As mentioned in section 1.2.2.2, CP-OFDM can be related to the definition of MC systems in section 1.2.2 by setting $N > M$ for CP length $N - M$, $K = 1$, g defined as in equation (1.30), and $\tilde{g}$ defined as in equation (1.31). This makes CP-OFDM a specific configuration of oversampled ($N > M$) BFDM since g and $\tilde{g}$ are biorthogonal (orthogonal yet not matched). Similar to FBMC, BFDM can be implemented efficiently using PPN [SS00].

1.2.3 Generalized frequency division multiplexing

In this work, our aim is to study MC systems in a relatively generalized form without limiting the study to a specific technique. To do so, we adopt a Frequency Division Multiplexing (FDM) system that generalizes all the ones discussed previously in this chapter, in addition to most of the FDM-based systems and other generalized forms such as Weighted Cyclic-Prefix Orthogonal Frequency Division Multiplexing (WCP-OFDM)[Roq12] for example. Note that this version of Generalized Frequency Division Multiplexing (GFDM) is adopted and called by this name for generalization purposes, yet it is not related to the well known GFDM of [FKB09]. As mentioned in the previous sections, such systems can be configured to match a specific common configuration by defining the transmitting and receiving pulse shapes g and $\tilde{g}$. The q^{th} sample transmitted due to an input symbol $c_{m,n}$ on the m^{th} subcarrier of the n^{th} MC symbol is written as:

$$s_{m,n}[q] = c_{m,n} g_{m,n}[q], \tag{1.33}$$

such that the q^{th} sample of the transmitting pulse $\boldsymbol{g}_{m,n}$ is:

$$g_{m,n}[q] = g[q - nN]\, e^{j2\pi \frac{m(q-nN)}{M}}. \tag{1.34}$$

$c_{m,n}$ are considered to be Quadrature Amplitude Modulation (QAM) symbols in this work. Using equations (1.33) and (1.34), the sample stream of all transmitted symbols summed over n and m will be:

$$s[q] = \sum_{n} \sum_{m} c_{m,n} g[q - nN]\, e^{j2\pi \frac{m(q-nN)}{M}}. \tag{1.35}$$

Following the definition of the channel in equation (1.22), the signal at the input of the receiver (complex baseband representation) will be expressed as:

$$r[q] = \sum_{l=0}^{L-1} h[q, l] s[q - l] + \omega[q], \tag{1.36}$$

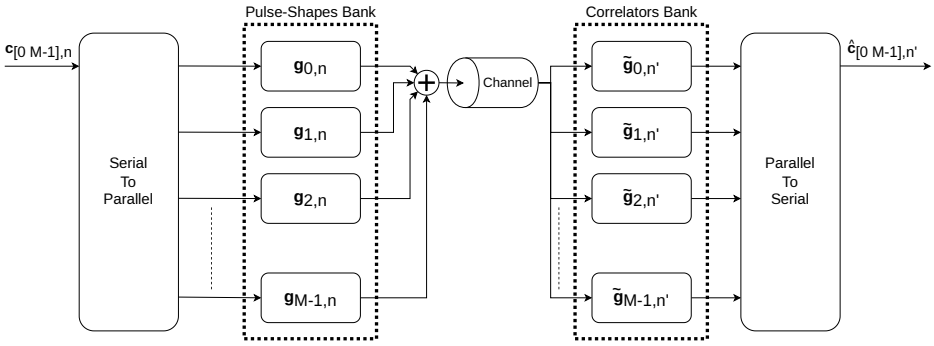

Figure 1.10: System model block diagram.

such that:

- $r[q]$ is the q^{th} sample of the received MC symbol stream $\boldsymbol{r}$,
- $h[q,l]$ is the q^{th} sample of the l^{th} path discrete time-varying channel,
- and $\omega[q]$ is the q^{th} realization of the additive white complex circular Gaussian noise $\boldsymbol{\omega}$.

For simplicity, since ω is a complex random process, we assume that for a complex constant C we have $C \times \omega = |C| \times \omega$, where the multiplication affects only the average amplitude without considering the phase. Using operations matched to those at the transmitter, the received constellation symbol at the m'^{th} subcarrier and the n'^{th} MC symbol $\hat{c}_{m',n'}$ for a specific transmitting subcarrier and symbol indices m and n can be expressed as:

$$\begin{aligned}\hat{c}_{m',n'}|_{m,n} = &\sum_{l}\sum_{q} \tilde{g}^{*}\left[q - n'N\right] \\ &\times \left(h\left[q,l\right] g\left[q - l - nN\right] c_{m,n} + \omega\left[q\right]\right) \\ &\times e^{-j2\pi \frac{(q-nN)(m'-m) - m'N(n'-n) + lm}{M}},\end{aligned} \tag{1.37}$$

having the q^{th} sample of the receiving pulse (or Hermitian symmetric of the receiving filter's impulse response) $\tilde{\boldsymbol{g}}_{m',n'}$ as:

$$\tilde{g}_{m',n'}\left[q\right] = \tilde{g}\left[q - n'N\right] e^{j2\pi \frac{m'(q-n'N)}{M}}. \tag{1.38}$$

This definition of the receiving pulse reflect a conventional linear correlation-based receiver. Summing equation (1.37) over all m and n will give the total contribution of the symbols such that:

$$\begin{aligned}\hat{c}_{m',n'} &= \sum_{n}\sum_{m} \hat{c}_{m',n'}|_{m,n} \\ &= \left\langle \boldsymbol{r}, \tilde{\boldsymbol{g}}_{m',n'} \right\rangle.\end{aligned} \tag{1.39}$$

The total system model is depicted in figure 1.10. Note that additional parts of the detection process (such as equalization) will be added in later chapters. Generalization of equation (1.39)

into an end-to-end matrix results in:

$$\hat{\boldsymbol{c}}_{n'} = \sum_{n} \boldsymbol{H}^{(n',n)} \boldsymbol{c}_n + \boldsymbol{\omega}_{n'}, \tag{1.40}$$

such that $\hat{\boldsymbol{c}}_{n'} = \left[\hat{c}_{0,n'}, \hat{c}_{1,n'}, ..., \hat{c}_{M-1,n'}\right]^T$, $\boldsymbol{c}_n = \left[c_{0,n}, c_{1,n}, ..., c_{M-1,n}\right]^T$, $\boldsymbol{\omega}_{n'} = \left[\omega_{0,n'}, \omega_{1,n'}, ..., \omega_{M-1,n'}\right]^T$ with $\omega_{m',n'} = \left\langle \boldsymbol{\omega}, \tilde{\boldsymbol{g}}_{m',n'} \right\rangle$, and

$$\begin{aligned} H_{m',m}^{(n',n)} = &\sum_{l} \sum_{q} \tilde{g}^* \left[q - n'N\right] h\left[q, l\right] g\left[q - l - nN\right] \\ &\times e^{-j2\pi \frac{(q-nN)(m'-m) - m'N(n'-n) + lm}{M}}. \end{aligned} \tag{1.41}$$

Following the support of g and $\tilde{g}$, we have $H_{m',m}^{(n',n)} \neq 0$ if and only if:

$$\begin{array}{cc} 0 \leq q - l - nN < KN & 0 \leq q - n'N < KN \\ nN + l \leq q < (K+n)N + l & n'N \leq q < (K+n')N \\ \implies \max(n + l/N, n')N \leq q < (K + \min(n + l/N, n'))N & \end{array}. \tag{1.42}$$

Equivalently, $H_{m',m}^{(n',n)} = 0$ for $|n + l/N - n'| \geq K$. As the design of $\boldsymbol{g}$ and $\tilde{\boldsymbol{g}}$ usually tries to achieve the relation in equation (1.28), it can easily be shown that this propagates to $\hat{c}_{m,n} \approx H_{m,m}^{(n,n)} c_{m,n} + \omega_{m,n}$ if $l = 0$ and $h\left[q_1, 0\right] \approx h\left[q_2, 0\right]$ when $|q_1 - q_2| \leq N$. This is related to the simplest scenario of a single path slow-varying channel where the normalized Doppler spread $F_d T_s \to 0$ and the delay spread $\mathcal{T} = 0$. In the next section, we describe the efficient implementation of such systems using FFT and IFFT.

1.2.3.1 Fast fourier transform implementation

In this section, we show how the considered generalized FDM system, similar to OFDM, FBMC and BFDM, can be implemented efficiently using IFFT and FFT. Note that such implementation details are not required to understand this manuscript, but we find it important to provide such details to address how such systems are implemented in practice. Before we go through how this system can be implemented using IFFT/FFT, we will discuss briefly why this is a point of interest instead of implementing it directly using the design equations provided in section 1.2.3. For this analysis, we will focus more on the transmitter-side implementation, as the receiver-side implementation matches it. If we look into equation (1.35) (and equation (1.39)), we can see that the transmission (and detection) procedures requires multiplications and summing over all symbols and subcarriers. If we consider focusing on the symbol n, we can see that its transmitted signal will require summing over all subcarriers ranging from $m = 0$ to $m = M - 1$ as all the subcarriers are transmitted simultaneously. This will require M multiplications having their results aggregated to generate a single sample of the transmitted signal. Knowing that the signal of every symbol has length NK, this will result in a total of MNK multiplications for each MC symbol. However, this straightforward implementation is extremely inefficient, where these multiplications are significantly

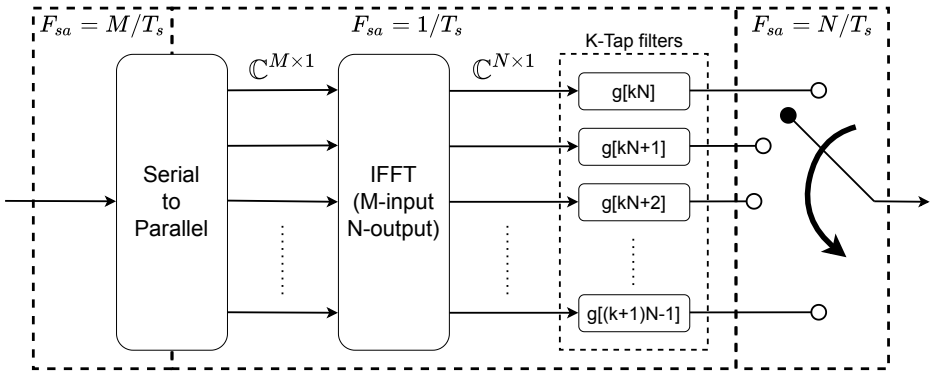

Figure 1.11: IFFT-based polyphase network implementation of a generalized MC transmitter.

redundant.

Consequently, we will consider reducing the redundancy by tackling the sources of redundancy consecutively. The first source of inefficient redundancy is the multiplication by the pulse shape itself. All the subcarriers are shaped using the same pulse shape but shifted into different frequencies. Therefore, while calculating the sample q, we can multiply by the pulse shape after summing over all the subcarriers instead of doing it earlier. This will reduce the number of multiplications by pulse shape taps from MNK to NK. As the pulse shaping in this case can be seen as an up-sampling problem, it can be implemented by polyphase filtering [MBMB07], which aligns perfectly with the current problem. Note that the count of multiplications by the frequency shifting samples ($e^{j\cdots}$) is still MNK. However, since the multiplication is now independent of the pulse shape, this will have a cyclic output of the multiplication, where the output repeats for every M samples. This leads to reducing the multiplication by the frequency shifting samples to M per subcarrier totaling M^2. The current state of optimization leads to M^2+NK multiplications, which still do not use the IFFT/FFT implementation. Note that asymptotically, the complexity will be dependent on M^2, and the term NK will be less significant. Here is where the importance of using IFFT/FFT implementation arises. The definition of the M^2 multiplications of an MC transmitter (and receiver) responsible frequency shifting matches the definition IFFT (and FFT). This allows reducing the computational complexity from M^2 to $Mlog_2(M)$ when M is a power of 2 [CT65], which is generally considered a trivial assumption, since it is only a matter of configuration. This reduces the total complexity of the system, where the transmitter side is depicted in figure 1.11, to $Mlog_2(M) + NK$. The following comments can be given on this figure to describe the behavior of the system:

1. the input constellation symbols are fed to the system at a sampling frequency $F_{sa} = M/T_s$ where every M inputs are grouped to form a single MC symbol input,
2. the group of M constellation symbols are fed parallely to the IFFT, which is computed in $Mlog_2(M)$ and outputs M OFDM-like samples,
3. the output of the IFFT is cyclically extended by having the output at index j be the same at the input at $i = j\%M$ with % the modulo operator, which will have no computational

cost as it is just a matter of output forwarding, noting that this is different from the N-point IFFT,

4. the N cyclic IFFT output samples are fed to N parallel filters of polyphase implementation with average length K (not exactly this length but an average length as it is possible to have the first few filters having one tap more than the rest where KN is necessarily an integer but not K),

5. the filter consuming the a^{th} output of the cyclic IFFT will have the samples of g at indices $kN + a$ with $k \in [0; K - 1]$ by what is known as a polyphase implementation of the filter g [MBMB07],

6. the output of the filters are then picked in a round-robin at a rate N/T_s so that each output symbol is delayed from the previous one by symbol time T_s consisting of N samples having a symbol length KN of duration KT_s,

7. since the samples per symbol time T_s are N at the output and M at the input of the system, we have different sampling rate at the input and at the output, being oversampled when $N > M$ (which is mainly considered in this work), undersampled when $N < M$ (like in [Maz75]), and critically sampled when $N = M$.

The receiver-side will have similar reversed procedure by: parallelizing the input samples, filtering with a polyphase implementation of $\tilde{g}$, applying FFT, then serializing. In the next section, we discuss the pulse shapes we consider for analysis in this work.

1.2.3.2 Pulse shapes

In this section, we introduce the pulse shapes that we use in this work to compare the MC systems introduced previously. To cover as many general cases as possible while considering a small number of pulse shapes, we consider the following pulse shapes due to their properties discussed later in this section: Rectangular (Rect), Out of Band Energy (OBE), Time-Frequency Localized (TFL), Root Raised Cosine (RRC), and Gaussian (Gauss). These pulses can be grouped into three families:

1. time-limited orthogonal pulses: Rectangular (Rect), Out of Band Energy (OBE) and Time-Frequency Localized (TFL),

2. frequency-limited orthogonal pulses: Root Raised Cosine (RRC),

3. and time and frequency semi-limited non-orthogonal pulses: Gaussian (Gauss).

Note that since the pulses Rect, OBE and TFL are time-limited, they will be defined over a single symbol period T_s forming N samples, no matter what K is defining the pulse shape length KN. When $K > 1$ is selected, samples outside the range of definition of the pulse are set to zero. On the other hand, RRC and Gauss are (mathematically) infinitely defined. In

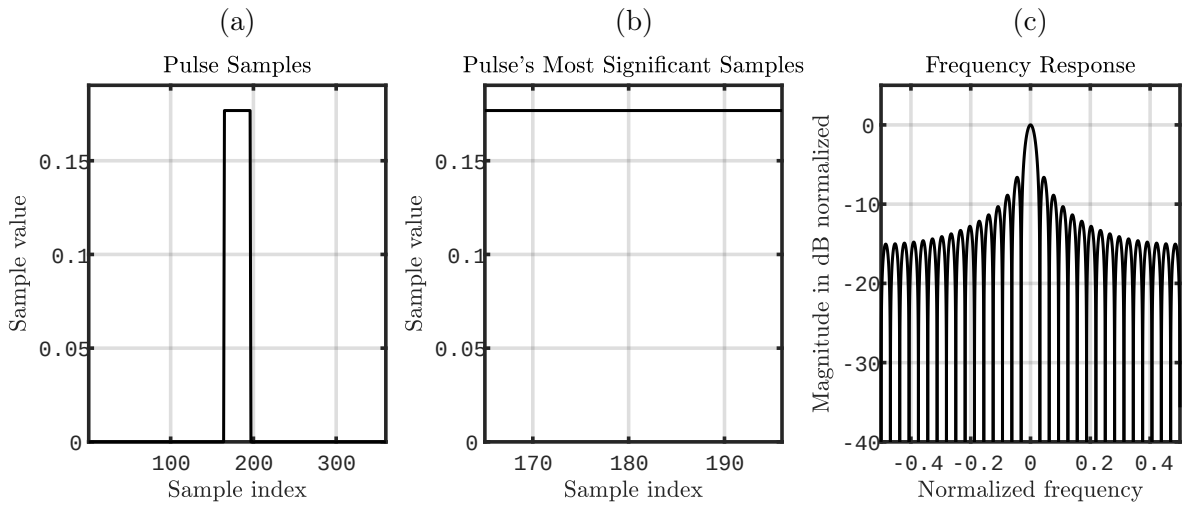

Figure 1.12: Rect pulse time and frequency response for $M = 32$ and $N = 40$.

this section, for representation purposes, we show the properties (and configuration) of these pulses while considering: $M = 32$, $N = 40$, and $K = 9$. Note that the ratio $(N-M)/M = 1/4$ is selected as it is a common configuration of the duration of the cyclic prefix in CP-OFDM. These pulse shapes are selected on the basis of the following criteria:

- Rect pulse shown in figure 1.12. As mentioned above, and shown in figure 1.12.a, this pulse is limited in time, and is padded with zeros for $K > 1$. However, for practical implementation, this pulse can be implemented using only the samples in figure 1.12.b. Notice that the practical 'most significant' samples are $M = 32$ samples. This is due to the fact that the Rect pulse shape shown in this section is that without CP. It can be converted to the CP version by extending its length to $N = 40$ samples so that the added $N-M = 8$ samples precede the original ones. The Rect pulse matches the orthogonality criterion in equation (1.28), although it is spreading in the frequency domain as shown in figure 1.12.c, which is the main disadvantage of Rect pulse as will be discussed in details later. This pulse is considered the simplest pulse to use and is adopted by OFDM and CP-OFDM. Therefore, we consider this pulse for comparison to account for them.

- OBE pulse shown in figure 1.13, used to compare with the time-limited orthogonal pulse shapes family. As shown in [PS11], OBE pulses are designed to have minimal out-of-band emissions as a time-limited pulse, where the band is simply the bandwidth allocated for a channel (B/M). This can be noticed through figure 1.13 where the time-limiting property is shown in (a) and (b), while the frequency response shown in (c) shows how OBE has 'side lobes' with lower energy compared to Rect. Note that this pulse occupies all the N samples in contrast to Rect, which uses M samples unless CP is used. In addition to that, CP is not possible to implement for such pulses as it is a unique property of cyclic pulses such as the Rect pulse. Similarly to Rect, this pulse is orthogonal to its time- and frequency-shifted versions satisfying equation (1.28). This pulse is considered for comparison as ICI is a major concern in fast-varying environments

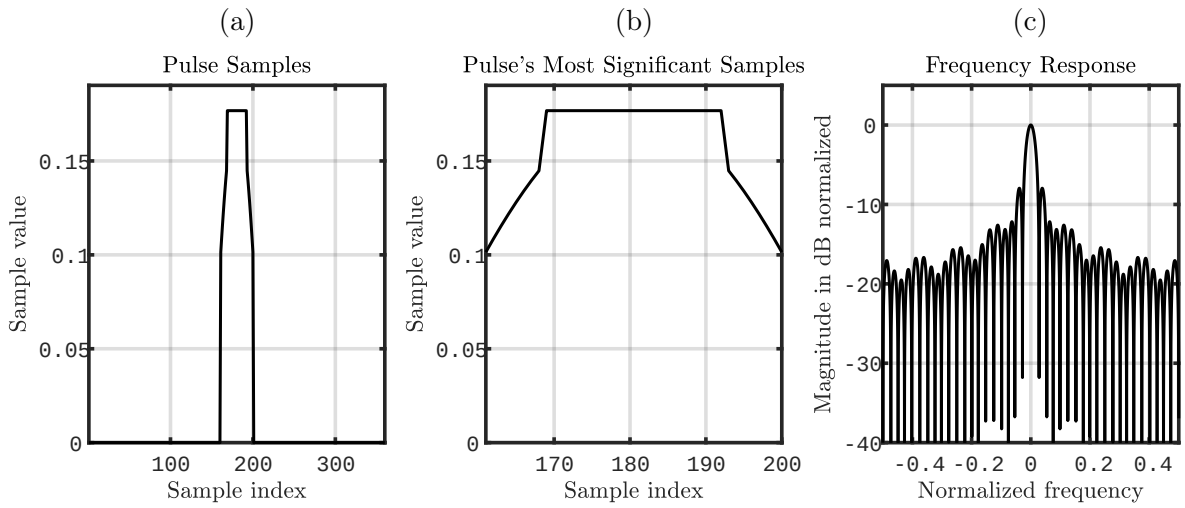

Figure 1.13: OBE pulse time and frequency response for $M = 32$ and $N = 40$.

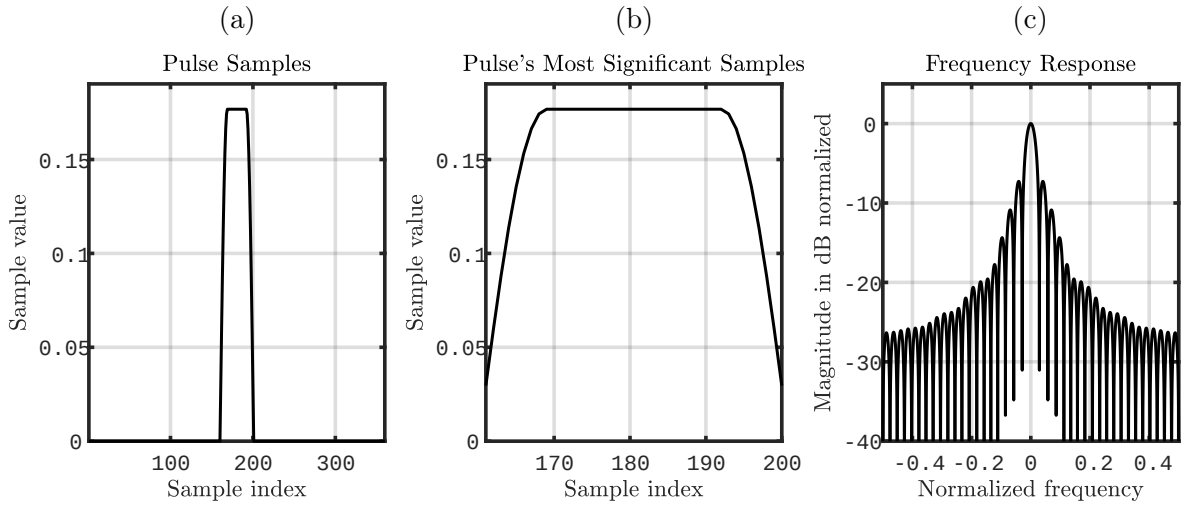

Figure 1.14: TFL pulse time and frequency response for $M = 32$ and $N = 40$.

as briefly discussed in section 1.1.4 and will be discussed in section 1.3.2. As OBE pulse minimized the out-of-band emission, it is expected to reduce ICI.

- TFL pulse shown in figure 1.14. The TFL pulse is similar to the pulse OBE in many aspects, where both are time-limited of length N, orthogonal, and designed following a minimization criterion that would assist in interference reduction. This pulse was proposed in the same work as OBE [PS11]. However, instead of minimizing the out-of-band energy, this pulse minimizes the product of second moments in time and frequency for discrete-time signals as define in [Dor98]. Note that this criterion considers both time and frequency localization, in contrast to OBE which focuses only on the frequency response of the pulse. It is worth mentioning the second moment gives more impact to values far from the center than values close to it. Taking into account the effect of this minimization criterion on the shape of the pulse, it can be seen from figure 1.14.b that the

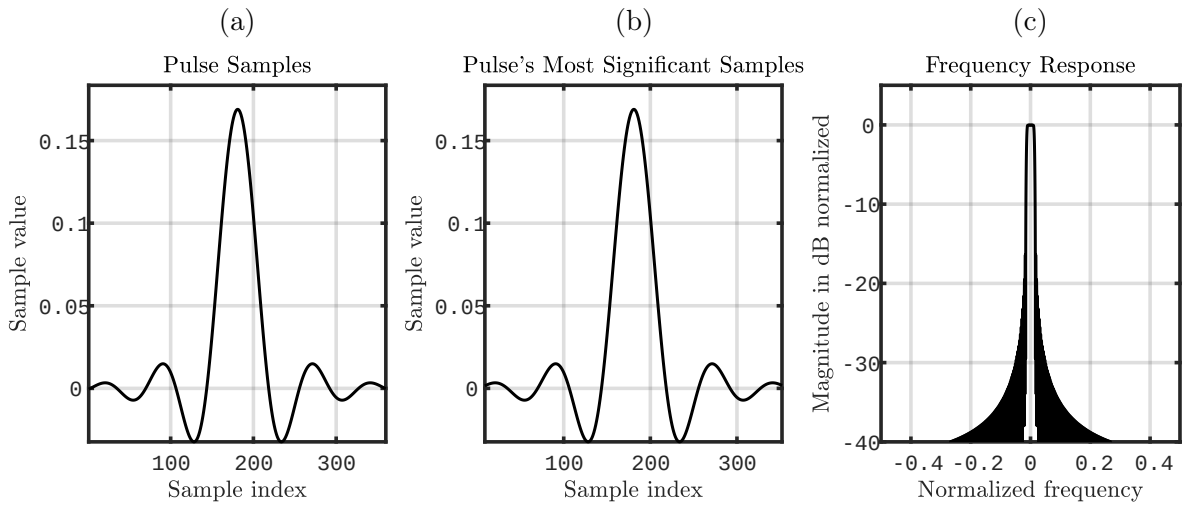

Figure 1.15: RRC pulse time and frequency response for $M = 32$, $N = 40$ and roll-off $\beta = 0.25$.

edges of the pulse in time decay smoothly toward values around zero. In the frequency domain, although we can see that the frequencies close to the center have response higher than Rect and OBE, it reduces more significantly at farther frequencies reaching levels lower than both Rect and OBE. ICI is not the only interference that should be avoided. ISI is another possible impairment that should be accounted for, especially when considering multi-path channels. As TFL is better 'localized' in both time and frequency domains, it is expected to reduce ISI and ICI. Therefore, it is considered for comparison in this work.

- RRC pulse shown in figure 1.15 referenced also as 'RRC$^{\beta}$' in this work, where β is the roll-off factor, used to compare with the band-limited orthogonal pulse shapes family. In this section, we use roll-off $\beta = (N - M)/M = 0.25$ since it is the maximum β that can be used while limiting the pulse bandwidth to B/M for total MC bandwidth B using the considered M and N. The RRC pulse samples were generated by taking samples at $t = kT_{sa}$ $k \in \mathbb{Z}$ using equation (1.43) below [DRL08]:

$$g_{\beta}(t) = \begin{cases} \frac{1}{T_{sa}}\left(1 + \beta\left(\frac{4}{\pi} - 1\right)\right), & t = 0 \\ \frac{\beta}{T_{sa}\sqrt{2}}\left[\left(1 + \frac{2}{\pi}\right) sin\left(\frac{\pi}{4\beta}\right) + \left(1 - \frac{2}{\pi}\right) cos\left(\frac{\pi}{4\beta}\right)\right], & t = \pm\frac{T_{sa}}{4\beta} \\ \frac{1}{T_{sa}} \frac{sin\left[\pi\frac{t}{T_{sa}}(1-\beta)\right] + 4\beta\frac{t}{T_{sa}} cos\left[\pi\frac{t}{T_{sa}}(1+\beta)\right]}{\pi\frac{t}{T_{sa}}\left[1 - \left(4\beta\frac{t}{T_{sa}}\right)^2\right]}, & \text{otherwise} \end{cases}. \tag{1.43}$$

Figure 1.15.a shows how the RRC pulse spreads significantly over time. This means that the consecutive pulse will overlap in time although they maintain (approximate) orthogonality among them. However, this might make consecutive RRC pulses vulnerable to channel variation, as will be discussed later in section 1.3.2. Figure 1.15.b shows that all the samples of the RRC pulse are considered 'significant'. In fact, RRC pulse will require an infinite length to be perfectly orthogonal. However, depending on the roll-off factor β, the pulse duration can be truncated keeping 'approximate' orthogonality. Fig-

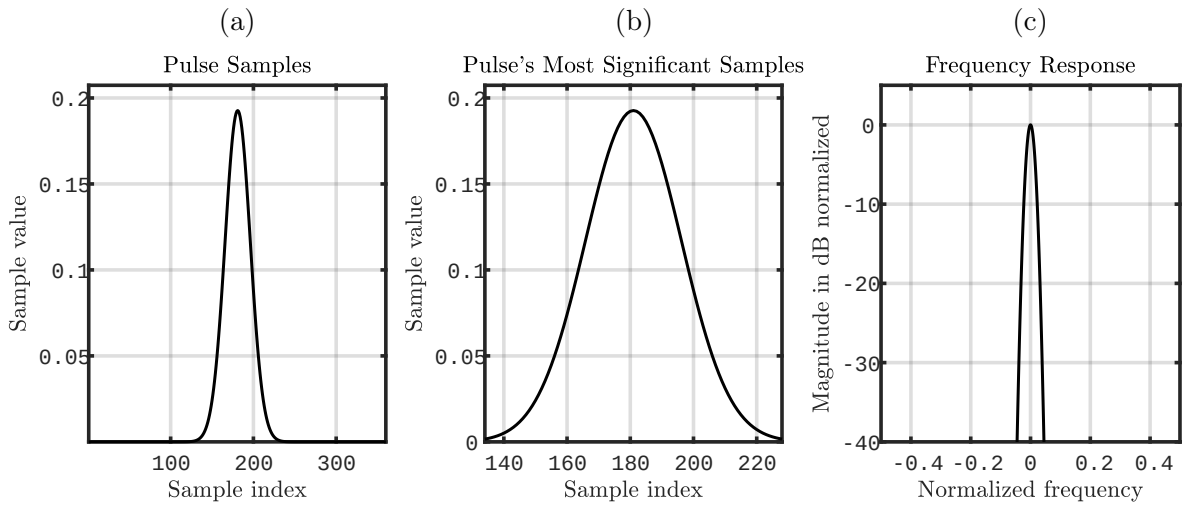

Figure 1.16: Gauss pulse time and frequency response for $M = 32$ and $N = 40$.

ure 1.15.c shows the frequency-limited frequency response of the considered RRC pulse. This will make MC systems using the RRC pulse have their subcarriers non-overlapping in frequency in addition to being orthogonal, contrary to the time-limited pulse shapes where they maintained orthogonality while overlapping in the frequency domain. The frequency-limited property makes the RRC pulse a candidate to reduce the impact of channel variation by significantly reducing ICI. Therefore, it was selected as one of the pulses to compare in this work.

- Gauss pulse shown in figure 1.16, used to compare with the non-orthogonal pulse shapes family, yet semi-limited in both time and frequency domain. Gauss were used for mobile communication in GSM through the Gaussian Minimum Shift Keying (GMSK) technique [MH81]. However, in this work, we configure Gauss pulse variance to achieve minimal and nearly equal ISI and ICI for static or slow-varying channels ($F_d T_s \to 0$) while using the considered M, N, and K. This was done by brute-force simulations using the Gaussian equation:

$$g_\sigma(t) = \frac{1}{\sigma\sqrt{2\pi}} e^{\frac{-t^2}{2\sigma^2}}, \tag{1.44}$$

for variance σ^2 and time instance $t = kT_{sa}$ $k \in \mathbb{Z}$. Although the Gauss pulse is infinitely defined, figure 1.16 shows how the 'most significant' samples are limited to a number of samples around the center. For the considered variance optimization criteria, we found that $K \approx 3$ is sufficient for the Gauss pulse implementation. Among the pulses considered for comparison, the Gauss pulse is the only one that does not satisfy equation (1.28). However, we find it an interesting pulse to use in comparison due its special property of having limited spreading in both time and frequency domains.

In the next section, we analyze the impact of multi-path propagation (delay spread) and channel variation (Doppler spread) on the MC systems.

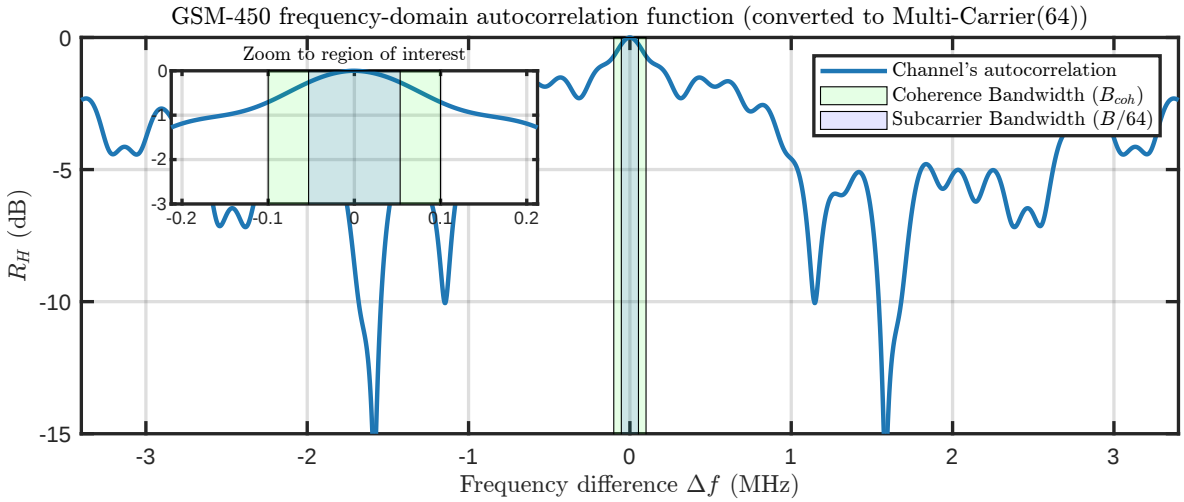

Figure 1.17: GSM-450 frequency-domain autocorrelation function and coherence bandwidth considering the standard GSM. Subcarrier bandwidth is also shown if we assume transmitting over the same channel using 64-carrier MC system.

1.3 Channel's Impact on Multicarrier Systems

In this section, we discuss how Multi-Carrier (MC) systems are impacted by the main two channel impairments in mobile communication: multi-path propagation which will be discussed in section 1.3.1 and shown how and why MC systems are robust against it, and channel variation which will be discussed in section 1.3.2 and shown how MC systems are vulnerable to this effect.

1.3.1 Multipath propagation and multicarrier systems

As we mentioned several times earlier in this chapter, MC systems are considered robust against multi-path propagation. Nothing can be considered ultimately resistant to any impairment. However, when we consider MC systems robust to multi-path frequency-selective channels, that is in comparison to the other alternative which uses a single-carrier. Therefore, we recall the GSM example we provided in section 1.1.3 for comparison. GSM channels are statistically expected to have a delay spread $\mathcal{T} = 5\mu$s. This leads to a coherence bandwidth $B_{coh} = 0.2$MHz, which is 34 folds of the narrowest GSM channel GSM-450 of bandwidth $B = 6.8$MHz. This will lead to frequency-selective behavior that causes difficulties in channel estimation, channel equalization, and symbol recovery. Assuming that we would replace GSM by an MC system when using the same channel to overcome this weakness, we will consider an $M = 64$ MC system. This system will divide the bandwidth B by M, leading to a subcarrier bandwidth of $B/M = 6.8\text{MHz}/64 = 0.10625\text{Mhz} \approx 1/2B_{coh}$ instead of having $B = 34B_{coh}$. Recalling figure 1.3 from section 1.1.3, we reproduced the same figure but adding the new subcarrier bandwidth in figure 1.17. The channel autocorrelation function is shown over the whole bandwidth of 6.8MHz. As discussed above, the coherence bandwidth (shaded in green)

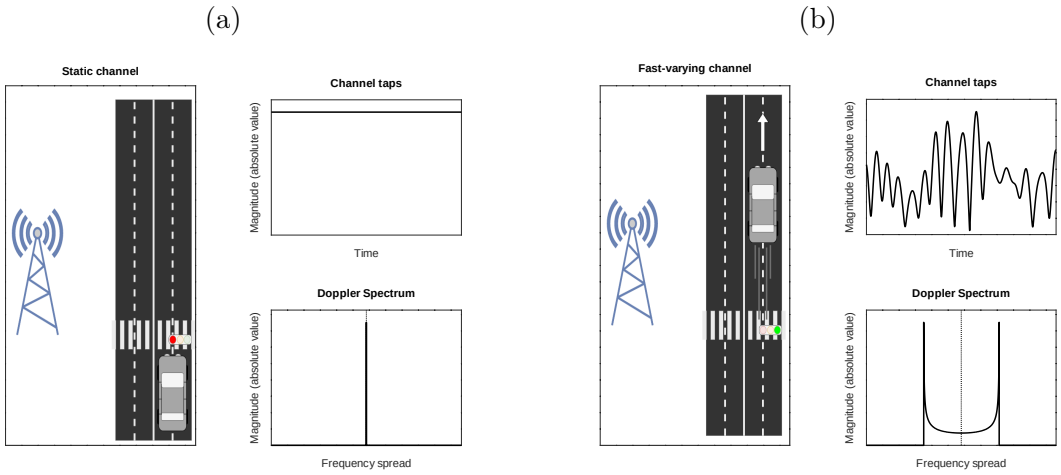

Figure 1.18: Slow (a) and fast (b) time-varying channels illustrations.

is very narrow compared to the GSM-450 bandwidth (spanning the whole X-Axis). On the other hand, after dividing the bandwidth B to 64 subcarriers, the new bandwidth (shaded in blue) appears to be narrower than the coherence bandwidth. This narrowed bandwidth is approximately fully correlated as it can be seen in the zoomed version of the figure. This will convert a single highly selective channel into 64 parallel channels with less selectivity. Consequently, if the number of subcarriers is high enough, this can result into having an approximately flat-fading channel per subcarrier. Due to the properties just described, MC are generally considered more robust to multi-path propagation, away from further improvements that some MC systems have (like CP-OFDM as discussed in section 1.2.2.2). In the next section, we discuss the other impairment we focus on in this work, which is channel variation, and its impact on MC systems.

1.3.2 Doppler spread and multicarrier systems

In this section, we discuss the impact of the Doppler spread on MC systems by focusing on two of the most common pulses: Rect and RRC. We first illustrate the impact of the motion on the time and frequency response of the channel. Later we discuss the impact of this channel response mutation on ISI and ICI. A more detailed discussion is provided in chapter 2.

1.3.2.1 Communication channel variation and system's parameters

For MC transmissions, since the data are multiplexed over several subcarriers, these subcarriers should have minimal cross-talk. For this reason, classical FDM techniques used pulse shaping with reduced subcarrier bandwidth and a guard-band between subcarriers. More advanced techniques like OFDM, FBMC, and BFDM reduced this cross-talk to zero without introducing guard-bands by designing orthogonal waveform. As seen in figure 1.18.a, a static (or slow fading) channel having no (or negligible) time-variation will have no (or negligible) spreading

in the Doppler frequency domain. Then, in static or slow fading channels – if no other impairments are considered – will maintain the properties of the designed pulse shapes in terms of interference avoidance. However, for both scenarios: basic and advanced techniques, a fast-moving transceiver will suffer from a fast-varying channel leading to a Doppler frequency spreading behavior as illustrated in figure 1.18.b. Such a Doppler frequency spreading channel will break the orthogonality and alter the time-frequency localization for orthogonal techniques and expand wider than the guard-band if it is not sufficient for classical FDM techniques; consequently, introduce ICI in both cases.

More accurately, to state if a *communication channel* is a slow or fast fading channel, we have to compare the dynamic parameters of the *propagation channel* to those of the *communication system*. A communication channel will be considered as a slow fading one if it has a negligible variation within one MC symbol period T_s expressed as $T_{\text{coh}} \gg T_s$, where T_{coh} is the coherence time of the channel. Equivalently, it means that the maximum Doppler spread F_d should be negligible compared to the symbol rate $F_s = 1/T_s$, *i.e.* $F_d \ll F_s$. In other words, the variation speed of a communication channel can be stated by the value of the normalized Doppler frequency $F_d T_s$, where T_s is the MC symbol time, and F_d the Doppler frequency. Using the just-mentioned $F_d T_s$ metric, a communication channel is considered to be slow-varying if $F_d T_s \ll 1$, conventionally recognized as $F_d T_s \leq 10^{-2}$ or 10^{-3}. In contrast, the fast-varying communication channel corresponds to an increase in F_d and then a decrease of T_{coh} such that $T_{\text{coh}} \to T_s$ so that $F_d T_s \to 1$ (or even further). A communication channel is conventionally recognized to be fast if $F_d T_s \geq 0.1$. Notice that for a channel to be invariant for some pulse of duration KT_s and maintain the orthogonality of the pulses, the variation should be negligible throughout the duration of the pulse KT_s not just over T_s. However, the study will consider the input parameter $F_d T_s$ to compare the pulses to get a fair comparison for a given Doppler spread and a given MC symbol rate $F_s = 1/T_s$, even if the pulses have different durations.

To facilitate further analysis in this section, we have the following:

- the channel is assumed to be a single path channel (only for this section) to focus on the channel variation impact,
- Δ_c is the subcarrier offset between the transmitting and receiving subcarrier frequency normalized to subcarrier bandwidth such that:

$$\Delta_c = m' - m, \tag{1.45}$$

- Δ_s is the time offset between the transmitting and receiving symbols normalized to symbol duration such that:

$$\Delta_s = n' - n, \tag{1.46}$$

- and Δ is a two-element array used to simplify the referencing to both Δ_c and Δ_s such that:

$$\Delta = [\Delta_c \;\; \Delta_s]. \tag{1.47}$$

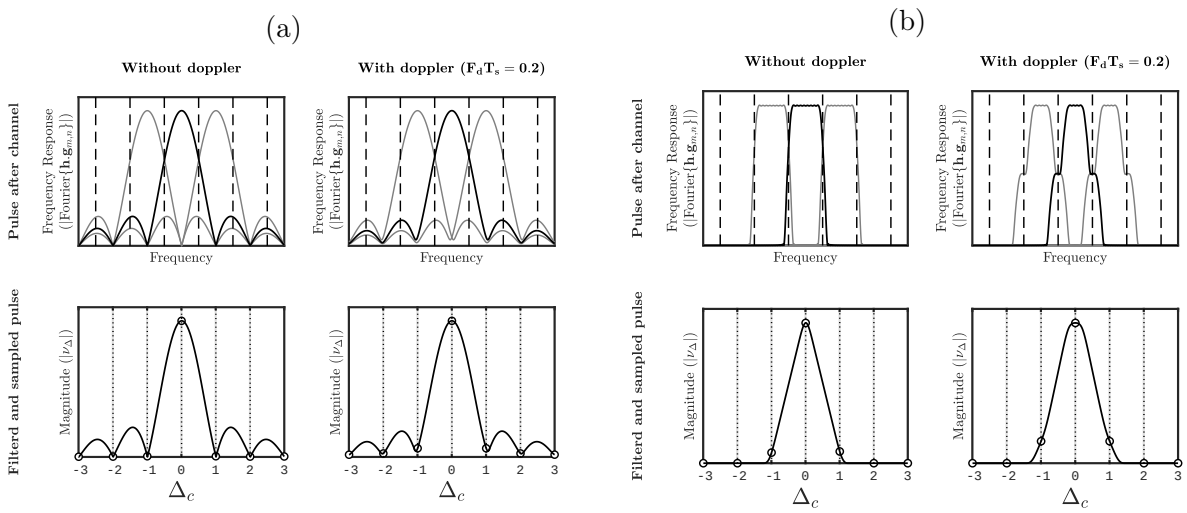

Figure 1.19: Doppler spread impact frequency-domain for Rect (a) and RRC (b) pulses.

We modify equation (1.28) used as a design target for the orthogonal pulse shapes to account for the channel values:

$$\nu_{\Delta} = \left\langle \boldsymbol{h}_n . \boldsymbol{g}_{m,n}, \tilde{\boldsymbol{g}}_{m',n'} \right\rangle \approx \begin{cases} \text{Const}, & \text{if } \Delta = [0 \;\; 0], \\ 0 & \text{otherwise}, \end{cases} \tag{1.48}$$

with $\boldsymbol{h}_n = [h[nN], h[nN+1], ..., h[nN+KN-1]]^T$ being the channel samples affecting the signal within the support of $\boldsymbol{g}_{m,n}$. This metric ν_{Δ} will match the approximation of equation (1.48) when the pulses can maintain approximate orthogonality even when having a variable channel. This approximation will not be always possible to be achieved, especially in fast variation, and the 'deviation' from it will account to the amount of ICI and ISI.

1.3.2.2 Doppler-generated-ICI

In this section, we discuss and illustrate the impact of channel variation on MC systems in frequency domain. A detailed illustration of the impact of Doppler spread in the frequency domain on the most popular time-limited pulse shape (Rect) and the most popular frequency-limited pulse shape (RRC) is shown in figure 1.19. In each sub-figure (a and b) of this figure, the first column represents the static channel scenario (without Doppler) or slow-varying channel. The second column represents the scenario with a fast-varying channel (strong variations within one T_s, such that $F_dT_s = 0.2$). The frequency-domain magnitude of one given subcarrier pulse after the channel is shown in the first row, with adjacent subcarriers shown in a shade of gray. The space between two vertical dashed lines delimits the minimal bandwidth, $B_{sc}^{\min} = 1/T_s$, for every subcarrier that is required to satisfy ICI and ISI free communication according to the Nyquist criterion [PS08]. It is worth mentioning that for the scenarios analyzed in figure 1.19, the system is configured such that the space between subcarriers, $F_s = 1/T_s$, corresponds to $B_{sc}^{\min}$, i.e. $F_s = B_{sc}^{\min}$. In the second row, the magnitude response to one given

transmit (TX) subcarrier pulse ($\boldsymbol{g}_{m,n}$) is computed after being subjected to channel's (possibly variable) gains ($\boldsymbol{h}_n.\boldsymbol{g}_{m,n}$). We show the matched correlation with RX pulses $|v_\Delta|$ with arbitrary RX Carrier Frequencies, where Δ_c is the difference between transmitting and receiving subcarrier frequencies normalized to F_s. Equivalently, the (continuous) solid-line plots reflects $|v_\Delta|$ for $\Delta_c \in \mathbb{R}$. The frequency of each RX subcarrier (which reflects RX Carrier Frequencies of integer multiple of F_s) is shown by vertical dotted lines and the magnitude calculated at each subcarrier is shown by a black circle. Equivalently, the values represented by the black circles reflects $|v_\Delta|$ for $\Delta_c \in \mathbb{Z}$. All for $\Delta_s = 0$ as we target, for now, the ICI only.

Focusing, for instance, on the impact of Doppler spread on the Rect pulse shown in figure 1.19.a, in a static channel, the symbol pulse is similar at the transmitter output and the receiver input. That's because the signal is multiplied by a constant. Consequently, the frequency-domain shape of the pulse is not altered. The magnitude at each subcarrier position after the receiving correlation is zero except for the desired center frequency since the pulse is perfectly aligned although not well localized ($|\nu_\Delta| = 0$ for $\Delta_c \in \mathbb{Z}^*$). It can be noticed that the value rapidly increases after getting zero at the exact subcarrier frequency. Therefore, any offset (or synchronization error) in the subcarriers grid position or Doppler spreading in the channel response will lead to severe interference at all subcarriers. For the time-varying channel, the symbol pulse at the receiving correlator input is different from the one at the output of the transmitting pulse shape due to multiplication by a variable channel gain within one symbol period T_s. Consequently, the pulse frequency is spread in the Doppler frequency domain. This change in the frequency response of the pulse leads to a different response after the correlation at the receiver, resulting in non-zero values even at RX subcarriers positions different than the center desired TX position. The just observed cross-talk can be called Doppler-generated-ICI as it breaks equation (1.48) by having $|\nu_\Delta| > 0$ for one or more values $\Delta_c \in \mathbb{Z}^*$.

Now, we focus on the 'other pole' of pulse shapes, the frequency-limited time-spreading RRC pulse shown in figure 1.19.b. We consider a roll-off factor $\beta = 0.25$ for representation purposes. It can be noticed that, even in a static channel, slight ICI is generated. This is due to the roll-off parameter of the RRC pulse shape used. In practice a 0 roll-off cannot be realized due to the infinite-length impulse response which is hard to truncate due to the strong side lobes. As we assume here a minimum subcarrier spacing ($F_s = 1/T_s$), this roll-off will generate interference. Note that the subcarrier spacing may however be greater in the general model of section 1.2.3. In a fast-varying channel, the spread in frequency increased the interference. However, it is still limited to the first adjacent neighbors in contrast to time-limited pulse shapes which had interference spreading over all the other subcarriers.

1.3.2.3 Doppler-generated-ISI

Another interesting impact of the Doppler effect in the time domain, already occurring for single carrier systems, is illustrated in figure 1.20 for the Rect pulse shape (a) and the RRC pulse shape (b). In each sub-figure of this figure, the first column represents the scenario of a static channel (without Doppler), and the second column represents the scenario with a fast-

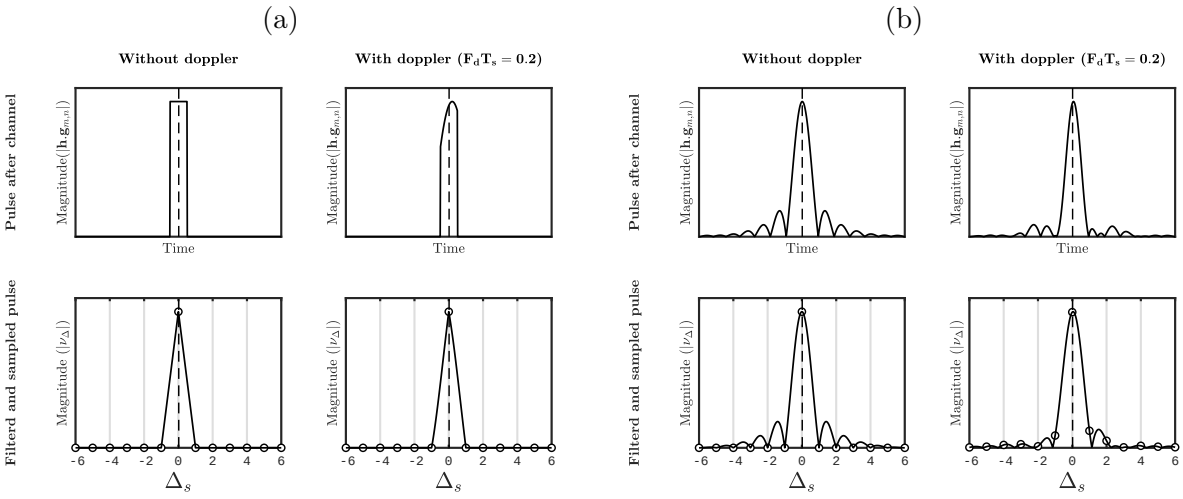

Figure 1.20: Doppler spread impact time-domain for Rect (a) and RRC (b) pulses.

varying channel (with strong normalized Doppler). The 0Hz subcarrier pulse after channel (corresponding to $\boldsymbol{h}_n.\boldsymbol{g}_{0,n}$) is shown in the first row and will next be considered as the only input for the receiver (in the input of $\tilde{g}_{0,n'}$ in figure 1.10). In the second row, we then show the magnitude response to this pulse after correlation, with the RX carrier frequency equal to the desired TX frequency ($\Delta_c = 0$), but computed for different time offsets.

The magnitude is calculated for each arbitrary time offset $\Delta_s \in \mathbb{R}$, and discrete symbol time offsets such that $\Delta_s \in \mathbb{Z}$ are shown by black circles. Due to having a time-limited pulse of Rect pulse shape as shown in figure 1.20.a, in a single path fast-varying channel, the pulse values will vary without introducing any interference power to the adjacent symbols. Consequently, the magnitude calculated in the second row is maximum at the desired symbol offset and zero otherwise for both scenarios with no Doppler and with high Doppler ($|\nu_\Delta| = 0$ for $\Delta_s \in \mathbb{Z}^*$).

On the other hand, for a frequency-limited/time-spreading pulse such as the RRC pulse shown in figure 1.20.b, in a single path static channel, although the pulse spreads in the time domain, it still maintains the orthogonality where the inner product at offsets of integer multiples of a symbol period is zero except for the desired symbol ($|\nu_\Delta| = 0$ for $\Delta_s \in \mathbb{Z}^*$). It means that the ISI-free Nyquist criterion [PS08] is satisfied. On the other hand, for fast-varying channels, the orthogonality is broken due to the alteration of the shape of the spreading pulse and consequently changing the results of the inner-products to have $|\nu_\Delta| > 0$ for some $\Delta_s \in \mathbb{Z}^*$ what can be called Doppler-generated-ISI. Although ISI is not the first concern to be usually considered when studying fast-varying channels, it appeared that for frequency-limited pulse shapes such as RRC, ISI might be more significant than ICI. More details about ISI and ICI are provided in chapter 2. In the next section, we describe a positive phenomenon resulted by Doppler spread, which is diversity.

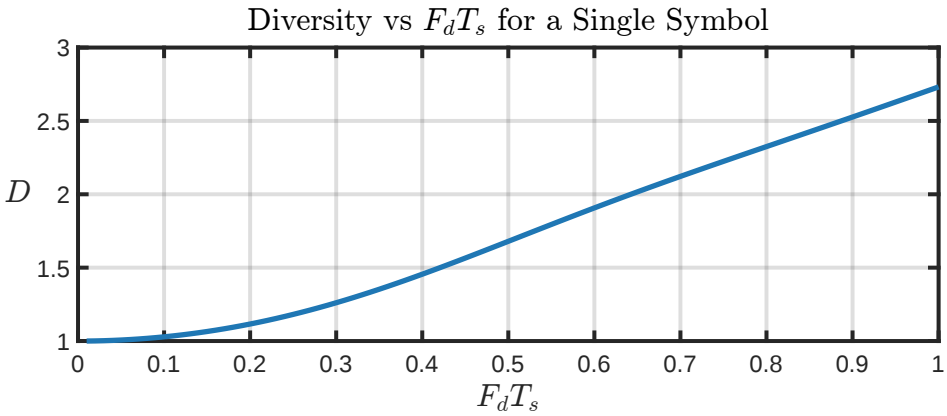

Figure 1.21: Doppler-generated-diversity in single symbol and single carrier scenario.

1.3.2.4 Doppler-generated-diversity

In the previous two sections, we have discussed the two types of interference that might be generated due to Doppler spread, ICI and ISI. In contrary, in this section, we provide discussion about a positive phenomenon that is generated by the Doppler spread, which is diversity the would lead to performance improvement. As we did in the previous two sections, we will isolate effects other than the desired one, like disregarding noise and other phenomenons affecting the signal. Therefore, we will provide the Doppler-generated-diversity analysis for only single symbol and single carrier. To quantify this diversity, we will use the equivalent number of independent branches for Rayleigh fading channels [DZB98]; [RJA01]. Following this derivation, we have:

$$D = 1 \Big/ \text{var}\left\{\frac{E_s}{\text{E}\{E_s\}}\right\}, \tag{1.49}$$

where D is the equivalent diversity order, E_s is the received symbol energy, var{.} is the variance operator, and E{.} is the expectation operator. As a simple model for this single symbol scenario, we have:

$$r[q] = h[q]c + \omega[q] \quad q \in [1; N], \tag{1.50}$$

where r is the complex baseband received signal, h is the Rayleigh channel complex tap with Jakes' Doppler spectrum (see equations (1.13) and (1.14)), c is the unitary power symbol, ω is additive white complex circular Gaussian noise, and N is the number of samples. The received symbol energy is then:

$$E_s = \sum_{q=1}^{N} ||h[q]c||^2. \tag{1.51}$$

In figure 1.21, we plot the diversity D versus the normalized Doppler spread F_dT_s for the provided setup. We fix the Doppler frequency F_d, and vary F_dT_s by increasing the number of samples N. The value of D is calculated using equations (1.49) to (1.51) numerically through using 10^6 realizations for every point of the plot. We can observe how the diversity continuously increase with the increase of F_dT_s. Note that such value of diversity reflect

equivalent number of independent branches based on variance of symbol energy, which can have non-integer values of D, in contrary to straight forward scenarios having D as an integer [Ros16]. This type of diversity in single path channel with a simple single carrier system is discussed in more details in appendix A.

In this section, we have provided computations of Doppler generated diversity without considering the complications of having multiple symbols, multiple carriers, and what receiver implementation is exploited. In MC systems, as the one we consider in this work, the three discussed effects of Doppler spread are combined, what makes the actual gain lower than the simple one provided. In section 3.6, we provide an approximation of the total diversity than can be generated by Doppler spread. In the next section, we provide a brief introduction and background on channel estimation and equalization in MC systems.

1.4 Channel Estimation and Equalization in Multicarrier Systems

In this section, we discuss some of the existing techniques for estimation, equalization, and joint estimation-equalization for MC systems. The contribution of this work in the context of equalization and estimation is presented in chapters 3 and 4, respectively. When considering channel estimation in MC systems, there are mainly two approaches:

- preamble-based estimation [Kof+13]; [Par+03]; [Lél+08] based on transmitting a block of preamble symbols before transmitting the data symbols,
- and comb-type pilot-based estimation [HW98]; [Col+02b]; [LLS08]; [RHS14] based on transmitting pilot subcarriers within the data symbols.

As we target fast-varying channels in this work, we are not interested in the former, and we will study only comb-type pilot-based estimation. The literature contains a lot of work in the context of channel estimation mainly for OFDM and FBMC.

Although FBMC is more general than OFDM, and its estimation [Sti+10]; [BWK15]; [Cui+15] and equalization [Iha+06]; [IL09]; [Lin+09]; [NLS12] problems are well investigated, we consider OFDM for this section as it is the most known variant of MC systems. The discussion of MC equalization in chapter 3 and channel estimation in chapter 4 is more detailed and considers general FDM as in section 1.2.3.

Various comb-type pilot-based OFDM channel estimation methods exist. The authors in [CVC01] proposed a time-domain channel estimation for time-varying channels. This technique requires Singular Value Decomposition (SVD) and matrix inversion of matrices of size in the order of the number of subcarriers which is usually very large; thus, it may not be feasible in practical systems. It is more common to consider frequency-domain estimation in OFDM like in [SL03], where pilot-based estimation is considered, then the channel response

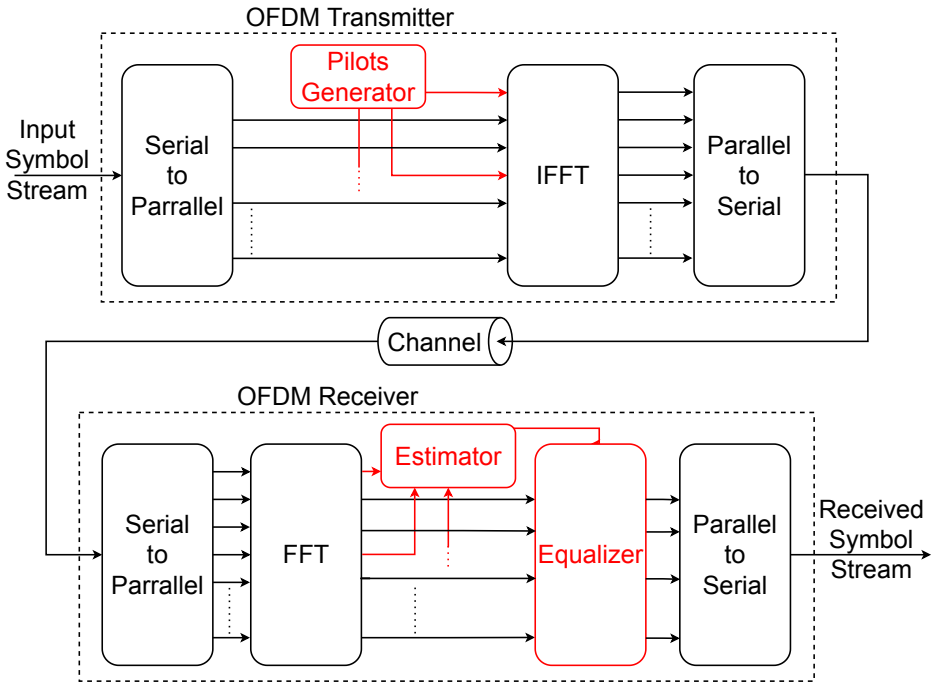

Figure 1.22: Comb-type pilot-based OFDM channel estimation and equalization.

is obtained by interpolation. Some other works consider some assumption on the channel like varying in a linear behavior within a single symbol [Tom+05]. However, such works lead into low performance in fast-varying channels. The authors in [MC05] proposed two methods to mitigate ICI in an OFDM system employing piece-wise linear approximation. Least Square (LS) estimation has been proposed in [ABS07], yet again being not very suitable for the rapidly varying channels in addition to high computational complexity. The list of pilot-assisted OFDM channel estimators is endless; however, the majority of estimators follows the concept depicted in figure 1.22. Similar to the basic OFDM of sections 1.2.2.1 and 1.2.3.1, a stream of symbols $c_{m,n}$ is parallelized to be transmitted over several subcarriers. However, since pilot subcarriers are to be inserted (assuming P subcarriers), if M subcarriers are to be used in total, only $M - P$ subcarriers can be used for data. Therefore, the symbols $c_{m,n}$ are packed into groups of $M - P$ symbols instead of M. As a result, the index m can take values such that:

$$m \in \{[0; M-1]\} - \mathcal{P}, \tag{1.52}$$

where $\mathcal{P}$ is the set of indices of the P pilot subcarriers. The most common distribution of the pilots is by (cyclically) equally distributing them over the M subcarriers by having the k^{th} pilot subcarrier index $p_k \in \mathcal{P}$:

$$p_k = \text{round}\left(k\frac{M}{P}\right), \tag{1.53}$$

for $k \in [0; P-1]$. Pilot symbols are generated – commonly as constants – and fed to the IFFT similar to the normal data symbols. At the receiver, after the FFT, the output at the pilot subcarriers is fed to the estimator. Commonly, the estimator uses the values observed at

the pilot subcarrier of the current symbol and the previous symbols (and possibly future ones implemented through delays) to interpolate the frequency response of the channel [Zha+09]. Several interpolation methods can be considered, and the Basis Expantion Model (BEM) is the most considered one especially when some statistical information of the channel is available. Examples of BEM are discrete Karhunen-Loeve [TO05], discrete-prolate spheroidal [ZM05], complex-exponential [GT98], and polynomial [HR08a] BEMs. Some works consider combining several BEMs [MT07]. This response is fed to an equalizer to account for the channel variation (and delay spread) to enable detection. Many existing works view the frequency domain channel matrix as being diagonal, thus completely ignoring ICI or strictly banded as in [HW07], [NC98], and [AJ04]. However, such assumptions are inaccurate in OFDM systems operating in time-varying channels, especially when varying rapidly.

It is clear that the equalization performance is dependent on the accuracy of the estimation. On the other hand, the estimation performance is dependent on the ICI that the pilot subcarriers receive from the data subcarriers. As mitigating this interference would improve the estimation performance, and thus the equalization performance, it is common to perform joint estimation and equalization in a decision feedback fashion in fast-varying channels. The works [CTW05] and [Tan+07] are concerned with channel estimation and equalization based on different BEM assumptions. An algorithm has been proposed in [HR10] for estimating the Rayleigh complex channel gains and detecting the data jointly for OFDM systems in fast fading channels, assuming the channel delays are known a priori. In [PSP10] and [SPP12], joint estimation and equalization have been presented for OFDM systems operating in high mobility channels based on the Space-Alternating Generalized Expectation-maximization (SAGE) technique.

OFDM strictly requires joint estimation and detection to perform well in fast-varying environments, as shown in all references cited above and [HR08b]. This is due to the spreading ICI of the Rect pulse adopted in OFDM as shown in section 1.3.2.2. As in this work we consider various pulse shapes that are not as spreading as OFDM, we deal with the equalization and estimation problems separately in chapters 3 and 4 respectively. In the next section, we introduce the organization of this document and summarize its contribution.

1.5 Document's Organization and Contribution

This work was carried out at "Grenoble Images Parole Signal Automatique Laboratoire" GIPSA-Lab, Grenoble, France, specifically in the Image and Signal Department in the "Geometrie, Apprentissage Information et Algorithmes" GAIA division. It was funded by LabEx PERSYVAL-Lab (ANR-11-LABX-0025-01) funded by the French program Investissement d'avenir and the Lebanese International University, Beirut, Lebanon. The objective of this work is to study the performance of pulse-shaped Multi-Carrier systems when operating in extremely fast-varying channels, analyze the impact of pulse-shape selection on the performance in such scenarios analytically and through testing, and provide relevant channel estimation and channel equalization techniques optimized to operate for rapidly varying channels.

In chapter 2, we theoretically calculate the interference power generated at every symbol and subcarrier due to the transmission of a specific symbol and subcarrier, when assuming conventional correlator receiver. The derived equations are used later in the same chapter to calculate the values of ISI, ICI, and the aggregate value Inter-Symbol and Inter-Carrier Interference (ISCI) for various scenarios. This analysis is done for single path and multi-path channels and verified by Monte Carlo simulations. Following the obtained values of ISCI, we then discuss the need of reducing the transmission density to reduce interference if no sophisticated equalization is employed. Theoretical interference power equations are extended to include arbitrary density reduction factors. In chapter 3, we discuss the importance of assisting equalization by performing time-domain preprocessing when considering multi-carrier communication over fast-varying Rayleigh channels. Two low-complexity time-domain-assisted equalizers are proposed and assessed when assuming perfect Channel State Information (CSI) then showed to have similar performance for realistic to inaccurate channel estimation. Bit Error Rate (BER) comparison is provided for several equalizers and pulse shapes, and additional processing in the time domain is shown to improve performance and benefit from channel variation rather than being negatively affected. Diversity–BER mapping is introduced to calculate a proposed Doppler-driven diversity equivalence per pulse shape. This is then linked to the pulse shape's properties. It is shown how pulses that are less localized in time tend to achieve higher Doppler-driven diversity equivalence. To account for ISI that can be issued by less localized pulse shapes in such scenarios, ISI-cancellation technique is proposed and shown to converge towards the ideal ISI-cancellation after a single iteration.

In chapter 4, we introduce the concept of adding comb-type pilots in the time-domain instead of frequency-domain to allow having continuous pilot over consecutive symbols independent of the considered pulse shapes. This new pilot insertion technique is then related to the existing form of pilots in OFDM by providing the pilot symbols required to have an equivalent output in both techniques. Estimation using these comb-type pilots is then proposed using the Wiener filters directly in the time-domain assuming statistical properties of the channel are known The performance of this estimation is then presented for various Doppler spread values and Signal to Noise Ratio (SNR) values and compared with state-of-the-art techniques. This filtering is considered to be optimal when using a frequency isolating pulse shape like the RRC.

1.6 Conclusion

In this chapter, we have discussed the details of the background and context of this work. We have described the properties of a mobile communication channel in section 1.1. We discussed the characteristics of such channels and described them mathematically. We defined the channel's two main properties we consider: the delay spread and the Doppler spread. We then derived the equivalent discrete-time channel to be used in the later parts. In section 1.2, we provided a brief history of MC systems. We then discussed the most common orthogonal MC systems: OFDM, CP-OFDM, FBMC, and BFDM. Later in the same section, we have discussed the generalized FDM system we assume for this work and provided its FFT implementation

in addition to the pulse-shapes that will be used for comparison in later chapters. After that, we checked the impact of the mobile channel discussed in section 1.1 on systems similar to the ones discussed in section 1.2, and provided the related discussion in section 1.3. In this section (1.3), we have discussed briefly how problems caused by the delay spread can be easily resolved in MC systems, while channel variation would cause negative effects that we called Doppler-generated-ICI and Doppler-generated-ISI in addition to creating a positive effect that we called Doppler-generated-diversity. Later in section 1.4, we discussed some of the channel estimation, channel equalization, and joint channel estimation-equalization techniques that are used in MC systems and mainly in OFDM. Finally, we have presented the organization of the document and its contribution in section 1.5.

Chapter 2

Inter-Symbol and Inter-Carrier Interference Analysis for Multicarrier Systems

Contents

In this chapter, we present a detailed theoretical derivation of the interference power generated at every received symbol and subcarrier due to the transmission of a specific symbol and subcarrier, for the general multi-carrier system through fading random channel described in the previous chapter. The derived equations are used later in the same chapter to calculate the values of Inter-Symbol Interference (ISI), Inter-Carrier Interference (ICI), and the aggregate value Inter-Symbol and Inter-Carrier Interference (ISCI) for various scenarios. This analysis is done for basic conventional correlator receiver in single path and multipath channels and verified by Monte Carlo simulation. Following the obtained values of ISCI, we then discuss the need of reducing the transmission density to reduce interference if no sophisticated equalization is employed. Theoretical interference power equations are extended to include arbitrary density reduction factors. As this chapter focuses on the impact of channel variation, delay spread, and pulse impairments, we disregard the noise.

2.1 Interference Computation

In this section, we compute the power observed at the receiver output, and we derive the statistical value of this power. After that, we use this derived power to provide the definition we adopt for the interference.

2.1.1 Received power for received-transmitted symbols pairs

To compute the received power, we recall equation (1.37) from section 1.2.3:

$$\begin{aligned}\hat{c}_{m',n'}|_{m,n} = &\sum_{l}\sum_{q} \tilde{g}^*[q-n'N] \\ &\times \left(h[q,l]g[q-l-nN]c_{m,n} + \omega[q]\right) \\ &\times e^{-j2\pi\frac{(q-nN)(m'-m)-m'N(n'-n)+lm}{M}}.\end{aligned}$$

Note that n and $n' \in \mathbb{N}$, m and $m' \in [0\ M-1]$, $l \in [0\ L-1]$ where L is the number of discrete time paths, and the range of q defined by equation (1.42). This equation describes how a constellation symbol $c_{m,n}$ transmitted over the subcarrier m of the Multi-Carrier (MC) symbol n is contributing into $\hat{c}_{m',n'}$ observed at the output for the receiving subcarrier m' of the MC symbol n'. In this chapter, as mentioned before, since we are focusing on interference analysis, we disregard the noise impact by setting $\omega[q] = 0$. Therefore, following the observation of equation (1.37), the contribution of a constellation symbol $c_{m,n}$ transmitted over subcarrier m of the MC symbol n to the power $\mathcal{P}_{m',n'}$ observed at the output for the receiving subcarrier m' of the MC symbol n' is:

$$\begin{aligned}\mathcal{P}_{m',n'}|_{m,n} = |\hat{c}_{m',n'}|_{m,n}|^2 &= \left(\hat{c}_{m',n'}\hat{c}^*_{m',n'}\right)\big|_{m,n} \\ &= \sum_{l}\sum_{l'}\sum_{q}\sum_{q'} \tilde{g}^*[q-n'N]\tilde{g}[q'-n'N] \\ &\times h[q,l]h^*[q',l']g[q-l-nN]g^*[q'-l'-nN] \\ &\times e^{j2\pi\frac{(q'-q)(m'-m)+(l'-l)m}{M}}|c_{m,n}|^2.\end{aligned} \tag{2.1}$$

To simplify the calculation, we introduce the index $\gamma = q - l - nN$ (and equivalently $\gamma' = q' - l' - nN$). Replacing in equation (2.1):

$$\begin{aligned}\mathcal{P}_{m',n'}|_{m,n} = &\sum_{l}\sum_{l'}\sum_{\gamma}\sum_{\gamma'} \tilde{g}^*[\gamma-(n'-n)N+l]\tilde{g}[\gamma'-(n'-n)N+l'] \\ &\times h[\gamma+nN+l,l]h^*[\gamma'+nN+l',l']g[\gamma]g^*[\gamma'] \\ &\times e^{j2\pi\frac{(\gamma'-\gamma)(m'-m)+(l'-l)m'}{M}}|c_{m,n}|^2.\end{aligned} \tag{2.2}$$

If the power received due to all the transmitted symbols is needed, this can be obtained through summing over all of them such that the total received power will be:

$$\mathcal{P}_{m',n'} = \sum_{n}\sum_{m} \mathcal{P}_{m',n'}|_{m,n}. \tag{2.3}$$

These equations permits to calculate the power based on a specific observation of transmission/reception. In the next section, we derive the statistically expected value of the interference power.

2.1.2 Theoretical received power

Following the observation-based received power derived in section 2.1, in this section, we will calculate the expected value of the received power depending on the transmitting and receiving subcarrier and symbol indices. Applying the expectation operator $E\{\}$ to the expression in equation (2.2), we have the following:

$$\begin{aligned} P_{m',n'}|_{m,n} &= E\left\{\mathcal{P}_{m',n'}|_{m,n}\right\} \\ &= \sum_{l}\sum_{l'}\sum_{\gamma}\sum_{\gamma'} \tilde{g}^*[\gamma-(n'-n)N+l]\tilde{g}[\gamma'-(n'-n)N+l'] \\ &\times g[\gamma]g^*[\gamma']e^{j2\pi\frac{(\gamma'-\gamma)(m'-m)+(l'-l)m'}{M}} \\ &\times E\left\{h[\gamma+nN+l,l]h^*[\gamma'+nN+l',l']|c_{m,n}|^2\right\}. \end{aligned} \tag{2.4}$$

Following the trivial assumption of normalizing the power of the transmitted symbols, we have $E\{|c_{m,n}|^2\}=1$. The power will accordingly be defined as:

$$\begin{aligned} P_{m',n'}|_{m,n} &= \sum_{l}\sum_{l'}\sum_{\gamma}\sum_{\gamma'} \tilde{g}^*[\gamma-(n'-n)N+l]\tilde{g}[\gamma'-(n'-n)N+l'] \\ &\times g[\gamma]g^*[\gamma']\sigma_l\sigma_{l'}R_h(\gamma-\gamma'+l-l',l-l')e^{j2\pi\frac{(\gamma'-\gamma)(m'-m)+(l'-l)m'}{M}}, \end{aligned} \tag{2.5}$$

where σ_l is the l^{th} path standard deviation, and R_h is the channel multi-dimensional autocorrelation function defined by:

$$R_h(\Delta_q,\Delta_l) = E\left\{h[q,l]h^*[q-\Delta_q,l-\Delta_l]\right\}. \tag{2.6}$$

However, following the Wide Sense Stationary Uncorrelated Scatterers (WSSUS) assumption considered in chapter 1, $R_h(\gamma-\gamma'+l-l',l-l')=0$ when $l\neq l'$. Therefore, we set $l=l'$ and remove the path index from R_h so that the expected received power can be written as:

$$\begin{aligned} P_{m',n'}|_{m,n} &= \sum_{l}\sigma_l^2\sum_{\gamma}\sum_{\gamma'} \tilde{g}^*[\gamma-(n'-n)N+l]\tilde{g}[\gamma'-(n'-n)N+l] \\ &\times g[\gamma]g^*[\gamma']R_h(\gamma-\gamma')e^{j2\pi\frac{(\gamma'-\gamma)(m'-m)}{M}}. \end{aligned} \tag{2.7}$$

As can be seen from equation (2.7), the expected power does not depend on the values of m, n, m', and n' but on the differences $m'-m$ and $n'-n$. Changing these differences by $\Delta_c = m'-m$ and $\Delta_s = n' - n$ defined in equations (1.45) and (1.46), respectively, in equation (2.7), we obtain equation (2.7) in terms of $\Delta = [\Delta_c\ \Delta_s]$:

$$\begin{aligned} P_{\Delta=[\Delta_c\ \Delta_s]} = \sum_l \sigma_l^2 \sum_\gamma \sum_{\gamma'} \tilde{g}^*[\gamma - \Delta_s N + l]\tilde{g}[\gamma' - \Delta_s N + l] \\ \times g[\gamma]g^*[\gamma']R_h(\gamma - \gamma')e^{j2\pi\frac{(\gamma'-\gamma)\Delta_c}{M}}. \end{aligned} \tag{2.8}$$

Following Jakes' model [Cla68]; [JC94] as discussed in section 1.1.4, the auto-correlation function R_h can be defined as:

$$R_h(\gamma - \gamma') = J_0(2\pi F_d T_{sa}(\gamma - \gamma')), \tag{2.9}$$

where J_0 is the Bessel function of its first kind and order 0, F_d is the Doppler frequency, and T_{sa} is the sample time. Finally, plugging this into equation (2.8), we have:

$$\begin{aligned} P_\Delta = \sum_l \sigma_l^2 \sum_\gamma \sum_{\gamma'} \tilde{g}^*[\gamma - \Delta_s N + l]\tilde{g}[\gamma' - \Delta_s N + l] \\ \times g[\gamma]g^*[\gamma']J_0(2\pi F_d T_{sa}(\gamma - \gamma'))e^{j2\pi\frac{(\gamma'-\gamma)\Delta_c}{M}}. \end{aligned} \tag{2.10}$$

In the next section, we provide the definition of interference we adopt for this work.

2.1.3 Interference definition

To be able to have comparison at the level of interference power, we need to introduce what definitions of power and interference we adopt. In MC systems, interference can be defined by two terms ICI and ISI. Ideally, the values of this interference should be zero (or negligible), and the total power received should be equal to the desired power, so that no "non-desired" part is observed. Equivalently, the power of the desired components P_{desired} at the output of the bank of RX pulse shapes represents all the receiver power P_{received} such that:

$$P_{\text{received}} \approx P_{\text{desired}} = P\big|_{m'=m,n'=n} = P_{\Delta=[0\ 0]}. \tag{2.11}$$

However, due to some channel or pulse shape imperfections, it is possible to have:

$$P_{\text{desired}} < P_{\text{received}} = P_{\text{desired}} + P_{\text{non-desired}}, \tag{2.12}$$

where $P_{\text{non-desired}}$ is the power received from the non-desired components, i.e. the interference power in this work. ICI is an impairment in MC systems caused mainly due to Doppler spread as shown in section 1.3.2.2. It is a form of signal distortion in which one symbol interferes with the symbols of the adjacent subcarriers. In this document, the value ICI refers to the

ratio defined below:

$$\mathrm{ICI} = \frac{P_{\mathrm{ICI}}}{P_{\mathrm{desired}}} = \sum_{\Delta_c} \frac{P_{\Delta=[\Delta_c\ 0]}}{P_{\Delta=[0\ 0]}} \qquad \Delta_c \in \mathbb{M}^*, \tag{2.13}$$

where $\mathbb{M}$ is the set of all possible (integer) values of Δ_c such that $\mathbb{M} = [-M/2; M/2-1]$, and $\mathbb{M}^*$ is the non-zero components of $\mathbb{M}$. ISI is another impairment in communication systems mainly due to delay spread. Another important possible cause of ISI for orthogonal pulse shapes that overlap in the time domain is the rapid variation of the channel where the orthogonality of the time successive adjacent pulse shapes may be broken, as shown in section 1.3.2.3. In this document, the value ISI refers to the ratio defined below:

$$\mathrm{ISI} = \frac{P_{\mathrm{ISI}}}{P_{\mathrm{desired}}} = \sum_{\Delta_c,\Delta_s} \frac{P_{\Delta=[\Delta_c\ \Delta_s]}}{P_{\Delta=[0\ 0]}} \qquad \Delta_s \in \mathbb{Z}^*, \tag{2.14}$$

where $\mathbb{Z}^*$ is the set of all non-zero integers. Although Δ_s is defined for $\mathbb{Z}^*$, $P_{\Delta=[\Delta_c\ \Delta_s]}$ practically have non-zero value only for $\Delta_s \in \mathbb{K}^*$ where $\mathbb{K} = \left[-K+1; K-1+\lceil\frac{L-1}{N}\rceil\right]$, and $\mathbb{K}^*$ is the non-zero components of $\mathbb{K}$. A term ISCI combining ICI and ISI is defined as:

$$\mathrm{ISCI} = \frac{P_{\mathrm{ISI}}+P_{\mathrm{ICI}}}{P_{\mathrm{desired}}} = \frac{P_{\mathrm{ISCI}}}{P_{\mathrm{desired}}} = \frac{\sum_{\Delta} P_{\Delta\neq[0\ 0]}}{P_{\Delta=[0\ 0]}} = \frac{P_{received}-P_{\Delta=[0\ 0]}}{P_{\Delta=[0\ 0]}} = \frac{P_{received}}{P_{\Delta=[0\ 0]}} - 1. \tag{2.15}$$

Therefore, ICI, ISI, and ISCI refer here to the Interference to Signal Ratio. This definition of the interference is adopted since it is the reciprocal of the Signal to Interference Ratio (SIR), fully relevant in absence of noise. Note that, from equation (2.10), we can see that the received power and by extension ICI, ISI, and ISCI, depend directly on two factors:

1. design of the pulse shapes g and $\tilde{g}$,
2. and the normalized Doppler spread $F_dT_s = NF_dT_{sa}$.

In the next section, we provide interference power analysis using the statistical and observation-based power observation in single path channels.

2.2 Interference in Single Path (Flat Fading) Channels

As mention in section 1.2, MC systems are mainly used to reduce the impact of multipath (like ISI and frequency selectivity). However, MC transmissions are also used for multiple access [Won+99], broadcasting [SLK97], satellite communications [WJ08], and terahertz communications [Her+17] through scenarios where a single path channel can be assumed. For example in terahertz communications, MC is used mainly for its parallelization feature to avoid implementation issues. In addition to that, we find it interesting to study the impact of the Doppler spread and pulse shapes without further effects to understand their impact. Consequently, in this section, we assume a single path channel ($L = 1$) with unit power ($\sigma_0^2 = 1$), and analyze

multipath scenarios in later sections. This assumption will reduce equation (2.2) to:

$$\begin{aligned}\mathcal{P}_{m',n'}|_{m,n} = &\sum_{\gamma}\sum_{\gamma'} \tilde{g}^*[\gamma-(n'-n)N]\tilde{g}[\gamma'-(n'-n)N] \\ &\times h[\gamma+nN]h^*[\gamma'+nN]g[\gamma]g^*[\gamma'] \\ &\times e^{j2\pi\frac{(\gamma'-\gamma)(m'-m)}{M}}|c_{m,n}|^2.\end{aligned} \tag{2.16}$$

and reduce equation (2.10) to:

$$\begin{aligned}P_{\Delta} = &\sum_{\gamma}\sum_{\gamma'} \tilde{g}^*[\gamma-\Delta_s N]\tilde{g}[\gamma'-\Delta_s N] \\ &\times g[\gamma]g^*[\gamma']J_0(2\pi F_d T_{sa}(\gamma-\gamma'))e^{j2\pi\frac{(\gamma'-\gamma)\Delta_c}{M}}.\end{aligned} \tag{2.17}$$

In later parts of this section, equation (2.16) will be used to perform Monte Carlo simulations of the interference power, and equation (2.17) will be used to calculate the expected interference power. Both to be used with equations (2.13) to (2.15) to calculate ICI, ISI, and ISCI. Note that for this section, as we assume single path channels, time-limited pulses such as Rectangular (Rect) pulse with a Cyclic-Prefix (CP) implementation, Out of Band Energy (OBE) pulse, and Time-Frequency Localized (TFL) pulse will not introduce ISI as discussed in section 1.3.2.3. Therefore, for such pulses, the focus will be only on ICI. For Gaussian (Gauss) and Root Raised Cosine (RRC) pulses, the discussion will focus on both ICI and ISI.

2.2.1 Simulations configuration and parameters

In this chapter, we are providing interference power values using both: the derived (statistical) theoretical, and Monte Carlo simulations. For the Monte Carlo results, we use 5000 observations, and we display them in figures using scattered markers signified by the subscript 'MC' in legends. The number of MC symbol sample spacing $N = 40$, the number of subchannels $M = 32$, and the pulse span in terms of MC symbols $K = 9$ are considered for this section (which leads to a pulse length of $K \times N = 360$ samples). The configuration of M and N results in $T_s = NT_{sa}$ and $F_s = \frac{B}{M} = \frac{N}{MT_s}$ for sample time T_{sa}, symbol time T_s, subcarrier spacing F_s, and total MC bandwidth B. Note that for the setup considered, a ratio of $N/M = 1.25 > 1$ is used, which signifies an oversampled Frequency Division Multiplexing (FDM) system with a subcarrier spacing $F_s = 1.25 \times B_{sc}^{min}$ (contrary to section 1.3.2 where $F_s = B_{sc}^{min}$). A ratio greater than 1 (oversampled) was adopted since according to Balian-Low Theorem [Bat88], it is not possible to get well time-frequency localized pulses while considering critical sampling. Equivalently, it is impossible to limit the pulse spreading in both time and frequency if the number of samples of the pulse equals the number of subcarriers. This localization property of the pulse shapes will be shown later to significantly affect the interference level and its distribution. The pulse shape at the receiver is assumed to be matched to the transmitter's pulse shape, which means that $\tilde{g}_{m,n} = g_{m,n}$. In the next section, we provide an analysis in terms of total interference.

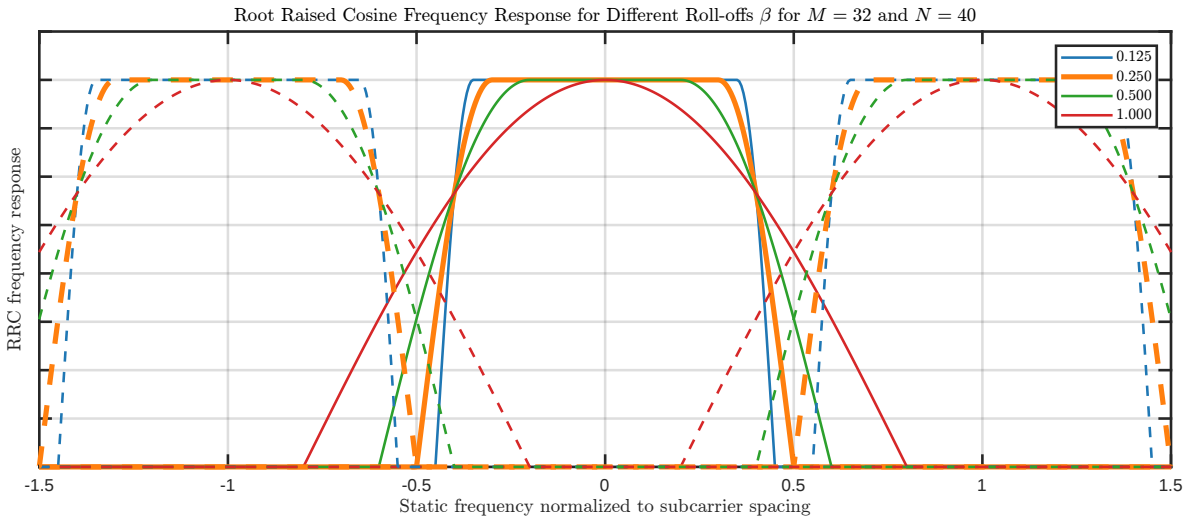

Figure 2.1: RRC frequency response for different values of roll-off β.

2.2.2 Total interference (ISCI) power comparison

To have a general view of the pulses performance, we first analyze the levels of ISCI (as defined in equation (2.15)) before providing more detailed analysis in later sections. We will consider checking the performance for the pulse shapes discussed in section 1.2.3.2. Note that one of these pulse shapes is RRC, which is parametrized by the roll-off factor β. As we have mentioned, we will reference the RRC pulse with roll-off β as RRC$^{\beta}$. We considered two values of the roll-off factor β for the RRC pulse:

1. $\beta = (N - M)/M = 0.25$ since it is the maximum β that can be used while limiting the pulse bandwidth to B/M for total MC bandwidth B using the M and N considered as seen in figure 2.1,
2. and $\beta = 1$ to limit Doppler-generated-ISI as much as possible (see section 1.3.2.3).

In figure 2.2, a plot of ISCI versus Doppler spread F_dT_s is shown. The axes floating in middle of the figure plots the same information with a logarithmic x-axis to emphasize the values at low F_dT_s. First of all, we can see in figure 2.2 that the simulation results obtained using equation (2.16) matches with the analytic formula presented in equation (2.17). This observation stands for all the Monte Carlo simulations of this chapter and will not be re-stated. For low Doppler spread, it is clear how the Gauss pulse shape generates the most ISCI due to its non-orthogonal nature (even for no Doppler spread). For the RRC pulse shape, although it is theoretically orthogonal, as a band-limited pulse shape it has an unlimited impulse response that cannot be realized. Consequently, for the RRC$^{\beta=1/4}$ pulse, it generates slight interference even for no Doppler spread due to the orthogonality broken by the truncation. On the other hand, for RRC$^{\beta=1}$, there is significantly higher interference where most of it is generated due to the high roll-off factor. Such an effect for roll-off 1 is because of having the pulse shape bandwidth of $\frac{2}{T_s}$ while the subcarrier spacing is $F_s = \frac{N}{MT_s} = \frac{1.25}{T_s}$. Time-limited pulse

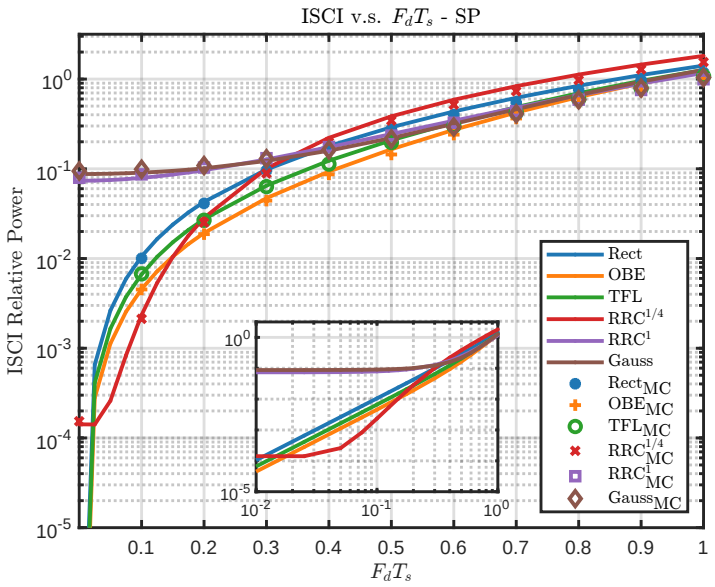

Figure 2.2: ISCI versus F_dT_s for different pulse shapes.

shapes, such as Rect, TFL and OBE, that can be easily realized, have no interference due to no Doppler spread. For all pulse shapes, ISCI increases as the Doppler spread increases as expected. However, RRC$^{1/4}$ pulse shape is the most affected one. Rect, OBE, and TFL are affected less than RRC$^{1/4}$ with OBE slightly better than the other time-limited pulse shapes. The Gauss pulse shape is the least affected by the Doppler spread since it has no orthogonality to be broken. RRC^{1} is also slightly affected since it is limited in both time and frequency domain with most of the interference accepted in the frequency domain.

It is known that the main concern due to the Doppler spread is ICI, as we show in section 1.3.2.2. Such effect is expected to be the lowest in frequency-limited pulse shapes, but it is shown that OBE, which is a time-limited frequency-unlimited pulse shape, has the lowest interference in single path channels. Consequently, further analysis is required focusing on the level of ICI and the level of ISI separately.

2.2.3 Inter-carrier interference

We will consider ICI-based analysis before the ISI as it is the main concern when considering a fast-varying channel, especially in single path channels.

2.2.3.1 ICI versus doppler spread

Figure 2.3 shows the levels of ICI (as defined in equation (2.13)) versus the normalized Doppler spread. It shows how time-limited pulse shapes, such as Rect pulse, OBE pulse, and TFL pulse, have the ICI plot similar to the ISCI plot of figure 2.2 due to the no time-overlapping

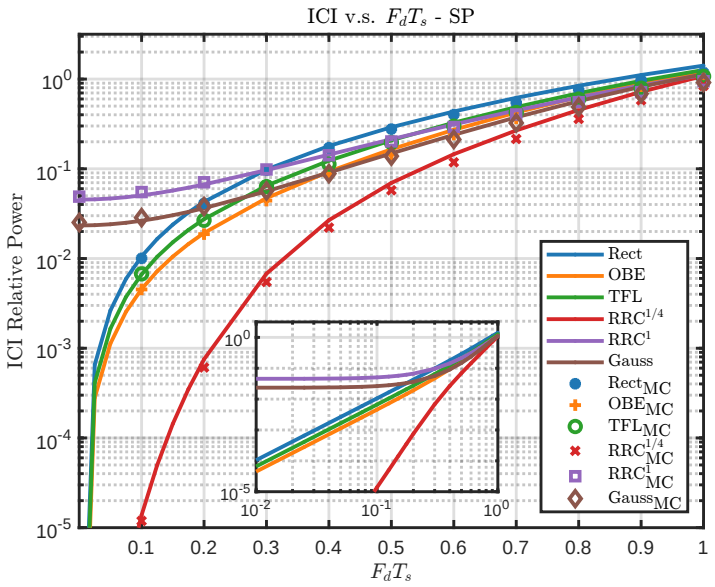

Figure 2.3: ICI versus F_dT_s for different pulse shapes.

nature of these pulse shapes. Regarding the pulse shapes Gauss and RRC, since they have ISI parts, they have ICI lower than ISCI. Figure 2.3 shows that RRC$^{1/4}$ pulse shape has the best performance in terms of ICI which is expected due to its frequency-limited nature (minimum out of band power). However, to have a better view of this interference, it is better to have a deeper look into its properties. In the next section, we present how this interference is distributed over subcarriers.

2.2.3.2 ICI versus received-transmitted carrier offset

Figure 2.4 shows the power normalized received per subcarrier offset per pulse shape for $F_dT_s = 0$ and $F_dT_s = 0.2$ in sub-figures (a) and (b) respectively all normalized to the desired power having $\Delta = [0\ 0]$. In other words, the term P_{Δ_c} is plotted versus Δ_c. To facilitate the reading and analysis of this figure, we recall the definition of ICI from section 2.1.3 equation (2.13):

$$\text{ICI} = \frac{P_{\text{ICI}}}{P_{\text{desired}}} = \sum_{\Delta_c} \frac{P_{\Delta=[\Delta_c\ 0]}}{P_{\Delta=[0\ 0]}} \qquad \Delta_c \in \mathbb{M}^*.$$

In figure 2.4, we plot $\frac{P_{\Delta=[\Delta_c\ 0]}}{P_{\Delta=[0\ 0]}}$ versus $\Delta_c \in \mathbb{M}$. Note that when $\Delta_c = 0$, this represents the desired power $P_{\Delta=[0\ 0]}$, while for $\Delta_c \neq 0$, it represents an ICI component coming from a sub-carrier $|\Delta_c|$ subcarriers away from the desired one. The values of $\mathcal{P}_\Delta$ and P_Δ are calculated equations (2.16) and (2.17) for simulated and expected values, respectively. These plots show that Rect, OBE and TFL pulse shapes have higher ICI than RRC$^{1/4}$, as it was shown previously in figure 2.3. In addition to that, we can see from figure 2.4.b that the interference of the three considered time-limited pulse shapes spread over the subcarriers, having the Rect with the worst spreading. TFL has a more contained interference thanks to its localization-based

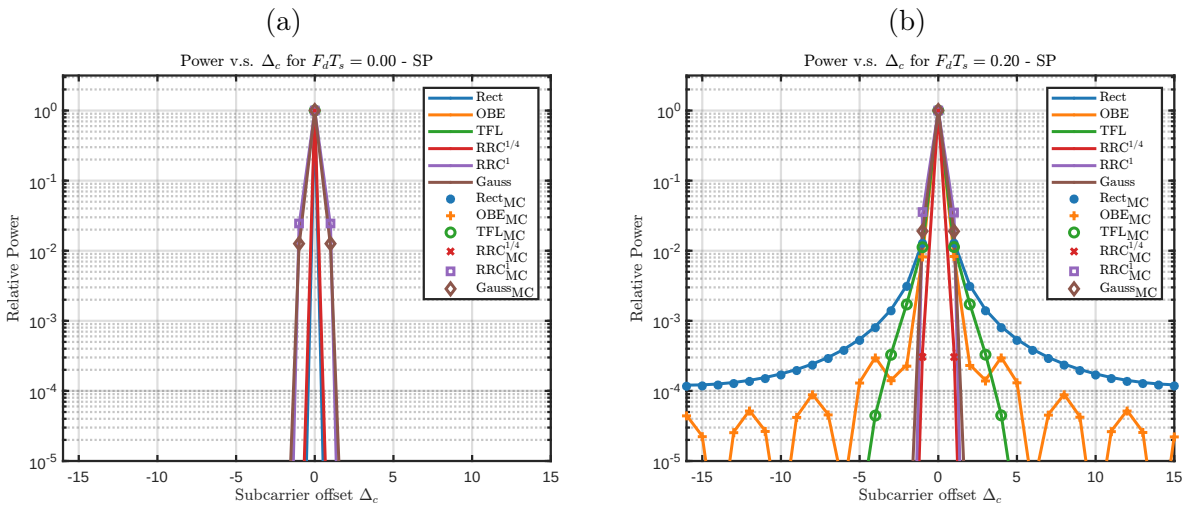

Figure 2.4: Normalized received power in response to a single TX pulse versus RX subcarrier offset Δ_c, for a) $F_dT_s = 0$ and b) $F_dT_s = 0.2$, both normalized to the power received at $\Delta_c = 0$.

optimization criterion. In contrast to that, as expected, RRC$^{1/4}$ significantly affects (and is affected by) only its two nearest neighbors. For the Gauss pulse shape, since it is semi-limited in both frequency and time domain, although it has a higher total interference than Rect, TFL and OBE, most of the interference power is on the nearest two neighbors and slight interference on the second nearest two neighbors. RRC^{1} has a behavior similar to Gauss in terms of ICI due to the high roll-off. This value of roll-off factor ($\beta = 1$) limits the 'tail' of the pulse, what increases its time-localization while maintaining fine frequency localization by spreading at only twice the minimum bandwidth. This relatively good localization comes at the cost of accepting ICI from the first two neighboring subcarriers. In the next section, we analyze the other type of interference, Inter-Symbol Interference (ISI).

2.2.4 Inter-symbol interference

As it was discussed in section 1.3.2.3, it is possible that fast-varying channel induces ISI for frequency-limited time-spreading pulse shapes. In this section, we will try to build an understanding of this phenomenon by first analyzing the ISI (as defined in equation (2.14)) versus F_dT_s, then by having a deeper look at its distribution and spreading over neighbor symbols.

2.2.4.1 ISI versus doppler spread

For the levels of ISI versus the normalized Doppler spread F_dT_s shown in figure 2.5, the values for Rect, TFL and OBE are not plotted, as mentioned before: time-limited non-overlapping pulses do not generate ISI for single path channels (ISI $\rightarrow$ 0). Although we assume a single path channel in this section, RRC$^{1/4}$ shows a significant ISI, in addition to having it increasing significantly with F_dT_s. Such a behavior is already shown in section 1.3.2.3. This explains

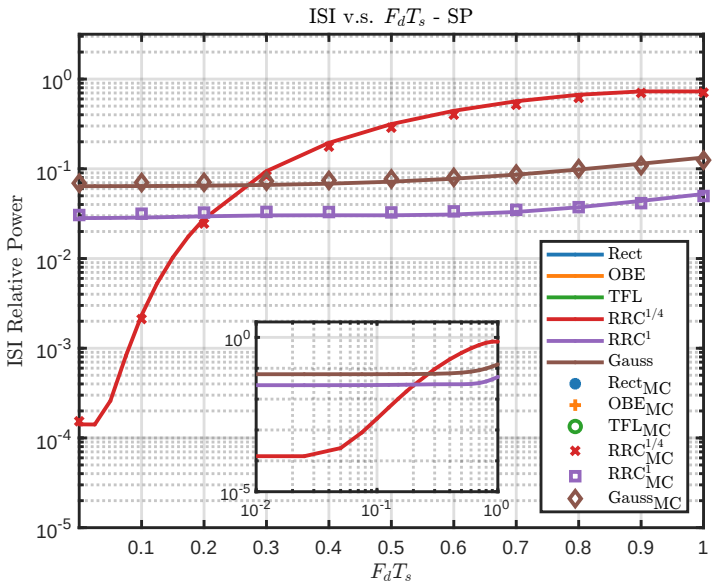

Figure 2.5: ISI versus F_dT_s for different pulse shapes.

the higher than expected total interference of RRC$^{1/4}$ shown in figure 2.2. Although the main concern of fast-varying channels is the frequency spread that causes ICI, it appears that ISI is more significant for frequency-limited orthogonal pulses like RRC. For the RRC^{1} pulse, the high roll-off factor (1) allows significant ICI, but mainly from the first two neighbors in the frequency domain. This also affects the values of ISI due to the cross-terms (interference coming from different symbols at different subcarrier frequencies). We can also notice that for RRC^{1}, in contrary to RRC$^{1/4}$, although high ISI values exist even for low F_dT_s, the value does not change significantly as F_dT_s increases. It can be seen that in the full range of analyzed F_dT_s values, the value of ISI is bounded by a variation of $\sim$ 3dB. This robustness of RRC^{1} against Doppler-generated-ISI is due to its fast decaying tail in the time domain. For the Gauss pulse, it has no orthogonality to be broken. Therefore, in single path channels, the ISI for Gauss pulses is approximately constant. In the next section, we present how this interference is distributed over the neighbor symbols.

2.2.4.2 ISI versus received-transmitted symbol offset

Figure 2.6 shows the power received per symbol offset per pulse shape for $F_dT_s = 0$ and $F_dT_s = 0.2$ in sub-figures (a) and (b), respectively, all normalized to the desired power having $\Delta = [0\ 0]$. To facilitate the reading and analysis of this figure, we recall the definition of ISI from section 2.1.3 equation (2.14):

$$\text{ISI} = \frac{P_{\text{ISI}}}{P_{\text{desired}}} = \sum_{\Delta_c, \Delta_s} \frac{P_{\Delta=[\Delta_c\ \Delta_s]}}{P_{\Delta=[0\ 0]}} \qquad \Delta_s \in \mathbb{K}^*.$$

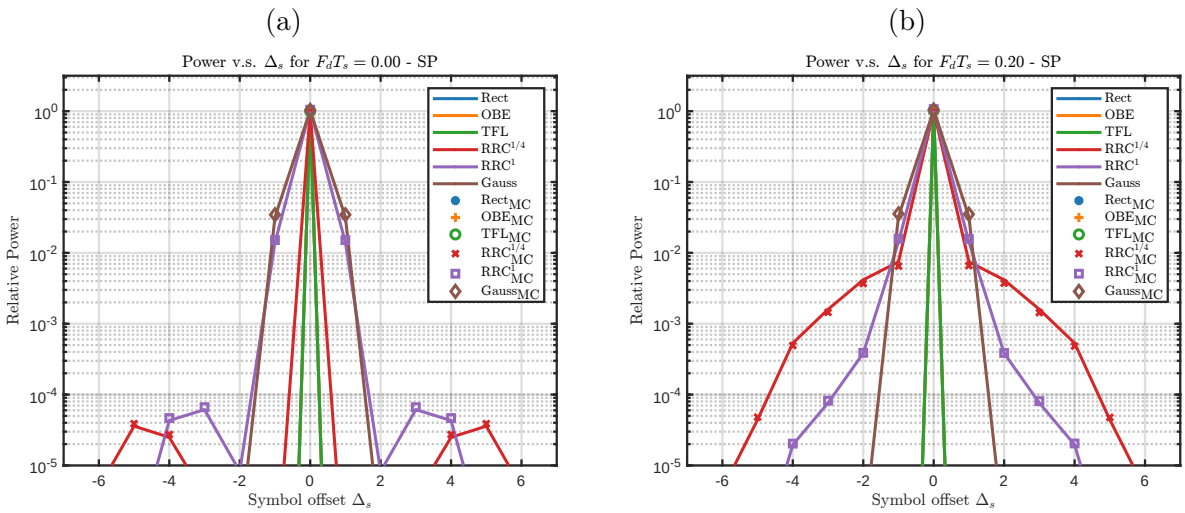

Figure 2.6: Received power in response to a single TX pulse versus RX symbol offset Δ_s, for a) $F_dT_s = 0$ and b) $F_dT_s = 0.2$, both normalized to the power received at $\Delta_c = 0$.

In figure 2.6, we plot $\sum_{\Delta_c} \frac{P_{\Delta=[\Delta_c\ \Delta_s]}}{P_{\Delta=[0\ 0]}}$ versus $\Delta_s \in \mathbb{K}$. Note that when $\Delta_s = 0$, we remove the ICI resulting from $\Delta_c \neq 0$ so that it represents the desired power $P_{\Delta=[0\ 0]}$. On the other hand, for $\Delta_s \neq 0$, we sum over $\Delta_c \in \mathbb{M}$ what represents an ISI component coming from a symbol $|\Delta_s|$ symbols away from the desired one. This means that it accounts for the power received by all the subcarriers, not only those that have the same frequency as the desired one. The values of $\mathcal{P}_\Delta$ and P_Δ are calculated using equations (2.16) and (2.17) for simulated and expected values, respectively. We can see that the time-limited pulse shapes Rect, OBE and TFL have only a peak at the desired symbol with $\Delta_s = 0$. These plots show that such pulses do not have ISI for single path channels even with Doppler spread similar to what was shown in section 1.3.2.3. On the other hand, RRC has ISI even for $F_dT_s = 0$, as shown in figure 2.6.a due to the breaking of the orthogonality by truncation. In addition to that, an increase in F_dT_s led to an increase in ISI for RRC pulses, with a much more significant impact for RRC$^{1/4}$. For the RRC^1 pulse, most of the ISI power is due to the cross-terms (from different subcarrier of different symbols) as mentioned before. For the Gauss pulse shape, since it is semi-limited in both the frequency and time domains, it has a higher total interference than RRC$^{1/4}$, but most of the interference power is on the nearest two neighbors and slightly on the second nearest two neighbors.

2.2.5 Summary of interference analysis in single path channels

In this section, the derived observation-based received power equations and the expected received power equations per transmitted and received symbol are used to calculate the level of interference (ISCI) in MC systems for different pulse shapes and Doppler spread values. It was shown that, as expected, non-time-overlapping pulses do not generate ISI in single path channels, while they exhibit significant ICI. It was also shown that the main concern of the time-overlapping pulses in fast-varying channels, even if they are designed to be orthogonal, is

ISI due to the mutation of the pulse's properties by the channel. We recall that our definition of ISI takes into account all the interference due to the MC symbols different to the current one, including subcarriers different than the desired one. A deeper look into the interference localization showed that:

- Rect, TFL and OBE pulses have ICI values spread in frequency over the many subcarriers, with TFL more localized and OBE have less total interference power,
- RRC$^{1/4}$ has ICI localized in frequency, but severe ISI spreading in time over multiple neighbor symbols, and are significantly affected by the increase of F_dT_s,
- RRC^{1} has ISI more localized in time, but ICI more spreading in frequency even in ideal channels,
- and Gauss pulse shape have the highest total interference, yet the most localized one in both frequency and time domains.

In the next section, we repeat the analysis done in this section, but for multipath channels.

2.3 Interference in Multi-Path (Frequency Selective) Channels

In the previous section, we have discussed in details the impact of Doppler spread in single path (flat fading) channel so that we can observe the behavior of the pulse shapes away from multipath frequency selectivity. In this section, we extend this analysis to the more general multipath fading scenario, including both time domain variation and frequency domain selectivity due to Doppler spread and channel delay spread respectively. Analysis will be provided in a comparative fashion, where we compare results in different multipath scenarios defined for Long-Term Evolution (LTE) with results in the single path scenario. In this section, we consider the following propagation models (adopted as LTE channel models by MathWorks [Mate]) for comparison:

- Single Path Channel (SP),
- LTE's Extended Pedestrian A model (EPA),
- LTE's Extended Vehicular A model (EVA),
- and LTE's Extended Typical Urban model (ETU).

However, since these models are defined in the continuous time, we perform the sampling procedure described section 1.1.5 to generate the equivalent discrete time channel. We assume the subcarrier spacing $F_s = 60$kHz as for the numerology 2 of the 5G standards [Ts1]. As we use the same system parameters as in section 2.2, we have $N = 40$. Beside their impact on the channels' taps sampling, these parameters define other system parameters like the total

Table 2.1: SP, EPA, EVA, and ETU channels sampled to the discrete-time channel with subcarrier spacing 60kHz and $N = 40$.

Tap index l	Power at delay l σ_l^2			
	SP	EPA	EVA	ETU
00	1.0e+00	8.0e-01	5.3e-01	4.6e-01
01		2.0e-01	3.7e-01	3.6e-01
02		6.6e-03	5.3e-02	2.4e-02
03		3.3e-05	2.6e-02	3.3e-02
04			1.1e-02	4.9e-02
05			3.1e-03	3.7e-02
06			3.1e-03	1.1e-02
07			9.7e-06	4.0e-04
08			2.1e-07	3.0e-06
09				2.8e-05
10				1.1e-03
11				2.3e-02
12				8.3e-03
13				2.9e-04
14				2.8e-06

bandwidth of the system $B = MF_s$, the sample time $T_{sa} = 1/B = 1/(MF_s)$, and the symbol time interval $T_s = NT_{sa} = N/(MF_s)$. The channel taps after sampling are shown in table 2.1. Note that since we are considering the more general multipath scenario, we can no longer use equations (2.16) and (2.17) as they were narrowed down to simplify the calculations for single path channels. In this section, we obtain the theoretical and Monte Carlo simulation values using equations (2.2) and (2.10), respectively. We still use equations (2.13) to (2.15) for the definitions of ICI, ISI, and ISCI.

Figure 2.7 shows the ISCI versus normalized Doppler spread F_dT_s for different pulse shapes in a) SP channel, used for comparison, b) EPA, a standard multipath propagation model of LTE for pedestrians,) EVA, a standard multipath propagation model of LTE for vehicles and d) ETU, a standard multipath propagation model of LTE for urban areas. Comparing the sub-figures (a) and (b) of figure 2.7, we can see that all the pulses had an increase in interference due to the delay spread except Rect. This increase is mainly observable at low F_dT_s, where for higher F_dT_s, the Doppler-generated interference become much more critical making it difficult to observe the delay-generated interference. That is because of the CP implementation which provides resistance to the impact of the delay spread. Another difference from the SP analysis is that TFL has less interference than OBE for low Doppler spreads. This is due to the difference in the optimization criteria of these pulses where OBE focusing on minimizing the out of band energy without considering ISI that might result from multipath scenarios. On the other hand, the TFL pulse optimization criterion tries to minimize spreading in both the frequency and time domains. However, both Rect (with CP) and TFL lose their favorability as F_dT_s increases as ICI becomes more critical. Therefore, we can observe that $\text{RRC}^{1/4}$ has the lowest interference for some values of F_dT_s greater than 0, while OBE regains its favorability

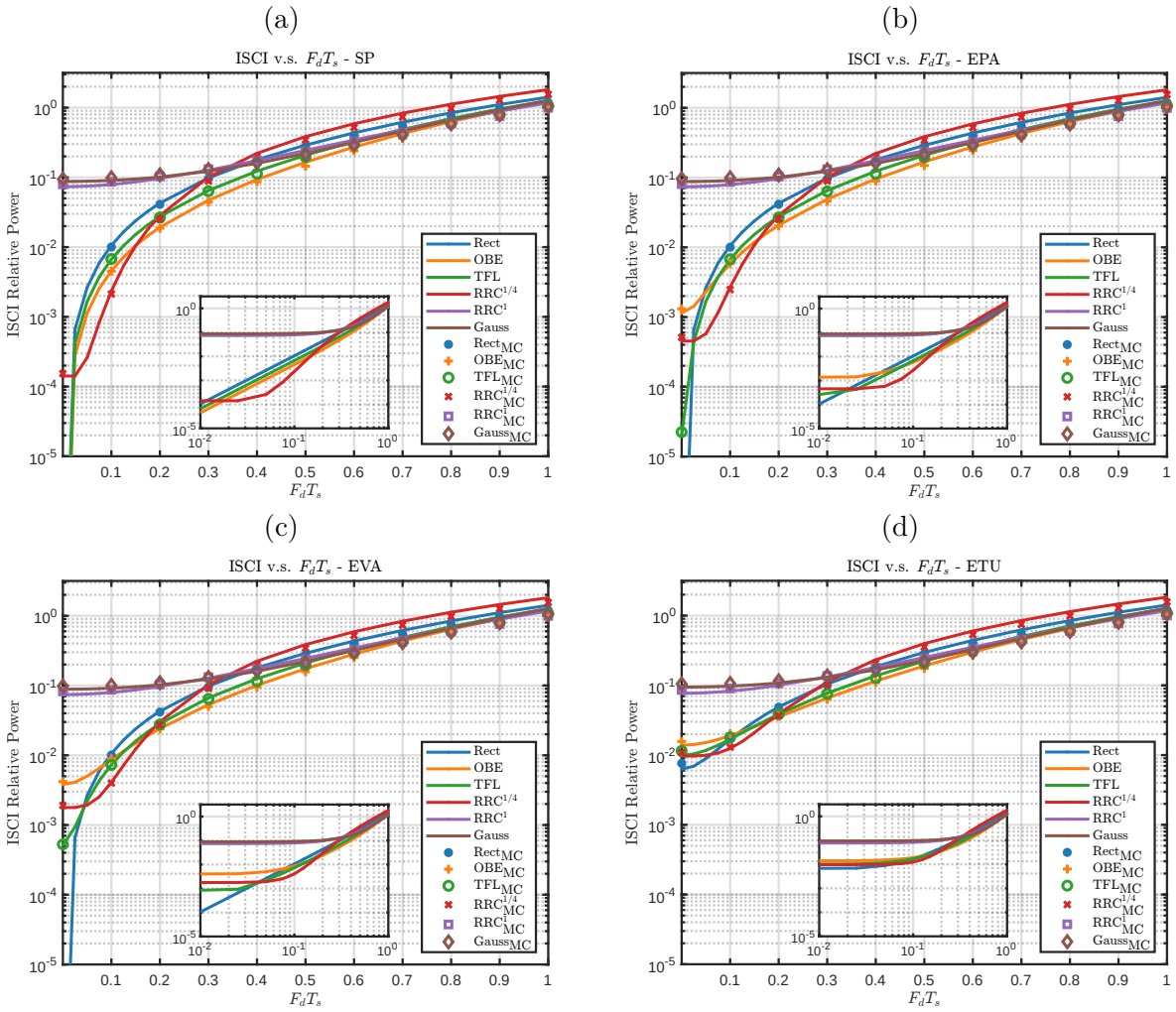

Figure 2.7: ISCI versus F_dT_s for different pulse shapes in a) SP, b) EPA, c) EVA, and d) ETU channels.

for higher values. A similar observation can be seen in figure 2.7.c representing the EVA scenario, except that the levels or interference are even higher. In figure 2.7.d representing the ETU scenario, we can see that Rect pulse shape has lost its ability to resist multipath propagation. This is due to having the delay spread ($14T_{sa}$) larger than the CP duration of $(N-M)T_{sa} = 8T_{sa}$.

To have a deeper look into this increase in interference, we look into the ISI details. We start by ISI (instead of ICI) since it is expected that multipath scenarios would affect the ISI more. We now consider only the ETU channel in addition to SP. Figure 2.8 shows ISI versus F_dT_s for different pulse shapes for SP and ETU in sub-figures (a) and (b), respectively. In the same figure, the sub-figures (c) and (d) show the normalized received power for different symbol offsets Δ_s for $F_dT_s = 0.2$ in the SP and ETU channels, respectively. It is clear from the figures that the main difference is that the ETU channel causes higher ISI than the SP channel. However, there are few more points that needs to be noticed:

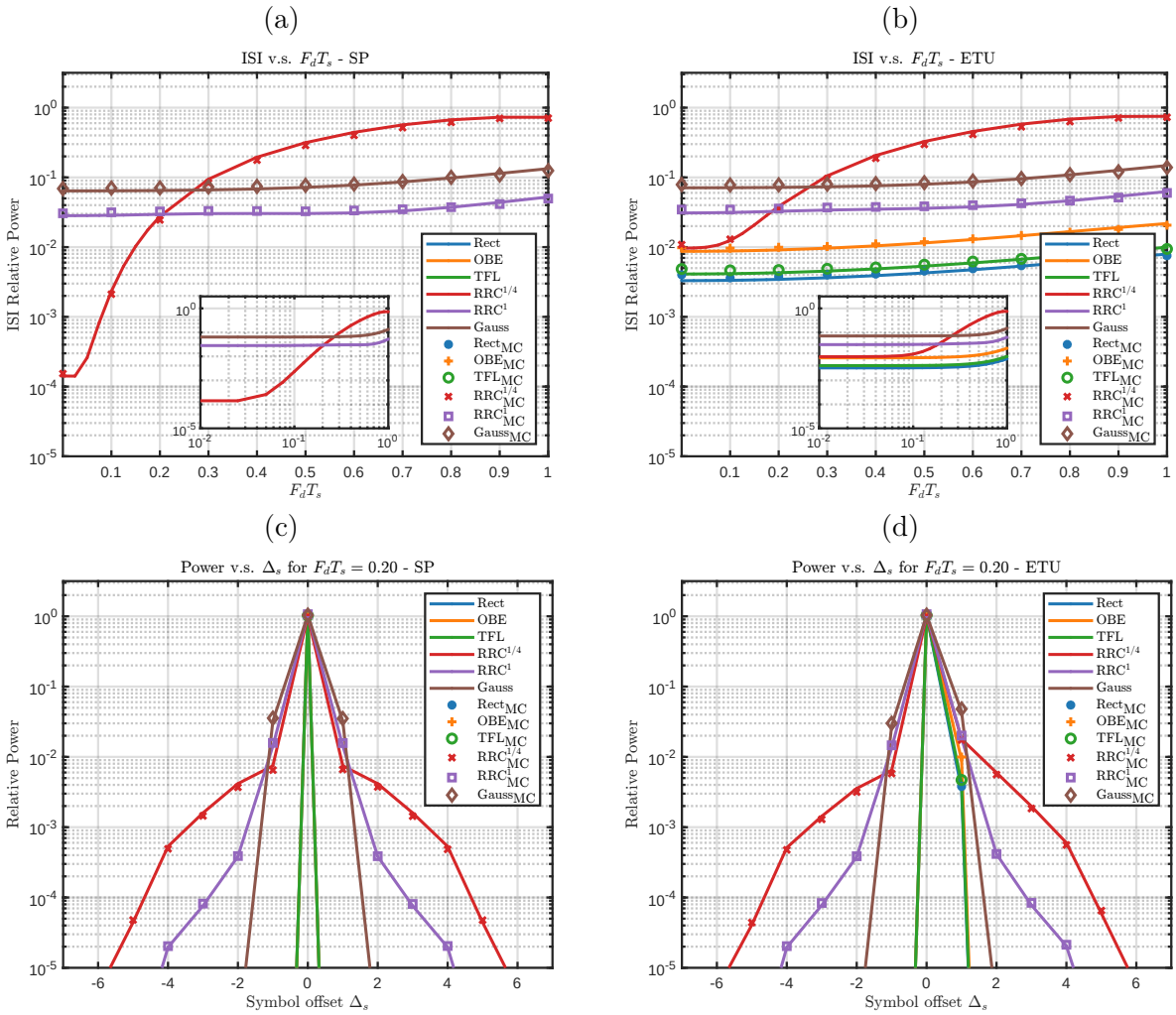

Figure 2.8: ISI versus F_dT_s for different pulse shapes in a) SP and b) ETU, and its distribution over neighbor symbols also for c) SP and d) ETU for $F_dT_s = 0.2$.

- although Rect pulse, applying the CP implementation, is highly resistive to multipath propagation, it has a performance similar to the other time-limited pulses when the delay spread is higher than the CP duration,
- the pulses RRC^1 and Gauss can parially resist the impact of both delay spread and Doppler spread, as they maintain an approximately fixed ISI, although initially high,
- most of the ISI generated because of the ETU channel is on the first future neighbor of the symbol of interest ($\Delta_s = 1$), as can be observed by comparing the sub-figures (c) and (d).

Although an increase in ISI can be noticed, the increase in the total interference appeared to be higher. Therefore, we also analyze the impact of the delay spread on ICI.

In figure 2.9, ICI versus the normalized Doppler spread F_dT_s is presented for SP and ETU

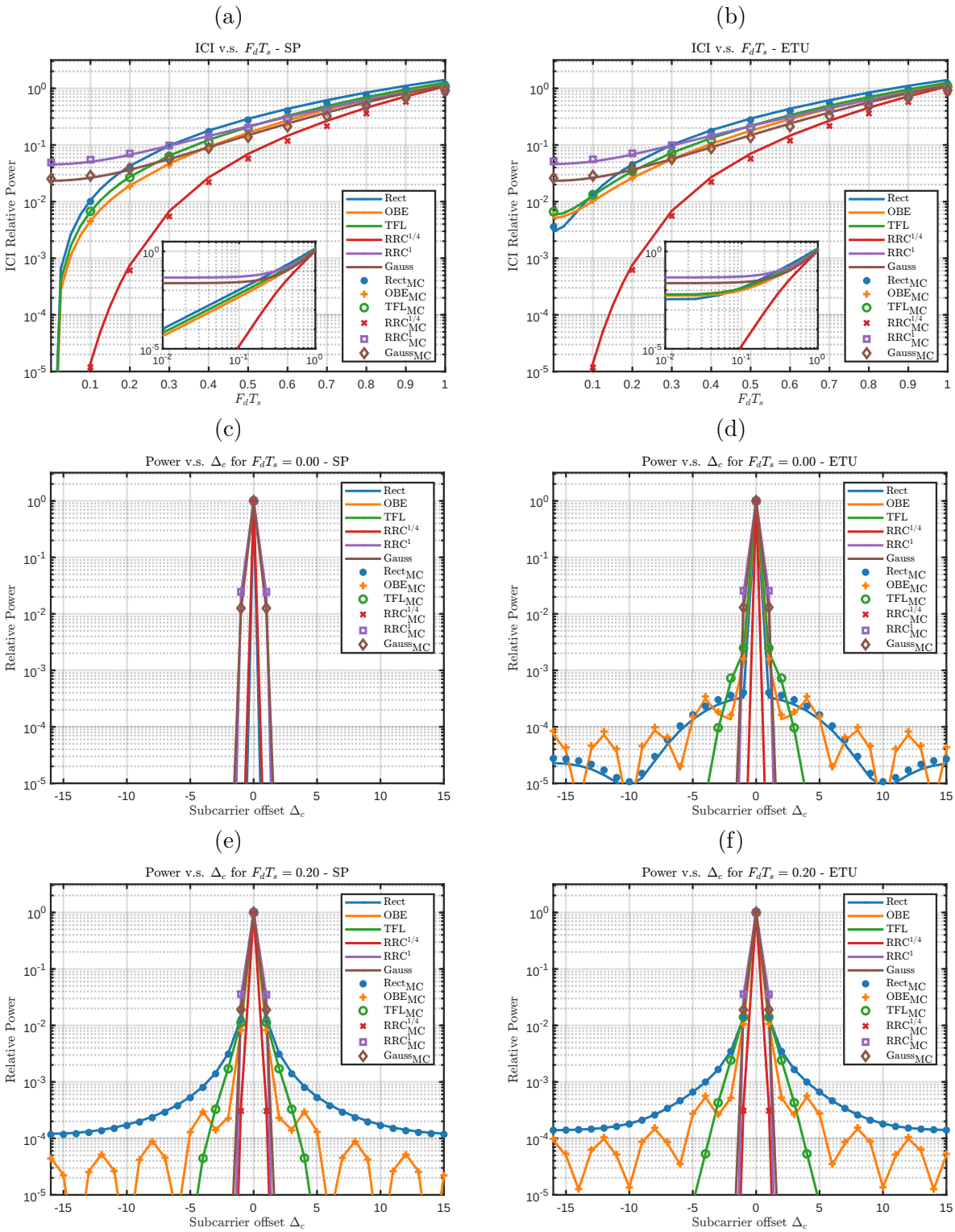

Figure 2.9: ICI versus F_dT_s for different pulse shapes in a) SP and b) ETU, and its distribution over neighbor subcarriers also for c,e) SP and d,e) ETU for $F_dT_s = 0$,$F_dT_s = 0.2$ respectively.

Table 2.2: Summary of the pulse shapes robustness to ISI and ICI and their localization.

Pulse Shape	Robustness		Localization	
	ISI	ICI	ISI	ICI
Rectangular	+ + +	− −	+ + +	− −
OBE	+ +	−	+ +	−
TFL	+ +	−	+ +	+
Gaussian	−	−	+ +	+ +
RRC$^{1/4}$	− −	+ +	− −	+ + +
RRC^{1}	− −	−	+ +	+ +

in the sub-figures (a) and (b), respectively. In the same figure, the sub-figures (c) and (d) show the normalized received power for different subcarrier offsets Δ_c for $F_dT_s = 0$ in the SP and ETU channels, respectively. Then the sub-figures (e) and (f) shows the normalized received power for different subcarrier offset Δ_c for $F_dT_s = 0.2$ in SP and ETU channels respectively. The first thing that can be noticed from sub-figures (a) and (b) is that the time-limited pulses have a significant increase in ICI because of multipath propagation even for non/slow time-varying channels. The reason behind this is that the delayed version of the symbols, cropped by the receiving pulse shape, have their subcarriers not orthogonal neither to each others nor to the subcarriers of the non-delayed versions. This effect will increase the ICI in multipath channels, making it an effect as important as the ISI generated by the delay spread. We can see from the sub-figure (c) that for non-varying single path channel, time-limited orthogonal pulses have completely no ICI as they are designed to be orthogonal. However, sub-figure (d) shows how the just discussed non-orthogonal delayed versions causes ICI spreading over the subcarriers even for $F_dT_s = 0$ in ETU channels. In addition to that, it is shown through comparison of sub-figures (e) and (f) that for $F_dT_s = 0.2$ (or any $F_dT_s > 0$), the ICI is generally higher for every subcarrier in ETU channels, especially for time-limited pulse shapes.

Both single path and multipath analysis showed how different pulses are sensitive to Doppler spread and/or delay spread in MC systems. Extremely high interference values would lead into non-usable channels in such setups. Among the pulse shapes discussed, we have seen that the pulse shapes used were spread in the time domain or in the frequency domain, except for the RRC^{1} and the Gauss pulse shapes. These pulses have been shown to have the highest levels of interference, while most of this interference was kept "contained" in a few symbols. The results of this section are summarized in table 2.2 showing the robustness to and localization of ISI and ICI per pulse shape. Following this, in the next section we discuss the possibility of reducing the system density and what impact such a reduction would have on different pulse shapes in terms of level of interference.

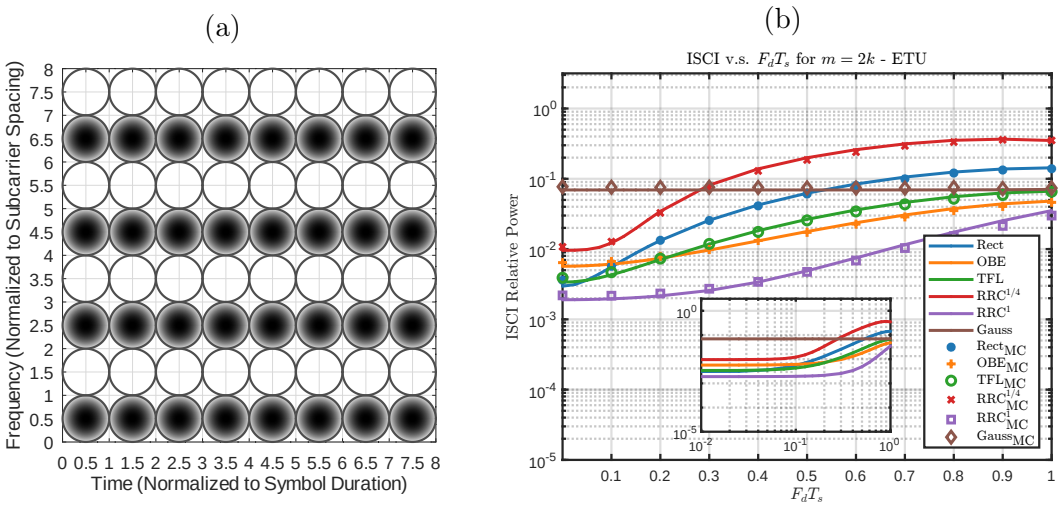

Figure 2.10: (a) Symbols allocation grid with reduction to 50% density defined by $m = 2k \mid k \in \mathbb{N}$ and (b) its relative ISCI versus F_dT_s plot for ETU channels.

2.4 Density Reduction

In the previous sections of this chapter, we have observed that extreme channel conditions in terms of Doppler spread and delay spread can lead to severe interference. Such levels of interference would lead to non-usable channels, especially when it is not possible to use high complexity equalizers. In this section, we analyze the interference levels when considering lower density schemes. By density, we refer to the ration between the number of transmitted symbols to the maximum number of symbols that can be possibly transmitted without introducing interference in ideal channels. This ratio is defined by $d = M/N$ in systems not considering density reduction schemes. Note that systems having $d > 1$ will introduce interference away from what design is adopted, while lower values of d reflects lower symbol rates. Systems employing density reduction schemes can reduce the interference without introducing additional complexity while maintaining the power efficiency. However, this comes at the cost of reducing the bandwidth efficiency as less resources will be used while reserving the same time/bandwidth of full-density transmission. In this section, we assume the ETU propagation model as we are targeting the extreme channel conditions scenario.

2.4.1 Hard density reduction

In this section, we discuss what we call *'hard'* density reduction. This scheme is based on reducing the density by turning off a number of subcarrier/symbol locations. First, we discuss the symbol allocation grid presented in figure 2.10.a. This grid is generated by using only the subcarriers that satisfy $m = 2k \mid k \in \mathbb{N}$. Note that such grid would reduce the transmission density to 50% as it is clear from the presented figure. This reduction mainly aims at reducing ICI and parts of ISI coming from the cross-terms (interference coming from different subcarriers of different symbols). It can be seen from figure 2.10.b that most pulse shapes have benefited

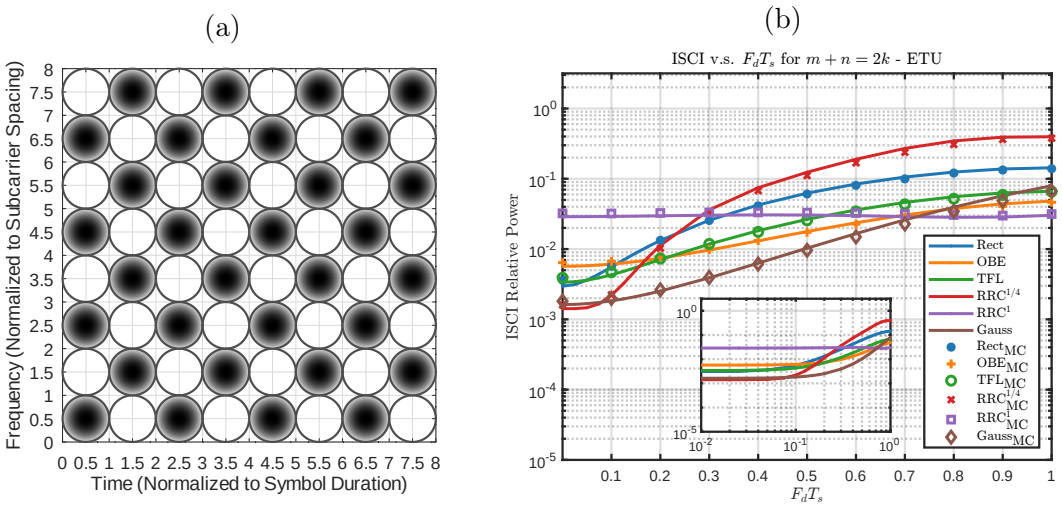

Figure 2.11: (a) Symbols allocation grid with reduction to 50% density defined by $m+n = 2k \mid k \in \mathbb{N}$ and (b) its relative ISCI versus F_dT_s plot for ETU channels.

significantly from this reduction compared to performance figure 2.2 from section 2.3.b. This is because even for pulse shapes that generate ICI which spreads over the whole spectrum, the first neighbors receive the highest level of interference. The pulse that benefited the least from this reduction is RRC$^{1/4}$, where the most significant effect for such pulses is the Doppler-generated-ISI as discussed in section 1.3.2.3. On the other hand, the pulse that benefited the most from this reduction is the RRC^{1}. We have seen in the previous sections that the RRC^{1} pulse has high interference because of being overlapping with the neighbor subcarriers, but most of this interference was to the nearest neighbors. In addition to that, most of its ISI comes from neighbor subcarriers of the MC symbols at neighbor time slots. Therefore, when the neighboring subcarriers are turned off, we can see that this pulse shape performs the best for any F_dT_s in the range being considered.

Another very interesting allocation grid that we considered for analysis is shown in figure 2.11.a. It also reduces the transmission density to 50%, but only with the use of subcarriers and symbols that satisfy $m+n = 2k \mid k \in \mathbb{N}$. As can be seen from the figure, this generates an alternating lattice of symbols. Such structure tries to reduce the nearest neighbors symbols and subcarriers interference. Figure 2.11.b shows that all pulses have significantly reduced interference in such a structure. However, it is clear that the Gauss has the best performance in general. The performance of the Gauss pulse in such structure is very similar to the performance of RRC^{1} using the structure in figure 2.11.a. However, in some scenarios it might be more interesting to use a Gauss pulse as it is easier to implement in terms of the system complexity (number of multipliers needed) due to the shorter impulse response. In addition to that, this will reduce the transmission delay as the Gauss pulses (with the criterion of variance we are considering - see section 1.2.3.2) normally requires only 3 symbols duration to be implemented.

One more trellis structure that we discuss is shown in figure 2.12.a. However, this structure reduces the allocation density to 25% instead of 50%. This is done using only the subcarriers

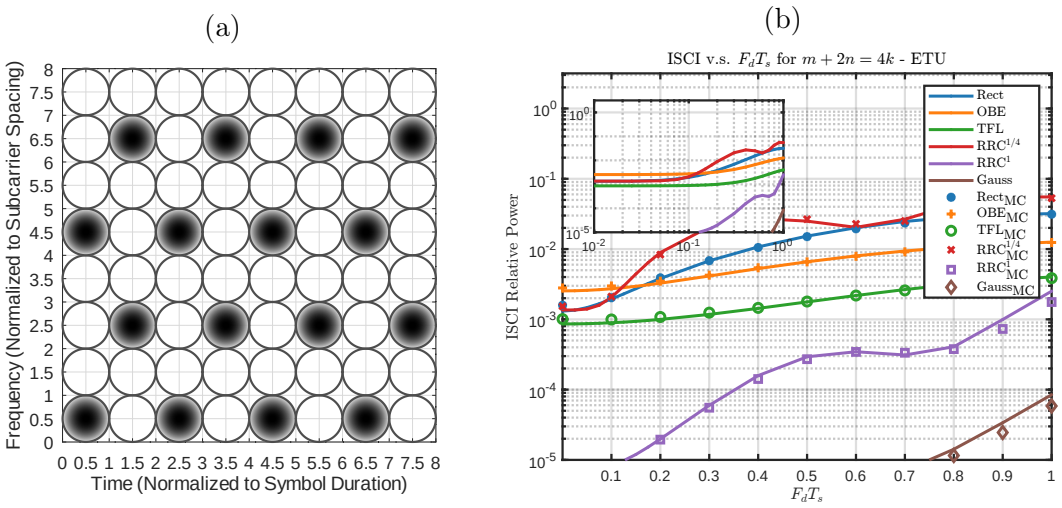

Figure 2.12: (a) Symbols allocation grid with reduction to 25% density defined by $m + 2n = 4k \mid k \in \mathbb{N}$ and (b) its relative ISCI versus F_dT_s plot for ETU channels.

and symbols that satisfy $m + 2n = 4k \mid k \in \mathbb{N}$. The intention behind such structure is maximizing the distance (normalized to subcarrier and symbol spacing) between the used positions. As expected, all pulses have significantly reduced total interference, as shown in figure 2.12.b. Among the time-limited pulses, the best pulse in such allocation schemes is the TFL pulse. This is because of its optimization criteria trying to maximize time and frequency localization, or equivalently reducing time and frequency spreading. This leads to a more localized interference in full density schemes, which have most of it canceled and such reduced density schemes. Therefore, in scenarios where the transmission time should be limited to single symbol duration, TFL pulses are the best to use. However, if the pulses are not required to be (very) limited in time, the Gauss is the best candidate in such schemes. Due to having the frequency response of the Gauss pulses as Gaussian too, it is semi-limited in both time and frequency domains as discussed in sections 1.2.3.2 and 2.2. This allows Gauss to benefit significantly from density reduction in both frequency and time domains. Therefore, it can be seen from figure 2.12.b that the interference when considering the Gauss pulse reached a maximum of 10^{-4} at $F_dT_s = 1$, and significantly less for lower values of F_dT_s. One additional interesting property of the Gauss pulses is that they maintain such values of interference without being orthogonal. For all the other pulses, to maintain their orthogonality, they require some *'alignment'* between the subcarriers or between the symbols. This is not a requirement for Gauss pulses, leading to the *'soft'* density reduction that we discuss in the next section.

2.4.2 Arbitrary soft density reduction

As shown in section 2.4.1 increasing the spacing (in both / either time and / or frequency) changes the interference levels of the pulse shapes differently. As a consequence, this changes the selection of the most adequate pulse shape in terms of interference reduction. However,

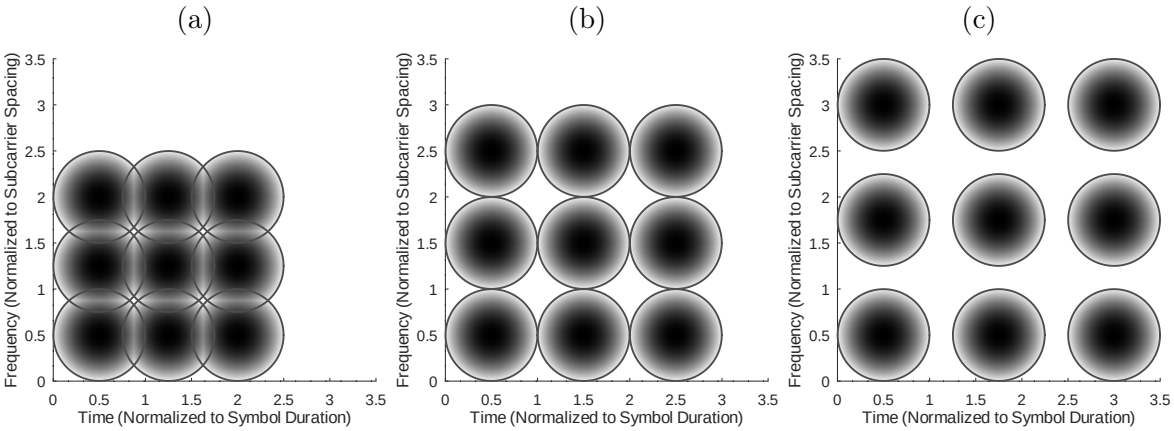

Figure 2.13: Symbols distribution over the symbol-offset/subcarrier-offset grid for a) $\Lambda = [0.75\ 0.75]$, b) $\Lambda = [1.00\ 1.00]$, and c) $\Lambda = [1.25\ 1.25]$.

due to the constrains in the positioning of orthogonal pulse shapes, the density reduction was analyzed by turning on/off a specific set of symbols. These constraints do not hold for the Gauss pulse. Therefore, for more dynamic analysis, in this section we adopt the *'arbitrary soft density reduction'* scheme. In contrary to section 2.4.1 which considered only integer factors of reduction (2 and 4), this scheme allows arbitrary factors of density reductions. To define the reduction factors, we introduce $\Lambda = [\lambda_c, \lambda_s]$, where λ_c is the subcarrier spacing factor and λ_s is the symbol spacing factor. The spacing increases or decreases depending on the values of Λ as illustrated in figure 2.13. Note that for such scheme, the total density reduction caused by Λ is $\lambda_s \times \lambda_c$. Injecting the just introduced Λ into the definition of the pulse shapes in equations (1.34) and (1.38), the updated pulse shapes will, respectively, be:

$$g_{m,n,\Lambda}[q] = g[q - n\lambda_s N] e^{j2\pi \frac{\lambda_c m \left(q - n\lambda_s N\right)}{M}}, \text{ and} \tag{2.18}$$

$$\tilde{g}^*_{m',n',\Lambda}[q] = \tilde{g}^*[q - n'\lambda_s N] e^{-j2\pi \frac{\lambda_c m' \left(q - n'\lambda_s N\right)}{M}}. \tag{2.19}$$

Similar to the derivations in sections 1.2.3 and 2.1, the received power using the pulse shapes updated in equation (2.18) and equation (2.19):

$$\begin{aligned} \mathcal{P}_{m',n',\Lambda}|_{m,n} = & \sum_{l} \sum_{l'} \sum_{\gamma} \sum_{\gamma'} \tilde{g}^*[\gamma - (n'-n)\lambda_s N + l] \tilde{g}[\gamma' - (n'-n)\lambda_s N + l'] \\ & \times h[\gamma + n\lambda_s N + l, l] h^*[\gamma' + n\lambda_s N + l', l'] g[\gamma] g^*[\gamma'] \\ & \times e^{j2\pi\lambda_c \frac{(\gamma'-\gamma)(m'-m)+(l'-l)m'}{M}} |c_{m,n}|^2. \end{aligned} \tag{2.20}$$

We introduce $N' = \lambda_s N$ and $M' = M/\lambda_c$ for simplicity. Note that it is required to have N' as an integer ($\lambda_s N = N' \in \mathbb{N}^*$) since it is used in symbol indices, and it is recommended to have M' as an integer to allow using the whole given bandwidth. It is to be noted that the bandwidth covered by using M' is equal to λ_c times the bandwidth when using M, but using M uniformly spaced subcarriers. To maintain the same bandwidth, M/λ_c subcarriers should

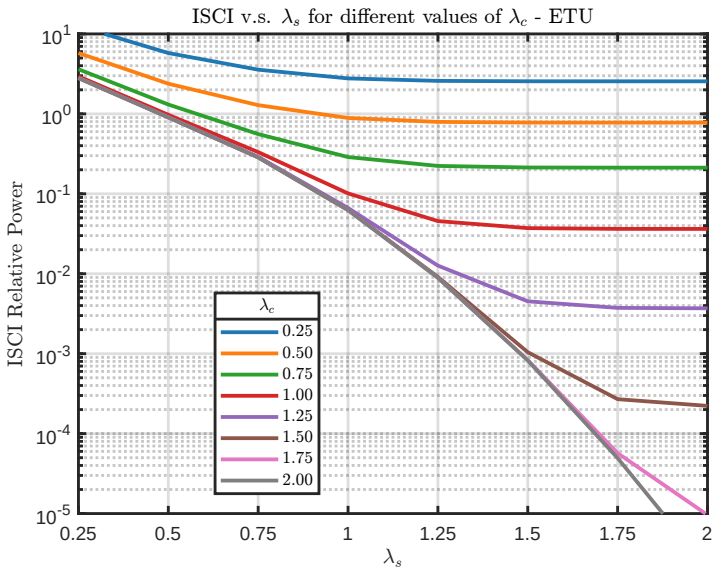

Figure 2.14: ISCI versus symbol frequency offset factor (λ_s) per subcarrier offset factor (λ_c) for a Gauss pulse shape, for $F_d T_s = 0.2$ in ETU channel.

be used. Similarly, for time allocation, the time covered by using N' is equal to λ_s times the duration when using N. Replaced by N' and M' in equation (2.20) the received power equation becomes:

$$\begin{aligned}\mathcal{P}_{m',n',\Lambda}|_{m,n} = &\sum_{l}\sum_{l'}\sum_{\gamma}\sum_{\gamma'}\tilde{g}^*[\gamma-(n'-n)N+l]\tilde{g}[\gamma'-(n'-n)N'+l'] \\ &\times h[\gamma+nN'+l,l]h^*[\gamma'+nN'+l',l']g[\gamma]g^*[\gamma'] \\ &\times e^{j2\pi\frac{(\gamma'-\gamma)(m'-m)+(l'-l)m'}{M'}}|c_{m,n}|^2.\end{aligned} \tag{2.21}$$

Similarly to the derivation of the received power in equation (2.10), the expected received power using the introduced Λ is

$$\begin{aligned}P_{\Delta,\Lambda} = &\sum_{l}\sigma_l^2\sum_{\gamma}\sum_{\gamma'}\tilde{g}^*[\gamma-\Delta_s N+l]\tilde{g}[\gamma'-\Delta_s N'+l] \\ &\times g[\gamma]g^*[\gamma']J_0(2\pi F_d T_{sa}(\gamma-\gamma'))e^{j2\pi\frac{(\gamma'-\gamma)\Delta_c}{M'}}.\end{aligned} \tag{2.22}$$

As expected, the plot in figure 2.14 shows how increasing the offset will induce a reduction in the levels of ISCI. It can be noticed that for every value of λ_c, there exists a threshold of λ_s that when reached, no further significant improvement in ISCI can be noticed. Since the frequency response of a Gauss pulse is also of Gaussian shape and due to the variance selected as discussed in section 1.2.3.2, the power is distributed between time and frequency nearly evenly. Consequently, it can be seen that the threshold mentioned above is approximately when $\lambda_s = \lambda_c$. Note that, as shown in figure 2.14, variables λ_s and λ_c can be used to decrease or increase the time-frequency density of the system. This will lead to the oversampling ratio

OR $= \frac{N'}{M'} = \frac{N\lambda_s\lambda_c}{M}$. Having OR $= 1$ will lead to a critically sampled system, OR > 1 will lead to an overcritical system, and OR < 1 will lead to an undercritical system, which is also known as Faster-Than-Nyquist system [Maz75]. Different interference values depending on λ_c and λ_s can be obtained for every F_dT_s. These can be used to configure λ_c and λ_s to minimize $\lambda_c \times \lambda_s$ while maintaining a level of interference below a threshold for a specific F_dT_s range.

2.5 Conclusion and Perspectives

In this chapter, we have derived equations for the interference power that calculate how much each transmitted subcarrier and symbol interfere with each received subcarrier and symbol for MC systems with conventional correlator-based receiver operating in time-varying multipath channels. The results are provided in two fashions: observation-based equations used for Monte Carlo simulation, and statistical equations used for theoretical analysis, where they appeared to match validating the derived equations. We used for comparison different pulse shapes selected based on different optimization criteria to understand the weaknesses and strengths of each pulse and its underlying criterion. Analysis was provided for single path and multipath channels. It was shown that for time-limited pulse shapes, such as Rect, OBE, and TFL, there is no ISI in single path channels. In time-varying channels, such pulses conduct high ICI, that is, spread over many / all subcarriers. In multipath channels, such pulses have significant ISI, in addition to an increase in the values of ICI. This multipath effect is less significant for the Rect pulse due to the CP implementation. However, it was shown that this advantage is lost when the delay spread duration is longer than the CP. RRC pulses was also considered for the comparison. We have considered two versions of this pulse: RRC$^{1/4}$ and RRC^{1}. It was shown that RRC$^{1/4}$ was the pulse affected the most by the channel variation. Although it has, as expected, the least ICI, it generates a significant ISI even in single path channels. In addition to that, this ISI increases as F_dT_s increases and significantly affects multiple symbols adjacent in the time domain. This makes such type of pulse shapes not suitable for fast-varying channels when no complex equalizers are used, either in single path or in multipath channels. On the other hand, RRC^{1}, and similarly Gauss, has a very high ICI and ISI in both single path and multipath scenarios even for slow/non-varying channels. However, in contrary to time-limited pulses that have interference spreading over many subcarriers, and RRC$^{1/4}$ that has interference spreading over many symbols, RRC^{1} and Gauss have their generated interference contained in few neighbors for both time and frequency domains. This special property allowed them to benefit the most from the density reduction schemes that were introduced in section 2.4. In such schemes, it appeared that for 50% density reduction, both RRC^{1} and Gauss are suitable options, while Gauss is better for 75% density reduction. These density reduction schemes would lead to a reduced bandwidth efficiency, yet they permit of having power-efficient communication in such extreme scenarios without needing high complexity equalization at the receiver. In addition to that, we have discussed a special ability of the Gauss pulse to have arbitrary density reduction, and showed its corresponding interference levels.

The results of this chapter and their underlying analysis raise the interest in multiple

question and problems. Some of these problems are discussed and dealt within this work, while other are kept as open questions for future works. These problems and questions include, but are not limited to, the following:

- How will these levels of interference will impact the performance in terms of Bit Error Rate (BER)? (Addressed in chapter 3)
- Will classical channel equalization techniques, or even techniques designed for fast-varying channels, be useful in such scenarios of extreme channel variation and high levels of interference? (Addressed in chapter 3)
- Will classical channel estimation techniques, or even techniques designed for fast-varying channels, be useful in such scenarios of extreme channel variation and high levels of interference? (Addressed in chapter 4)
- How will the interference levels be affected in offset-based real-valued techniques like Filter-Bank Multi-Carrier with Offset Quadrature Amplitude Modulation (FBMC-OQAM)?
- How will other impairments that are also critical in high-frequency channels like phase noise impact the interference levels?

Chapter 3

Time Domain Aided Equalization for Multicarrier Systems Over Fast-Fading Channels

Contents

In the previous we have statically and experimentally calculated the power of interference and its distribution in Multi-Carrier (MC) systems operating in fast-varying environments. We have observed how such scenarios lead to high level interference that might become intolerable. We have also discussed how it is expected that such interference would significantly affect the performance of the communication, what might make some communications channels not even usable if it is not countered with suitable equalizers. In this chapter, we discuss the

importance of assisting equalization by performing time domain preprocessing when considering multi-carrier communication over fast-varying Rayleigh channels. Two low-complexity time domain-assisted equalization procedures are proposed and assessed when assuming perfect Channel State Information (CSI) then showed to have similar performance for realistic channel estimation error. Bit Error Rate (BER) comparison is provided for several equalizers and pulse shapes, and the time domain additional processing was shown to improve the performance and to benefit from channel variation instead of being negatively affected. Diversity–BER mapping is introduced to calculate the proposed Doppler-driven diversity equivalence per pulse shape. This is then linked to the pulse shape's properties. It is shown how pulses that are less localized in time tend to achieve higher Doppler-driven diversity equivalence. To account to Inter-Symbol Interference (ISI) that can be issued by less localized pulse shapes in such scenarios, ISI-cancellation technique is proposed and showed to converge toward ideal ISI-cancellation after a single iteration. But first, in the next section, we discuss the most common frequency domain equalizers to compare with the proposed technique.

3.1 Frequency Domain Equalization Techniques

As a good equalization is mandatory to obtain a reliable communication system, we consider several equalizers to be compared in the scope of this work. We start first by presenting existing frequency domain equalizers. Some equalizers are considered for being classically used, and others are considered for being proved to be suboptimal following the framework they are designed in.

3.1.1 Linear Minimum Mean Square Error (MMSE)

A classical and considerable optimization criterion when designing any kind of estimator is minimizing the mean square error. As equalization is an estimation problem, MMSE equalizers are commonly used. However, the classical MMSE equalizer in MC systems is the one-tap equalizer (also called diagonal equalizer, or single-tap per-subcarrier equalizer, in order to qualify its structure). The taps are computed under the MMSE minimization criteria [SKJ94]. Due to its structure, such equalization neglects the fact that, in some scenarios, significant errors are introduced due to Inter-Carrier Interference (ICI) and just consider (per sub-carrier) Signal to Noise Ratio (SNR) by performing:

$$\text{Equalized Value} = \frac{\text{Observed Value} \times \text{Conjugate}\big(\text{Channel Value}\big)}{\big(\text{Channel Magnitude}\big)^2 + \frac{\text{Noise Power}}{\text{Received Power}}}. \tag{3.1}$$

Applying this general MMSE to the derivations of section 1.2.3, the equalized symbol $\check{c}_{m',n'}$ will be:

$$\check{c}_{m',n'} = \frac{\hat{c}_{m',n'} \times \left(H_{m',m'}^{(n',n')}\right)^*}{\left|H_{m',m'}^{(n',n')}\right|^2 + \text{SNR}^{-1}}. \tag{3.2}$$

This makes use of the information available only on the diagonal of the channel matrix, which is not efficient for high values of normalized Doppler spread.

3.1.2 Linear Least Square (LS)

The linear single-step LS equalizer follows the Mean Squared Error (MSE) minimization criteria, but now for a more complex multi-tap equalization structure implemented through matrix operations [RBL05] such that:

$$\check{\boldsymbol{c}}_{n'} = \left(\boldsymbol{H}^{(n',n')}\right)^H \left(\boldsymbol{H}^{(n',n')}\left(\boldsymbol{H}^{(n',n')}\right)^H + \mathrm{SNR}^{-1}\boldsymbol{I}\right)^{-1} \hat{\boldsymbol{c}}_{n'}, \tag{3.3}$$

where $()^H$ is the conjugate transpose operator. Although this matrix implementation considers more information than the (one-tap) MMSE, it does not consider the knowledge of the set of possible symbols (constellation), which if used may improve the performance if symbol detection is performed while suppressing the interference.

3.1.3 Successive Interference Suppression (SIS)

SIS considers the knowledge of the channel matrix and constellation, and is based on decisions. Equalization is performed recursively as described in [HR08a]:

- Ordering: selecting the diagonal element of the channel matrix that was not selected before and having the highest magnitude,
- Detection: performing a one-tap equalization (Zero-Forcing (ZF) or MMSE) to the corresponding symbol then detect it,
- and Suppression: regenerate the interference due to the detected symbol using the channel matrix and remove it from the signal.

This technique is not considered directly in the comparison since the QR decomposition technique, described in the next section, represents its extension.

3.1.4 QR decomposition

QR decomposition-based equalizer is built using the same concept as SIS. However, it applies QR decomposition to the channel matrix such that $\boldsymbol{H} = \boldsymbol{Q}\boldsymbol{R}$ where $\boldsymbol{Q}$ is a unitary matrix and $\boldsymbol{R}$ is a triangular matrix. The vector of the received symbols $\hat{\boldsymbol{c}}_{n'}$ is then multiplied by the conjugate transpose of $\boldsymbol{Q}$ making the equivalent channel matrix triangular ($\boldsymbol{Q}^H\boldsymbol{H} = \boldsymbol{Q}^*\boldsymbol{Q}\boldsymbol{R} = \boldsymbol{R}$). This permits having a simpler and more performant SIS [HR10] because of the triangular equivalent channel shape. However, the system being considered is an MC

system parameterized by the transmitting and receiving pulse shapes. This might lead to have some information about the channel lost through the transition from time domain to frequency domain. An example of that is truncation of the Cyclic-Prefix (CP) at the receiver in Cyclic-Prefix Orthogonal Frequency Division Multiplexing (CP-OFDM), which truncates also the channel information within the CP samples. In addition to that, it is possible that we benefit from the channel variation in the time domain. Consequently, in the next section, we look into some possible time domain processing to be done on the receiver to check its impact on the system's performance.

3.2 Time Domain Preprocessing

In this section, we discuss the time domain preprocessing techniques that will be used in the comparative discussion provided later in this chapter. It is important to note that some time domain preprocessing exists for Orthogonal Frequency Division Multiplexing (OFDM), but in the context of shortening the channel's impulse response to be less than the CP duration [MYR96], which signifies the practicality of such approach. In this work, the goal of an additional time-domain processing before the frequency domain processing (consisting in a bank of pulse matched filter for the first step) is different. The underlying motivation is to lead to a receiver structure able to ease the management of one or two tasks : interference reduction or/and fading reduction. Regarding the reduction of the fading impact, the receiver structure should be able to catch the potential diversity linked to the time domain channel variation, as described in chapter 2, section 1.3.2.4 (Doppler-generated-diversity) and related appendix A (Doppler-driven Diversity in single carrier systems). However, as seen even in the simplified single symbol single carrier interference free case (see appendix A, figure A.3), a simple pulse matched filter (as the first step of the frequency domain processing) is not sufficient, and we need additional process taking into account the channel variation, assumed known in this chapter (channel estimation will be adressed in the next chapter). So we present in this section some additional possible time-domain preprocessing, and discuss their capabilities. We first provide the expressions of such processing for single path channels, then we extend it to multipath.

3.2.1 Preprocessing in single path channels

In this section, we discuss the time domain preprocessing that we will consider for this work and their expression in single path channels. We first discuss using MMSE in time domain in section 3.2.1.1, then we discuss what we call Matched Channel Multiplier (MCM) in section 3.2.1.2.

3.2.1.1 Time domain MMSE in single path channels

We consider the MMSE technique performed in the time domain, not to be confused with the frequency domain version discussed in section 3.1.1. This follows the same concept as in equation (3.1), however to be applied in the time domain just after receiving the signal and before feeding it to the correlator banks. Thus, the processed signal $s^{\dagger}$ is defined as:

$$s^{\dagger}[q] = \frac{r[q]\, h^{*}[q]}{|h[q]|^{2} + \mathrm{SNR}^{-1}}. \tag{3.4}$$

This type of preprocessing targets to 'revert' the impact of the channel so that it minimizes the error between the transmitted signal and the received one. This leads to two properties of the time domain MMSE: 1) since it (partially) reverts the channel's impact, it does not require further processing in frequency domain (to be able to manage the interference), but 2) for the same reason, it cannot benefit from the Doppler-generated diversity discussed in section 1.3.2.4.

3.2.1.2 Time domain MCM in single path channels

Another time domain processing technique, MCM, is considered in this work. In this technique, we propose to perform correlation with the channel's matched filter. Since we assume a single-path channel, this is equivalent to a one-tap matched filter, that is, multiplying by the conjugate of the channel value:

$$s^{\dagger}[q] = r[q]\, h^{*}[q]\,. \tag{3.5}$$

This operation will permit to have a real-valued positive equivalent channel due to conjugate multiplication, in addition to giving more weight to the channel's taps with higher values (or maximizing the SNR), which should have a beneficial effect on the potentiality to capture diversity (see appendix A). However, in contrary to MMSE which can be used alone as a time domain equalizer, this technique keeps (or even increases) the spread in the Doppler frequency domain. This effect is trivial due to the convolutive behavior in the frequency domain to the multiplication in the time domain. Consequently, it must be used along with a frequency domain equalization technique like the ones mentioned in section 3.1. To do so, it is required to compute the new equivalent channel $h^{\dagger}$ in the perspective to pass it to the later process. The equivalent channel is:

$$h^{\dagger}[q] = h[q]\, h^{*}[q] = |h[q]|^{2}\,. \tag{3.6}$$

This combination of time domain and frequency domain processing is depicted in figure 3.1. The combination of these two processing types is expected to have a beneficial effect on the potentiality to capture diversity, since we perform both channel and pulse matched filtering (see appendix A). However, we have also to take into account the interference, it is why for the frequency domain equalizer, we consider possible more advanced processing than the simple one-tap equalizer. In this work, we concatenate MCM with the frequency domain QR equalization technique which we find to have the best performance with MCM. We name this

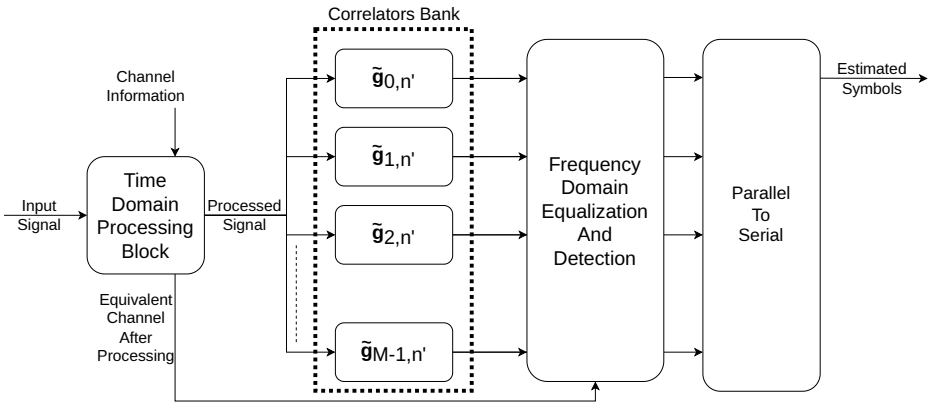

Figure 3.1: MC Receiver with Time Domain Processing Block and Frequency Domain Equalization and Detection.

combination MCMQR. In the next section, we extend the discussed time domain preprocessing to operate in multipath channels.

3.2.2 Preprocessing in multipath channels

To be able to extend the techniques discussed in the previous section to be used in multipath channels, we first rewrite the received signal model. In section 1.2.3, we have expressed the baseband discrete complex received signal in equation (1.36) as:

$$r[q] = \sum_{l=0}^{L-1} h[q,l]s[q-l] + \omega[q].$$

We rewrite this equation in matrix format to be:

$$\boldsymbol{r} = \boldsymbol{\mathcal{H}}\boldsymbol{s} + \boldsymbol{\omega}, \tag{3.7}$$

such that $\boldsymbol{r}$ is the received samples vector, $\boldsymbol{s}$ is the transmitted samples vector, $\boldsymbol{\omega}$ is the circular complex Gaussian noise, and $\boldsymbol{\mathcal{H}}$ is the matrix diagonalizing the channel's response $h[q,l]$ such that:

$$\mathcal{H}[i,j] = h[i, i-j]. \tag{3.8}$$

This format of representation will simplify the analysis of the processing. However, one very important property of $\boldsymbol{\mathcal{H}}$ that should be kept in mind is that it is a sparse matrix defined by its diagonals. This means that if we need to represent a $rows \times cols$ matrix $\boldsymbol{\mathcal{H}}$ that is defined by $diags$ diagonals, will require $\leq diagscols$ elements to be represented instead of $rowscols$ where $diags \leq rows$. In the next section, we revisit the MMSE time domain processing, but in matrix format to consider multipath channels. Then in the section after it, we revisit the MCM time domain processing, again in matrix format to consider multipath channels.

3.2.2.1 Time domain MMSE in multipath channels

In this section, we extend the MMSE processing of section 3.2.1.1. Similar to how we apply equation (3.4) to minimize the MSE for the received signal of equation (1.36) (with $L = 1$), we apply the matrix form equivalent to solve this problem [Sch04] so that:

$$\boldsymbol{s}^{\dagger} = \boldsymbol{\mathcal{H}}^{H} \left(\boldsymbol{\mathcal{H}}\boldsymbol{\mathcal{H}}^{H} + \boldsymbol{I}\frac{\sigma_{\omega}^{2}}{\sigma_{s}^{2}} \right)^{-1} \boldsymbol{r}, \tag{3.9}$$

where $\boldsymbol{s}^{\dagger}$ is the processed samples vector, and σ_{ω}^{2} and σ_{s}^{2} are the powers of the noise ω and 'desired' signal s respectively. Note that a matrix format of such operations is defined for a limited number of samples. When such operations are to be applied on a stream of sample having an undefined or very large length, it should be approximated by grouping the samples into chunks (blocks) of samples to be processed each separately. There will be a slight overlap between block samples depending on the delay size, but we neglect it in this implementation. In this work, we consider a chunk of size N so that the samples of each symbol offset duration are processed together. This will modify the equation (3.9) to include the symbol index n such that:

$$\boldsymbol{s}_{n}^{\dagger} = \boldsymbol{\mathcal{H}}_{n}^{H} \left(\boldsymbol{\mathcal{H}}_{n}\boldsymbol{\mathcal{H}}_{n}^{H} + \boldsymbol{I}\frac{\sigma_{\omega}^{2}}{\sigma_{s}^{2}} \right)^{-1} \boldsymbol{r}_{n}. \tag{3.10}$$

However, in contrary to MMSE in single path which can be used alone as a time domain equalizer, this technique might be used along with a frequency domain equalization technique like the ones mentioned in section 3.1. Consequently, we compute the new equivalent channel $h^{\dagger}$ in the perspective to pass it to a later process. This can be done by first computing the diagonalized channel using:

$$\boldsymbol{\mathcal{H}}_{n}^{\dagger} = \boldsymbol{\mathcal{H}}_{n}^{H} \left(\boldsymbol{\mathcal{H}}_{n}\boldsymbol{\mathcal{H}}_{n}^{H} + \boldsymbol{I}\frac{\sigma_{\omega}^{2}}{\sigma_{s}^{2}} \right)^{-1} \boldsymbol{\mathcal{H}}_{n}. \tag{3.11}$$

Then, this diagonalized channel should be vectorized by reversing equation (3.8) through:

$$h_{n}^{\dagger}[q, l] = \mathcal{H}_{n}^{\dagger}[q, q - l]. \tag{3.12}$$

Note that if $L = 1$, we have $\mathcal{H}$ a diagonal matrix, which makes this extension equivalent to the simpler form of section 3.2.1.1.

3.2.2.2 Time domain MCM in multipath channels

Similar to how we extended the MMSE processing in the previous section to support multipath channels, we will use the matrix form of the received signal in equation (3.7) to extend the MCM technique. Following the same concept of section 3.2.1.2, we have:

$$\boldsymbol{s}^{\dagger} = \boldsymbol{\mathcal{H}}^{H}\boldsymbol{r}. \tag{3.13}$$

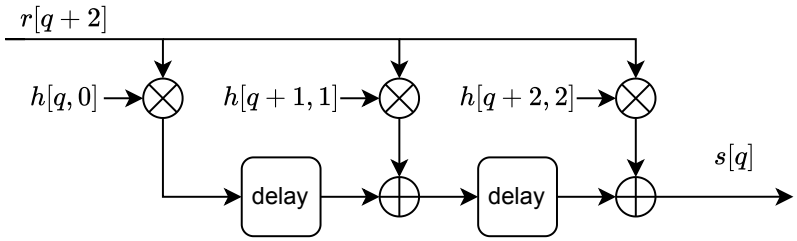

Figure 3.2: MCM equivalent FIR filter illustration for a number of (consecutive) paths $L = 3$.

We here face the same problem of requiring chunks of samples as in the previous section. However, the solution in this case is much simpler and more efficient. Note that due to the definition of $\boldsymbol{\mathcal{H}}$ in equation (3.8), the matrix $\boldsymbol{\mathcal{H}}$ can be considered as a lower-triangular Toeplitz matrix if $h[q, l]$ is constant for each path l (corresponding to a static/slow-varying channel). It is known that such forms of matrix multiplication are equivalent to filtering by convolution as it can be seen from sample-based version of such operation in equation (1.36). It is also known that the complex conjugate multiplication of such matrices is equivalent to the symmetric conjugate filtering, or matched filtering. Therefore, the matrix multiplication performed in equation (3.13) can be simplified to a simple L-taps filter with an exception that the taps of this filter are variable. To pin down this filtering mathematically we expand equation (3.13) to the scalar format:

$$s^{\dagger}[q] = \sum_{i} (\boldsymbol{\mathcal{H}}^{H})[q, i] r[i] = \sum_{i} (\mathcal{H}[i, q])^{*} r[i]. \tag{3.14}$$

Following the definition of $\boldsymbol{\mathcal{H}}$ in equation (3.8), we rewrite equation (3.14) as:

$$s^{\dagger}[q] = \sum_{i} h^{*}[i, i - q] r[i] = \sum_{k=0}^{L-1} h^{*}[q + k, k] r[q + k], \tag{3.15}$$

with $k = i - q$. As can be seen from this equation, the preprocessed signal $s^{\dagger}$ can be obtained using an L-tap filter whose taps depend on q, which is illustrated in figure 3.2 for $L = 3$. However, similarly to the previous sections, this will require deriving the new equivalent channel $h^{\dagger}$. This can be done by further extending equation (3.15) using equation (1.36) so that the preprocessed signal $s^{\dagger}$ can be written as:

$$s^{\dagger}[q] = \sum_{k=0}^{L-1} h^{*}[q + k, k] \sum_{j} h[q + k, j] s[q + k - j] + \sum_{k=0}^{L-1} h^{*}[q + k, k] \omega[q + k]. \tag{3.16}$$

Rewriting this equation while setting $j = l + k$ leads to:

$$s^{\dagger}[q] = \sum_{l} \left(\sum_{k=0}^{L-1} h^{*}[q + k, k] h[q + k, l + k] \right) s[q - l] + \omega'[q], \tag{3.17}$$

where $\omega'[q] = \sum_{k=0}^{L-1} h^*[q+k,k]\omega[q+k]$. This can be rewritten as

$$s^\dagger[q] = \sum_{l=1-L}^{L-1} h^\dagger[q,l]s[q-l] + \omega'[q], \tag{3.18}$$

where the new equivalent channel $h^\dagger$ can be expressed as:

$$h^\dagger[q,l] = \sum_{k=0}^{L-1} h^*[q,k]h[q+k,l+k]. \tag{3.19}$$

Note that the range of l is defined by $[-k; L-1-k]$ for being parameter of h, while $k \in [0; L-1]$ for being parameter of h^*, then we have $l \in [1-L; L-1]$. Note that if $L = 0$, we have equations (3.15) and (3.19), equivalent to equations (3.5) and (3.6) of section 3.2.1.2.

3.3 Complexity Analysis

In this section, we examine the order of complexity of the existing and proposed equalization techniques. Through this section, we replace the use of the number of subcarriers M and number of samples between successive symbols N by the lowercase letters m and n respectively to have a neater notation. The complexity orders of the equalizers are as follows:

- **Frequency domain MMSE:**
  A single-tap frequency domain MMSE equalizer performs a single multiplication per sub-carrier with a value that can be obtained in $O(1)$, making its complexity order $m \times O(1) = O(m)$.

- **Frequency domain LS**:
  A multi-tap frequency domain LS equalizer includes two matrix multiplications and one matrix inversion, each can be performed with complexity $O(m^{2.3727})$ [Wil12]. This leads to an order of complexity $O(m^{2.3727})$.

- **Frequency domain SIS**:
  The SIS procedure includes 1) ordering that has the complexity $O(m\ \log m)$ [Cor01], 2) detection per sub-carrier that has the complexity $m \times O(1) = O(m)$, and 3) suppression per sub-carrier having the complexity of $m \times O(m) = O(m^2)$ having a total order of complexity of $O(m^2) + O(m \log m) + O(m) = O(m^2)$.

- **Frequency domain *QR***:
  The QR decomposition-based equalizer is an SIS preceded by QR decomposition which is known to have the complexity $O(m^3)$, and one matrix multiplication. This results in total complexity of $O(m^3) + O(m^{2.3727}) + O(m^2) = O(m^3)$.

- **Time domain MMSE:**
  Time domain MMSE equalizer in single path channels from section 3.2.1.1 performs a

Table 3.1: Summary of the equalizers complexity order.

Complexity order	$\mathbf{MMSE}_f$	$\mathbf{LS}_f$	$\mathbf{SIS}_f$	$\mathbf{QR}_f$	$\mathbf{MMSE}_t$	$\mathbf{MCM}_t$
In single path	M	$M^{2.3727}$	M^2	M^3	N	L
In multipath	M	$M^{2.3727}$	M^2	M^3	$N^{2.3727}$	nL^2

single multiplication per sample with a value that can be obtained in $O(1)$, making its complexity order $n \times O(1) = O(n)$. In multipath channel, the procedure in section 3.2.2.1 is similar to the frequency-domain LS, what requires operations in the order of $O(n^{2.3727})$, (since we are using a chuck/block size N, renamed here to n, as discussed in section 3.2.2.1).

- **Time domain MCM**:
  MCM equalizer performs a single multiplication per sample with a value that can be obtained in $O(1)$, making its complexity order $n \times O(1) = O(n)$. In multipath channel, the procedure in section 3.2.2.2 requires operations in the order $O(L)$ per sample to compute equation (3.15) and operations in the order $O(L)$ to compute equation (3.19) per sample per path. This leads to a total complexity of $O(L) + 2L \times O(L) = O(L^2)$ per sample. As we are normalizing complexity to symbol duration, this leads to $O(nL^2)$.

These values of complexity order are summarized in table 3.1. In the next section, we provide simulations and performance analysis for the discussed equalizers.

3.4 BER Simulations and Analysis

In this section, we provide BER-based simulations and analysis for MC systems operating in a downlink mobile channel. We consider the generalized Frequency Division Multiplexing (FDM) system discussed in section 1.2.3 with the receiver extended as in figure 3.1 and using the pulse shapes discussed in section 1.2.3.2: Rectangular (Rect) pulse (using the CP-OFDM implementation), Out of Band Energy (OBE) pulse, Gaussian (Gauss) pulse equally spreading in time and frequency (normalized to symbol time and frequency slot), and Root Raised Cosine (RRC) pulse (with roll-off factor $\beta = 0.25$). For simplicity and clarity, we disregarded in this section Time-Frequency Localized (TFL) as its performance appeared to be almost identical to OBE and RRC with $\beta = 1$ as it is interesting only in density reduction schemes (see section 2.4) that are not considered for this section. We first provide the performance of all the equalizers combined with every pulse shape, then summarize the observed performance in a comparative fashion.

For comparison purposes, we consider two references: 1) '*Slow Fad.*' corresponding to the theoretical BER of a Rayleigh slow-fading channel provided by [SA98] and adopted by Proakis [PS08] and MATLAB *berfading* [Mata] function; and 2) '*ML*' corresponding to the best possible performance obtained by the Maximum Likelihood (ML) criterion implemented by an exhaustive search in time domain just after the signal is received. When *ML* is not

intractable due to ISI, we alternatively compute *'ML*'* which is simply a frequency-domain exhaustive search but without accounting to the ISI. This *'ML*'* metric also corresponds to the best possible performance for frequency domain equalization.

Since we will implement the ML as a benchmark, we cannot use high Quadrature Amplitude Modulation (QAM) order or number of subcarriers M. For example, if we use 16QAM and $M = 64$, we will need a dictionary of size $16^{64} \approx 1.1579 \times 10^{77}$ for the brute force search for each symbol. Therefore, simulations are performed for $M = 4$, $N = 5$, and 4QAM. However, we provide at the end of the comparison, in section 3.4.6, the performance for higher values, but excluding the ML benchmark to verify the analysis. A stream of 10^5 MC symbols (4×10^5 QAM symbols) is used for every simulated value of BER. We have $K = 1$ for Rect and OBE by their nature, $K = 5$ for Gauss, and $K = 9$ for RRC.

In legends, operations performed in the time domain are sub-scripted with t, and operations performed in the frequency domain are sub-scripted with f. We provide simulations for both single path and multipath channels. For multipath channels, we consider two paths with equal power that are separated with $0.2T_s$ since it is the CP duration we consider for the Rect pulse. In this section, we assume perfect CSI (delays, SNR, channel taps) except when specified otherwise in section 3.4.6.

3.4.1 BER performance with Rect (CP-OFDM)

In this section we provide BER-based performance analysis for the considered MC system while using the Rect pulse shape. As mentioned before, the transmitting Rect pulse will be of a duration NT_{sa} higher than the receiving Rect pulse MT_{sa}. This setup makes the Rect-shaped MC system equivalent to CP-OFDM.

In figure 3.3.a) F_dT_s is fixed at 0.25 with a **single path channel**, and BER is plotted versus normalized SNR E_b/N_0. Note that the value of *Slow Fad.* reference is independent of the selected value of F_dT_s since it is a theoretical value of BER in slow fading channels ($F_dT_s \approx 0$). Such a channel appears for each MC symbols as a simple gain, but changes from one MC symbol to another, then no waveform distortion, but also no diversity. As expected all the plots decrease as E_b/N_0 increases. We can see that the worse performing technique is MMSE_f which is classically adopted for Rect pulses (or CP-OFDM). This is quite normal because this equalization method is designed without considering ICI and high values of normalized Doppler spread F_dT_s as the one we are considering. We can notice that the QR_f and MCMQR techniques are almost at the same BER level which is slightly higher than the *Slow Fad.* reference. On the other hand, LS_f and MMSE_t that have identical performance which is closer to the ML reference.

In figure 3.3.b) E_b/N_0 is fixed at 10 dB with a single path channel, and BER is plotted versus normalized Doppler spread F_dT_s. In this figure, one might notice that the *Slow Fad.* reference has a fixed value. This is because this reference does not dependent on the value of F_dT_s but on the value of E_b/N_0, which is fixed here. By focusing on the values around $F_dT_s = 0$, we can see that all the techniques converges to approximately one point, even the

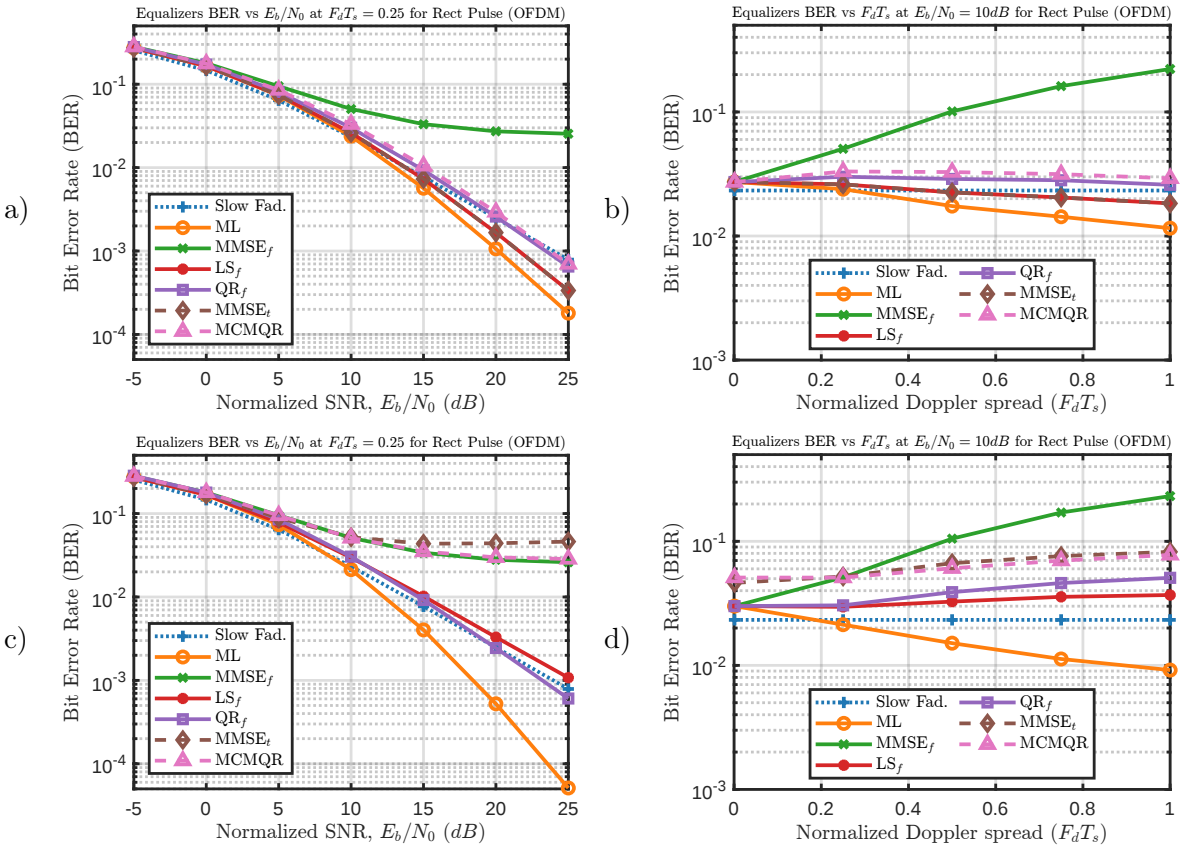

Figure 3.3: Equalizers BER (a,c) vs E_b/N_0 at $F_dT_s = 0.25$ and (b,d) vs F_dT_s at $E_b/N_0 = 10$ dB for Rect-pulsed MC System. (a,b) for single path channels and (c,d) for 2-path channel with delay spread $\mathcal{T} = 0.2T_s$.

ML reference. However, we can notice that this BER point is above the *Slow Fad.* reference. This behavior is because of having the CP-OFDM power efficiency reduced by having part of the received signal (the CP) dropped out at the receiver without being using in the detection process. In this figure, we can notice, as expected, that the classical MMSE_f has its BER increasing as F_dT_s increases. On the other hand, the ML reference is decreasing as F_dT_s increases. This signifies that although the classical receiver suffers from performance degradation as the Doppler spread increases, there is room of improvement such that we can in contrary benefit from the Doppler spread. The state-of-the-art LS receiver showed to have performance improving as Doppler spread increases in single path channels. However, this performance comes at the cost of high complexity being in the order of $O(m^{2.3727})$ as discussed in section 3.3. On the other hand, the proposed time domain MMSE_t have resulted in almost identical performance, yet having a complexity of $O(n)$ as mentioned in section 3.3.

In figure 3.3.c) and .d) equalizers BER vs E_b/N_0 at $F_dT_s = 0.25$ and vs F_dT_s at $E_b/N_0 =$ 10 dB, respectively, for Rect-pulsed MC System. In both figures, 2-path channel with delay spread $\mathcal{T} = 0.2T_s$ and equal power for both paths is assumed. Note that this delay spread is of the same duration of the CP, which means it is the highest $\mathcal{T}$ of section 1.2.2.2 before introducing ISI. We can see from these two figures that all the equalization techniques perform

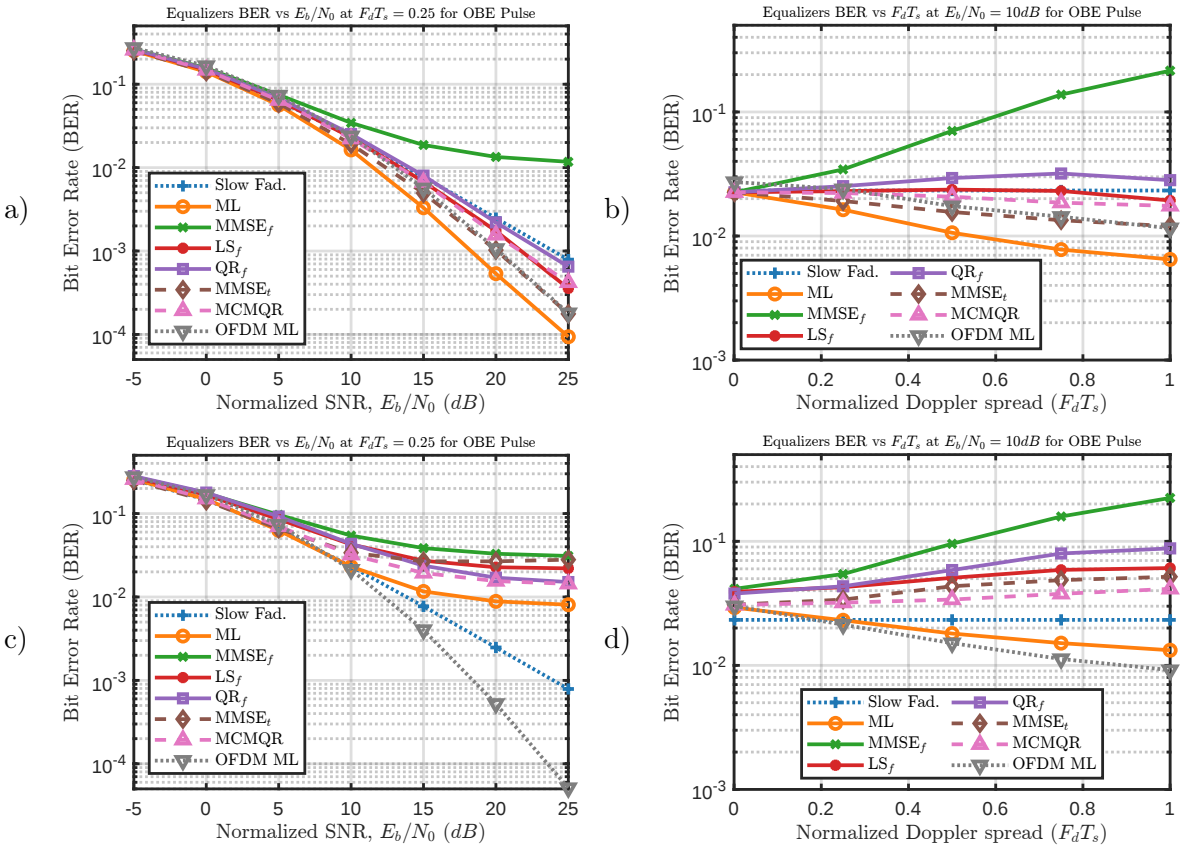

Figure 3.4: Equalizers BER (a,c) vs E_b/N_0 at $F_dT_s = 0.25$ and (b,d) vs F_dT_s at $E_b/N_0 = 10$ dB for OBE-pulsed MC System. (a,b) for single path channels and (c,d) for 2-path channel with delay spread $\mathcal{T} = 0.2T_s$.

worse than the slow fading channel reference, although the ML benchmark BER decreases as F_dT_s increases. The degradation due to interference in high speed 2-paths channel can not be compensated by the time-domain diversity captured by the considered schemes, making the trade-off unbalanced in favor of interference. Note that the ML performance is even better than the single path scenario, what signifies the presence of further diversity caused by multipath propagation. This is left as an open problem to achieve performance closer to ML in such scenarios.

3.4.2 BER performance with OBE

In this section we provide BER-based performance analysis for the considered MC system while using the OBE pulse shape. In figure 3.4, we provided BER plots similar to those of figure 3.3, but while considering the OBE pulse shape. As CP-OFDM is the currently most used MC system, we consider one additional benchmark which is *OFDM ML*, extracted from section 3.4.1. As expected, the performance for all the scenarios shown in figure 3.4 shows how the classical frequency domain MMSE_f has a very bad performance, being the

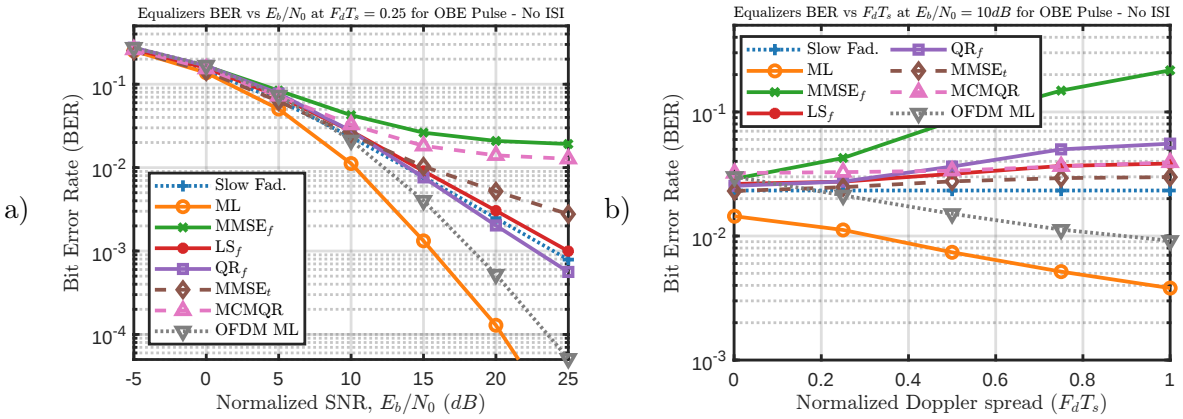

Figure 3.5: Equalizers BER a) vs E_b/N_0 at $F_dT_s = 0.25$ and b) vs F_dT_s at $E_b/N_0 = 10$ dB for OBE-pulsed MC System with ISI cancellation. Both for 2-path channels with delay spread $\mathcal{T} = 0.2T_s$.

worst among the discussed techniques. Similar to when considering the Rect pulse shape in section 3.4.1, we can see that the BER when considering the ML receiver is decreasing with the increase of the normalized Doppler spread F_dT_s. The OBE and Rect pulse shapes has a lot of similarities, and consequently they have significantly similar performance for different techniques. However, we can notice that OBE has its performance better in general. In single path channels of figure 3.4.a) and b), one of the most important things to be noticed is that we have the BER of ML considering the OBE pulse lower than *OFDM ML* benchmark. One of the reasons of this performance is that it has reduced ICI as discussed in chapter 2. In addition to that, it uses the whole pulse duration to receive the signal, in contrary to CP-OFDM (Rect), which loses a part of its power (and then the power efficiency) due to dropping out part of the signal (the CP duration) without using it. This is expected as CP-OFDM is designed to operate in multipath channels. The performance in these scenarios shows that the best technique is the proposed time domain MMSE$_t$ which has approximately the same performance as the intractable *OFDM ML*. However, when considering multipath channels as shown in figure 3.4.c) and d), OBE BER is significantly higher than CP-OFDM due to the increase in ISI. This performance was expected as OBE pulse shapes accepts ISI, and does not have a built-in ISI cancellation procedure as CP in CP-OFDM.

For such pulse shapes, we can employ an ISI cancellation procedure to counter this weakness. We discuss the procedure of ISI cancellation we consider for this work in section 3.5. In figure 3.5, we provide the equalizers BER a) vs E_b/N_0 at $F_dT_s = 0.25$ and b) vs F_dT_s at $E_b/N_0 = 10$ dB for OBE-pulsed MC System with ISI cancellation. Both sub-figures, a) and b), consider 2-path channels with delay spread $\mathcal{T} = 0.2T_s$ with equal power for both paths. We can see that, if ISI cancellation is employed, OBE-pulsed MC systems over-perform the CP-OFDM. This can mainly be noticed by the significant gap between the ML reference of the two systems. Through figure 3.5.a), we can see that the best performing equalizer at high E_b/N_0 is QR$_f$, while the best equalization technique in countering high F_dT_s is the time domain MMSE$_t$. However, unfortunately, in this work, we were not able to benefit from a diversity gain sufficient to compensate the interference degradation in multipath variable

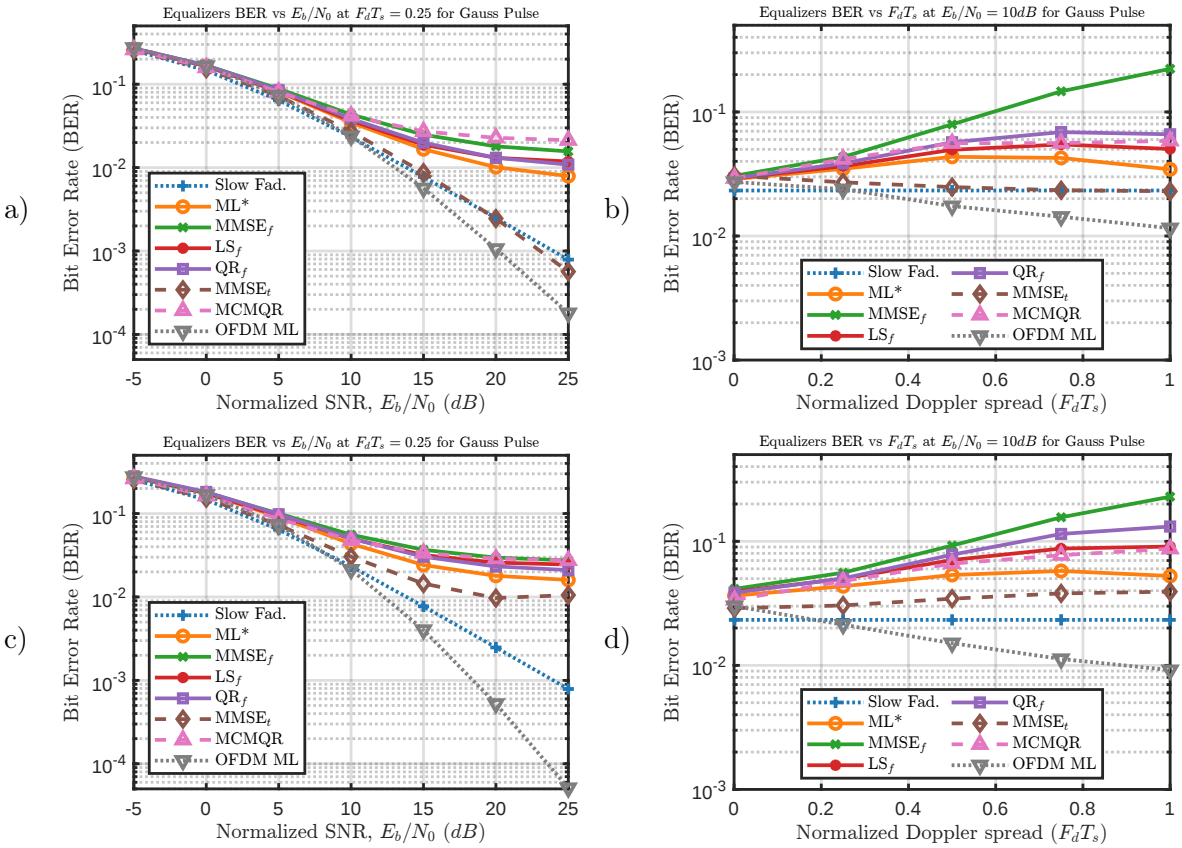

Figure 3.6: Equalizers BER (a,c) vs E_b/N_0 at $F_dT_s = 0.25$ and (b,d) vs F_dT_s at $E_b/N_0 = 10$ dB for Gauss-pulsed MC. (a,b) for single path channels and (c,d) for 2-path channel with delay spread $\mathcal{T} = 0.2T_s$.

channels when considering time-limited pulse shapes such as OBE and Rect. This is left as an open problem to achieve performance closer to ML in such scenarios. In the next section, we consider a less-localized pulse shape for analysis: the Gauss pulse shape.

3.4.3 BER performance with Gauss

In this section, we perform analysis similar to the ones in the previous two sections, but while considering the Gauss time semi-limited and frequency semi-limited non-orthogonal pulse shape. As a reminder, we consider the variance of the Gauss pulse shape as discussed in section 1.2.3.2, where the pulse is designed to have interference equally spreading to ISI and ICI in static channels. In figure 3.6, we present the performance of the equalizers considered in this work when considering the Gauss pulse shapes. Equalizers BER (a,c) vs E_b/N_0 at $F_dT_s = 0.25$ and (b,d) vs F_dT_s at $E_b/N_0 = 10$ dB. (a,b) for single path channels and (c,d) for 2-path channel with delay spread $\mathcal{T} = 0.2T_s$ with equal power for both paths. As we mentioned before, when *ML* is not intractable due to ISI, we alternatively compute *'ML*'* which is simply a frequency domain exhaustive search but without accounting to the ISI, which is the case for Gauss

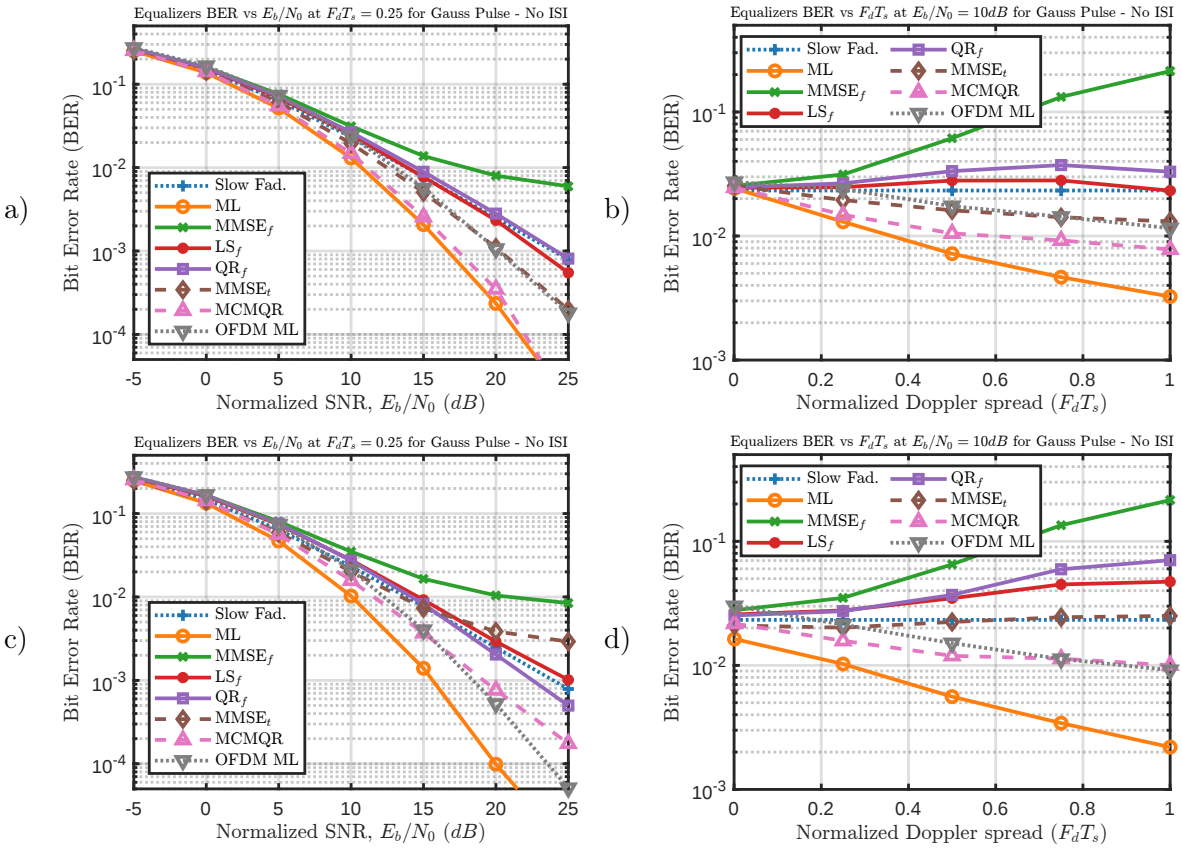

Figure 3.7: Equalizers BER (a,c) vs E_b/N_0 at $F_dT_s = 0.25$ and (b,d) vs F_dT_s at $E_b/N_0 = 10$ dB for Gauss-pulsed MC System with ISI cancellation. (a,b) for single path channels and (c,d) for 2-path channel with delay spread $\mathcal{T} = 0.2T_s$.

pulse. This *'ML*'* metric also corresponds to the best possible performance for frequency domain equalization. As expected, in this figure we can notice that the performance when considering the Gauss is significantly worse than when considering time-limited pulses like Rect and OBE, where all the techniques suffer from BER floor. This is normal since the techniques being considered only removes ICI, while as we have seen in section 2.2.4, ISI has significant disturbance when considering Gauss pulse shapes. Consequently, employing ISI cancellation procedures, like the one we provide in section 3.5, is mandatory when considering Gauss pulse shape. However, it is important to note that when ISI cancellation is not considered MMSE$_t$ has the best estimation performance in all scenarios, which will be used in a later discussion.

In figure 3.7, we reproduce all the plots of figure 3.6, but while considering ISI cancellation. Note that we are now able to compute ML instead of *ML**. As expected, the classical frequency domain MMSE$_f$ has the worse performance in all the scenarios. The more advanced frequency domain equalizers like LS and QR appears to have performance similar to slow varying channel in single path channels of figure 3.7.a) and b). From figure 3.7.d) we can see that these types of equalizers perform badly for high Doppler spreads. On the other hand we can see that ML BER decreases versus F_dT_s in a fashion very similar to that of OBE in figures 3.4 and 3.5. However, for the Gauss pulse discussed in this section, we can see that the MCMQR technique

has provided the best performance in all the scenarios having a performance very similar to the intractable *OFDM ML* benchmark. Note that this outperforms all the techniques/pulse shapes discussed for now, operates efficiently in highly dispersive channels in both time and frequency domains, and performs better with the increase of F_dT_s turning the weakness of ICI to a benefit of diversity. In addition to this, the observed performance proves our claim that the significant degradation was due to the ISI which can be easily canceled as we will show in section 3.5. Another important conclusion of this observation is the relevance and importance of the time domain preprocessing we are proposing, although this was harder to observe when considering time-limited pulse shapes. In previous sections, we considered the performance of the time-limited pulse shapes using different equalizers. In this section, we have degraded the time localization (increased the time-spreading) a little for two reasons: first, improve the frequency localization; second, capture time diversity of the channel variation by having longer pulse duration. In the next section, we will reduce the time localization even more by considering the most frequency-localized pulse: RRC.

3.4.4 BER performance with RRC

In this section, we provide the BER-based analysis when considering the RRC pulse shape. In figure 3.8, we provide equalizers BER vs E_b/N_0 at $F_dT_s = 0.25$ and vs F_dT_s at $E_b/N_0 = 10$ dB for RRC-pulsed MC System in subfigures a) and b) respectively. Both for single path channels. Note that in these subfigures, we can find that the *ML** reference has a BER floor around 2×10^{-2}, and similarly all the frequency domain equalizers. On the other hand, we can find that the time domain MMSE$_t$ performs very similarly to the *OFDM ML* benchmark. The bad performance of the equalizers in RRC pulse shape is mainly caused by the ISI as discussed in sections 1.3.2.3 and 2.2.4.1. However, the time-domain MMSE$_t$ tries to minimize the impact of the channel while considering the presence of noise, and consequently restoring the orthogonality between RRC pulses that are neighbors in the time domain. This significantly reduces the impact of ISI leading to have a very good performance when considering the RRC pulse even though we are not considering any ISI cancellation. In figure 3.8.c) and .d), same plots are provided for the assumed 2-path channel with delay spread $\mathcal{T} = 0.2T_s$. In these two figures, we still observe that all the equalizers have very bad performance except the time-domain MMSE$_t$. However, it is not performing as good as in single path channels, but still providing acceptable performance.

In figure 3.9, we provide similar plots as figure 3.8, but while considering ISI cancellation as we did in section 3.4.3 for the Gauss pulse, and as we will explain in section 3.5. We will provide the analysis for all the subfigures a, b, c, and d at once as the performances in all these scenarios while considering RRC pulse shape with ISI cancellation are similar. The first very important observation is the comparison between the ML performance with the *OFDM ML* benchmark. Through this comparison, we can notice that the RRC pulse shape has far better possible performance compared to the Rect (CP-OFDM), even for multipath scenarios. Another important observation is that the time domain MMSE$_t$ equalizer provides the same performance with and without ISI cancellation. This performance is better than all the frequency domain even when considering ISI cancellation. In other words, the time

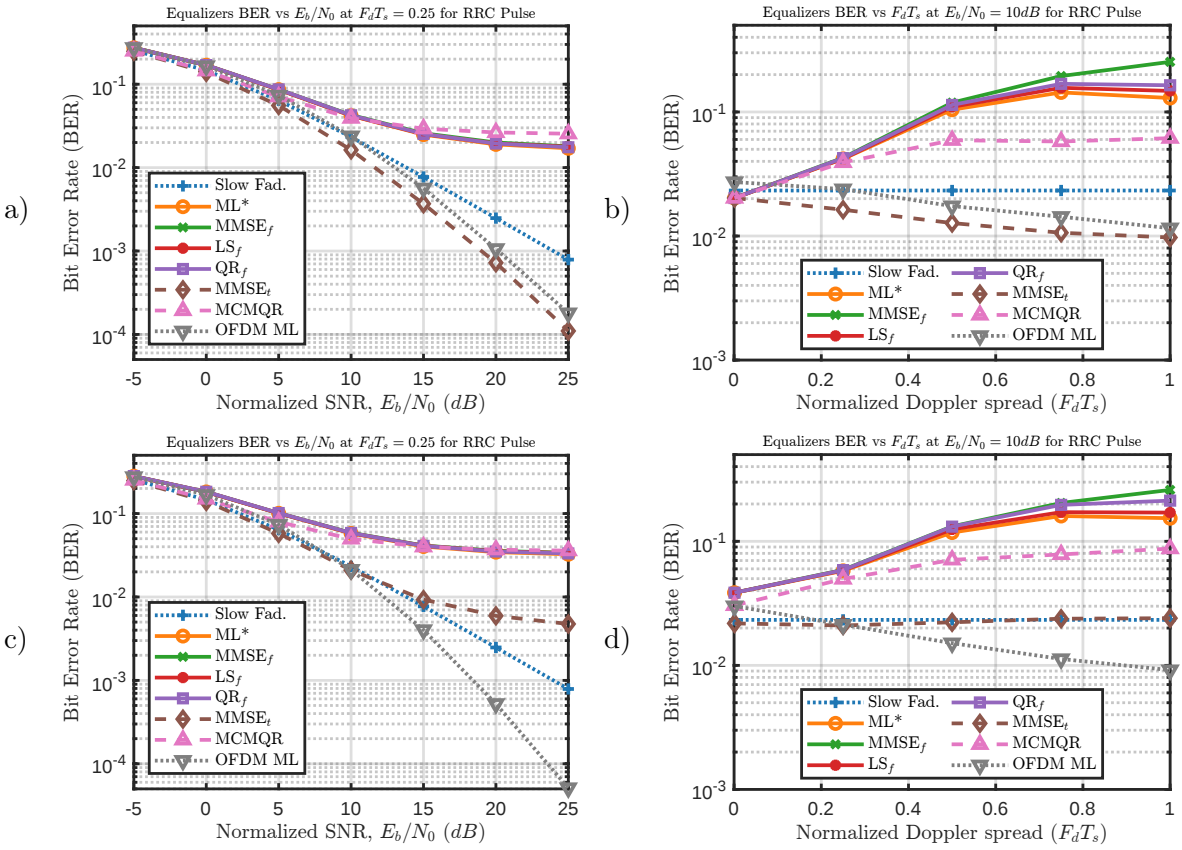

Figure 3.8: Equalizers BER (a,c) vs E_b/N_0 at $F_dT_s = 0.25$ and (b,d) vs F_dT_s at $E_b/N_0 = 10$ dB for RRC-pulsed MC System. (a,b) for single path channels and (c,d) for 2-path channel with delay spread $\mathcal{T} = 0.2T_s$.

domain MMSE_t while accepting the interference performs better than all the frequency domain equalizers while canceling it. The most important observation to be considered here is the brilliant performance of MCMQR. We can observe from figure 3.9.a) and .b) that the MCMQR performance is extremely close to the ML performance in single path channels, and from figure 3.9.c) and .d) that its performance is less close to ML, but still very close. In all cases, the achievable tractable MCMQR performance for the RRC-pulsed MC systems is far better than the non-achievable intractable ML performance of CP-OFDM. In the next section, we sum up the performance analysis provided in this section and the previous ones.

3.4.5 Results synthesis and BER performance analysis

In this section, we summarize the performance analysis provided in the previous section. This is performed by concatenating the BER plots of the best practical performance obtained for every pulse shape, in addition to the important reference plots. In specific, we compare the following: *Slow Fad.* reference to compare with the theoretical performance in slow fading channels, *OFDM ML* reference to compare with the best possible performance of CP-OFDM,

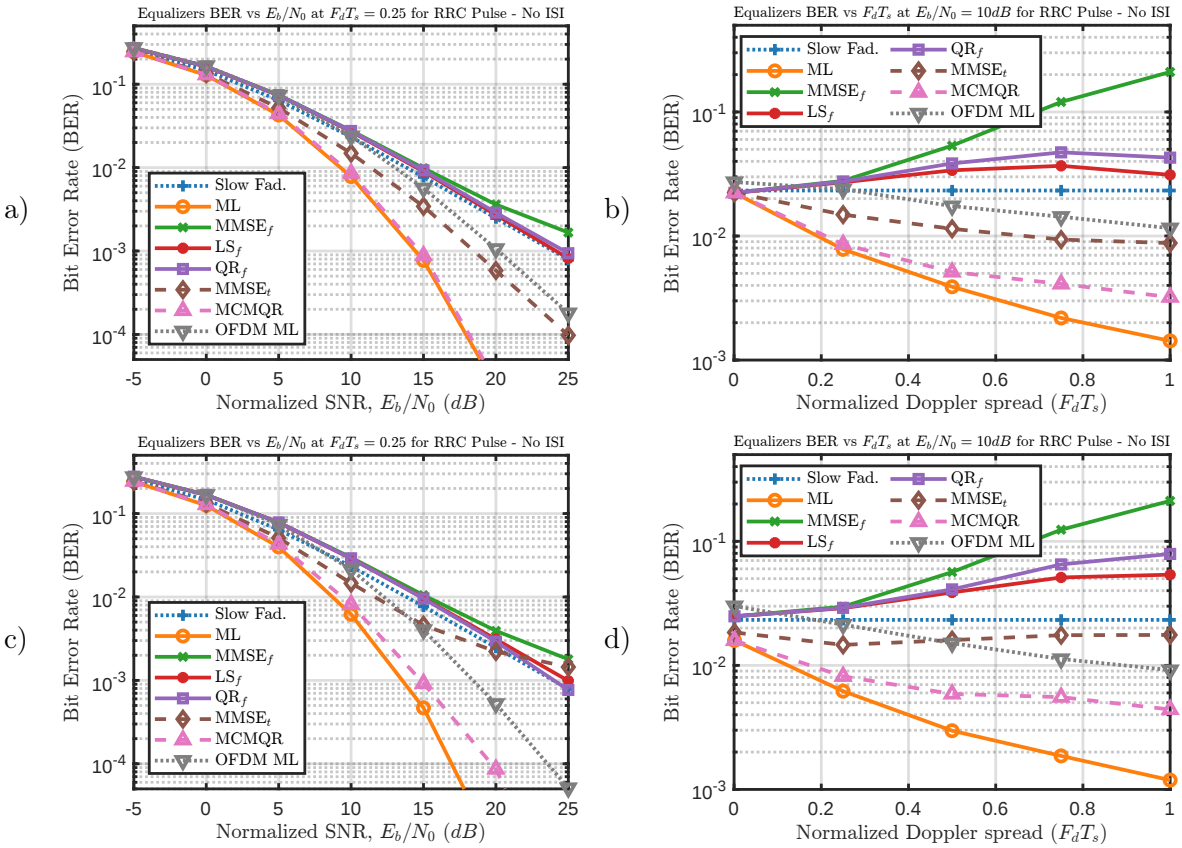

Figure 3.9: Equalizers BER (a,c) vs E_b/N_0 at $F_dT_s = 0.25$ and (b,d) vs F_dT_s at $E_b/N_0 = 10$ dB for RRC-pulsed MC System with ISI cancellation. (a,b) for single path channels and (c,d) for 2-path channel with delay spread $\mathcal{T} = 0.2T_s$.

Rect ML$_f$ the best practical performance with Rect pulse (CP-OFDM), frequency domain LS$_f$ for Rect pulse, time domain MMSE$_t$ for OBE pulse, time domain MMSE$_t$ for Gauss pulse, MCMQR for Gauss pulse with ISI cancellation (No ISI), time domain MMSE$_t$ for RRC pulse, and MCMQR for RRC pulse with ISI cancellation (No ISI). In figure 3.10, we provide plots similar to the ones in the previous sections, but using the setups mentioned above. In figure 3.10.a, we provide BER versus normalized SNR E_b/N_0 at $F_dT_s = 0.25$ for these setups, and in figure 3.10.b, we provide BER versus normalized Doppler spread F_dT_s at $E_b/N_0 = 10$ dB. Both figures for single path channels. In legend, we provide both the name of the pulse shape and the equalization technique, and we concatenated the term *No ISI* to the setups employing ISI cancellation. We also consider using dotted lines (...) for benchmarks and dashed lines (___) for plots assuming ISI cancellation for simplicity. In figure 3.10.a, we observe that all the setups performs better than the slow fading channels. One of the most important conclusions of this observation is that, in contrary to expectation, we can worry less about time variation when employing these setups, or equivalently frequency spreading. It is commonly known that increasing the pulse duration is a very good solution to counter the channel delay spread as discussed in section 1.3.1. However, this increase in the pulse duration (T_s) is an obvious increase in the normalized Doppler spread (F_dT_s), which

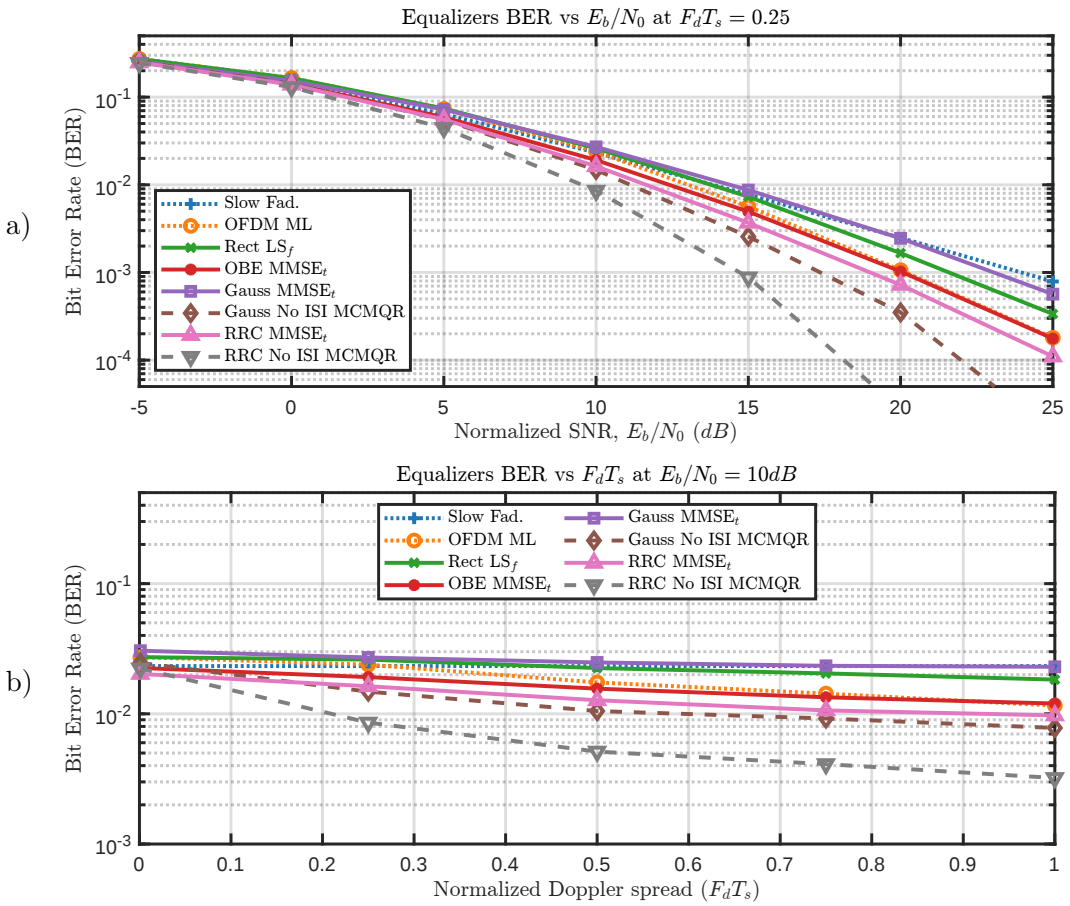

Figure 3.10: BER a) vs E_b/N_0 at $F_dT_s = 0.25$ and b) vs F_dT_s at $E_b/N_0 = 10$ dB for the best pulse shape/equalizer combinations. Both for single path channels.

becomes a major concern for multi-carrier systems as discussed in section 1.3.2, especially when considering classical one tap frequency domain equalizers as shown in sections 3.4.1 to 3.4.4. However, through the observation just made for figure 3.10.a, we can assume that having an increased pulse duration would perform better in fast varying channel when suitable processing is employed. This observation can be confirmed through figure 3.10, where the increase of F_dT_s results in better performance for most of the techniques leading to a Doppler driven diversity. For the detailed comparison, we will consider only the Rect pulse and the RRC pulse since they are the currently used pulse and the best performing pulse respectively. In figure 3.10.a, if we compare the required E_b/N_0 to have BER $\approx 3.5 \times 10^{-4}$, we require $E_b/N_0 \approx 25$ dB for the Rect pulse with LS$_f$ matrix equalizer to achieve this performance. On the other hand, to have the same level of BER with the RRC pulse shape is achieved through the proposed time domain MMSE$_t$ at $E_b/N_0 \approx 20$ dB. Furthermore, if ISI cancellation is employed, this BER is achievable using the RRC and the proposed MCMQR at $E_b/N_0 \approx 16$ dB. This means, using RRC pulse shape and the proposed techniques, we obtained a 9 dB gain in single path channels at $F_dT_s = 0.25$ when targeting BER $\approx 3.5 \times 10^{-4}$. However, the actual gain is far better than that. As we can notice from figure 3.10.b, the performance gap between the proposed and the state-of-the-art techniques increases as F_dT_s increases, which signifies

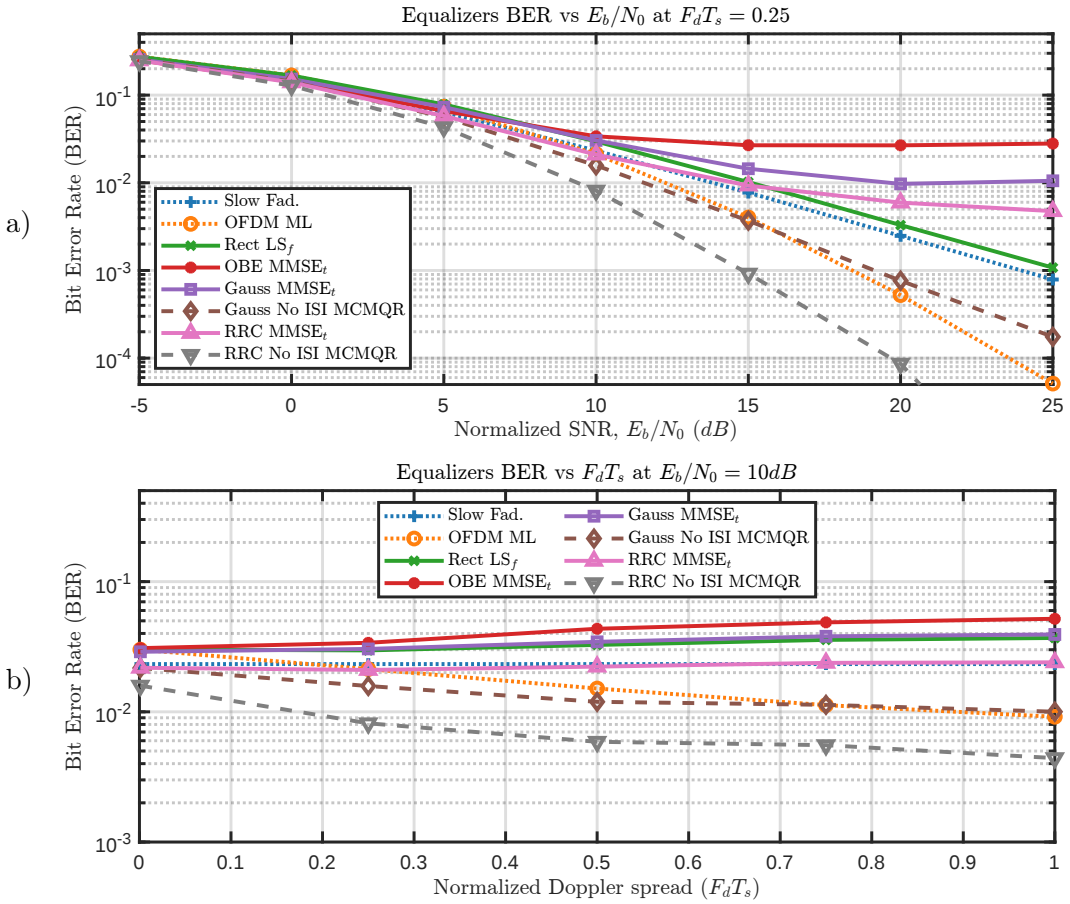

Figure 3.11: BER a) vs E_b/N_0 at $F_dT_s = 0.25$ and b) vs F_dT_s at $E_b/N_0 = 10$ dB for the best pulse shape/equalizer combinations. Both for 2-path channel with delay spread $\mathcal{T} = 0.2T_s$.

that the gain increases with F_dT_s. Moreover, as we can notice from figure 3.10.a, the gap between the proposed and the state-of-the-art techniques increases as E_b/N_0 increases, where the 'slope' of the proposed technique becomes steeper at higher E_b/N_0. This observation reflects the existence of Doppler-driven diversity captured in the time domain as discussed in section 1.3.2.4 and will be discussed in section 3.6.

In figure 3.11, we provide plots similar to those of figure 3.10, but for 2-path channel with delay spread $\mathcal{T} = 0.2T_s$ instead of single path channel. In sections 3.4.1 to 3.4.4, we observed that, in general, the ML receiver performs in the considered 2-path channels better than the single path channel. Although multipath propagation is considered as an impairment, it appears that, similarly to what we have seen in channel variation, the multipath propagation provides some type of diversity. In section 3.2.2, we have extended our proposed time domain preprocessing to support multipath channels. Although this extension leads to a very good performance, it did not capture the diversity caused by multipath propagation (at least in a fully satisfactory manner), as can be seen through comparing figures 3.10 and 3.11. Our proposed work successfully captured diversity caused by channel variation, but capturing both Doppler-driven and delay-driven diversity simultaneously and in a fully satisfactory way is kept

as an open question as it is not achieved by any of the proposed and state-of-the-art techniques. However, the observation of having Doppler-driven gain and diversity captured by the proposed techniques is still observable in the multipath scenario. Again, we will only consider in this comparison the Rect pulse and the RRC pulse since they are the currently used pulse and the best performing pulse respectively. Although we can observe from figure 3.11.b that the RRC MMSE$_t$ performs better than Rect LS$_f$ versus F_dT_s, it is the opposite versus E_b/N_0 as observed in figure 3.11.a. Therefore, it is difficult to compare them, but the important part of this is that RRC MMSE$_t$ has acceptable performance, which would be enough for ISI cancellation as will be seen in section 3.5. On the other hand, we can still observe that when ISI cancellation is employed, using MCMQR with RRC provides significant performance gain. The performance of Rect LS$_f$ hits BER $\approx 10^{-3}$ at $E_b/N_0 = 25$ dB, while using MCMQR with RRC pulse shape when ISI cancellation is employed can reach the same BER at $E_b/N_0 = 15$ dB. Consequently, even in multipath scenarios that CP-OFDM (Rect pulse shape) is specialized in and designed for, the proposed receiver structure with the designed MCMQR provides a 10 dB gain when using RRC pulse shape and ISI cancellation for reaching BER $= 10^{-3}$ at $F_dT_s = 0.25$. Again, the actual gain is far better than that, where the performance gap between the proposed and the state-of-the-art techniques increases as F_dT_s increases, which signifies that the gain increases with F_dT_s as can be seen in from figure 3.11.b. In addition to that we can notice from figure 3.11.a, the gap between the proposed and the state-of-the-art techniques increases as E_b/N_0 increases, where the 'slope' of the proposed technique becomes steeper at higher E_b/N_0 which reflects the existence of Doppler-driven diversity captured in the time domain. In the next section, we verify that the analysis provided in sections 3.4.1 to 3.4.5 are valid for more realistic situations.

3.4.6 Verification of BER performance in more realistic scenarios

In the introduction of section 3.4, we have mentioned that due to technical purposes, it is difficult to provide ML benchmark for high values of M. In addition to that, we assumed through sections 3.4.1 to 3.4.5 that the channel is perfectly known. In this section, we provide in section 3.4.6.1 the performance summary for higher number of sub-carriers M, and we provide in section 3.4.6.2 the performance summary when considering errors in channel estimation. These more realistic situations are analyzed to validate the analysis of sections 3.4.1 to 3.4.5.

3.4.6.1 BER for higher number of subcarriers

In this section, we try to validate the analysis of sections 3.4.1 to 3.4.5 for a realistic number of sub-carriers. We repeat the simulations to obtain the BER while considering number of subcarriers $M = 64$ and number of samples shift per symbol $N = 80$. A stream of 10^4 MC symbols (64×10^4 QAM symbols) is used for every simulated value of BER. We provide the BER only for setups discussed in section 3.4.5, and only BER v.s. E_b/N_0 at a fixed F_dT_s. These setups are considered to avoid redundancy as they include all the important parts of the observations. In figure 3.12 we provide BER vs E_b/N_0 at $F_dT_s = 0.25$ for the best pulse

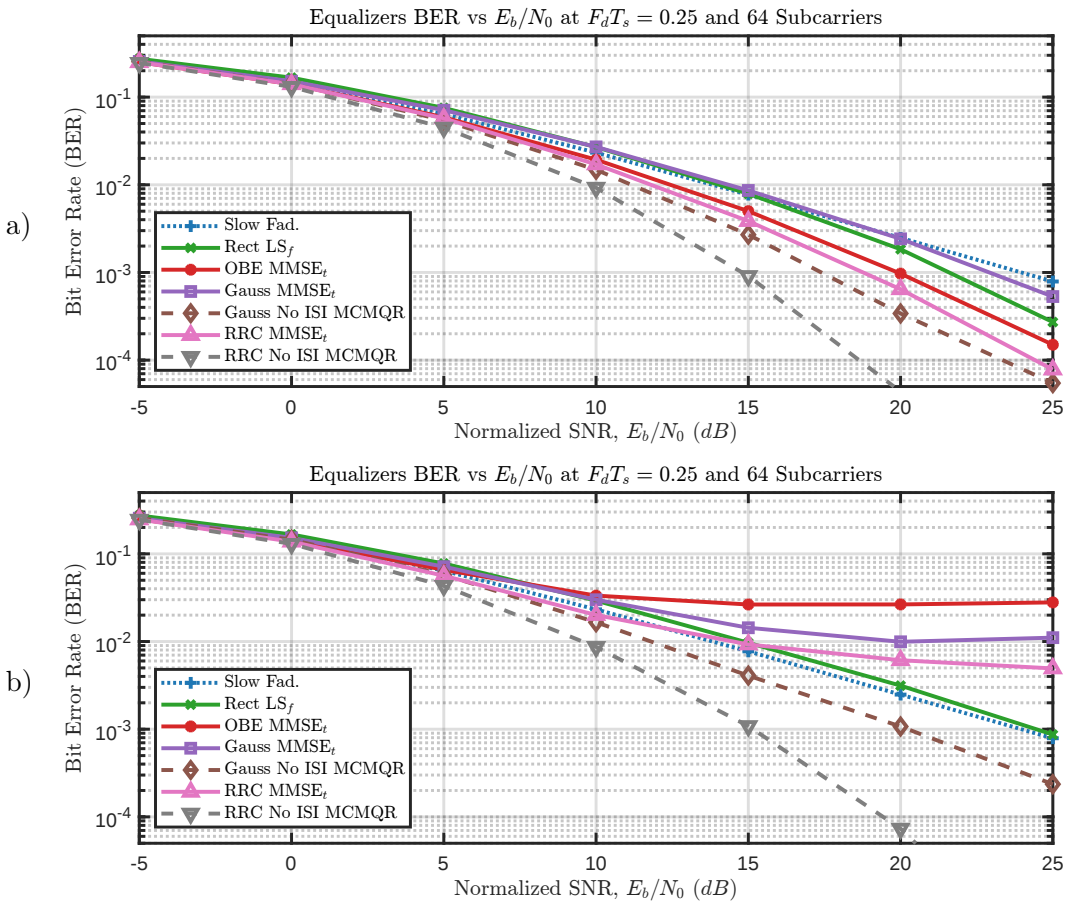

Figure 3.12: BER vs E_b/N_0 at $F_dT_s = 0.25$ for the best pulse shape/equalizer combinations for $M = 64$ and $N = 80$, a) single path and b) 2-path channel with delay spread $\mathcal{T} = 0.2T_s$.

shape/equalizer combinations for $M = 64$ and $N = 80$, a) single path and b) 2-path channel with delay spread $\mathcal{T} = 0.2T_s$. We can observe that all the performance plots are almost identical to those of figure 3.10.a and figure 3.11.a. Similarly to the $M = 4$ plots, we can see that using the proposed RRC MCMQR with ISI cancellation, we can obtain about 8 dB gain compared to Rect LS$_f$ at BER $\approx 3 \times 10^{-4}$ in single path channels with $F_dT_s = 0.25$, and we can obtain about 10 dB gain compared to Rect LS$_f$ at BER $\approx 10^{-3}$ in multipath channels with $F_dT_s = 0.25$. This confirms that all the analyses provided in sections 3.4.1 to 3.4.5 are valid for a higher number of sub-carriers. In the next section, we check the validity of the analysis when channel information is not perfectly known.

3.4.6.2 BER CSI error sensitivity

In previous sections, we have provided analysis for the situation where channel information is assumed to be perfectly known. In this section, we keep part of this assumption where the delays and SNR as assumed to be accurate which is a common assumption in the literature. However, we assume that the channel taps are not accurately estimated. We create this

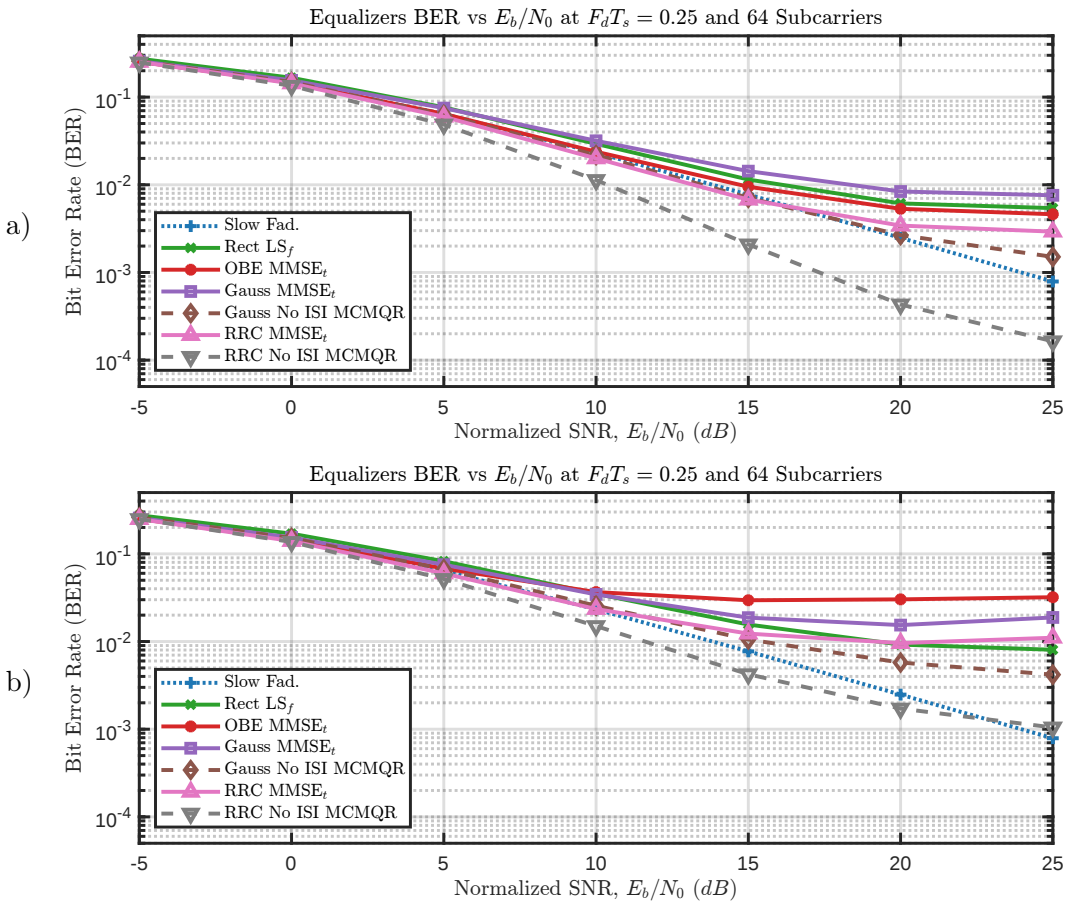

Figure 3.13: BER vs E_b/N_0 at $F_dT_s = 0.25$ for the best pulse shape/equalizer combinations for $M = 64$ and $N = 80$, a) single path and b) 2-path channel with delay spread $\mathcal{T} = 0.2T_s$. Both assuming MSE in channel estimation -20 dB.

artificial inaccuracy by adding complex random white Gaussian circular the unitary-power noise to the channel response. A added noise is of normalized power -20 dB so that the channel response MSE is -20 dB. Note that this is considered as an inaccurate channel estimation especially at high SNR as shown in [HR10] and chapter 4. We repeat the simulations to obtain the BER while considering $M = 64$ and $N = 80$. A stream of 10^4 MC symbols (64×10^4 QAM symbols) is used for every simulated value of BER. We provide the BER only for setups discussed in section 3.4.5, and only BER v.s. E_b/N_0 at a fixed F_dT_s. These setups are considered to avoid redundancy as they include all the important parts of the observations. In figure 3.12 we provide BER vs E_b/N_0 at $F_dT_s = 0.25$ for the best pulse shape/equalizer combinations for $M = 64$ and $N = 80$, a) single path and b) 2-path channel with delay spread $\mathcal{T} = 0.2T_s$. Both assuming MSE in channel estimation -20 dB. As expected, all the techniques are negatively affected by the added channel estimation error. The behavior of the plots has some error floor introduced by the estimation error. However, a notable observation is that comparison between the plots is still very similar, where what was better with perfect channel knowledge, still tends to be better with inaccurate channel knowledge. We can also observe in figure 3.13.a that in single path channels, the BER of RRC MCMQR with ISI cancellation is

$\sim 2\times10^{-4}$ with a tremendous improvement compared to Rect LS$_f$ reaching BER $\approx 6\times10^{-3}$ at the same $E_b/N_0 = 25$ dB. In the same figure, we can observe that this same BER of $\sim 6\times10^{-3}$ is achievable by the proposed RRC MCMQR with ISI cancellation at $E_b/N_0 \approx 12$ dB, which reflect a gain of $\sim$ 13 dB in such scenarios. Similar gain can be observed in figure 3.13.b for multipath channels reaching also $\sim$ 13 dB for BER $\approx 8 \times 10^{-3}$. In this section, we have reconsidered the analysis we provided in sections 3.4.1 to 3.4.5 but in more realistic scenarios in terms of number of subcarriers and inaccurate channel estimation. In addition to that, it appeared that the proposed MCMQR with RRC pulse shape and ISI cancellation is more robust to channel estimation errors than the state-of-the-art LS$_f$ technique used with CP-OFDM(Rect pulse shape). However, for now, in all the discussions we have considered we have assumed perfect ISI cancellation. In the next section, we discuss the ISI cancellation technique that we adopt for this work.

3.5 Inter-Symbol Interference Cancellation

In this section, we consider an ISI-cancellation approach. The proposed approach is based on the following steps:

0. pre-estimate the symbols $\tilde{c}_{m,n}$ while neglecting the interference,
1. at each symbol, build the reconstructed received signal $\tilde{r}$ based on the pre-estimate and the channel information:
$$\tilde{r}_n[q] = \sum_{l=0}^{L-1} h[q,l] \sum_m g[q-nN]\, e^{j2\pi \frac{m(q-nN)}{M}} \tilde{c}_{m,n}, \tag{3.20}$$
2. obtain the 'clean' signal r' by removing the interference using the received and reconstructed signals:
$$r'_n[q] = r[q] - \sum_{n' \neq n} \tilde{r}_{n'}[q], \tag{3.21}$$
3. then estimate the symbols using r'.

This technique is performed by executing the steps 1 to 3 iteratively, while considering the final estimate of an iteration as a pre-estimate for the next one, as depicted in figure 3.14. Equivalently, a single iteration would involve 2 estimations with the first step being the pre-estimate, while a double iteration would have 3 estimations, and N iterations would include $N+1$ estimations. However, a single iteration is usually considered sufficient, where only a pre-estimate and a final estimate are required. Various estimation (equalization) techniques have different sensitivities to interference. Consequently, we allow different techniques for different steps of estimation. This will optimize the performance by allowing the pre-estimate technique to be resistant to ISI, while later techniques have better performance when ISI is canceled.

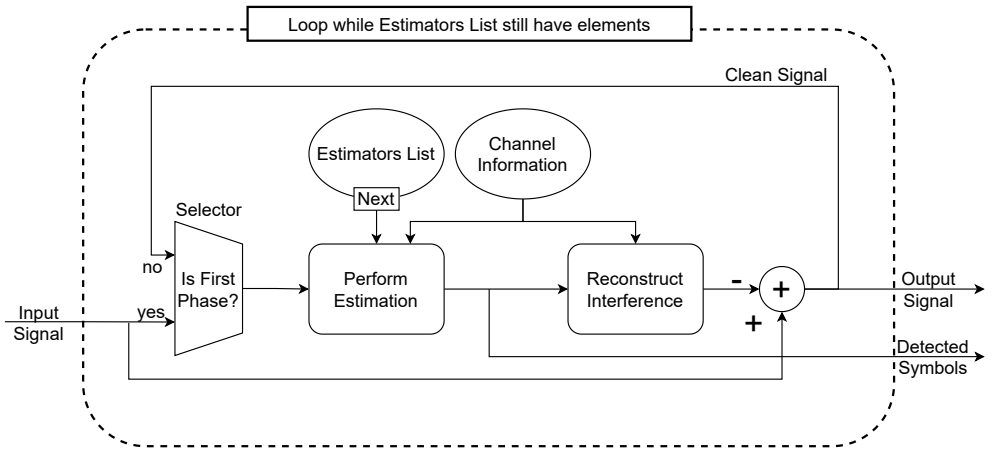

Figure 3.14: Multi-Carrier Inter-Symbol Interference cancellation Flow.

In previous sections, we have found that the most interesting pulse to perform ISI cancellation is for the RRC pulse shape. This is not only because the RRC appeared to perform extremely better than other pulses when ISI is canceled, but also because we observed that the proposed time domain MMSE_t performs very well with RRC in presence of ISI. Consequently, in this section, we will analyze the performance of the adopted ISI cancellation scheme only for the RRC pulse shape. Since the proposed time domain MMSE_t appeared in section 3.4.4 to be very robust to the ISI, we will consider it for the pre-estimate phase. On the other hand we will consider the proposed MCMQR for later phases of detection as it proved to significantly perform better than the other techniques when ISI is canceled. As done in the previous sections, we will provide plots for the obtained performance along with some reference plots to assess the performance comparatively. For this section, we will consider the following references:

1. '*Slow Fad.*' corresponding to the theoretical BER of a Rayleigh slow-fading channel provided by [SA98] and adopted by Proakis [PS08] and MATLAB *berfading* [Mata] function,

2. 'Rect LS_f' corresponding to the state-of-the-art (and best performing) frequency-domain matrix equalizer technique to use with the currently adopted CP-OFDM (Rect pulse shape),

3. and 'MCMQR Without ISI' corresponding to the performance of MCMQR when using the RRC pulse shape with perfect ISI cancellation.

Since we are focusing on the RRC pulse shape, we will not mention that in legends, and we will assume it is the RRC pulse shape by default. As we are using an iterative approach with possibly different techniques for different iterations, we will combine the techniques used by a + sign in the legends. Specifically, we will have three plots:

1. 'MMSE_t' reflecting BER when considering the time domain MMSE_t without ISI cancel-

a)

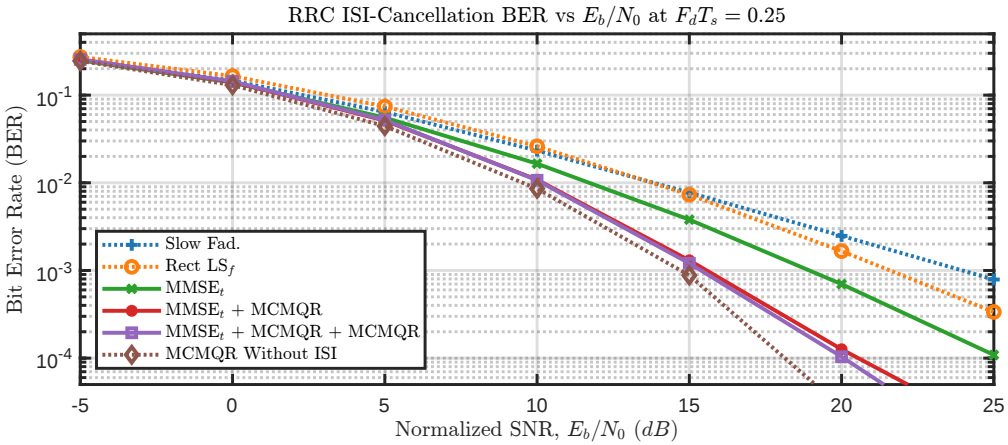

b)

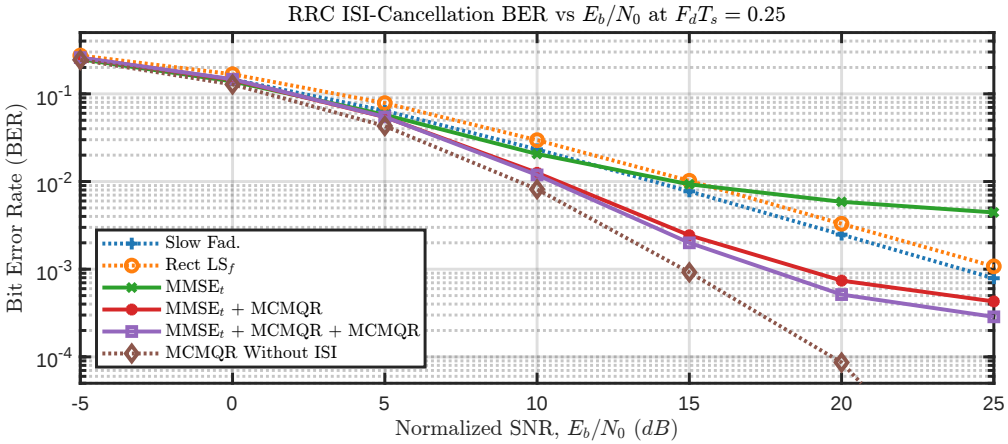

Figure 3.15: BER vs E_b/N_0 at $F_dT_s = 0.25$ for the RRC-pulsed MC system at different iterations of ISI cancellation. Channel assumed to be a single path channel in figure (a) and 2-path channel with delay spread $\mathcal{T} = 0.2T_s$ in figure (b). Channel is perfectly known in both figures.

lation,

2. 'MMSE$_t$ + MCMQR' reflecting the BER after one iteration of ISI cancellation while having the outcome of 'MMSE$_t$' as a pre-estimate,

3. and 'MMSE$_t$ + MCMQR + MCMQR' reflecting the BER after two iterations of ISI cancellation while having the outcome of 'MMSE$_t$ + MCMQR' as a pre-estimate.

Every point of the plots is obtained through a stream of 10^5 MC symbols.

In figure 3.15.a, we provide BER vs E_b/N_0 at $F_dT_s = 0.25$ for the RRC-pulsed MC system at different iterations of ISI cancellation. Channel is assumed to be a single path channel and perfectly known. As can be seen from this figure, and as we suggested in the introduction of this section, the ISI cancellation performance converges after a single iteration (MMSE$_t$+MCMQR) where the second iteration (MMSE$_t$+MCMQR+MCMQR) is extremely close to the first one and being very close to the perfect ISI cancellation. Further iterations are

not presented in these plots, but they are tested and shown to have negligible improvement for the first few iterations, then start having alternating increase and decrease in performance converging to value very close to the two-iterations plot. In addition to that, in such scenarios, comparing to the state-of-the-art LS_f plot, we can observe that the first iteration outcome (MMSE_t + MCMQR) leads to a gain of $\sim$ 7.5 dB at BER = 3.5×10^{-4}, being only 1.5 dB less than the perfect ISI cancellation. This shows how the proposed techniques (MMSE_t, MCMQR, and ISI cancellation) for RRC pulse shape, significantly outperform the state-of-the-art techniques for CP-OFDM in single path channels.

However, the more challenging scenario for such comparison is the multipath channels, especially since CP-OFDM is designed with multipath robustness in mind. Therefore, in figure 3.15.b, we provide BER vs E_b/N_0 at $F_dT_s = 0.25$ for the RRC-pulsed MC system at different iterations of ISI cancellation, assuming to be a 2-path channel with delay spread $\mathcal{T} = 0.2T_s$ that is perfectly known. Note that this delay spread is of the same duration of the CP, which means it is the highest $\mathcal{T}$ of CP-OFDM before introducing ISI. We can observe that, similarly to the single path scenario presented in figure 3.15.a, the performance of ISI cancellation converges after a single iteration (MMSE_t + MCMQR), where the second iteration (MMSE_t+MCMQR+MCMQR) results is very similar. As expected, the cancellation procedure operated with lower performance (higher BER) due to the more challenging channel. However, the performance is still very similar for E_b/N_0 below 15 dB. Now, comparing to the state-of-the-art LS_f plot in multipath scenario, we can observe that the first iteration outcome (MMSE_t + MCMQR) leads to a gain of $\sim$ 7 dB at BER = 10^{-3}, being only 3 dB less than the perfect ISI cancellation. This shows how the proposed techniques (MMSE_t, MCMQR, and ISI cancellation) for RRC pulse shape, significantly outperform the state-of-the-art techniques for CP-OFDM even in multipath channels.

The tremendous performance gain discussed above is obtained for perfect channel knowledge. Therefore, we need to confirm if this performance gain still exists for less accurate channel knowledge, as ISI cancellation relies on the accuracy of the channel information. Consequently, we reproduce the same simulation, but while adding a complex circular white Gaussian noise to the unitary power channel response with MSE = -20 dB before using it for ISI cancellation. In figure 3.16.a, we provide BER vs E_b/N_0 at $F_dT_s = 0.25$ for the RRC-pulsed MC system at different iterations of ISI cancellation. Channel is assumed to be a single path channel and partially known with MSE ≈ -20 dB. As can be seen from this figure, similarly to the error-free channel estimation scenario, the ISI cancellation performance converges after a single iteration (MMSE_t + MCMQR) where the second iteration (MMSE_t+MCMQR+MCMQR) is extremely close to the first one, but not as close to the perfect ISI cancellation. In addition to that, in such scenarios, comparing to the state-of-the-art LS_f plot, we can observe that the first iteration outcome (MMSE_t + MCMQR) leads to a gain of $\sim$ 12 dB at BER = 6×10^{-3}, being only 1 dB less than the perfect ISI cancellation. This shows how the proposed techniques (MMSE_t, MCMQR, and ISI cancellation) for RRC pulse shape, significantly outperform the state-of-the-art techniques for CP-OFDM in single path channels even when the channel is not perfectly known. In contrary to that, the proposed techniques are much more robust to the errors in channel estimation. In figure 3.16.b, we provide BER vs E_b/N_0 at $F_dT_s = 0.25$ for the RRC-pulsed MC system at different iterations

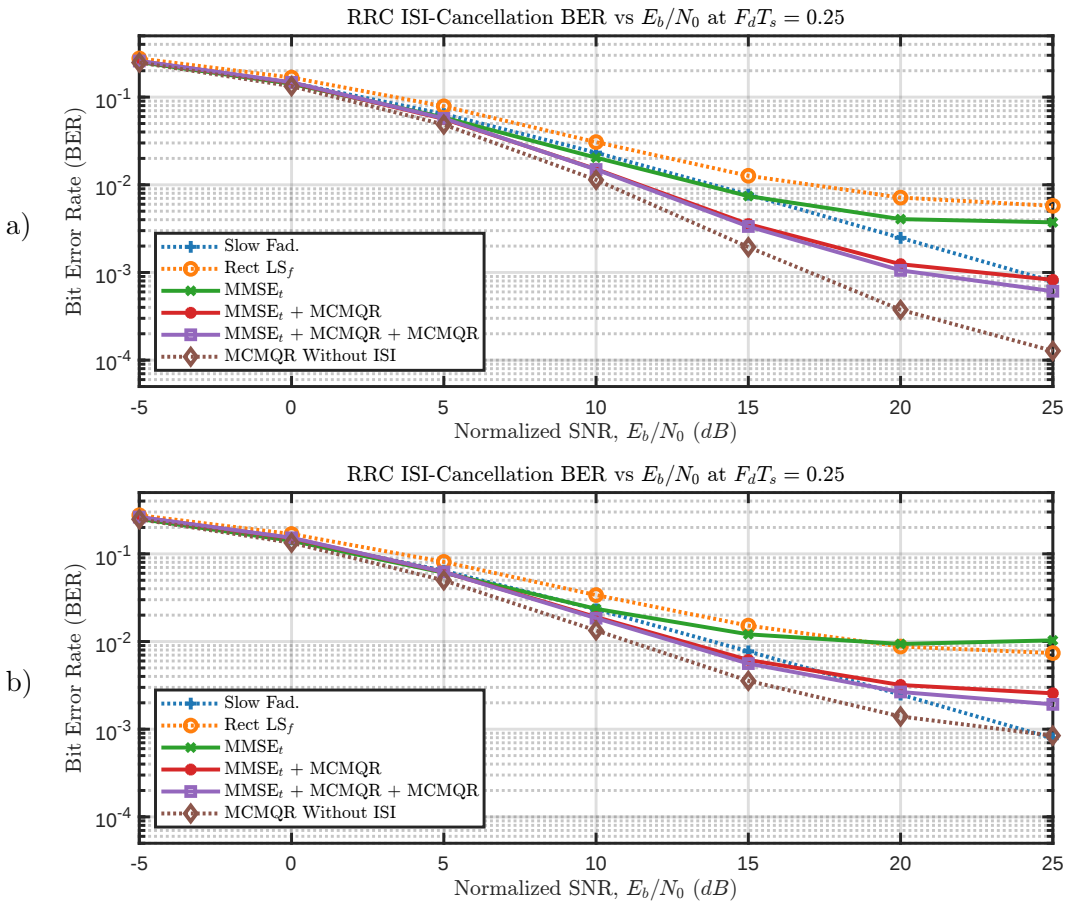

Figure 3.16: BER vs E_b/N_0 at $F_dT_s = 0.25$ for the RRC-pulsed MC system at different iterations of ISI cancellation. Channel assumed to be a single path channel in figure (a) and 2-path channel with delay spread $\mathcal{T} = 0.2T_s$ in figure (b). Channel is partially known in both figures, with MSE ≈ -20 dB.

of ISI cancellation, assuming to be a 2-path channel with delay spread $\mathcal{T} = 0.2T_s$ that is partially known with MSE ≈ -20 dB. We can observe that, similarly to the other scenarios, the performance of ISI cancellation converges after a single iteration (MMSE$_t$ + MCMQR), where the second iteration (MMSE$_t$+MCMQR+MCMQR) results is very similar. Comparing to the state-of-the-art LS$_f$ plot in multipath scenario, we can observe that the first iteration outcome (MMSE$_t$ + MCMQR) leads to a gain of $\sim$ 12 dB at BER $= 8 \times 10^{-3}$, being only 1 dB less than the perfect ISI cancellation. Again, this shows how the proposed techniques (MMSE$_t$, MCMQR, and ISI cancellation) for RRC pulse shape, significantly outperform the state-of-the-art techniques for CP-OFDM even in single path and multipath channels, in both scenarios of having the channel perfectly or partially known.

3.6 Doppler-Driven Time Diversity

In previous sections of this chapter, we have shown how using a different pulse shape, mainly the RRC pulse shape, in addition to a suitable equalization technique, can lead to a significant improvement in the performance. In addition to that, we have observed that this performance gain increases with the increase of the normalized Doppler spread F_dT_s, in contrary to the behavior of classical receivers implementing the frequency domain one tap MMSE$_f$. We have claimed through our discussion, and shown in section 1.3.2.4 and appendix A, that a performance gain with the increase F_dT_s is due to some equivalent diversity generated by the variation in the time domain. We were not able to directly compute this equivalent diversity order due to the complications of having several factors affecting it. However, we have noticed that the ability of capturing this diversity differs significantly depending on the selected pulse shape. Consequently, to obtain an estimated quantification of this gain in performance per pulse shape, we define the following:

- $\mathcal{D}_{E_b/N_0}$ maps the positive integer number of diversity branches d to the BER at a specific E_b/N_0 such that BER $= \mathcal{D}_{E_b/N_0}\{d\}$ is obtained using the unified approach provided by [SA98] and adopted by Proakis [PS08] and MATLAB *berfading* [Mata] function to obtain slow-fading BER for specific E_b/N_0 and diversity order,
- $\mathcal{D}^{-1}_{E_b/N_0}$ be the inverse maping of $\mathcal{D}_{E_b/N_0}$ such that $\mathcal{D}^{-1}_{E_b/N_0}\left\{\mathcal{D}_{E_b/N_0}\{d\}\right\} = d$,
- and $\mathcal{U}_{E_b/N_0}$ be the *'pchip'* interpolator of $\mathcal{D}^{-1}_{E_b/N_0}$ allowing arbitrary values of d.

Using the just-defined mapping $\mathcal{U}$, we can map any simulated BER to the equivalent (arbitrary) diversity order or Doppler-driven diversity equivalence. The plots of this section contain information very similar to those of section 3.4, but orient them to a diversity-based fashion instead of BER. The original definition of diversity assumes very high SNR ($\rightarrow$ inf), but we consider only three values of E_b/N_0: 5 dB, 10 dB, and 15 dB. The reason behind this is that we provide our results based on simulations instead of theoretical derivations, what makes simulating conditions leading to a very low BER not applicable with the available simulation power. However, we provide these three values of E_b/N_0 as we find that they result in practical scenarios to be simulated and sufficient to provide the required analysis.

In figure 3.17, we provide the Doppler-driven diversity equivalence ($\mathcal{U}_{E_b/N_0}\{\text{BER}\}$) vs F_dT_s for different pulse shapes and E_b/N_0 considering ML receiver, ISI cancellation, and single path channel. We consider that this setup permits observing the diversity without the impact of the quality of the receiver while transmitting over single path channels. We can observe that in all the scenarios, the minimum diversity is at $F_dT_s \approx 0$ which reaches 1. This value is normal as it reflects the slow-varying channel scenario, but the interesting observation is that for all the pulses, the diversity increases with F_dT_s. In addition to that, it appears to be increasing in an approximately linear fashion with F_dT_s. Looking into the variation with E_b/N_0, we can notice that higher E_b/N_0 results in higher diversity order. If the diversity order is to be analyzed as the slope of the BER graphs (provided in section 3.4), this means that the slope gets steeper as E_b/N_0 increases. The simulation capacity we have was not enough to simulate

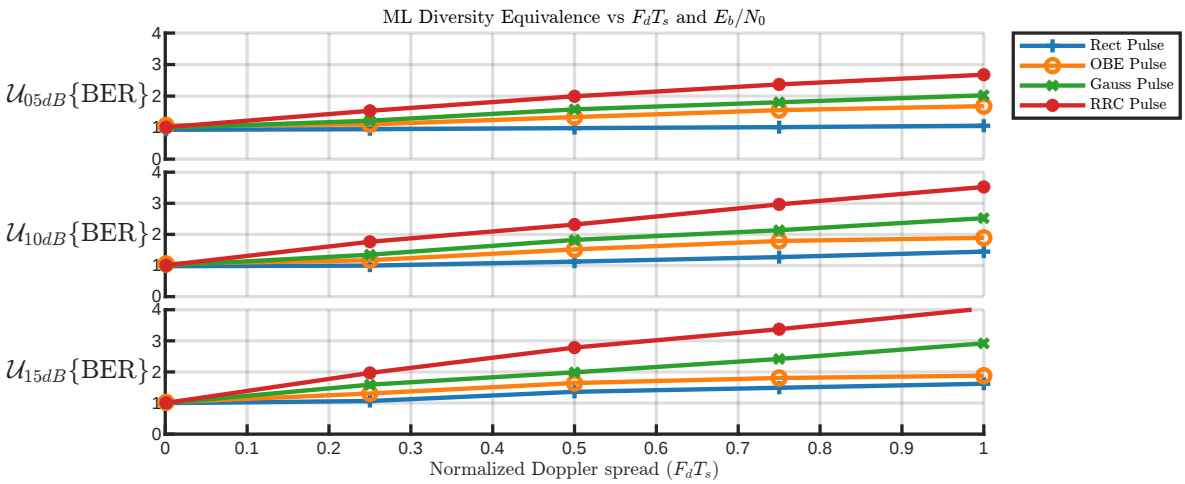

Figure 3.17: Doppler-driven diversity equivalence ($\mathcal{U}_{E_b/N_0}\{\text{BER}\}$) vs F_dT_s for different pulse shapes and E_b/N_0 considering ML receiver, ISI cancellation, and single path channel.

scenarios with lower BER to check at what value the diversity will converge to a fixed value. The highest achieved diversity is obtained by RRC pulse, and can be approximated by the line $1+3.5F_dT_s$ at $E_b/N_0 = 15$ dB. At the same E_b/N_0, the diversity reached by Gauss pulse can be approximated by $1+2F_dT_s$, the diversity reached by OBE pulse can be approximated by $1+F_dT_s$, and the diversity reached by Rect pulse can be approximated by $1+0.6F_dT_s$. By comparing the pulses ability to capture the diversity, we can see that the longer the pulse is in duration, the more diversity it is able to capture.

The analysis provided above concerns the single path scenarios only. In figure 3.18, we provide Doppler-driven diversity equivalence ($\mathcal{U}_{E_b/N_0}\{\text{BER}\}$) vs F_dT_s for different pulse shapes and E_b/N_0 considering ML receiver, ISI cancellation, and 2-path channel with delay spread $\mathcal{T} = 0.2T_s$. We consider that this setup permits observing the diversity without the impact of the quality of the receiver while transmitting over multipath channels. We can observe that in all the scenarios, the minimum diversity is at $F_dT_s \approx 0$. However, in contrary to the single path scenario, this value is slightly above 1. This diversity obtained in slow-varying channels is due to the multipath propagation, which can be seen as a source of diversity by itself. The observations of having the equivalent diversity increasing by a linear fashion with F_dT_s, and having higher E_b/N_0 resulting in higher diversity persist compared to single path scenarios. The highest achieved diversity is obtained by RRC pulse, and can be approximated by the line $1.2+3.5F_dT_s$ at $E_b/N_0 = 15$ dB. At the same E_b/N_0, the diversity reached by Gauss pulse can be approximated by $1.2+2F_dT_s$, the diversity reached by OBE pulse can be approximated by $1.2+1.5F_dT_s$, and the diversity reached by Rect pulse can be approximated by $1+F_dT_s$. Comparing the pulses' ability to capture the diversity, we can see that the longer the pulse is in duration, the more diversity it is able to capture, similarly to the behavior in single path channels.

The analysis of the two scenarios of single path and multipath channels provided above are performed for ML receivers. However, it is possible that not all the available diversity

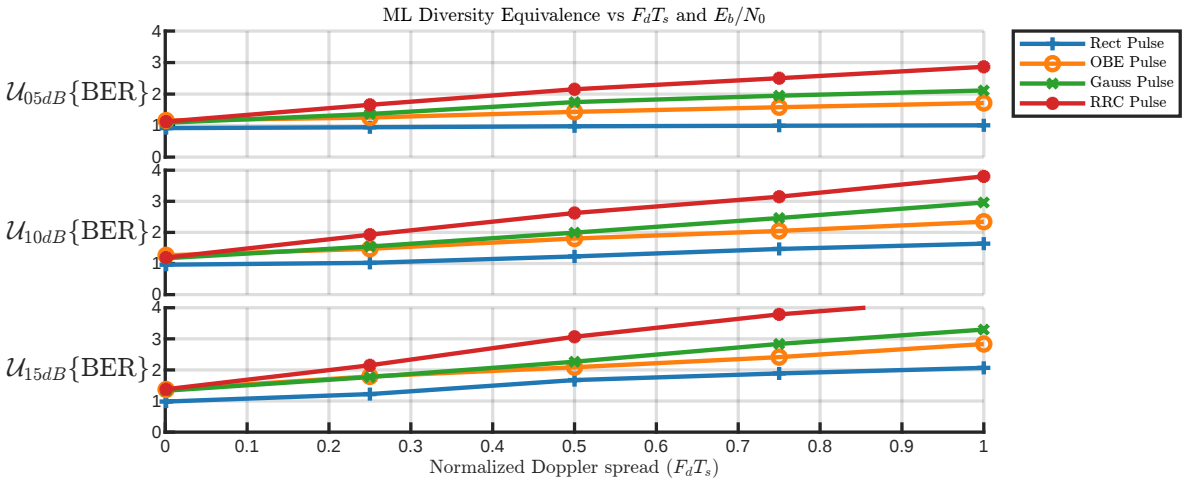

Figure 3.18: Doppler-driven diversity equivalence ($\mathcal{U}_{E_b/N_0}\{\text{BER}\}$) vs F_dT_s for different pulse shapes and E_b/N_0 considering ML receiver, ISI cancellation, and 2-path channel with delay spread $\mathcal{T} = 0.2T_s$.

is observable by practical receivers. Therefore, in figure 3.19, we provide the Doppler-driven diversity equivalence ($\mathcal{U}_{E_b/N_0}\{\text{BER}\}$) vs F_dT_s for different pulse shapes and E_b/N_0 considering the best practical receiver per pulse, ISI cancellation, and single path channel. We consider that this setup permits observing the impact of the quality of the receiver on the diversity while transmitting over single path channels. We can observe again that in all the scenarios, the minimum diversity is at $F_dT_s \approx 0$, where this value is being around 1. However, the most important difference that we can observe by comparing to the ML plots of figure 3.17 is that the diversity no longer increases linearly with F_dT_s, but curved slightly downward. At $F_dT_s = 1$, the highest achieved diversity is obtained by RRC pulse, which is 3.2 at $E_b/N_0 = 15$ dB, compared to 4.5 for the ML receiver. Similarly, for the Gauss pulse it is 2 instead of 3, for the OBE pulse it is 1.5 instead of 2, and for the Rect pulse it is 1.2 instead of 1.8. We still have the pulses with the longer duration capturing more diversity than the pulses with shorter ones. However, the present techniques are still not able to capture all the diversity as we have just seen, where there is still space of improvement in terms of diversity.

In the previous part of this section, we have observed that the available practical equalizers, for all pulse shapes, can still achieve diversity from channel variation in single path channels, even though they are not able to achieve the full diversity. In figure 3.20, we provide the Doppler-driven diversity equivalence ($\mathcal{U}_{E_b/N_0}\{\text{BER}\}$) vs F_dT_s for different pulse shapes and E_b/N_0 considering the best practical receiver per pulse, ISI cancellation, and 2-path channel with delay spread $\mathcal{T} = 0.2T_s$. Similarly, we can observe that the diversity does not increase linearly. However, we have two very critical points to distinguish right here. First, the Rect and OBE fail to achieve any diversity due to the Doppler spread, while the Gauss and RRC pulse still manage to capture the diversity. Second, when comparing the ML performance in single path channels (figure 3.17) and multipath channels (figure 3.18), we can observe that more diversity is captured in multipath channels. In contrary to that, when comparing the practical equalizers performance in single path channels (figure 3.19) and multipath channels

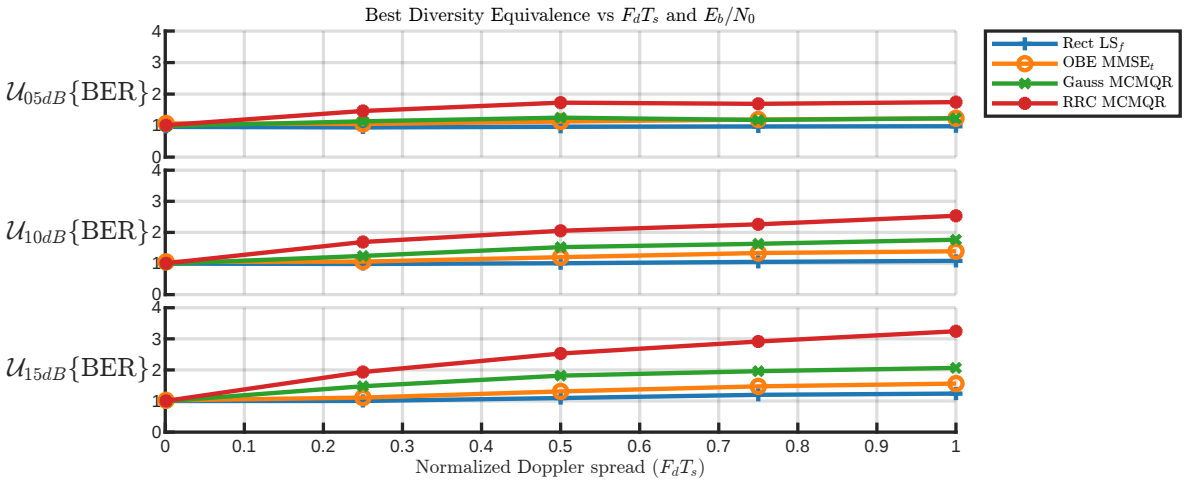

Figure 3.19: Doppler-driven diversity equivalence ($\mathcal{U}_{E_b/N_0}\{\text{BER}\}$) vs F_dT_s for different pulse shapes and E_b/N_0 considering the best practical receiver per pulse, ISI cancellation, and single path channel.

Table 3.2: Relative Second Moment of different pulse shapes.

Pulse shape	Rect	OBE	Gauss	RRC($\beta = 0.25$)
Relative Second Moment	1.00	1.14	1.34	4.40

(figure 3.20), we can observe that less diversity is captured in multipath channels. At $F_dT_s = 1$, the highest achieved diversity is obtained by RRC pulse, which is 2.9 at $E_b/N_0 = 15$ dB, compared to 5 for the ML receiver. Similarly, for the Gauss pulse it is 2 instead of 3.5, for the OBE pulse it is 1 instead of 3, and for the Rect pulse it is 1 instead of 2. This signifies that although more diversity is available to be captured in multipath scenarios, existing techniques fails to capture diversity in both dimensions. However, our proposed techniques are still able to capture part of this diversity, but the design of equalizers that captures diversity in both time and frequency domains simultaneously is kept as an open question.

As a result to all the analysis provided above, we can consider that the diversity equivalence tends to be higher for pulses spreading more in the time domain. This spreading property can be quantified using the centered second moment:

$$\mu_2\left\{\boldsymbol{g}.\tilde{\boldsymbol{g}}^*\right\} = \sum_q |(q-c)|^2\, g\left[q\right] \tilde{g}^*\left[q\right] / \sum_q g\left[q\right] \tilde{g}^*\left[q\right], \tag{3.22}$$

assuming that the pulses $\boldsymbol{g}$ and $\tilde{\boldsymbol{g}}$ are centered at $q = c$. In general, the center c is the point of symmetry of the pulse (e.g. $g[c-k] = g[c+k]$), being the midpoint of the flat region of Rect and OBE, and the maximum point of the Gauss and RRC pulses. Table 3.2 shows the second moment of different pulse shapes relatively to the Rect (CP-OFDM) pulse second moment. Although this property does not directly reflect the Doppler-driven diversity equivalence a pulse can achieve due to the channel variations, it provides insights about it as the pulses with higher spreading (second moment μ_2) – or in other words pulses that are less localized in time

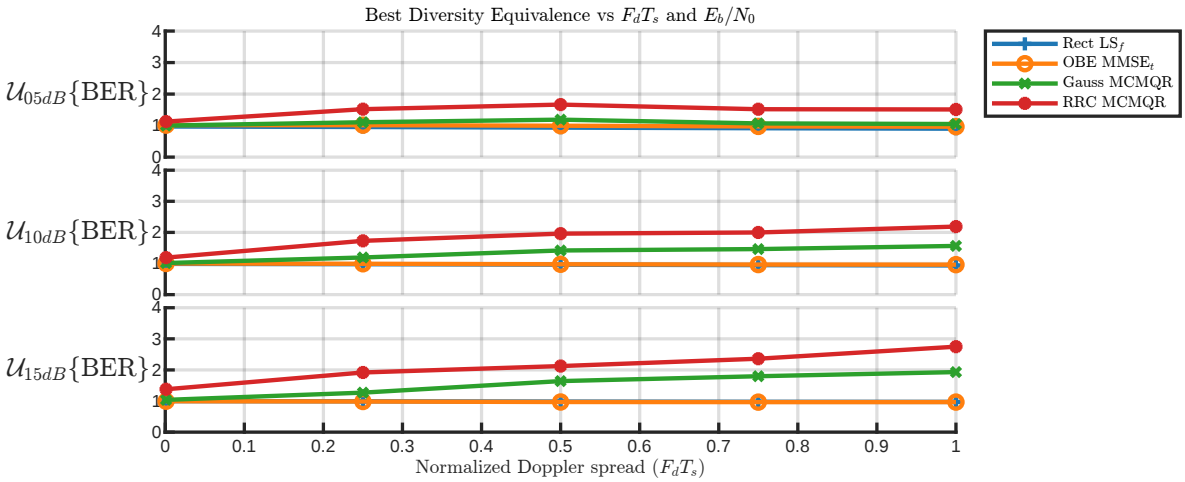

Figure 3.20: Doppler-driven diversity equivalence ($\mathcal{U}_{E_b/N_0}\{\text{BER}\}$) vs F_dT_s for different pulse shapes and E_b/N_0 considering the best practical receiver per pulse, ISI cancellation, and 2-path channel with delay spread $\mathcal{T} = 0.2T_s$.

– tend to have a higher ability to achieve diversity.

3.7 Conclusion and Perspectives

In this chapter, we discussed the importance of assisting equalization by performing time domain preprocessing when considering multi-carrier communication over fast-varying Rayleigh channels. We have defined the structure of the receiver that can be used to include both/either, preprocessing in the time domain and final equalization in the frequency domain. Classical and state-of-the-art frequency domain equalization techniques that are considered for CP-OFDM were presented. Two low-complexity time domain-assisted equalization techniques were proposed supporting both single path and multipath channels. Complexity analysis for the frequency domain and the time domain techniques was provided in terms of order of number of operations. BER comparison was provided for several equalizers and pulse shapes, and the time domain additional processing was shown to improve the performance and to benefit from channel variation instead of being negatively affected, exploiting what we called Doppler-driven diversity. Diversity–BER mapping was introduced to calculate a proposed Doppler-driven diversity equivalence per pulse shape. It was shown how pulses that are less localized in time tend to achieve higher Doppler-driven diversity equivalence. To account to ISI that can be issued by less localized pulse shapes in such scenarios, ISI-cancellation technique was proposed and showed to converge toward ideal ISI-cancellation after a single iteration. As a conclusion, we have observed that using the proposed MCMQR technique with the proposed ISI cancellation procedure and RRC pulse shape provides ∼7 dB gain compared to the state-of-the-art frequency domain matrix equalizer LS$_f$ with CP-OFDM in both single path and multipath channels when the channel is perfectly known. Moreover, this gain will increase to ∼12 dB when the channel is partially known with normalized MSE = −20 dB,

which illustrates how the adopted proposed system is more robust to channel estimation errors. We have also observed that this gain will increase for lower BER targets due to the diversity captured by the RRC pulse shape.

However, among all these tremendous advantages, we have observed some limitations and questions that are kept for future perspectives of this work:

- How can we capture part of the available diversity in doubly fading channels using time-limited pulse shapes like Rect and OBE?
- How can we improve the proposed techniques to capture more diversity (or to achieve a better trade-off between diversity gain and interference reduction) in multipath variable channels instead of being negatively affected by the multipath propagation?
- The proposed system introduced major performance improvement for an increase in complexity. How much improvement does this add to the power efficiency of the system?
- One of the most important advantages of this system is that it will be feasible to increase the pulse's duration without worrying about performance degradation, but in contrast, benefiting from it through capturing diversity. However, how much can we increase the pulse duration before it starts introducing non-tolerable communication delays?
- How can such techniques integrate into MIMO systems? and how will it combine with spacial multiplexing?
- How would phase noise affect this kind of processing?
- What will be the performance of systems like the proposed one when offset-based modulations are employed?
- How feasible is it to integrate this system to some existing standards?
- The most possible candidate systems to use the proposed techniques are THz communication based systems due to the Doppler-based problems they face. However, will the Jakes model considered for simulation of this work still be valid for such systems? If not, what will be the performance of the proposed techniques following different models?

All these questions, and much more, can be considered to open doors for the extension of this work. Part of these questions that are not mentioned above is: how would such systems integrate a channel estimation technique? And will it be possible to obtain accurate channel estimation for such extremely high values of Doppler spread? These will be the questions that we will try to answer in the next chapter of this manuscript.

Chapter 4

Pilot Scheme and Time Domain Channel Estimation Strategy for Multicarrier Communication over Fast Fading Channels

Contents

In this chapter, we discuss our proposed high performance multipath channel taps (at sample level) estimation technique using comb-type pilots. We propose to perform channel estimation directly in time domain before the transition to frequency domain. This is performed through simple filtering of the pilot sub-carriers in the perspective to isolate them from data sub-carriers, then use their values to estimate the channel taps. Although this technique is valid for any pulse-shaped Multi-Carrier (MC) system, we will analyze it only for Root Raised Cosine (RRC) in this chapter. This is because, first, it appeared in the previous chapter to have the best performance when considering time-domain preprocessing, and second, because it is expected (due to the bounded frequency response) to have easier pilot isolation. We will provide later in this chapter the detailed structure of this estimation system and the motivation behind it. However, for now, since the frequency spreading is the main source of difficulty in such estimation, we adopt decoupling the data-communication and the estimation process so that:

- the pilot bandwidth is not controlled by the transmitting pulse shape allowing it to avoid interference,

- and the receiving filter of the pilots is not controlled by the data-receiving filter allowing it to be narrower to avoid interference, or wider to capture more variation.

More details are provided in section 4.2. The expected and simulated performance in terms of Mean Squared Error (MSE) for different conditions is then provided. After that, we will combine it with the equalization proposed in the previous chapter to analyze the performance in a complete scenario.

4.1 Channel Estimation Structure

In this section, we discuss the structure of the channel estimation technique we use, and how it integrates in the transmitting/receiving Frequency Division Multiplexing (FDM) system. Before going into the details of this system, it is important to note that in this work, we will consider inserting the pilots in time domain by adding them to the transmitted signal. The pilots should be generated separately as pure tones. It is easy to observe that in the basic Orthogonal Frequency Division Multiplexing (OFDM), this is identical to have traditional pilot symbols having the value 1. Since we adopt RRC pulse in this chapter, the behavior of adding the pilots in the time domain or setting symbols to 1 in the frequency domain will be slightly different. Therefore, we adopt adding them in time domain which will assist in the proposed channel estimation technique. In figure 4.1, we represent the full transmitting/receiving flow diagram used in this work, including channel estimation, which helps in understanding the proposed structure. We explain the flow by explaining each block separately.

- Bits generator: takes as parameters the total number of subcarriers M, the number of pilot subcarriers per MC symbol P, the number of subcarriers reserved per pilot W (so that the P pilots reserves WP subcarriers), the number of symbols to be transmitted N_s, and the constellation size Q. These values are needed to generate $N_s(M - WP)log_2Q$ bits so that the number of bits fits the flow requirements.

- Bits to QAM: takes the output of 'Bits generator' as input, and Q as a parameter. It maps the generated bits to Quadrature Amplitude Modulation (QAM) symbols using the gray coding implementation [BER76].

- Spacing for pilots: takes the output of 'Bits to QAM' as input, and M, P, and W as parameters. This block places WP zeros among every $M - WP$ QAM symbols to have every group of $M - WP$ QAM symbols distributed over M subcarriers. In this work, we adopt having P groups of zeros, each consisting of W zeros, which permits to have P pilots each reserving W QAM symbols/subcarriers (even if using only part of their bandwidth). The mathematical details if this pilot allocation are discussed later.

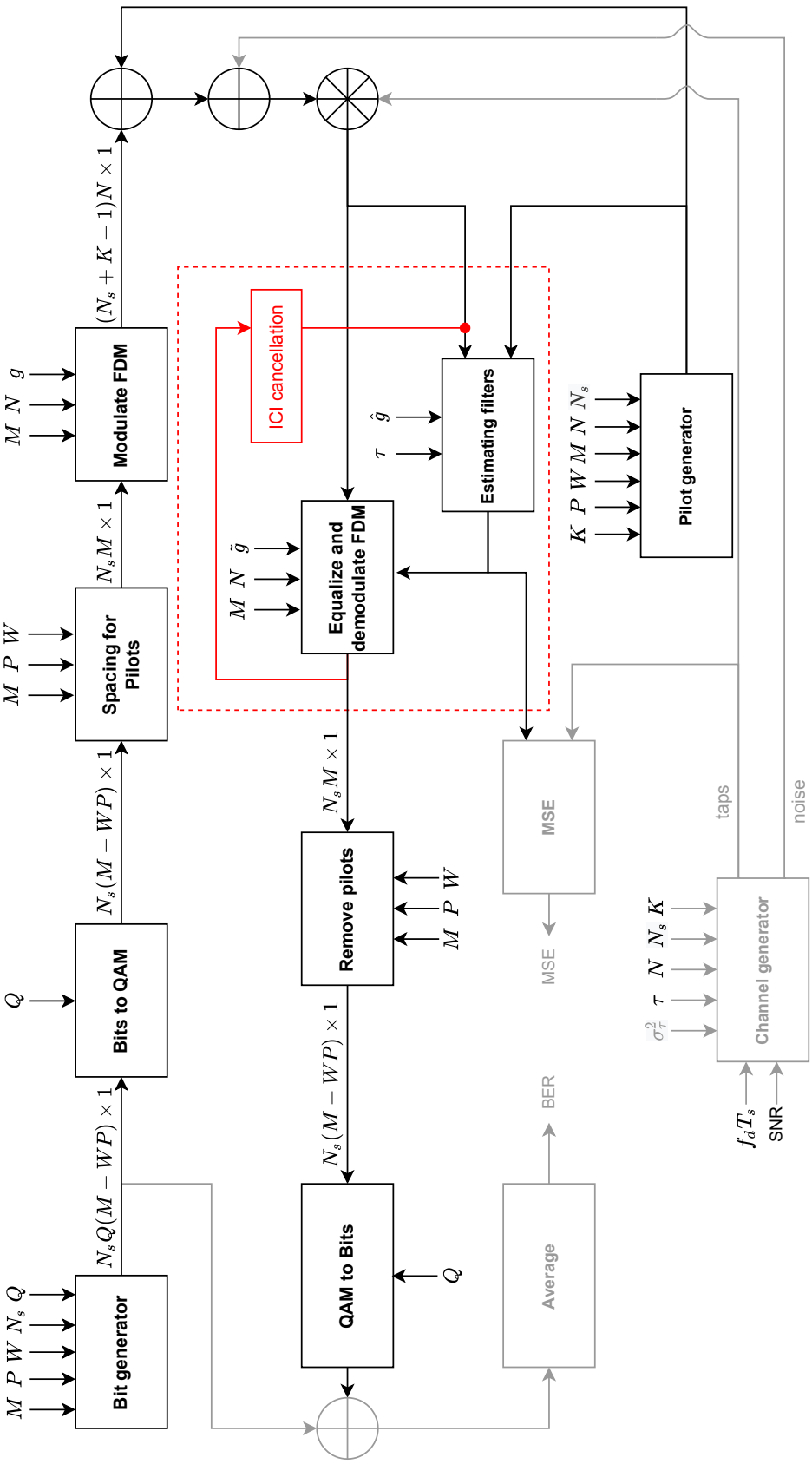

Figure 4.1: FDM transmitting and receiving flow diagram with pilot insertion and channel estimation.

- Pilot generator: generate the pilot subcarriers separately. Requires the parameters K, P, W, M, N, and N_s to generate the P pilots accordingly. Note that the pilots are generated independently of the MC symbols, but should be aware of the FDM configuration to sample the pilot frequencies correctly. The pilot frequencies are defined to be at the centers of the W pilot-reserved subcarrier blocks. For example, if $W = 1$, the pilot frequency will be at the center of the pilot-reserved subcarrier, if $W = 2$, it will be at the edge between the two pilot-reserved subcarriers, if $W = 3$, it will be at the center of the middle pilot-reserved subcarrier, etc. Note that this block normalizes the power per pilot to the system's average subcarrier power.

- Modulate FDM: takes the QAM symbols (separated by zeros for pilots) from 'Spacing for Pilots' block, and requires M, N, and the transmitting pulse shape g. This block generates the FDM modulated signal as described in section 1.2.3. As mentioned in the introduction, we adopt the RRC pulse shape. We configure the roll-off β to be $1 - N/M$ as done in the previous chapters (sections 1.2.3, 2.2, 2.3 and 3.4).

- Channel generator: this block is implicit, and the system is not aware of it, yet it affects the system. It is visible only in simulation scenarios, therefore, it is represented with a gray color in figure 4.1. This block requires the signal size (known through N, N_s, and K) and the channel's state information (normalized Doppler spread (F_dT_s), Signal to Noise Ratio (SNR), paths' delays (τ), and the paths' powers (σ_τ^2)) to generate the channel with suitable properties. It generates channel taps following the Jakes's model [JC94], and complex Additive White Gaussian Noise (AWGN) based on the given SNR (assuming that the transmitted signal is normalized).

- Mathematical Operators blocks ($\oplus$ and $\circledast$): $\oplus$ addition block and $\circledast$ convolution block. These blocks are used to apply the model of equation (1.36):

$$r[q] = \sum_{l=0}^{L-1} h[q,l]s[q-l] + \omega[q].$$

  The addition operator $\oplus$ is also used in the binary format in figure 4.1, reflecting the XOR operator.

- Estimating filters: the channel estimation procedure adopted in this work is based on isolating the pilot frequencies from those holding the data symbols. Therefore, it requires having an isolation filter $\hat{g}$ that is generated based on the channel conditions (F_dT_s and SNR). We assume that some of the channel information (delays τ, F_dT_s, and SNR) are invariant over communication time and known to the receiver, which is a common (and realistic) assumption for the channel estimation problem [HR10]. Therefore, to assist in the estimation process, the delays τ is fed to this block. Note that the pilots are also fed to this process, which is required in any pilot-based channel estimation procedure. Practically, pilot generators that generate the pilots for the transmitter and the receiver are not the same as they are separated, but it is generated similarly for both, and consequently identical. The details of the estimation and the isolating filter are discussed later in this chapter.

- Equalize and demodulate FDM: the equalization and demodulation are two related but separated processes. However, since equalization might be done in time domain, in frequency domain, or combine both, and might include additional recursive procedures like the interference cancellation, we kept them presented by one block for simplicity of illustration. Equalization in high speed variable environments was discussed in chapter 3, and we will consider it for this block.

- ICI Cancellation: since the adopted estimation is based on pilots isolation as discussed previously, and high Doppler spread might lead to severe Inter-Carrier Interference (ICI), recursive estimation - equalization - ICI cancellation can be used. However, since this concept is not performed generally in this work and is only needed when data-pilot interference rises as discussed later in this chapter, it is colored with red in figure 4.1 and considered beyond the scope of this work.

- Remove Pilots: similarly to the 'Pilot Spacing' block, this block requires M, P and W as parameters. However, it has an opposite effect where instead of inserting zeros in pilot-reserved positions, it removes whatever is observed on those position after the 'Equalize and demodulate FDM' step is already performed.

- QAM to Bits: takes the output of 'Remove Pilots' as input, and Q as a parameter. It maps the received QAM symbols to bits using the Gray coding implementation [BER76].

- MSE: this block is implicit, and the system is not aware of it, as it is used only to calculate a metric. It is visible only in simulation scenarios, therefore, it is represented with a gray color in figure 4.1. It takes the true channel taps from 'Channel generator' and the estimated channel taps from 'Estimating filters' and calculate the MSE between them.

- Average: this block is implicit, and the system is not aware of it, as it is used only to calculate a metric. It is visible only in simulation scenarios, therefore, it is represented with a gray color in figure 4.1. It takes the transmitted binary data from 'Bit generator' and the received binary data from 'QAM to Bits' and calculate the Bit Error Rate (BER) by averaging the result of the XOR between them.

As it can be noticed from figure 4.1 and its detailed description above, the channel estimation and the communication procedure are decoupled (except if recursive ICI cancellation is employed). This is achieved thanks to the isolation concept adopted in our scheme. One of the benefits of this decoupling is that the communication filters (g and $\tilde{g}$) and the pilot-isolating filter ($\hat{g}$) can be designed independently. In addition to that, this can transform the estimation problem from a very complicated process to a simple estimation in AWGN scenario. In the next section, we describe this decoupling, and how it is reflected in the frequency response of the whole communication process.

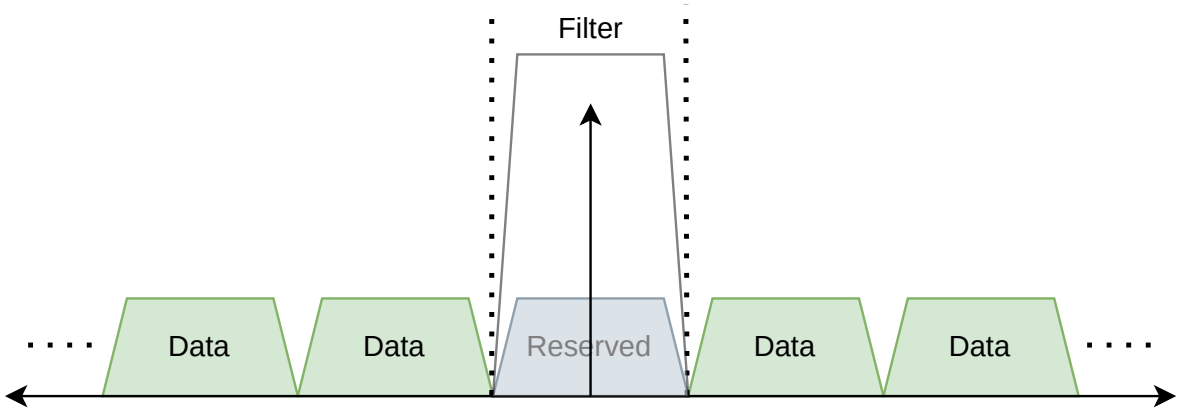

Figure 4.2: Frequency domain representation of data symbols and single-tone pilot for a number of subcarriers reserved for a pilot $W = 1$.

4.2 Asynchronous Single Tone Pilots Strategy

In this section, we analyze the asynchronous single tone pilots strategy mentioned before, and explain why we adopted it in this work. In chapter 3, we have seen that employing time domain pre-processing can significantly enhance equalization in MC systems operating in fast-varying environments, especially when considering the RRC pulse shape. However, the discussed techniques require estimating the channel taps in the time domain, which is not common in MC systems. The reason behind this is that the process of transferring from time domain to frequency domain (specifically the Fast Fourier Transform (FFT)) performs per-MC symbol averaging of the time domain taps. A workaround to estimate the sample-time channel is to perform interpolation of the values observed in frequency domain [Col+02a]; [Col+02b]; [SL03]; [HR08a]; [HR09]. Alternatively, we propose to estimate the channel directly in time domain when considering frequency limited pulse shapes (like the RRC), which is performed by isolating the pilot carriers from data carriers. In addition to that, we do not perform the pilot insertion at the frequency domain/QAM symbol level, but directly in time domain in the form of a single-frequency tone. In figure 4.2, we present an illustration of the frequency domain power distribution when inserting single-tone pilot reserving a single subcarrier. In this figure, the data subcarriers are presented in green, the pilot-reserved subcarrier is presented in gray (which has the value 0), and the black peak in the center represents the single-tone pilot. The boundaries of the pilot-reserved subcarrier is marked with vertical black dots. In classical systems where the estimation is performed using the information observed in the frequency domain, the pilot uses the same filter as the data symbols, which is illustrated in figure 4.2 and marked by 'Filter'. In figure 4.3, we present the same illustration of figure 4.2, but when considering channel variation for a Rayleigh channel following the Jakes model with $F_d T_s = 0.125$. In shaded green, we can observe the spreaded data subcarriers, and in shaded gray, we can observe the spreaded pilot. As illustrated, the spreaded pilot follows the channel spectrum since it is a single-tone pilot. For this level of $F_d T_s$, all the variations of the channel (the whole channel spectrum) are included in the flat region of the filter. However, since the filter is aligned to the whole allocated subcarrier bandwidth, it can be noticed that the filter

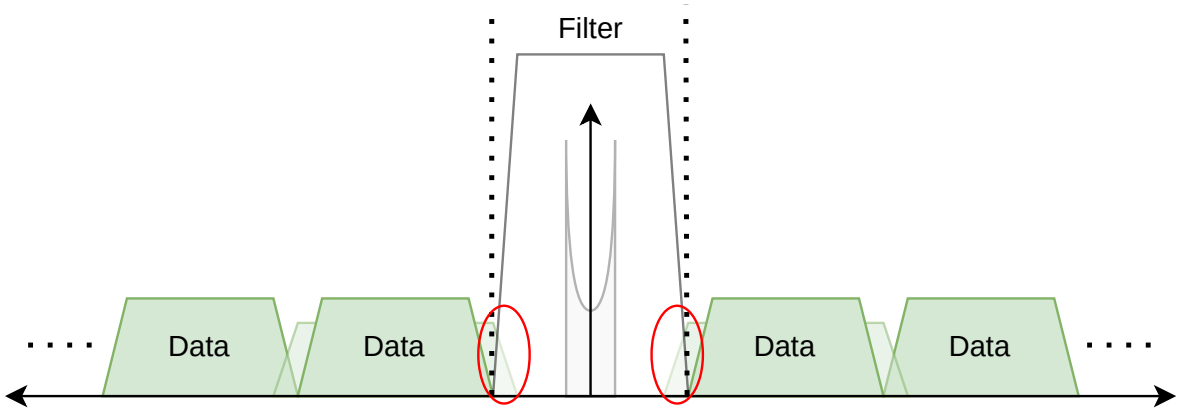

Figure 4.3: Frequency domain representation of data symbols and single-tone pilot for a number of subcarriers reserved for a pilot $W = 1$ with Jakes Rayleigh channel for $F_d T_s = 0.125$.

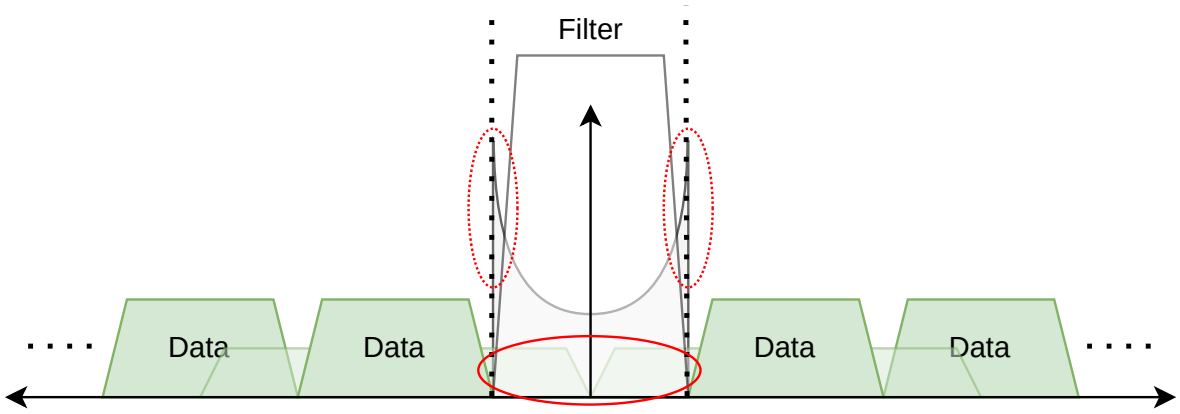

Figure 4.4: Frequency domain representation of data symbols and single-tone pilot for a number of subcarriers reserved for a pilot $W = 1$ with Jakes Rayleigh channel for $F_d T_s = 0.5$.

also includes interference from neighbor subcarriers as marked in red. In addition to that, the unneeded width of the filter includes additional useless bandwidth beyond the pilot spreading. Although some of this spectrum does not include interference, it includes additional noise that can be avoided. In addition to that, accepting ICI is not the only concern this type of filtering suffers from. For example, figure 4.4 shows the same plot for $F_d T_s = 0.5$. As can it be seen from the solid red circle, ICI significantly affects the channel. Moreover, as marked by the dotted red circles, another problem of estimation is that the pilot might spread beyond the filter bandwidth due to significant channel variation. However, since in our implementation the estimation and the data communication systems are decoupled, it is possible to have the filter for the pilots $\hat{g}$ different from the data carriers filters g and $\tilde{g}$. Consequently, we can have a filter which is adapted to the pilot spreading so that it accepts only the needed part of the subcarrier bandwidth as shown in figure 4.5 for $F_d T_s = 0.25$. The filter appears to capture all the channel variation, while avoiding the interference as shown by the blue circles knowing that we consider twice the variation of figure 4.3. As it can be seen from this figure, this value of $F_d T_s$ (0.25) is the maximum possible value that permits capturing the channel variation

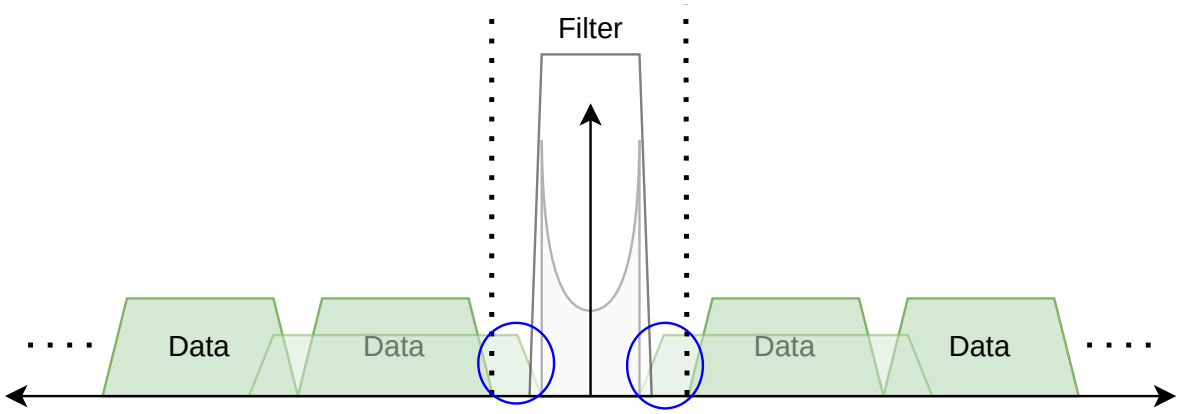

Figure 4.5: Frequency domain representation of data symbols and single-tone pilot for a number of subcarriers reserved for a pilot $W = 1$ with Jakes Rayleigh channel for $F_dT_s = 0.25$ and narrower filter (half-carrier passband).

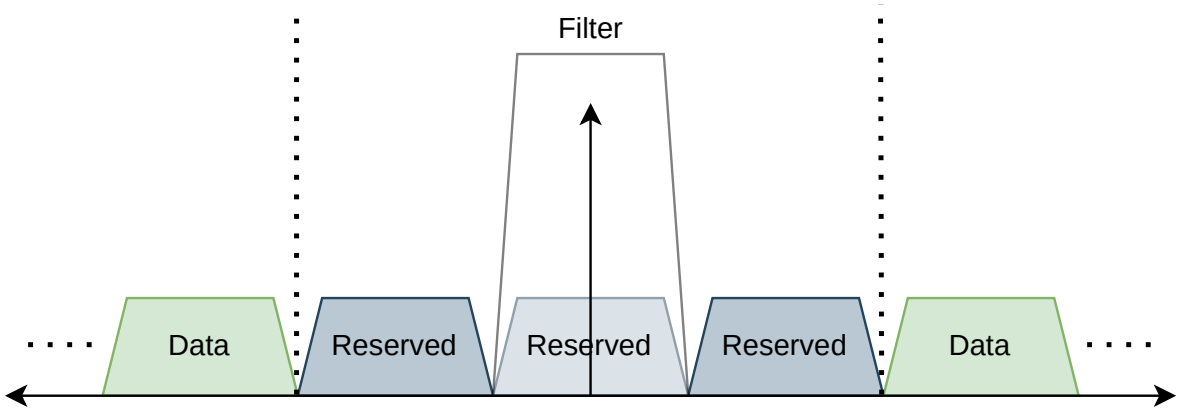

Figure 4.6: Frequency domain representation of data symbols and single-tone pilot for a number of subcarriers reserved for a pilot $W = 3$.

while avoiding the interference. We call this value of F_dT_s the '+ICI' limit, since after this value, it is mandatory to have ICI. That is why higher values of F_dT_s, like $F_dT_s = 0.5$ of the scenario in figure 4.4 will require another solution for the interference. One solution is to perform recursive interference cancellation and estimation as described in section 4.1 (the parts marked in red).

Another solution is to expand the bandwidth reserved for the pilot by increasing the number of reserved subcarriers W. In figure 4.6, we provide the frequency domain representation of data symbols and single-tone pilot for a number of subcarriers reserved for a pilot $W = 3$. This figure, similarly to figure 4.2, keeps the pilot filter similar to the data filter where it captures one complete subcarrier bandwidth. However, the difference is that the '+ICI' bound now reflects a higher F_dT_s thanks to the higher W. For $W = 3$, the '+ICI' bound is at $F_dT_s = 0.75$. This makes capturing the variation for $F_dT_s = 0.5$ free of interference, contrary to what was observed through figure 4.5. However, while using a filter having a subcarrier

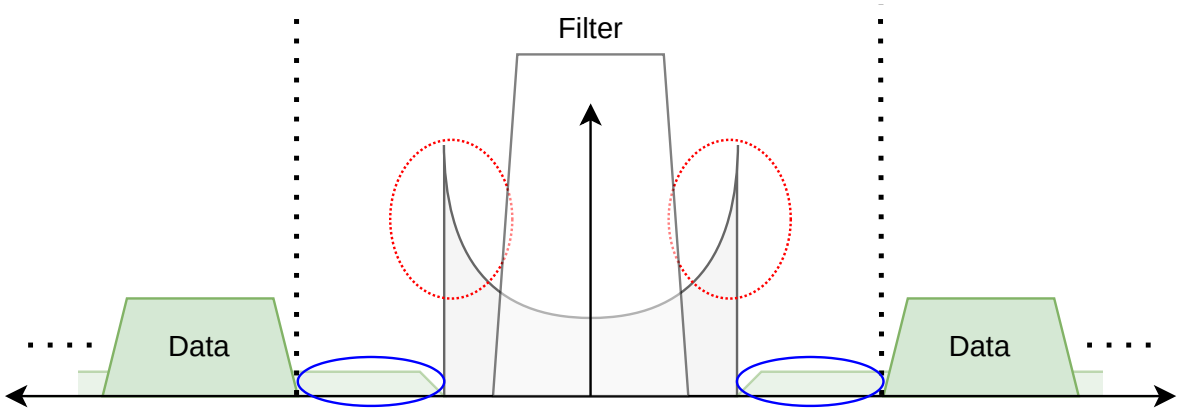

Figure 4.7: Frequency domain representation of data symbols and single-tone pilot for a number of subcarriers reserved for a pilot $W = 3$ with Jakes Rayleigh channel for $F_dT_s = 0.75$.

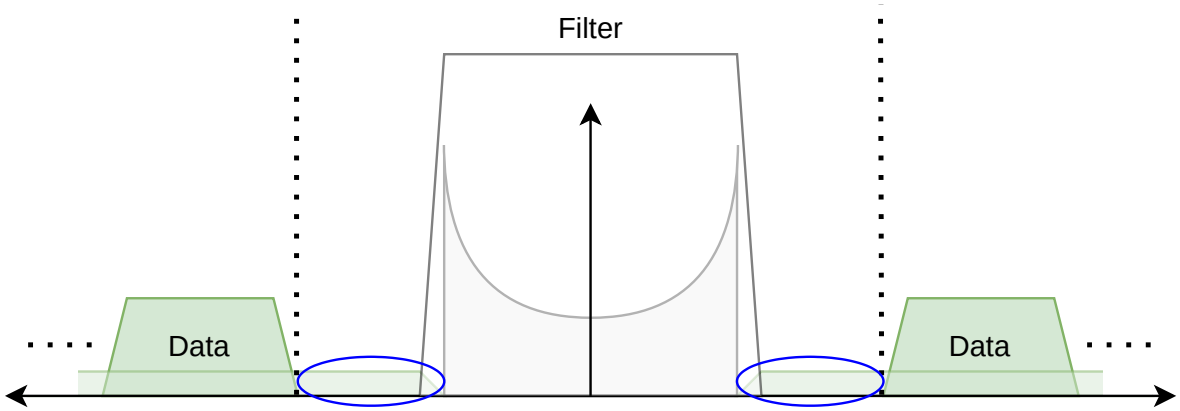

Figure 4.8: Frequency domain representation of data symbols and single-tone pilot for a number of subcarriers reserved for a pilot $W = 3$ with Jakes Rayleigh channel for $F_dT_s = 0.75$ and wider filter.

bandwidth, capturing variation due to $F_dT_s = 0.75 > 0.5$ will not be possible. As observed in figure 4.7, this will not be due to the interference (as we respect the '+ICI' bound), but to the inability of such filter to capture such bandwidth (as shown by red circles in the figure). Consequently, contrary to requiring a narrower pilot filter in order to capture the variations without inducing interference for $F_dT_s < 0.5$, increasing the filter bandwidth is required in such scenarios. In figure 4.8, we provide frequency domain representation of data symbols and single-tone pilot for a number of subcarriers reserved for a pilot $W = 3$ with Jakes Rayleigh channel for $F_dT_s = 0.75$, and a pilot filter with bandwidth wider than subcarrier frequency. As it can be observed, adapting the filter in such scenarios to be wider can capture all the variations of the channel without inducing interference for F_dT_s up to 0.75. Note that if the filter is a simple band pass (or low pass of center assumed to be 0) having its pass region as a flat region, configuring the filter for a value F_dT_s will make the filter valid for any lower F_dT_s. That is because such filters will simply just isolate the pilots from the data. However, this will make the filter accept more noise, making the resulting error not depending on the

actual F_dT_s but on the F_dT_s used for configuration. On the other hand, if a special filter is used that has its passband not flat, this property will not hold. Consequently, in this work, we will consider filters that we configure per-F_dT_s to cover as general cases as possible. In next section, we provide the mathematical formulation required for analyzing and implementing our scheme.

4.3 Mathematical Formulation

In this section, we formulate mathematically the structure of the pilots we adopt, and the relevant proposed estimation process. First we define the following:

- p_k^W, the set of subcarriers reserved for the k^{th} pilot with $k \in [0; P-1]$,
- $p_k^{(i)}$, the i^{th} entry of p_k^W with $i \in [0; W-1]$,
- $p_k = \frac{1}{W}\sum_{i=0}^{W-1} p_k^{(i)}$, the frequency of the k^{th} pilot normalized to subcarrier frequency (not necessarily an integer),
- and $p_{\text{range}} = \left\{p_k^W \ \forall \ k \in [0; P-1]\right\}$ the set of all subcarriers reserved for the P pilots.

Since we assume P equidistant pilot subcarriers (in the frequency domain), the first (0^{th}) subcarrier index of the subcarriers reserved for the k^{th} pilot $p_k^{(0)}$ is defined by:

$$p_k^{(0)} = k\frac{M}{P}, \tag{4.1}$$

where $k \in [0; P-1]$. Note that this assumes that M/P is an integer. This normally holds to obtain equidistant pilot subcarriers as it is only a matter of system's configuration. However, for generalization, when M/P is not an integer, a workaround to obtain the pilot subcarriers indices is setting:

$$p_k^{(0)} = \text{round}\left(k\frac{M}{P}\right). \tag{4.2}$$

Following this definition, $p_k^{(i)}$, the set of subcarriers reserved for the k^{th} is defined by:

$$p_k^W = \left\{p_k^{(0)} + i \ \forall \ i \in [0; W-1]\right\}. \tag{4.3}$$

On the other hand, knowing that the total number of subcarriers is M with indices $m \in [0; M-1]$, the set of subcarrier indices that can still be used for data are:

$$d_{\text{range}} = [0; M-1] \ominus p_{\text{range}}, \tag{4.4}$$

where $\ominus$ is the set difference operator. Following this allocation of data symbols and pilots, we modify the definition of the transmitted signal of equation (1.35) in chapter 1 to support

the presence of the pilots. The q^{th} of the transmitted signal s can then be transmitted as:

$$s\left[q\right] = s_{\text{data}}\left[q\right] + s_{\text{pilot}}\left[q\right], \tag{4.5}$$

where s_{data} represents the samples generated due to the transmission of data symbols, and s_{pilot} represents the samples generated due to the transmission of pilots. The samples generated due to the transmission of the data symbols s_{data} are then defined (similar to equation (1.35)) by:

$$s_{\text{data}}\left[q\right] = \sum_{n} \sum_{m \in d_{range}} g\left[q - nN\right] e^{j2\pi \frac{m(q-nN)}{M}} c_{m,n}. \tag{4.6}$$

Since we assume pure harmonic 'asynchronous' pilots as previously discussed, we define the samples generated due to the transmission of the pilots s_{pilot} by:

$$s_{\text{pilot}}\left[q\right] = \frac{1}{\sqrt{N}} \sum_{k=0}^{P-1} e^{j2\pi \frac{p_k q}{M}}. \tag{4.7}$$

Note that $\frac{1}{\sqrt{N}}$ is a power normalization factor assuming that a subcarrier power is normalized to 1. We recall equation (1.36) representing the received signal:

$$r\left[q\right] = \sum_{l=0}^{L-1} h\left[q,l\right] s\left[q-l\right] + \omega[q].$$

The received signal due to the transmission of the pilots signal s_{pilot} is then:

$$r_{\text{pilot}}\left[q\right] = \frac{1}{\sqrt{N}} \sum_{l=0}^{L-1} h\left[q,l\right] \sum_{k=0}^{P-1} e^{j2\pi \frac{p_k (q-l)}{M}} + \omega[q], \tag{4.8}$$

obtained through replacing s by s_{pilot} in equation (1.36). Equivalently, the (noiseless) received signal due to the transmission of the k^{th} pilot is:

$$r_k\left[q\right] = \frac{1}{\sqrt{N}} \sum_{l=0}^{L-1} h\left[q,l\right] e^{-j2\pi \frac{p_k l}{M}} e^{j2\pi \frac{p_k q}{M}}. \tag{4.9}$$

The estimation Finite Impulse Response (FIR) filter with impulse response $\hat{g}_k$ provides an estimation $\hat{r}_k$ of the image of $h[q,l]$ observable from r_k by isolating it from other carriers. $\hat{r}_k$ can then be obtained by:

$$\begin{aligned} \hat{r}_k\left[q\right] &= \sum_{\alpha} \hat{g}_k^*\left[q-\alpha\right] r_k\left[\alpha\right] \\ &= \sum_{\alpha} \hat{g}^*\left[q-\alpha\right] r_k\left[\alpha\right] e^{-j2\pi \frac{p_k \alpha}{M}}. \end{aligned} \tag{4.10}$$

Note that we use $\hat{g}$ as a shorthand to $\hat{g}_0$, and the filter $\hat{g}$ implicitly considers the normalization factor $\frac{1}{\sqrt{N}}$. This can be re-written as:

$$\hat{r}_k\left[q\right] = \sum_{l=0}^{L-1} h\left[q,l\right] e^{-j2\pi\frac{p_k l}{M}} + \epsilon_k\left[q\right], \tag{4.11}$$

where ϵ_k is the 'isolation' error produced by $\hat{g}_k$, which consists of mainly three parts:

1. noise captured by the filter,
2. interference received from neighbor subcarriers,
3. and imperfections of the filter itself, which mainly have a response that is not perfectly flat in the passband region of interest.

Beside this error, we can observe that each estimated channel image $\hat{r}_k$ is a weighted sum of the target channel taps. This can be re-modeled in a matrix format:

$$\hat{\boldsymbol{r}}\left[q\right] = \boldsymbol{E}\ \boldsymbol{h}\left[q\right] + \boldsymbol{\epsilon}[q] \tag{4.12}$$

where:

$$\begin{aligned}
\hat{\boldsymbol{r}}\left[q\right] &= \left[\hat{r}_0\left[q\right]\ \ldots\ \hat{r}_{P-1}\left[q\right]\right]^T, \\
\boldsymbol{h}\left[q\right] &= \left[h\left[q,0\right]\ \ldots\ h\left[q,L-1\right]\right]^T, \\
\boldsymbol{\epsilon}\left[q\right] &= \left[\epsilon_0\left[q\right]\ \ldots\ \epsilon_{P-1}\left[q\right]\right]^T, \text{ and} \\
\boldsymbol{E} &= \begin{bmatrix} e^{-j2\pi\frac{p_0 0}{M}} & \cdots & e^{-j2\pi\frac{p_0(L-1)}{M}} \\ \vdots & \ddots & \\ e^{-j2\pi\frac{p_{P-1}0}{M}} & & e^{-j2\pi\frac{p_{P-1}(L-1)}{M}} \end{bmatrix}.
\end{aligned} \tag{4.13}$$

This will split the channel estimation procedure into two steps:

1. filtering/isolating the pilots using $\hat{g}_k$ as represented in equation (4.10),
2. and extracting the channel taps through inverting the weighted sums represented in matrix format in equation (4.12).

For the second step, we will adopt the 'zero-forcing' concept by neglecting $\boldsymbol{\epsilon}$. Consequently, the best extraction technique following this concept is well known and can be obtained by:

$$\hat{\boldsymbol{h}}\left[q\right] = \boldsymbol{E}^{+}\hat{\boldsymbol{r}}\left[q\right], \tag{4.14}$$

where $\hat{\boldsymbol{h}}\left[q\right] = \left[\hat{h}\left[q,0\right]\ \ldots\ \hat{h}\left[q,L-1\right]\right]^T$ is the vector of estimated channel taps, and $\boldsymbol{E}^{+}$ is the pseudo-inverse of $\boldsymbol{E}$, and can be obtained by:

$$\boldsymbol{E}^{+} = \left(\boldsymbol{E}^{\mathrm{H}}\boldsymbol{E}\right)^{-1}\boldsymbol{E}^{\mathrm{H}}. \tag{4.15}$$

This is commonly known as pseudo-inversion. Note that for this pseduo-inversion to be valid, it is required to have $\boldsymbol{E}$ not a rank-deficient matrix (tall or at least square). In other words, we should have $P \geq L$ for a number of pilot subcarriers P and number of paths L, which is a common assumption in channel estimation. In addition to that, it is to note that this method will not work for paths having their (discrete) delays an integer multiple of the number of pilots P, which is known as a 'pathological' scenario for equally spaced subcarriers (not strictly for our approach). This can be solved through having non-equally distributed pilots, but this is beyond the scope of this work. The filters used for isolation will be discussed in next section along with simulation results.

4.4 Performance Analysis

In this section, we provide simulations of the proposed channel estimation technique, discuss the filters that were used for these simulations, provide the performance in terms of MSE and BER, and analyze the resulting outcomes.

4.4.1 Adopted pilot filters

In this section we discuss the filters we use for comparison as pilot filters. As mentioned earlier in this chapter, the main target of the pilot filter is to isolate pilots from neighbor subcarriers. Note that this is a block filtering that should be performed offline, where we consider them to be FIR filters of the length of 50 MC symbols. We will compare three types of filters that will be discussed in the next three sections accordingly.

4.4.1.1 Flat passband filter

In a general scenario, where only F_dT_s is known (or at least maximum supported F_dT_s), following the discussion of section 4.2, it is trivial that the best filter to be used is a flat passband filter. The (flat) passband of this filter should be from $-F_dT_s$ to F_dT_s, and should reject anything outside this range. This is the case of the classical perfect low-pass filter with an infinite *sinc* pulse response. However, this filter is not realizable. Consequently, we consider using the classical window-based FIR filter design adopted by Mathworks in Matlab function *fir1* [Matc] with an impulse of 50 symbols length. We consider, by default, using the Hamming window for the filter design. Moreover, since the channel's Power Spectral Density (PSD) has more power at the edges than the center, we consider to set the configuration F_dT_s slightly larger than the actual F_dT_s to avoid distortion caused by the 'rolloff' of the filter ($F_dT_s + 0.01$). In the later sections, this filter is referred to as FIR1.

4.4.1.2 PSD-aware filter

In the previous section, we have discussed the FIR1 filter that is designed only accounting to the Doppler spread. However, when the PSD of the channel and that's of the received signal are assumed to be available and Wide Sense Stationary (WSS) processes, it is known that the Wiener filter is optimal in terms of Minimum Mean Square Error (MMSE) [Wie+49]. However, the main difficulty for such a filter is that it is defined in frequency domain such that $\hat{\boldsymbol{G}}$, the frequency response of $\hat{\boldsymbol{g}}$, is defined by:

$$\hat{G}[v] = \frac{S_h[v]}{S_r[v]}, \tag{4.16}$$

where $\boldsymbol{S}_h$ and $\boldsymbol{S}_r$ are the PSDs of the channel and the received signal respectively. The impulse response is then obtained by applying inverse (discrete) Fourier transform to $\hat{\boldsymbol{G}}$. For $\boldsymbol{S}_h$, as we follow the Jakes's spectrum assumption, the channel PSD is well known (see section 1.1.4). However, similarly to the problem of the 'ideal' flat FIR filter discussed before, this PSD is extremely sharp and consequently has an infinite and non-causal impulse response which can not be implemented. In order to implement it, we apply windowing to the autocorrelation function of the channel, then apply Fourier transform to obtain a smooth PSD. We apply the flat top window function obtained using the *flattopwin* Matlab function [Matd], since we found it, by trial and error, to lead to the best performance (among the conventionally used windows). This 'mutation' of the PSD used for the design of the Wiener filter will reduce the accuracy of this filter making it non-optimal, yet has a considerable performance to be used in the comparison.

That's for the properties of $\boldsymbol{S}_h$. However, for $\boldsymbol{S}_r$, we adopt two models for it: noise-only, discussed in this section and noise+interference, discussed in the next one. For the noise-only model, we have $\boldsymbol{S}_r = \boldsymbol{S}_h + \boldsymbol{S}_n$, where $\boldsymbol{S}_n$ is the (white) noise PSD. It is well known that the Wiener filter has an expected error of $\sum_v S_h[v] - \hat{G}[v]S_h[v]$ [Wie+49] which can be easily obtained through minimizing the MSE. However, the filter $\hat{g}$ is defined to be $\hat{G}[v] = S_h[v]/S_r[v]$ as in equation (4.16). Therefore, in the noise only scenario, since $S_r[v] = S_h[v] + S_n[n]$ we have:

$$\begin{aligned}
&\sum_v S_h[v] - \hat{G}[v]S_h[v] = \sum_v S_h[v](1 - G[v]) = \sum_v S_h[v](1 - S_h[v]/S_r[v]) \\
&= \sum_v S_h[v](S_r[v] - S_h[v])/S_r[v] \\
&= \sum_v S_h[v]/S_r[v](S_r[v] - S_h[v]) \\
&= \sum_v \hat{G}[v]S_n[v] = \left\langle \hat{\boldsymbol{G}}, \boldsymbol{S_n} \right\rangle.
\end{aligned} \tag{4.17}$$

This representation of the expected MSE is more intuitive as it reflects, as previously discussed, the quantity of noise captured by the filter $\hat{g}$. We will use the same methodology to calculate the expected error for the FIR1. In the later sections, this noise-only designed Wiener filter referred to as WNR_n.

4.4.1.3 PSD and interference-aware filter

In the previous section, we have shown the details of designing a Wiener filter, following the knowledge of the PSDs of only the channel and the noise. In this section, we present the other Wiener filter we consider that is aware of the PSDs of the channel, the noise, and the interference. This is reflected simply by having $\boldsymbol{S}_r = \boldsymbol{S}_h + \boldsymbol{S}_n + \boldsymbol{S}_i$, where $\boldsymbol{S}_i$ is the PSD of the interfering spectrum coming mainly from the two neighbor subcarriers. Consequently, we have two versions of the Wiener filter for comparison, the noise-only designed Wiener filter referred to as WNR$_n$, and the noise+interference designed Wiener filter referred to as WNR. Note that WNR$_n$ and WNR will be identical for F_dT_s lower than the '+ICI' limit where the interference term will not affect the design. Similarly to the expected error of the WNR$_n$, the total expected error of WNR will be $\left\langle \hat{\boldsymbol{G}}, \boldsymbol{S_n} + \boldsymbol{S_i} \right\rangle$, where the $\left\langle \hat{\boldsymbol{G}}, \boldsymbol{S_n} \right\rangle$ reflects the noise captured by the filter, and $\left\langle \hat{\boldsymbol{G}}, \boldsymbol{S_i} \right\rangle$ reflects the interference captured by the filter. In the next few sections, we provide performance analysis while considering these three filters: FIR1, WNR$_n$, and WNR.

4.4.2 Performance for $W = 1$

In this section we provide and discuss the performance of the proposed channel estimation scheme while considering the number of subcarriers reserved per pilot $W = 1$. We perform the simulation for a stream of RRC-shaped MC symbols of size $N_s = 1000$. Each MC symbol has the total number of subcarriers (data and pilots-reserved) $M = 32$, and consecutive MC symbols are separated by $N = 40$ samples. The number of pilots considered is $P = 8$, and the channel is assumed to be a 2-path channel with delay spread $\mathcal{T} = T_s/8$ with equal power per path. Similarly to chapter 3, the RRC pulse is used with a rolloff factor $\beta = N/M - 1 = 0.25$. We will consider comparing the three filters we previously discussed:

- FIR1: the window-based filter design adopted by Matlab's *fir1* function [Matc],
- WNR$_n$: the truncated Wiener filter [Wie+49] while considering only the desired signal and the noise for the design,
- and WNR: the truncated Wiener filter [Wie+49] while considering the desired signal, the noise, and the interference for the design.

For the plots in this section and the later ones, we have two plots for each filter: solid line plot for the statistical expected value of MSE ($\left\langle \hat{\boldsymbol{G}}, \boldsymbol{S_n} + \boldsymbol{S_i} \right\rangle$) reflected with expectation operator in legends (e.g. E{FIR1}), and scattered symbols reflecting performance obtained by Monte-Carlo simulation. To compare with classical channel estimation schemes designed to estimate the time-domain taps of fast-varying channels, we also provide the benchmark performance obtained using through the interpolation method. This method is based on the classical approach of inserting constant data symbols at the pilot subcarriers, receive (similar to data symbols) the value of these pilots, normalize it to the constant pilot symbols, and interpolate

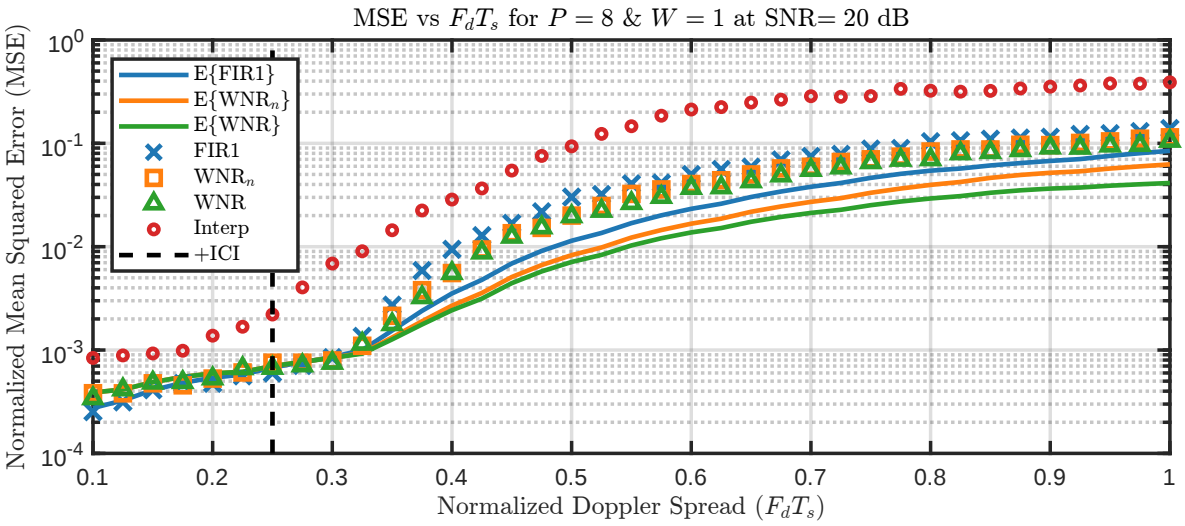

Figure 4.9: Statistical and Monte-Carlo estimation normalized MSE versus normalized Doppler spread (F_dT_s) for FIR1, WNR$_n$, WNR and Interp techniques in RRC-pulse shaped MC system. $N = 80$, $M = 64$, $P = 8$, $W = 1$ and SNR=20 dB are used.

the value over multiple consecutive MC symbols to obtain channel taps values. We consider using *spline* cubic interpolation [Matb], making the algorithm similar to the polynomial fitting-based technique proposed in [HR08a] for OFDM, but this time with RRC pulse shape MC (which performs better due to reduced ICI). We refer to this technique as *Interp* in the legends. We also draw a vertical dashed line for the '+ICI' bound in the versus F_dT_s plots.

In figure 4.9, we provide the performance of the estimation versus normalized Doppler spread (F_dT_s) in terms of normalized MSE for FIR1, WNR$_n$, WNR and Interp techniques in RRC-pulse shaped MC system when using $N = 80$, $M = 64$, $P = 8$, $W = 1$ and SNR=20 dB. The first thing one might notice in this figure is that the classical Interp method has the worst performance for any F_dT_s. This can be observed, mainly in two metrics: first, that the MSE of the Interp method is approximately one order higher than all of the others, and second, the 'change of trend' of the Interp method or the rapid increase starts from F_dT_s around 0.17, while around 0.32 for the others. One of the things to be concluded here is the effect of the '+ICI' boundary previously discussed in section 4.2. We know that, due to having the pulses tightly aligned in the frequency domain for the classical comb-type pilots, any $F_dT_s > 0$ will lead to some interference. Therefore, the classical Interp technique suffers from interference in all cases, so it has a rapid increase in the MSE due to this before reaching the '+ICI' boundary. However, this interference is less significant for low F_dT_s, and consequently we have the MSE lead by the level of noise. As F_dT_s increases, we have the rise of two phenomenons that were discussed in section 4.2 that causes the increase in MSE. The first one is the ICI, which, as just mentioned, exists at any $F_dT_s > 0$ for the Interp method and increases with the increase of F_dT_s. The other one is discussed also in section 4.2 and illustrated in figure 4.7, where the spreading of the pilots goes beyond the range of the receiving filter, making the filter not able to capture channel's variations.

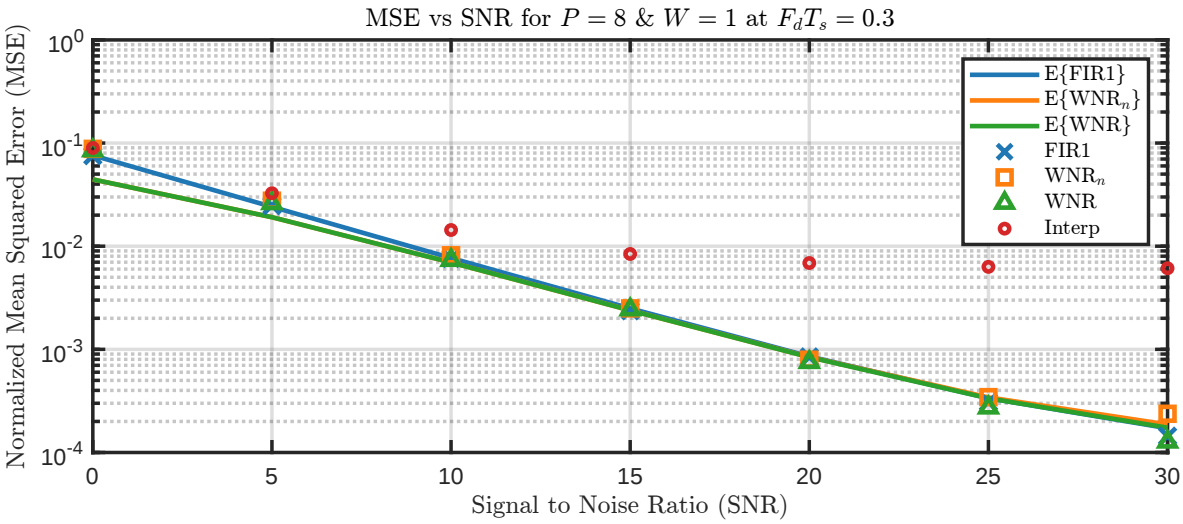

Figure 4.10: Statistical and Monte-Carlo estimation Normalized MSE versus SNR for FIR1, WNR$_n$, WNR and Interp techniques in RRC-pulse shaped MC system. $N = 80$, $M = 64$, $P = 8$, $W = 1$ and $F_dT_s = 0.3$ are used.

For the other three methods (that all uses our proposed technique but for different filters), figure 4.9 can be split into three parts: $F_dT_s <$ '+ICI' $= 0.25$, $0.25 < F_dT_s < 0.32$, and $F_dT_s > 0.32$. For $F_dT_s < 0.25$, the data subcarriers do not interfere with the pilot subcarriers when considering the proposed scheme as discussed in section 4.2. Therefore, only noise contributes to the error in estimation having it minimized by limiting the noise accepted through limiting the filters' bandwidths. In such case, the two filters WNR and WNR$_n$ are identical since the interference does not contribute to the error. For $0.25 < F_dT_s < 0.32$, although we start to have interference, the level of interference is insignificant making the error graph behavior very similar to $F_dT_s < 0.25$ for the three filters. For $F_dT_s > 0.32$, the error caused by the interference became more significant than that caused by the noise, making the MSE increase rapidly. It is important to note that the WNR has slightly less error than WNR$_n$ and FIR1 as it takes interference into account in design, yet not with a difference enough to consider it performing better than them. In addition to that, although we can see that the statistical and Monte-Carlo errors are almost identical for $F_dT_s < 0.32$, we observe a difference between them for $F_dT_s > 0.32$ due to the inability of perfectly considering PSD of the channel spreading as discussed in section 4.4.1 and consequently the interference. However, the general trends of the performance are still very similar. Through these plots, it is observable that the performance is almost identical for the three filters, with WNR slightly better in ranges of F_dT_s with high interference as it considers that in its design.

In figure 4.10, we provide the performance of the estimation versus SNR in terms of normalized MSE for FIR1, WNR$_n$, WNR and Interp techniques in RRC-pulse shaped MC system when using $N = 80$, $M = 64$, $P = 8$, $W = 1$ and $F_dT_s = 0.3$. As expected, the estimation MSE decreases with the increase of SNR for all the methods. Again, the proposed technique (with the three filters) performs better than the Interp method. The performance for the three filters is almost identical, and decreases linearly with SNR, except for high SNR (near

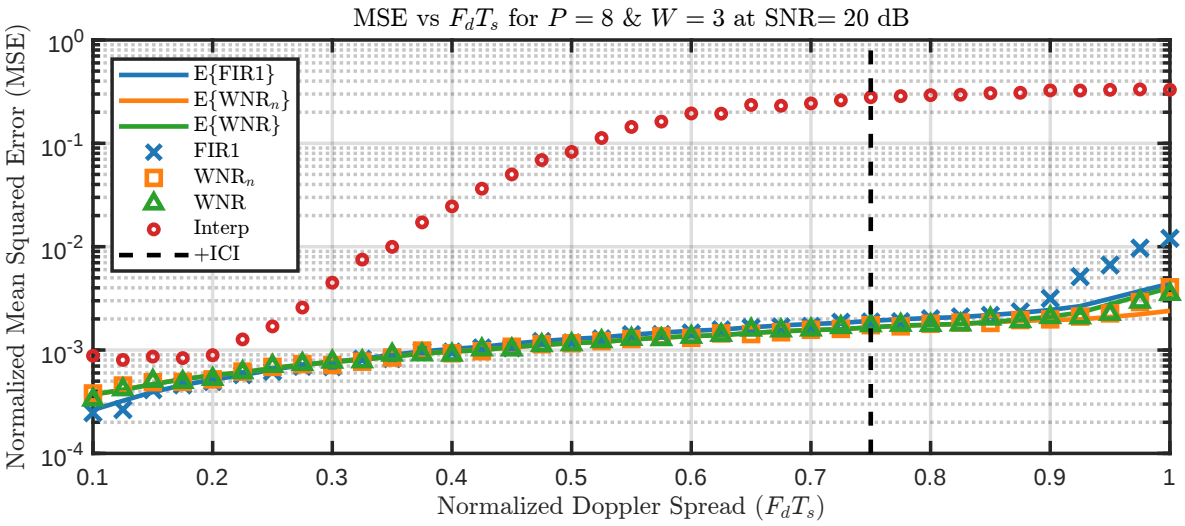

Figure 4.11: Statistical and Monte-Carlo estimation normalized MSE versus normalized Doppler spread (F_dT_s) for FIR1, WNR$_n$, WNR and Interp techniques in RRC-pulse shaped MC system. $N = 80$, $M = 64$, $P = 8$, $W = 3$ and SNR=20 dB are used.

30 dB) which signifies approaching some floor. Since we have $0.25 < (F_dT_s = 0.3) < 0.32$, this floor signifies the slight level of interference we discussed. On the other hand, for the Interp method, we have a higher MSE floor due to the interference and inability to capture all the channel variations (see section 4.2 figure 4.7). This shows again how far better is the proposed method compared to classical ones, and proves the relevance of the single-tone pilot approach. However, it is interesting to check the performance of both classical and single-tone techniques in case of reserving more than a single carrier for the pilots. Therefore, in the next section, we provide this analysis.

4.4.3 Performance for $W = 3$

In this section, we provide simulations and analysis similar to the ones of the previous section, but for a number of subcarriers reserved for a single pilot $W = 3$. We consider $W = 3$ without considering $W = 2$ to be able to compare with the classical Interp estimation method as such methods, in contrary to the proposed one, only support odd values of W (pilot can not be placed between two subcarriers). For the other parameters, they are similar to the ones of the previous section with $N_s = 1000$, $M = 64$, $N = 80$, $P = 8$, and the channel is assumed to be a 2-path channel with delay spread $\mathcal{T} = T_s/8$ with equal power per path. In figure 4.11, we provide the performance of the estimation versus normalized Doppler spread (F_dT_s) in terms of normalized MSE for FIR1, WNR$_n$, WNR and Interp techniques in RRC-pulse shaped MC system for SNR=20 dB. One of the first things to be noticed in this figure is that the '+ICI' limit is now set to 0.75 because of increasing W. Another very important observation is that the performance of the classical Interp method is very similar to that of the previous section and figure 4.9. Since we have $W = 3$, this means that the two neighbor subcarriers of the pilot are turned off, what will avoid interference for classical methods till $F_dT_s = 0.5$ (and

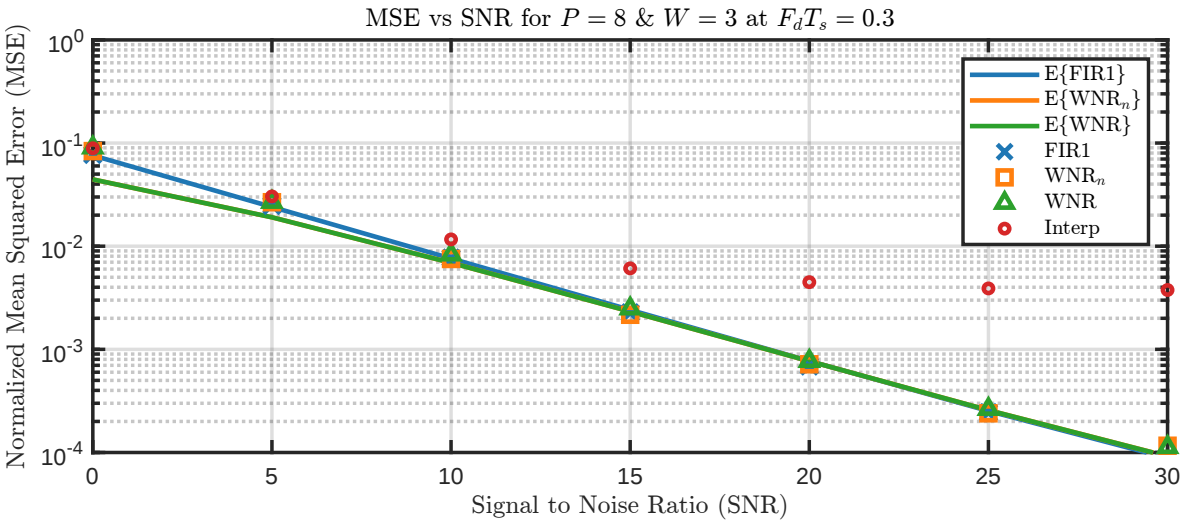

Figure 4.12: Statistical and Monte-Carlo estimation Normalized MSE versus SNR for FIR1, WNR$_n$, WNR and Interp techniques in RRC-pulse shaped MC system. $N = 80$, $M = 64$, $P = 8$, $W = 3$ and $F_dT_s = 0.3$ are used.

for the proposed method till 0.75). However, we can observe that, similarly to the $W = 1$ scenario, the severe degradation in performance starts from $F_dT_s \sim 0.2$. This behavior is actually due to the phenomenon discussed in section 4.2 and illustrated in figure 4.7 of having the receiving filter not able to capture all the variations of the channel due to its bandwidth. Moreover, the adopted Jakes's spectrum [JC94] has a significant part of its spreading at its edges due to the tub shape (∪), making the degradation very fast. Therefore, away from the interference, the Interp method, or any classical frequency-domain based method, will suffer from this phenomenon.

On the other hand, in the same figure 4.11, we can observe that the proposed technique has significantly benefited from this interference avoidance thanks to the configurable pilot filter bandwidth. Similarly to the previous section, the plots can be split into three parts: $F_dT_s < 0.75$, $0.75 < F_dT_s < 0.9$, and $F_dT_s > 0.9$. For $F_dT_s < 0.75$, the data subcarriers do not interfere with the pilot subcarriers when considering the proposed scheme as discussed in section 4.2. Therefore, only noise contributes to the error in estimation having it minimized by limiting the noise accepted through limiting the filters' bandwidths. In such case, the two filters WNR and WNR$_n$ are identical since the interference does not contribute to the error. For $0.75 < F_dT_s < 0.9$, although we start to have interference, the level of interference is insignificant making the error graph behavior very similar to $F_dT_s < 0.75$ for the three filters. For $F_dT_s > 0.9$, the error caused by the interference became more significant than that caused by the noise, making the MSE increase rapidly. This proves again the significance of the approach, and how this technique can convert a very complicated interference-rich problem with information-losing filtering into a few simple noisy pilots that can be processed with relatively low error that depends only on the noise.

In figure 4.12, we provide the performance of the estimation versus SNR in terms of

normalized MSE for FIR1, WNR$_n$, WNR and Interp techniques for the same system with $W = 3$ and $F_dT_s = 0.3$. The plots of this figure are very similar to those of figure 4.10 having $W = 1$. Again, we have the Interp method suffering from an error floor and the proposed technique having its error decreasing with SNR linearly. However, the first difference that can be pointed out compared to the $W = 1$ figure is that the error floor of the Interp method has dropped from 6×10^{-3} to 3×10^{-3}, where the difference in the error was the contribution of the interference into this error floor. The other difference is that in the $W = 1$ plots, the three filters using our proposed technique seemed to approach an error floor at E_b/N_0 approaching 30 dB, while it keeps going linearly in this figure. This is due to the fact that for figure 4.10, the value $F_dT_s = 0.3$ is above the '+ICI' limit that is 0.25 for $W = 1$. On the other hand, in figure 4.12, due to having $W = 3$ and consequently the '+ICI' limit at $F_dT_s = 0.75$, the value $F_dT_s = 0.3$ is now significantly below this limit and consequently converting the estimation problem into a simple noise-only problem. However, to ensure the validity of this analysis, we require analyzing the performance in an actual noise only scenario, which will be done in the next section.

4.4.4 Estimation in noise-only scenarios

In the previous sections, we have provided simulations and analysis for the scenario while having $W = 1$, and to improve the interference avoidance range we have tested also the scenario of having $W = 3$. The analysis provided lead to a result that the proposed technique was able to completely avoid the interference in relevant scenarios and convert the problem to a simple noisy scenario, while the classical technique fails to capture the channel's variations even when interference is avoided. However, to verify the validity of this analysis, we require providing the results of scenarios that actually conducts no interference. In this section, we provide this analysis through turning off all the data subcarriers by setting all the input symbols to zeros. This will permit to transmit the pilots only, which reflects an actual noise-only scenario. Since the simulations of this section are interference-free, we omit the WNR results as WNR and WNR$_n$ are identical in such scenarios. For the other parameters, they are similar to the ones of the previous section with $N_s = 1000$, $M = 64$, $N = 80$, $P = 8$, and the channel is assumed to be a 2-path channel with delay spread $\mathcal{T} = T_s/8$ with equal power per path.

In figure 4.13, we provide the performance of the estimation versus normalized Doppler spread (F_dT_s) in terms of normalized MSE for FIR1, WNR$_n$ and Interp techniques in the considered system with SNR=20 dB while turning off all the data subcarriers. The first thing to be observed in this figure is that the classical Interp method (or any frequency domain pilots method) has exactly the same performance in the noise-only scenarios. This is due to the previously discussed phenomenon of having the pilot spreading beyond the range of the receiving filter. In addition to that, we can observe that FIR1 and WNR has almost the same performance, and both have performance *(almost)* identical to having $W = 1$ for $F_dT_s < $ *(0.32)* 0.25, and having $W = 3$ for $F_dT_s < $ *(0.9)* 0.75. This proves again the significance of the approach, and the success of isolating the pilots in relevant scenarios converting the complicated estimation problem into a simple noisy problem. Note that due

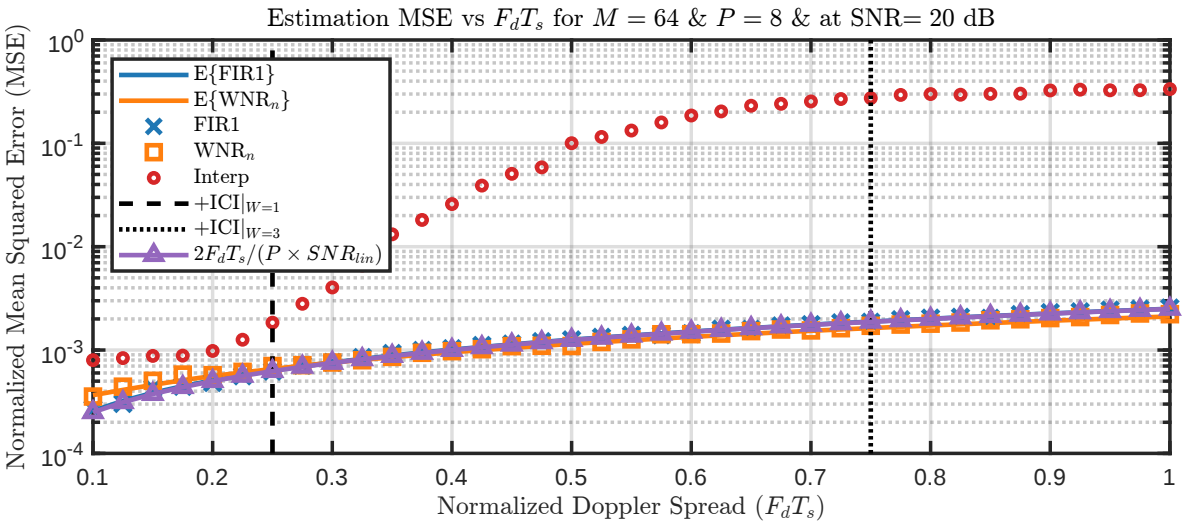

Figure 4.13: Statistical and Monte-Carlo estimation normalized MSE versus normalized Doppler spread (F_dT_s) for FIR1, WNR$_n$ and Interp techniques in RRC-pulse shaped MC system. $N = 80$, $M = 64$, $P = 8$ and SNR= 20 dB are used. All the data symbols are set to zero.

to this simplification, the estimation error can now be approximated by:

$$2F_dT_s/(P \times \text{SNR}_{\text{lin}}) \tag{4.18}$$

for the considered range of F_dT_s where SNR$_{\text{lin}}$ is the SNR in the linear scale, where this is valid even in realistic scenarios for ranges with no interference ($F_dT_s <$ '+ICI'). As the performance is found to be almost identical for FIR1, WNR$_n$, and WNR, we adopt (and advise) using FIR1 for: 1) its simplicity in terms of design, and 2) its flat passband allowing it to be configured for a maximum F_dT_s instead of a specific one. In the next section we provide a full scenario combining the propositions of this chapter and those of chapter 3.

4.5 Complete scenario analysis (BER)

In the previous sections, we have provided detailed analysis of the performance of the proposed channel estimation technique in terms of the Mean Squared Error (MSE). As mentioned in the introduction of this chapter, the main motivation behind adopting RRC pulse shape and designing an estimator that is adapted to work the best with it is the performance observed in chapter 3. Consequently, in this section, we combine the channel estimation technique proposed in this chapter with the equalization procedure proposed in the previous one to check the overall performance in terms of BER. We use the complete scenario described in section 4.1 and illustrated in figure 4.1. For the simulations of this section, we maintain the same configuration as before with $N_s = 1000$, $M = 64$, $N = 80$, $P = 8$, and the channel is assumed to be a 2-path channel with delay spread $\mathcal{T} = T_s/8$ with equal power per path. We consider QAM modulation of constellation size 4, and as previously mentioned, we only

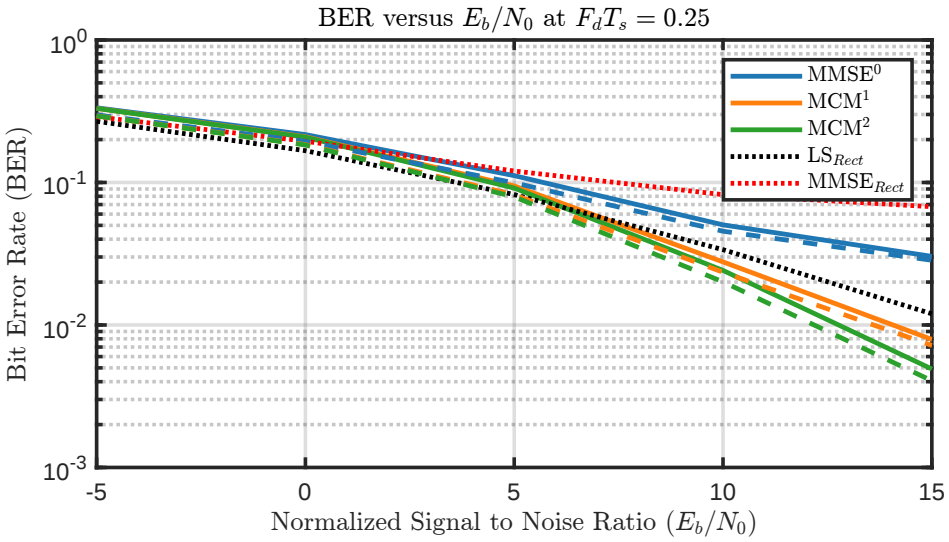

Figure 4.14: Bit error rate (BER) versus normalized signal to noise ratio (E_b/N_0) at normalized Doppler spread $F_dT_s = 0.25$ for the RRC-pulsed MC system at different iterations of channel estimation, ISI cancellation, and equalization for $M = 64$, $N = 80$, $P = 8$ and $W = 1$. Channel assumed to be a 2-path channel with delay spread $\mathcal{T} = T_s/8$ with equal power per path. Solid lines represent performance with our proposed estimation technique, and dashed lines represent the performance with perfect channel knowledge. The black and red dotted line reflects performance of multi-tap LS and single-tap MMSE equalizer for CP-OFDM respectively with perfect channel knowledge.

consider the FIR1-based estimation. It is to be noted that in this section we generate using the normalized signal to noise ratio E_b/N_0 not to be confused with the simple per subcarrier SNR considered in the previous sections, where the two are related by:

$$E_b/N_0 = \text{SNR} - \log_{10}(\log_2(Q)). \tag{4.19}$$

In figure 4.14, we provide the BER versus normalized signal to noise ratio (E_b/N_0) at normalized Doppler spread $F_dT_s = 0.25$ for the RRC-pulsed MC system at different iterations of channel estimation, ISI cancellation, and equalization when using $W = 1$. We use the solid lines to represent performance with our proposed estimation technique, and we use the dashed lines to represent the performance with perfect channel knowledge. The black and red dotted line reflects performance of multi-tap LS and single-tap MMSE equalizer for CP-OFDM respectively with perfect channel knowledge provided for comparison. We didn't consider channel estimation for CP-OFDM since our scheme is not intended to be used with such pulse shapes. The legend follows the format technique$^{\text{iteration}}$ where it signifies the equalization iteration it represents and the technique used at that iteration. We recall from chapter 3 that we consider the MMSE^0 and MCM^1 as a single iteration with MMSE^0 considered as pre-estimate, and the output of each iteration considered as a pre-estimate to the next one. As it can be observed through this figure, the performance using our proposed technique is very close to the performance with perfect channel knowledge. Moreover, similarly to what we observed

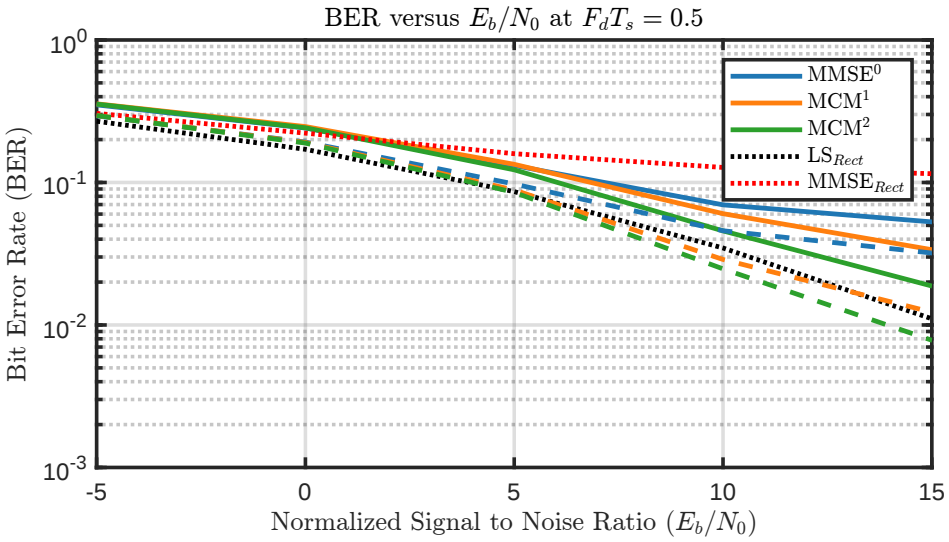

Figure 4.15: Bit error rate (BER) versus normalized signal to noise ratio (E_b/N_0) at normalized Doppler spread $F_dT_s = 0.50$ for the RRC-pulsed MC system at different iterations of channel estimation, ISI cancellation, and equalization for $M = 64$, $N = 80$, $P = 8$ and $W = 1$. Channel assumed to be a 2-path channel with delay spread $\mathcal{T} = T_s/8$ with equal power per path. Solid lines represent performance with our proposed estimation technique, and dashed lines represent the performance with perfect channel knowledge. The black and red dotted line reflects performance of multi-tap LS and single-tap MMSE equalizer for CP-OFDM respectively with perfect channel knowledge.

in chapter 3, the proposed techniques has a performance better than the state-of-the-art multi-tap LS equalizer when used with CP-OFDM, in addition to the diversity observable by having a better slope in BER reduction versus E_b/N_0. Note that this LS equalizer is a sophisticated multi-tap equalizer, while the commonly used equalizer, single-tap MMSE, can easily be seen to be far worse than the other considered technique (for more details, see chapter 3). This signifies again the relevance and benefits of all the proposed approaches: preprocessing, time-domain estimation, single tone pilots, etc. The main reason of this performance in channel estimation is the ability to isolate the pilots from data symbols. This was possible to be done mainly because, in this scenario, we consider $F_dT_s = 0.25$ that does not exceed the '+ICI' limit (which is 0.25 for $W = 1$). Therefore, it would be interesting to test a value of $F_dT_s > 0.25$ when using $W = 1$.

In figure 4.15, similarly to figure 4.14, we provide the BER versus E_b/N_0 at $F_dT_s = 0.50$ for the RRC-pulsed MC system at different iterations of channel estimation, ISI cancellation, and equalization when using $W = 1$. We use the solid lines to represent performance with our proposed estimation technique, and we use the dashed lines to represent the performance with perfect channel knowledge. The black and red dotted line reflects performance of multi-tap LS and single-tap MMSE equalizer for CP-OFDM respectively with perfect channel knowledge provided for comparison. We didn't consider channel estimation for CP-OFDM since our scheme is not intended to be used with such pulse shapes. We can clearly observe in this figure that in this scenario, the BER with channel estimation is now higher than that with perfect

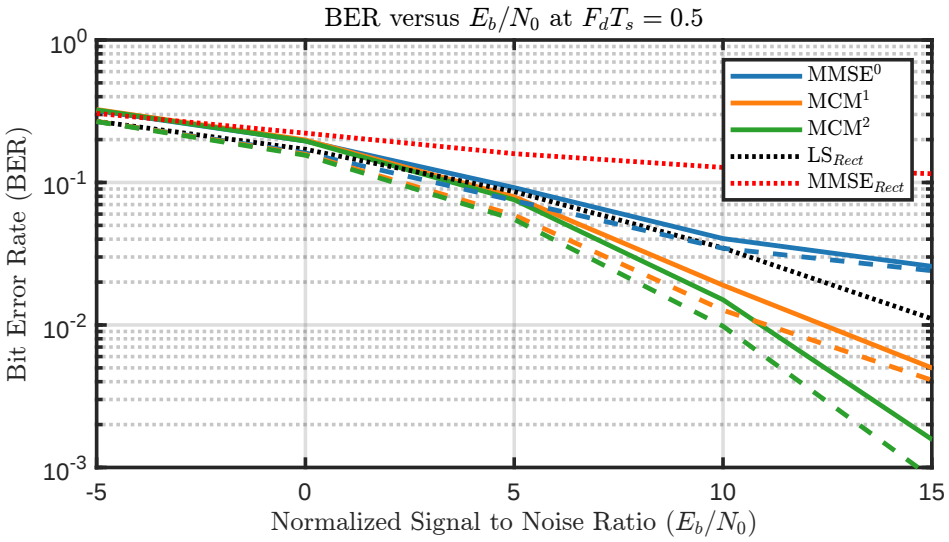

Figure 4.16: Bit error rate (BER) versus normalized signal to noise ratio (E_b/N_0) at normalized Doppler spread $F_dT_s = 0.50$ for the RRC-pulsed MC system at different iterations of channel estimation, ISI cancellation, and equalization for $M = 64$, $N = 80$, $P = 8$ and $W = 3$. Channel assumed to be a 2-path channel with delay spread $\mathcal{T} = T_s/8$ with equal power per path. Solid lines represent performance with our proposed estimation technique, and dashed lines represent the performance with perfect channel knowledge. The black and red dotted line reflects performance of multi-tap LS and single-tap MMSE equalizer for CP-OFDM respectively with perfect channel knowledge.

channel knowledge. This difference is because of the data to pilot interference, which makes the channel estimation less accurate as shown in section 4.4.2 where estimation MSE was at $F_dT_s = 0.5$ two orders higher than that of $F_dT_s = 0.25$ for $W = 1$. However, in chapter 3 we have shown that the BER decreases with the increase of F_dT_s when considering our proposed equalizer, while we can see that the plots of figure 4.15 has higher BER compared to those of figure 4.14, even the ones with perfect channel knowledge. We have already mentioned and discussed several times that for $F_dT_s >$ '+ICI', we have degradation in the estimation performance. Equivalently, similarly to having data to pilot interference that decreases estimation performance, we have, in the opposite direction, pilot to data interference decreasing the equalization performance. This interference can be canceled recursively, but this is beyond the scope of this work. However, to support such high values of F_dT_s, for improving both the estimation and the equalization, we should consider a higher value of W.

In figure 4.16, similarly to figures 4.14 and 4.15, we provide the BER versus E_b/N_0 at $F_dT_s = 0.50$ for the RRC-pulsed MC system at different iterations of channel estimation, ISI cancellation, and equalization, but while using $W = 3$. We use the solid lines to represent performance with our proposed estimation technique, and we use the dashed lines to represent the performance with perfect channel knowledge. The black and red dotted line reflects performance of multi-tap LS and single-tap MMSE equalizer for CP-OFDM respectively with perfect channel knowledge provided for comparison. We didn't consider channel estimation for CP-OFDM since our scheme is not intended to be used with such pulse shapes. As it can

be seen in this plot, the performance with the proposed channel estimation technique is again very close to that with perfect channel knowledge, but not as close as in figure 4.14. The reason behind this difference, as discussed in sections 4.4.2 and 4.4.3, is that increasing F_dT_s requires increasing the pilot filter's bandwidth, and then increasing the amount of noise captured by the filter. However, we can see a significant reduction in BER compared to the scenario of having $F_dT_s = 0.25$ in figure 4.14. This explains again the impact of ICI on the performance of both the estimation and equalization procedure, and shows how the channel estimation technique proposed in this chapter allows only a negligible error further than perfect channel knowledge (< 1 dB).

4.6 Conclusion and Perspectives

In this chapter, we have provided a new channel estimation procedure (including dedicated pilots scheme) based on the isolation of comb-type pilots designed to operate in multicarrier systems having band-limited pulse shapes. The new technique is based on a new pilots model added to the signal asynchronous to the multicarrier symbols periods, which was described and discussed in details how and why it is used. We provide mathematical formulation of this technique with the ability to reserve multiple subcarriers for a single pilot. The introduced technique was compared to the classical interpolation based channel estimation, and proved to be significantly better for all the considered scenarios. In addition to that, we have explained why synchronous pilot symbols-based techniques that are commonly used for sample-time estimation can not estimate the channels with relatively high Doppler spread, and showed how the proposed technique operates at such conditions with high accuracy similar to estimation for slow-varying channels. This estimation technique was also combined with the equalization techniques previously proposed to assess the performance of the complete scenario. The BER obtained was almost identical to the one with perfect channel knowledge with a difference (in E_b/N_0) of $\sim$1 dB, and it proved the ability of obtaining Doppler driven diversity in practice.

This exceptional performance of this technique, especially observed when combined with the previously proposed equalization concept, motivates extending this work. The authors of this work find the following possible extensions in the perspective of this work:

- Study an ICI cancellation algorithm to account for pilot-data interference.
- Search for more robust distribution of pilots, as the equally distributed scheme showed to have weaknesses for some scenarios.
- The proposed technique uses only the pilots to estimate the channel, while using the estimated data symbols to help for an iterative estimation may improve it.
- Re-implement the proposed technique with pulse shapes different than the RRC, and extend the technique accordingly.

Chapter 5

General Conclusion and Perspectives

In this work we deal with the problem of fast fading channels in wireless communication when considering multicarrier systems. We approach the problem in the context of analyzing the impact of such channel conditions on the communication process and quantifying it. We then extended this quantification of the impact on the system to the analysis of the observable impact on the overall performance of the system, and proposed solution to the observed degradation. We also provided a new concept for accurately estimating how the channel affects the communication in realistic scenarios, which is required to counter the aforementioned degradation. In this chapter, we first recapitulate the contributions of this work, and then provide the authors' vision of its possible extensions.

5.1 Conclusion and contribution

In chapter 1 we have discussed the details of the background and context of this work. We have described the properties of a mobile communication channel, discussed the characteristics of such channels, and described them mathematically. We then gave a brief history of Multi-Carrier (MC) systems and discussed the most common orthogonal MC systems: Orthogonal Frequency Division Multiplexing (OFDM), Cyclic-Prefix Orthogonal Frequency Division Multiplexing (CP-OFDM), Filter-Bank Multi-Carrier (FBMC), and Bi-orthogonal Frequency Division Multiplexing (BFDM). Later, we discussed the generalized Frequency Division Multiplexing (FDM) system that we assume for this work, and provided its Fast Fourier Transform (FFT) implementation in addition to the pulse shapes that will be used for comparison. After that, we briefly discussed how problems caused by delay spread can be easily solved in MC systems, while channel variation would cause what we call Doppler-generated-Inter-Carrier Interference (ICI) and Doppler-generated-Inter-Symbol Interference (ISI) in addition to creating what we call Doppler-generated-diversity. This chapter (chapter 1) has therefore pedagogically provided and built the 'tools' required for the later parts of this work by having a detailed introduction to the context of the work.

In chapter 2, we have derived equations for the interference power that calculate how much each transmitted subcarrier and symbol interfere with each received subcarrier and symbol for MC systems operating in time-varying multipath channels. The results were provided in two fashions: observation-based equations used for Monte Carlo simulation, and statistical equations used for theoretical analysis, where they appeared to match validating the derived equations for conventional correlator receiver. We used for comparison different pulse shapes

selected based on different optimization criteria to understand the weaknesses and strengths of each pulse and its underlying criterion. Analysis was provided for single path and multipath channels. It was observed that the time-limited pulses are more vulnerable to ICI, while frequency-limited pulses conducted very high ISI. We also studied the impact of reducing the transmission density by turning off a number of subcarriers/symbols. In addition to that, we have discussed having arbitrary density reduction, and showed its corresponding interference levels. Parts of the work discussed in this chapter were published through the following papers:

- Ahmad Hamdan et al. "On multi-carrier systems robustness to Doppler in fast varying flat fading wireless channel." In: *Digital Signal Processing* 117 (2021), p. 103189
- Ahmad Hamdan et al. "Interference Analysis for Multi-Carrier Systems Over Fast-Fading Multipath Channels." In: *2021 IEEE Latin-American Conference on Communications (LATINCOM)*. Santo Domingo, Dominican Republic: IEEE, Nov. 2021, pp. 1–6

In chapter 3, we discuss the importance of assisting equalization by performing time domain preprocessing when considering multi-carrier communication over fast-varying Rayleigh channels. We have defined the receiver structure that can be used to incorporate both/either time domain preprocessing and frequency domain equalization. Classical and state-of-the-art frequency domain equalization techniques considered for CP-OFDM have been presented. Two low-complexity, time-domain-assisted equalization techniques have been proposed that support both single-path and multipath channels. Complexity analysis for the frequency domain and time domain techniques was provided in terms of the order of the number of operations. Bit Error Rate (BER) comparison was provided for several equalizers and pulse shapes, and the additional time domain processing was shown to improve performance and to benefit from channel variation instead of being negatively affected by exploiting what we call Doppler-driven diversity. Diversity–BER mapping was introduced to compute a proposed Doppler-driven diversity equivalence per pulse shape. It was shown how pulses that are less localized in time tend to achieve higher Doppler-driven diversity equivalence. To account for the ISI that may be emitted by less localized pulse shapes in such scenarios, an ISI cancellation technique was proposed and shown to converge to the ideal ISI cancellation after a single iteration. As a conclusion, we have observed that using the proposed MCMQR technique with the proposed ISI cancellation procedure and Root Raised Cosine (RRC) pulse shape provides ~ 7 dB gain compared to the state-of-the-art CP-OFDM with frequency domain Least Square $(\text{LS})_f$ matrix equalizer in both single-path and multipath channels when the channel is perfectly known. Moreover, this gain increases to ~ 12 dB when the channel is partially known with normalized Mean Squared Error (MSE) $= -20$ dB, illustrating how the adopted proposed system is more robust to channel estimation errors. We have also observed that this gain increases for lower BER targets due to the diversity captured by the RRC pulse shape. Parts of the work discussed in this chapter have been published in the following paper:

- Ahmad Hamdan et al. "Equalization With Time Domain Preprocessing for OFDM and FBMC in Flat Fading Fast Varying Channels." In: *2022 IEEE 6th International Symposium on Telecommunication Technologies (ISTT)*. Johor Bahru, Malaysia: IEEE, Nov. 2022, pp. 1–6

In chapter 4, we have provided a new channel estimation based on the isolation of comb-type pilots designed to operate in multicarrier systems with band-limited pulse shapes. The new technique is based on a new pilot model added to the signal asynchronous to the multicarrier symbols periods, which has been described and discussed in detail how and why it was used. We provide a mathematical formulation of this technique with the ability to reserve multiple subcarriers for a single pilot. The introduced technique was compared with the classical interpolation-based channel estimation and proved to be significantly better in all considered scenarios. In addition, we have explained why synchronous pilot symbol-based techniques, which are commonly used for sample-time estimation, cannot estimate the channels with relatively high Doppler spread, and have shown how the proposed technique works under such conditions with high accuracy, similar to estimation for slowly varying channels. This estimation technique was also combined with the previously proposed equalization techniques to evaluate the performance of the entire scenario. The BER obtained was almost identical to that obtained with perfect channel knowledge, with a difference (in E_b/N_0) of $1dB$, and it proved the ability to obtain Doppler-driven diversity in practice.

5.2 Perspective for future works

Following the analysis and propositions provided in this work, many questions arise that open a window to many possible extensions of this work. The perspective for future work based on this thesis, as seen by the authors, includes, but is not limited to, the following:

- In this thesis, we have provided a detailed interference analysis based on the assumed system model and the derived equations. Although this covers a wide variety of systems in use, it does not cover all of them. One of the common concepts that should be analyzed is the offset-based systems such as Filter-Bank Multi-Carrier with Offset Quadrature Amplitude Modulation (FBMC-OQAM). Consequently, **we recommend extending this work to support offset-based systems**.

- One of the motivations for using such extremely high levels of normalized Doppler spread in this work is the possibility of having such values when we consider the use of multicarrier systems over high carrier frequencies. However, this work considers classical channel conditions for modeling the system. **We find it very important to extend this work by considering more THz-oriented channel conditions (e.g., varying channel models, phase noise, jitter, etc.)**.

- In this work, specifically in chapter 3, we have observed that time-limited pulse shapes (such as the Rectangular (Rect) and Out of Band Energy (OBE)) pulses have the ability to capture Doppler-generated diversity (through ML), but this is not achieved. The proposed time-domain aided equalization have successfully captured the diversity for the frequency limited pulse shape RRC. We find it interesting to **explore the possibility of practically capturing the diversity when considering time-limited pulse shapes**.

- We also observed in chapter 3 that our proposed technique was able to capture the Doppler-generated diversity while being robust to multipath channels. However, the ML performance shows that additional diversity can be obtained due to multipath propagation, which is not captured by our proposed technique. Since capturing this type of delay-generated diversity is interesting, we believe it is important to try to **find an equalization technique that captures both Doppler-generated and delay-generated diversity**.

- One of the main advantages of this system is that it will be feasible to increase the pulse duration without worrying about performance degradation, but on the contrary benefit from it by capturing diversity. However, this comes at the cost of increased complexity, which is reflected in the power consumed by the system for the computations and the delay caused by the additional processing and the longer symbol duration. For this, **an analysis should be done on how the overall system power efficiency is affected (improved due to diversity or degraded due to additional computation) and how much the added delay can be tolerated**.

- Multiple-Input Multiple-Output (MIMO) antenna systems, especially massive MIMO, have gained a great interest in recent years. This interest came to have them as an important part of 5G, and considered as a key enabling technology of 6G, especially for systems operating on high carrier frequency. Therefore, it is extremely important to **analyze the content of this work in the context of MIMO systems, and extend it to support MIMO systems wherever needed**.

- In this thesis, we have proposed a highly accurate channel estimation technique, especially adapted to extremely fast varying environments, when considering frequency-limited pulse shapes operating directly in the time domain. We have discussed in the main text that this technique, like any equally distributed comb pilot based technique, has weaknesses for some special scenarios. In addition, we only used the pilots to estimate the channel without any (recursive) help from the estimated data. Consequently, we consider it important to **reimplement and test the proposed estimation technique for pulse shapes different from RRC, more robust pilot distributions, and including some data-aided schemes**.

- The research done in this work assumes a customized (yet generic) system and environment with (almost) everything normalized to make the analysis as general as possible. We find it necessary to **project the content of this work to real values and examples while trying to approach standards**.

Appendix A

Doppler-driven Diversity in Single Carrier Systems

In this appendix, we discuss the Doppler-driven diversity in classical single carrier systems through a flat-frequency (single-path) Rayleigh channel with Jakes' Doppler spectrum. We first discuss how the normalized Doppler spread F_dT_s affects the channel taps and the relevant correlation function. We then look into the distribution of the symbol energy E_s depending on the value of F_dT_s, and how this can be mapped into a value of diversity. Finally, we analyze the impact of such diversity on the Bit Error Rate (BER).

A.1 Doppler Spread Impact on Correlation

In figure A.1, we proved the real valued taps of channel examples and relative correlations functions for Rayleigh single-path channels with Jakes' Doppler spectrum for $F_dT_s = 0.1$, $F_dT_s = 10$, and $F_dT_s = 1000$. Note that in order to emphasize phenomena, we consider in this appendix also very high normalized Doppler frequency values, which are out of the scope of the Ph.D. We can see that the increase in Doppler spread decreases the similarity between samples, which can be statistically observed through the correlation function. For a low value of Doppler spread F_dT_s, we can see that the channel taps are almost equal (within one symbol duration Ts, but would slowly randomly change for one symbol to another), which provides no diversity and has the equivalent number of independent branches $D = 1$. This quasi-equality can be statistically observed from the correlation function, which has the value ≈ 1 for all the symbol duration span T_s for $F_dT_s = 0.1$. For a very high Doppler spread, we can observe that the samples become approximately uncorrelated. This sample uncorrelation can be statistically observed from the correlation function, which has the value ≈ 0 for all the symbol duration span T_s except at 0 for $F_dT_s = 1000$. When N samples are completely uncorrelated, it is known this provides a degree of diversity $D = N$. However, this become more complicated when that sampled are neither identical nor uncorrelated, but has some degree of correlation between them like what is observed for $F_dT_s = 10$.

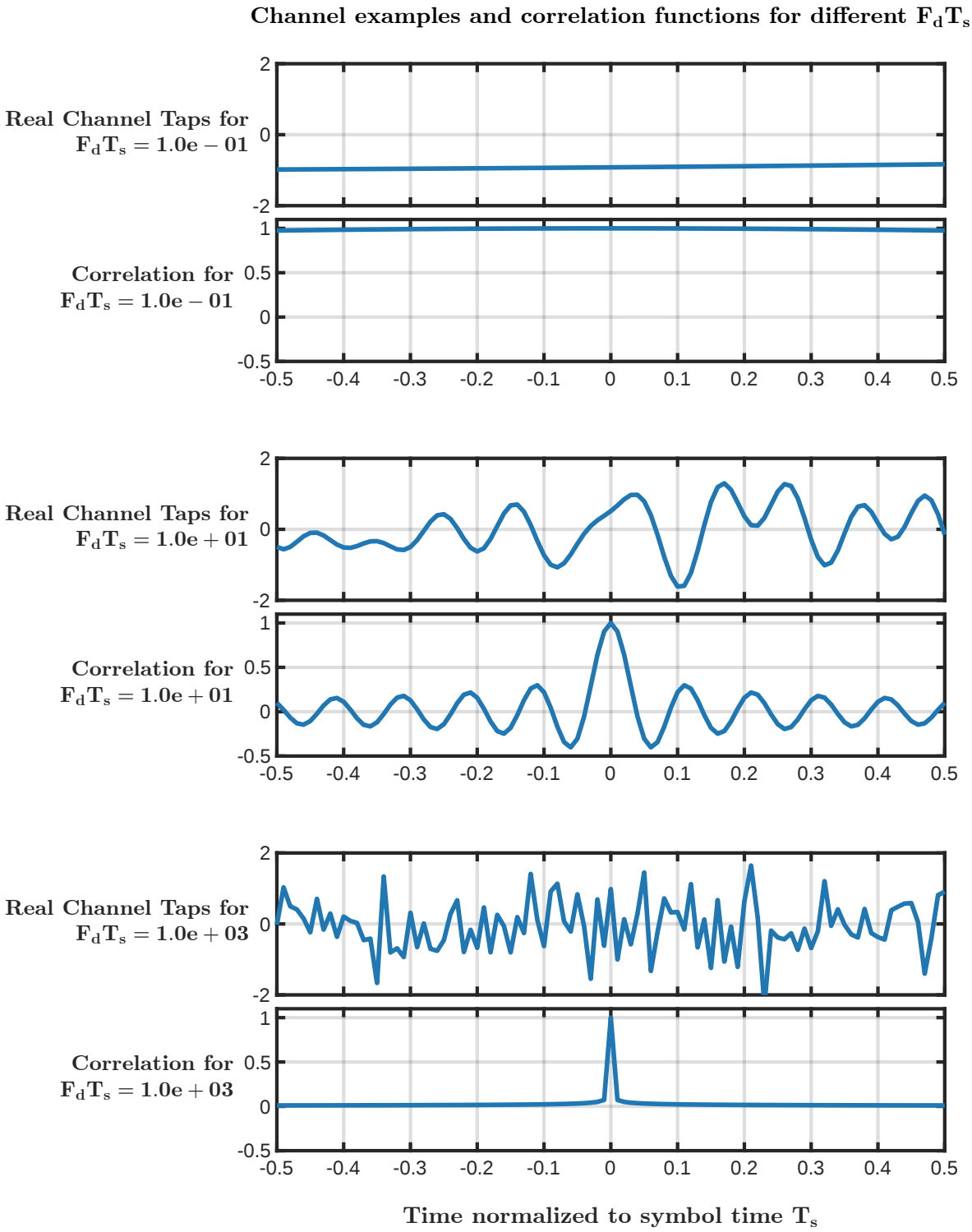

Figure A.1: Real valued taps of channel examples and relative correlations functions for Rayleigh single-path channels with Jakes' Doppler spectrum for $F_dT_s = 0.1$, $F_dT_s = 10$, and $F_dT_s = 1000$.

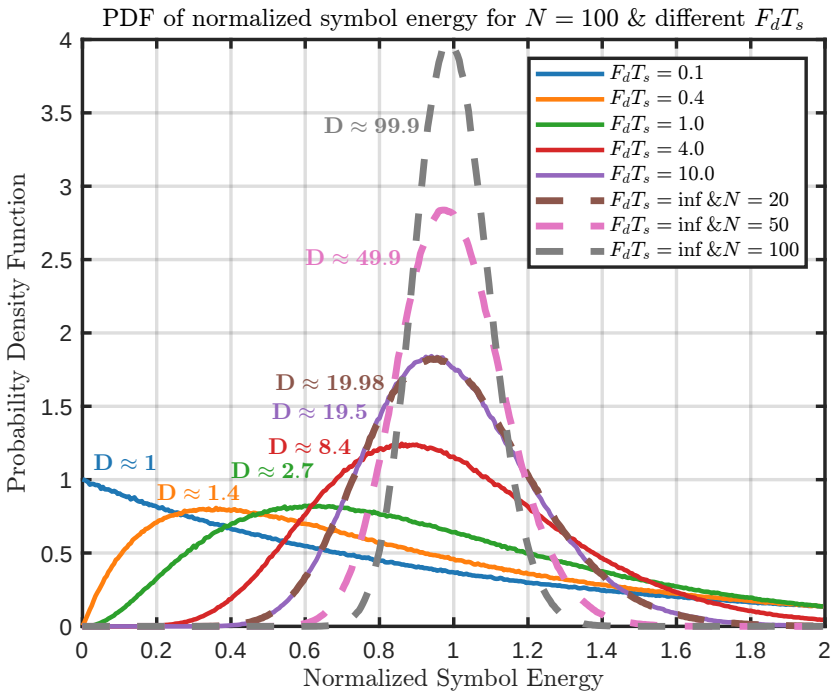

Figure A.2: Probability density function of normalized symbol energy for $N = 100$ (by default) and different values of F_dT_s.

A.2 The Equivalent Number of Independent Branches

To study these intermediate cases, we consider analyzing the equivalent number of independent branches provided by [DZB98]; [RJA01] which can be simply obtained by:

$$D = 1 \Big/ \text{var}\left\{\frac{E_s}{\text{E}\{E_s\}}\right\}, \tag{A.1}$$

where E_s is the symbol energy, which is a random variable due to the Jakes' Rayleigh fading effect. We consequently can empirically calculate the equivalent number of independent branches.

Although calculating the variance of the symbol energy is considered sufficient for calculating the equivalent number of independent branches D, we provide a more detailed view on the properties of the distribution of the symbol energy E_s. Therefore, in figure A.2 we provide the simulated probability density function of the normalized symbol energy for $N = 100$, unless specifies otherwise, and different values of F_dT_s. Different values of N are also used for completely uncorrelated samples ($F_dT_s \to \inf$). Over the plots, with similar colors as the relative lines, the value of D for the setup considered is shown. It is known from the formula that the equivalent number of independent branches is the (normalized) inverse of the variance of the symbol energy. From the figure we can see that distribution of the energy for low Doppler spreads has higher variance (all has mean 1 because E_s is normalized). Actually, in the case of $F_dT_s = 0.1$, we find an exponential distribution with mean 1. We then get high

probability to have amplitude with very low values, which reflects the fading effect. However, as the Doppler spread increases, we observed that the values are more concentrated around the mean, and fewer values away from it (an close to zero). This signifies decrease in the variance, and equivalently increase in the equivalent number of independent branches D. We can observe that when the Doppler spread become very high ($F_dT_s \to \inf$), D will be capped at N ($D \leq N$) since the variance will be at a minimum $1/N$. This reflects the previous discussed case of having N independent samples.

We can also notice that the distribution of the symbol energy E_s follows a normalized chi-squared distribution which is described in appendix B, with $k = 2D$ degrees of freedom. The factor 2 is due to having the signal consisting of real and imaginary part. The chi-squared distribution is by definition the distribution of the sum of the squares of Gaussian independent variables with zero mean and same variance, which here appears as (two folds of) the equivalent independent branches. However, due to normalizing the symbol energy, we have a normalized version of the chi-squared distribution. Note that since D is not an integer, k is not an integer also, which mutates a little the definition of the chi-squared, but maintains the properties. As discussed in appendix B for the properties of the normalized chi-squared, and contrary to the classical chi-squared, the variance decreases with k linearly (variance is $2/k$).

From figure A.2, we can also observe that for very high F_dT_s (10 for example), the degrees of freedom D equals approximately $2F_dT_s$ in the case where $N \leq 2F_dT_s$, since the number of independent branches D component cannot be greater than the number of samples N (i.e. $D \leq N$). This can be observed in the same figure where for completely uncorrelated N samples ($F_dT_s \to \inf$), the number of equivalent independent branches approximately equals N, with $D \approx 19.98$ for $N = 20$, $D \approx 49.9$ for $N = 50$, and $D \approx 99.9$ for $N = 100$.

A.3 The Equivalent Diversity and Bit Error Rate

To ensure more if the calculated equivalent number of independent branches practically achieves the relative diversity, we should check if this is observed at the level of BER. Therefore, in figure A.3, we provide the BER versus E_b/N_0 for different F_dT_s while using 4-QAM and number of samples per symbol $N = 20$. Simple rectangular pulse was assumed, with a single path Rayleigh channel. Simulations were performed using 10^8 symbols. Solid line plots reflect classical pulse shape matched filter receivers. Dashed line plots reflect pulse shape and channel matched filter receivers. Dotted line represents theoretical value of BER in slow-fading channels with optimal Maximum Ration Combining receiver for $D = N$ branches of diversity. Two important observations can be made. First, if we use pulse shape and channel matched filter, which is the optimal receiver in the considered scenario (with a receiver matched to the global pulse including the channel), we can strongly benefit from diversity in order to reduce fading effect when F_dT_s increases (Note that in this scenario, we have no interference). Secondly, we can however see that for the classical pulse shape matched filter (represented by solid lines), the BER slightly increases with F_dT_s, having very bad performance. This type

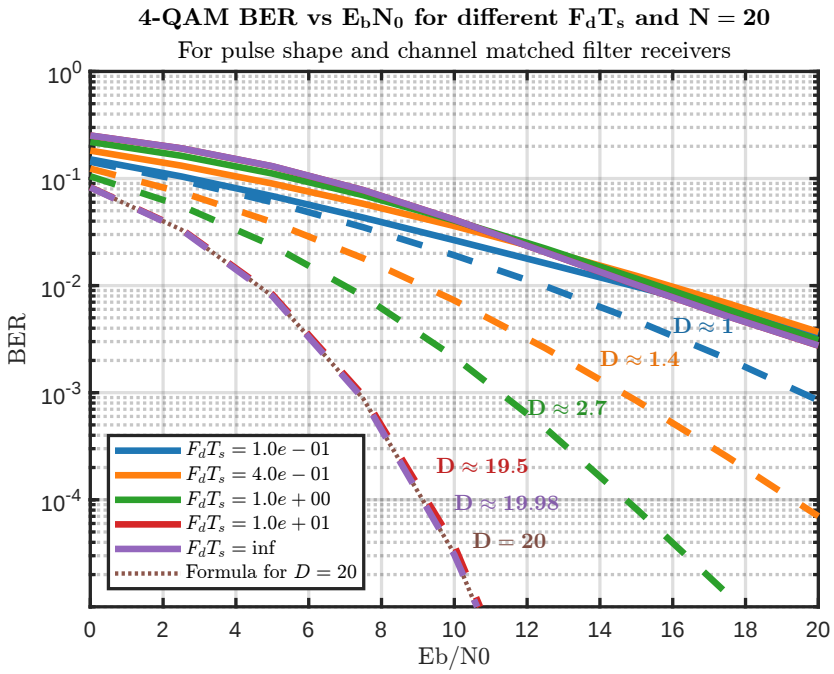

Figure A.3: BER versus E_b/N_0 for different F_dT_s while using 4-QAM and number of samples per symbol $N = 20$. Solid line plots reflect classical pulse shape matched filter receivers. Dashed line plots reflect pulse shape and channel matched filter receivers. Dotted line represents theoretical value of BER in slow-fading channels for $D = N$ branches of diversity.

of receivers is used widely, and is 'built-in' in many receiver architectures like the Orthogonal Frequency Division Multiplexing (OFDM) and Filter-Bank Multi-Carrier (FBMC) receivers. Such observation contradicts with the analysis provide earlier of obtaining diversity with the increase of F_dT_s. So, diversity can be available in high Doppler scenario, but we have to use appropriate receveir to catch it.

A.4 Conclusion

In conclusion, in a free-interference scenario, when considering the pulse shape and channel matched filter receiver, which is not commonly adopted especially in Multi-Carrier (MC) systems, we can take advantage of the claimed time diversity, in order to reduce the fading effect and improve the BER. This diversity is not straight forward to compare with the classical theoretical branches of diversity concept since it is not strictly an integer. However, for $F_dT_s = 10$, this comparison is possible since it provides equivalent number of independent branches $D \approx 19.5 \approx 2F_dT_s$. From figure A.3, we can observe that the BER versus E_b/N_0 plot for $F_dT_s = 10$ ($D \approx 19.5$) with pulse shape and channel matched filter is almost identical to the theoretical slow-fading BER with 20 branches of diversity. Again this also matches with the BER for independent samples ($F_dT_s \to \inf$) with $N = 20$. However, it is important to note that this benefit on the BER is observed with a receiver which is not the common receiver

in the multi-carrier system (which is matched only to the pulse and not to the channel). And it is observed in an interference-free scenario (single symbol single carrier). In a more realistic system, we will have to take also into account the interference phenomenon, which is very strong in presence of high Doppler, and some trade-off may appear between interference management and fading reduction.

Appendix B

Normalized Chi-Squared Distribution

In this Appendix, we discuss what we call the normalized chi-squared distribution. It is known that the chi-squared distribution is parametrized by the degree of freedom k, and has its mean equal to its order. We simply normalize this distribution to have its mean always equal to 1 as in [Ros]. We first discuss the chi-squared distribution, and then we introduce the normalized chi-squared and how the properties relevant to this work changes accordingly.

B.1 Chi-squared distribution

The chi-squared distribution of order k is the distribution of the sum of the square of k independent Gaussian-distributed variables. This can also be interpreted in multiple different ways, like the distribution of the squared magnitude of a vector of length k. Another interpretation is the distribution of the (sample-normalized) energy of a signal formed of k samples. Note that these interpretations follows the assumption of having real values. For complex (real and imaginary) values, the value of degrees of freedom k is doubled. For example, if we consider a complex signal of N samples, the energy of this signal will follow chi-squared distribution with $k = 2N$ degrees of freedom. In specific, if have k independent variables x_i with $i \in [0; k-1]$ and $x_i \sim \mathcal{N}(0, 1)$, we then have X defined by:

$$X = \sum_{i=0}^{k-1} x_i^2,$$

follows the chi-squared distribution of order k: $\mathcal{X}_k^2$, and due to independence, we have $\mathrm{E}(X) = k\,\mathrm{E}(x_i^2) = k$.

In figure B.1.a), we plot the probability density function $f_k(x)$ of the chi-square distribution for multiple values of degree of freedom k. Two very interesting properties of any distribution are the mean and the variance. For the chi-squared distribution, the mean equals the degrees of freedom k, and the variance equals $2k$. Since the total area under a probability distribution function equals the total probability 1, it is normal to observe that the maximum 'height' of the curve reduces for higher values of k where the variance increases linearly with k.

In figure B.1.b), we plot the relative cumulative distribution function $F_k(x)$. We can observe that the higher k is, the slower the increase in cumulative distribution function is. This again reflects the spreading of the chi-squared distribution for higher value of k, statistically

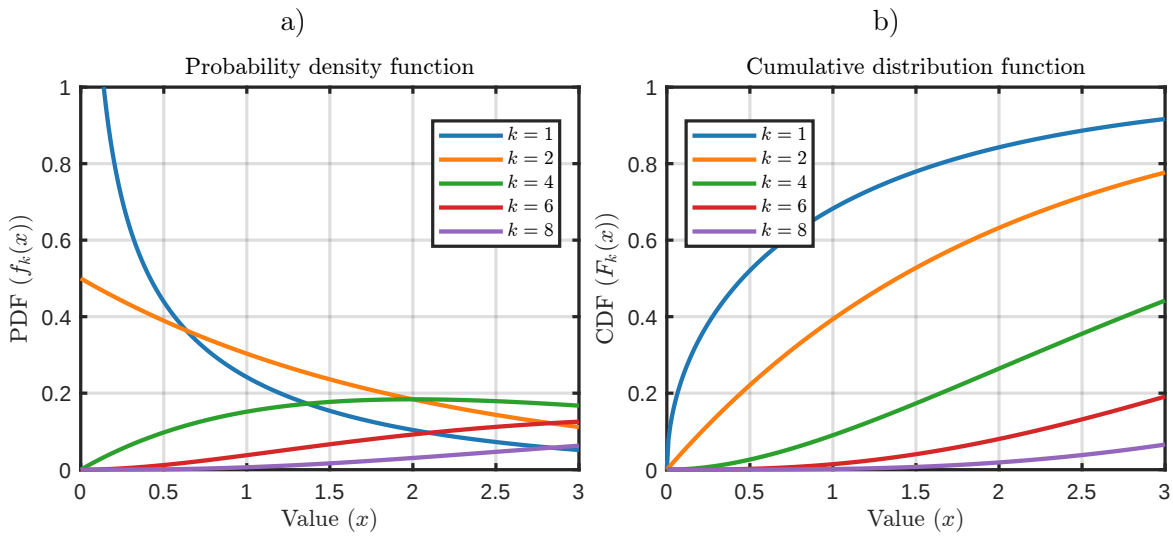

Figure B.1: Chi-squared a) probability density function and b) cumulative distribution function for multiple values of degrees of freedom k

observed through the variance $2k$.

We have mentioned before that the mean of the chi-squared distribution equals the degrees of freedom k. However, in some cases, like the scenario we have mentioned of modeling energy of a symbol, we might be interested in having the means normalized to 1.

B.2 Normalized chi-squared distribution

In this section, we present the slightly modified chi-squared distribution to have its mean always 1 instead of k. In other words, we need to model the distribution of the mean squared value of k independent Gaussian variables instead of the sum of squares. That is, for k independent variables x_i with $i \in [0; k-1]$ and $x_i \sim \mathcal{N}(0,1)$, we then have X defined by:

$$X = \frac{1}{k}\sum_{i=0}^{k-1} x_i^2,$$

follows the normalized chi-squared distribution of order k: $\mathbb{\chi}_k^2$. This modification propagates to all the properties of the chi-squared distribution, but we will focus only on the impact on mean (which will be set to 1), variance, probability density function, and cumulative distribution function.

The chi-squared distribution is usually referred as χ_k^2. We will refer to the normalized chi-squared as $\mathbb{\chi}_k^2$. As mentioned previously, the reason of introducing $\mathbb{\chi}_k^2$ is to normalize to have the mean as 1. This Since for χ_k^2 the mean is known to equal k, it is simple to normalize it to one directly through the probability density function ($f_k(x)$ for χ_k^2 and $g_k(x)$ for $\mathbb{\chi}_k^2$). This

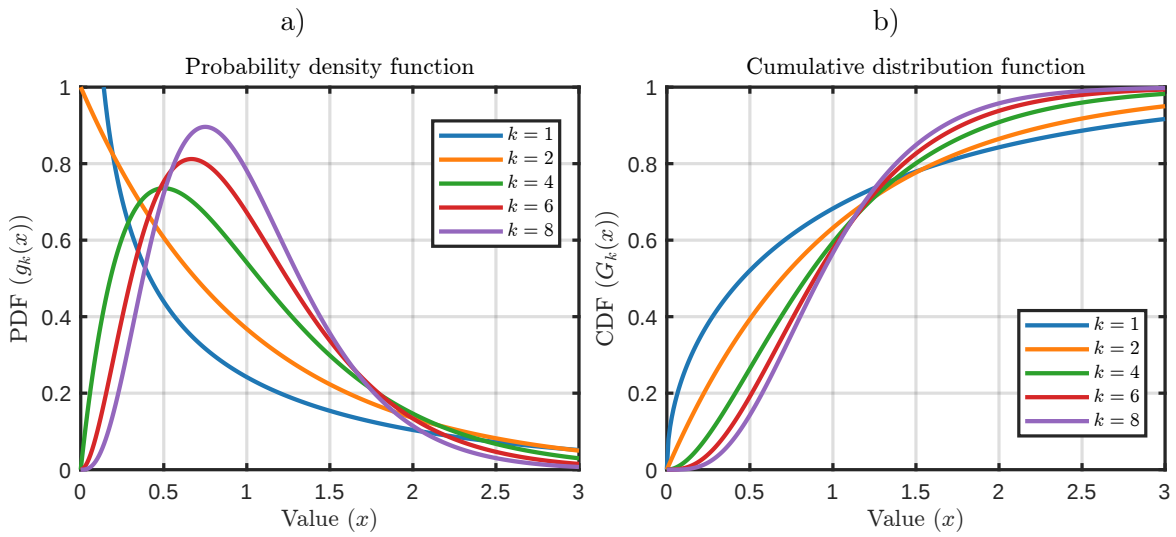

Figure B.2: Normalized chi-squared a) probability density function and b) cumulative distribution function for multiple values of degrees of freedom k

is done by setting $g_k(x) = f_k(k \times x)$. However, this makes the total area under the curve (the total probability) less than 1, specifically $1/k$. To fix this, we should set $g_k(x) = k \times f_k(k \times x)$. This configuration of $g_k(x)$ performs contraction of the x-axis by a factor of k moving the mean to always 1. Moreover, it also reduces the standard deviation with k, which accordingly reduces the variance by k^2 folds. Consequently, the new variance is $2k/k^2 = 2/k$. As a recap, the just defined normalized chi-squared distribution $\mathbb{\chi}^2_k$ has a mean $\mathrm{E}(X) = 1$ and variance $var(X) = 2/k$.

In figure B.2.a), we plot the probability density function $g_k(x)$ of the normalized chi-square distribution for multiple values of degree of freedom k. The plot for $k = 1$ in this figure is the same as for figure B.1.a), since it is normalized by 1. However, for the rest of the plots, we can observe a significant difference. Mainly, it is visible that the probability density function become more concentrated around 1 for all the values of $k > 1$. In addition to that, the 'width' of the function become narrower for higher values of k, with the 'peak' increasing with k and its relative x getting closer to 1. Furthermore, contrast to $\mathcal{X}^2_k$ which has its variance increasing with k $(2k)$, $\mathbb{\chi}^2_k$ has the variance decreasing with k $(2/k)$, which is reflected by the width reduction just mentioned.

In figure B.2.b), we plot the relative cumulative distribution function $G_k(x)$. Contrast to $\mathcal{X}^2_k$ which has its cumulative distribution function lower (and increasing more slowly) for higher values of k, $\mathbb{\chi}^2_k$ has the cumulative distribution function get steeper, with its fastest variation around 1. In addition to that, $\mathbb{\chi}^2_k$ with higher k gets closer to saturation ($G_k(x) \approx 1$). This again signifies the reduction and variance, and having higher probability to obtain values around 1.

The described variant of chi-squared, being normalized, better describes many problems where we have the mean squared value of the variables in analysis being normalized, instead

of having the normalization done per variable. Some example of such problems are the power analysis, energy analysis when normalized to energy of block of samples, etc.

Bibliography

[ABS07] Andrea Ancora, Calogero Bona, and Dirk TM Slock. "Down-sampled impulse response least-squares channel estimation for LTE OFDMA." In: *2007 IEEE International Conference on Acoustics, Speech and Signal Processing-ICASSP'07*. Vol. 3. IEEE. 2007, pp. III–293 (cit. on p. 37).

[ADFR19] Mohamed A Aboul-Dahab, Mohamed M Fouad, and Radwa A Roshdy. "Generalized discrete Fourier transform for FBMC peak to average power ratio reduction." In: *IEEE access* 7 (2019), pp. 81730–81740 (cit. on p. 19).

[Age35] DV Ageev. "Bases of the theory of linear selection. Code demultiplexing." In: *Proceedings of the Leningrad Experimental Institute of Communication* 3 (1935), p. 35 (cit. on p. 15).

[AJ04] Chandranath RN Athaudage and A Dhammika S Jayalath. "Enhanced MMSE channel estimation using timing error statistics for wireless OFDM systems." In: *IEEE Transactions on Broadcasting* 50.4 (2004), pp. 369–376 (cit. on p. 38).

[Aul79] Tor Aulin. "A modified model for the fading signal at a mobile radio channel." In: *IEEE Transactions on Vehicular Technology* 28.3 (1979), pp. 182–203 (cit. on p. 4).

[Bat88] Guy Battle. "Heisenberg proof of the Balian-Low theorem." In: *Letters in Mathematical Physics* 15.2 (1988), pp. 175–177 (cit. on p. 46).

[Bel63] Philip Bello. "Characterization of randomly time-variant linear channels." In: *IEEE transactions on Communications Systems* 11.4 (1963), pp. 360–393 (cit. on p. 7).

[BER76] James R Bitner, Gideon Ehrlich, and Edward M Reingold. "Efficient generation of the binary reflected Gray code and its applications." In: *Communications of the ACM* 19.9 (1976), pp. 517–521 (cit. on pp. 104, 107).

[BWK15] Jamal Bazzi, Petra Weitkemper, and Katsutoshi Kusume. "Power efficient scattered pilot channel estimation for FBMC/OQAM." In: *SCC 2015; 10th International ITG Conference on Systems, Communications and Coding*. VDE. 2015, pp. 1–6 (cit. on p. 36).

[Car+97] Richard D Carsello et al. "IMT-2000 standards: Radio aspects." In: *IEEE Personal Communications* 4.4 (1997), pp. 30–40 (cit. on p. 15).

[Cha66] Robert W Chang. "Synthesis of band-limited orthogonal signals for multichannel data transmission." In: *Bell System Technical Journal* 45.10 (1966), pp. 1775–1796 (cit. on pp. 15, 16, 19).

[Cha70] Robert W Chang. *Orthogonal frequency multiplex data transmission system*. US Patent 3,488,445. Jan. 1970 (cit. on pp. 15, 16, 19).

[Cla68] Richard Hedley Clarke. "A statistical theory of mobile-radio reception." In: *Bell system technical journal* 47.6 (1968), pp. 957–1000 (cit. on pp. 10, 11, 44).

[Col+02a] Sinem Coleri et al. “Channel estimation techniques based on pilot arrangement in OFDM systems.” In: *IEEE Transactions on broadcasting* 48.3 (2002), pp. 223–229 (cit. on p. 108).

[Col+02b] Sinem Colieri et al. “A study of channel estimation in OFDM systems.” In: *Proceedings IEEE 56th vehicular technology conference.* Vol. 2. IEEE. 2002, pp. 894–898 (cit. on pp. 36, 108).

[Cor01] Thomas Cormen. *Introduction to algorithms.* Cambridge, Mass: MIT Press, 2001 (cit. on p. 75).

[CT65] James W Cooley and John W Tukey. “An algorithm for the machine calculation of complex Fourier series.” In: *Math. Comp. 19 (1965), 297-301* (1965) (cit. on pp. 15, 17, 23).

[CTW05] Tao Cui, Chintha Tellambura, and Yue Wu. “Low-complexity pilot-aided channel estimation for OFDM systems over doubly-selective channels.” In: *IEEE International Conference on Communications, 2005. ICC 2005. 2005.* Vol. 3. IEEE. 2005, pp. 1980–1984 (cit. on p. 38).

[Cui+15] Wenjia Cui et al. “Coded auxiliary pilots for channel estimation in FBMC-OQAM systems.” In: *IEEE Transactions on Vehicular Technology* 65.5 (2015), pp. 2936–2946 (cit. on p. 36).

[CVC01] Yang-Seok Choi, Peter J Voltz, and Frank A Cassara. “On channel estimation and detection for multicarrier signals in fast and selective Rayleigh fading channels.” In: *IEEE Transactions on Communications* 49.8 (2001), pp. 1375–1387 (cit. on p. 36).

[DiT52] M DiToro. “Distant radio communication theory.” In: *Transactions of the IRE Professional Group on Antennas and Propagation* (1952), pp. 212–212 (cit. on p. 5).

[Dor98] Miloš I Doroslovački. “Product of second moments in time and frequency for discrete-time signals and the uncertainty limit.” In: *Signal Processing* 67.1 (1998), pp. 59–76 (cit. on p. 26).

[DRL08] Steredenn Daumont, Basel Rihawi, and Yves Lout. “Root-raised cosine filter influences on PAPR distribution of single carrier signals.” In: *2008 3rd International Symposium on Communications, Control and Signal Processing.* IEEE. 2008, pp. 841–845 (cit. on p. 27).

[DZB98] Jean-François Diouris, James Zeidler, and Soodesh Buljore. “Space-path diversity in CDMA using a compact array.” In: *Annales des télécommunications.* Vol. 53. 11. Springer. 1998, pp. 425–434 (cit. on pp. 35, 135).

[FB11] Behrouz Farhang-Boroujeny. “OFDM versus filter bank multicarrier.” In: *IEEE signal processing magazine* 28.3 (2011), pp. 92–112 (cit. on p. 19).

[FKB09] Gerhard Fettweis, Marco Krondorf, and Steffen Bittner. “GFDM-generalized frequency division multiplexing.” In: *VTC Spring 2009-IEEE 69th Vehicular Technology Conference.* IEEE. 2009, pp. 1–4 (cit. on p. 20).

[GT98] Georgios B Giannakis and Cihan Tepedelenlioglu. "Basis expansion models and diversity techniques for blind identification and equalization of time-varying channels." In: *Proceedings of the IEEE* 86.10 (1998), pp. 1969–1986 (cit. on p. 38).

[Ham+21a] Ahmad Hamdan et al. "Interference Analysis for Multi-Carrier Systems Over Fast-Fading Multipath Channels." In: *2021 IEEE Latin-American Conference on Communications (LATINCOM)*. Santo Domingo, Dominican Republic: IEEE, Nov. 2021, pp. 1–6 (cit. on pp. 130, 151).

[Ham+21b] Ahmad Hamdan et al. "On multi-carrier systems robustness to Doppler in fast varying flat fading wireless channel." In: *Digital Signal Processing* 117 (2021), p. 103189 (cit. on pp. 130, 151).

[Ham+22] Ahmad Hamdan et al. "Equalization With Time Domain Preprocessing for OFDM and FBMC in Flat Fading Fast Varying Channels." In: *2022 IEEE 6th International Symposium on Telecommunication Technologies (ISTT)*. Johor Bahru, Malaysia: IEEE, Nov. 2022, pp. 1–6 (cit. on pp. 130, 151).

[Har61] Frank R Hartman. "Single and multiple channel communication: A review of research and a proposed model." In: *Audiovisual communication review* 9.6 (1961), pp. 235–262 (cit. on p. 15).

[Her+17] Maria Freire Hermelo et al. "Spectral efficient 64-QAM-OFDM terahertz communication link." In: *Optics express* 25.16 (2017), pp. 19360–19370 (cit. on p. 45).

[HR08a] Hussein Hijazi and Laurent Ros. "Polynomial estimation of time-varying multipath gains with intercarrier interference mitigation in OFDM systems." In: *IEEE Transactions on Vehicular Technology* 58.1 (2008), pp. 140–151 (cit. on pp. 38, 69, 108, 118).

[HR08b] Hussein Hijazi and Lorent Ros. "Estimation de canal radio-mobile à evolution rapide dans les systems OFDM." In: *Institut polytechnique de Grenoble* (2008) (cit. on p. 38).

[HR09] Hussein Hijazi and Laurent Ros. "Rayleigh time-varying channel complex gains estimation and ICI cancellation in OFDM systems." In: *European Transactions on Telecommunications* 20.8 (2009), pp. 782–796 (cit. on p. 108).

[HR10] Hussein Hijazi and Laurent Ros. "Joint data QR-detection and Kalman estimation for OFDM time-varying Rayleigh channel complex gains." In: *IEEE Transactions on Communications* 58.1 (2010), pp. 170–178 (cit. on pp. 38, 69, 90, 106).

[HW07] Xiaozhou Huang and Hsiao-Chun Wu. "Robust and efficient intercarrier interference mitigation for OFDM systems in time-varying fading channels." In: *IEEE Transactions on Vehicular Technology* 56.5 (2007), pp. 2517–2528 (cit. on p. 38).

[HW98] Meng-Han Hsieh and Che-Ho Wei. "Channel estimation for OFDM systems based on comb-type pilot arrangement in frequency selective fading channels." In: *IEEE Transactions on Consumer Electronics* 44.1 (1998), pp. 217–225 (cit. on p. 36).

[Iha+06] Tero Ihalainen et al. "Channel equalization in filter bank based multicarrier modulation for wireless communications." In: *EURASIP Journal on Advances in Signal Processing* 2007 (2006), pp. 1–18 (cit. on p. 36).

[IL09] Aissa Ikhlef and Jérôme Louveaux. "An enhanced MMSE per subchannel equalizer for highly frequency selective channels for FBMC/OQAM systems." In: *2009 IEEE 10th Workshop on signal processing advances in wireless communications*. IEEE. 2009, pp. 186–190 (cit. on p. 36).

[JC94] William C Jakes and Donald C Cox. *Microwave mobile communications*. Wiley-IEEE press, 1994 (cit. on pp. 44, 106, 121).

[KG70] A Kaye and D George. "Transmission of multiplexed PAM signals over multiple channel and diversity systems." In: *IEEE Transactions on Communication Technology* 18.5 (1970), pp. 520–526 (cit. on p. 15).

[Kof+13] Eleftherios Kofidis et al. "Preamble-based channel estimation in OFDM/OQAM systems: A review." In: *Signal processing* 93.7 (2013), pp. 2038–2054 (cit. on p. 36).

[LD76] Shung-Wu Lee and G Deschamps. "A uniform asymptotic theory of electromagnetic diffraction by a curved wedge." In: *IEEE transactions on antennas and propagation* 24.1 (1976), pp. 25–34 (cit. on p. 4).

[Lee66] WC-Y Lee. "Theoretical and experimental study of the properties of the signal from an energy density mobile radio antenna." In: *17th IEEE Vehicular Technology Conference*. Vol. 17. IEEE. 1966, pp. 121–128 (cit. on p. 5).

[Lél+08] Chrislin Lélé et al. "Channel estimation methods for preamble-based OFDM/OQAM modulations." In: *European Transactions on Telecommunications* 19.7 (2008), pp. 741–750 (cit. on p. 36).

[Lin+09] Hao Lin et al. "An Analysis of the EIC Method for OFDM/OQAM Systems." In: *J. Commun.* 4.1 (2009), pp. 52–60 (cit. on p. 36).

[LLS08] Chrislin Lele, Rodolphe Legouable, and Pierre Siohan. "Channel estimation with scattered pilots in OFDM/OQAM." In: *2008 IEEE 9th Workshop on Signal Processing Advances in Wireless Communications*. IEEE. 2008, pp. 286–290 (cit. on p. 36).

[Mata] Mathworks. *berfading function reference*. URL: `https://www.mathworks.com/help/comm/ref/berfading.html` (cit. on pp. 76, 92, 96).

[Matb] Mathworks. *Cubic spline data interpolation function reference*. URL: `https://www.mathworks.com/help/matlab/ref/spline.html` (cit. on p. 118).

[Matc] Mathworks. *fir1 function reference*. URL: `https://www.mathworks.com/help/signal/ref/fir1.html` (cit. on pp. 115, 117).

[Matd] Mathworks. *flattopwin function reference*. URL: `https://www.mathworks.com/help/signal/ref/flattopwin.html` (cit. on p. 116).

[Mate] Mathworks. *Propagation Channel Models*. URL: `https://www.mathworks.com/help/lte/ug/propagation-channel-models.html` (cit. on p. 53).

[Maz75] James E Mazo. "Faster-than-Nyquist signaling." In: *The Bell System Technical Journal* 54.8 (1975), pp. 1451–1462 (cit. on pp. 24, 64).

[MBMB07] Uwe Meyer-Baese and U Meyer-Baese. *Digital signal processing with field programmable gate arrays*. Vol. 65. Springer, 2007 (cit. on pp. 23, 24).

[MC05] Yasamin Mostofi and Donald C Cox. "ICI mitigation for pilot-aided OFDM mobile systems." In: *IEEE Transactions on Wireless Communications* 4.2 (2005), pp. 765–774 (cit. on p. 37).

[MH81] Kazuaki Murota and Kenkichi Hirade. "GMSK modulation for digital mobile radio telephony." In: *IEEE Transactions on communications* 29.7 (1981), pp. 1044–1050 (cit. on p. 28).

[MT07] Yi Ma and Rahim Tafazolli. "Channel estimation for OFDMA uplink: a hybrid of linear and BEM interpolation approach." In: *IEEE Transactions on Signal Processing* 55.4 (2007), pp. 1568–1573 (cit. on p. 38).

[MYR96] Peter JW Melsa, Richard C Younce, and Charles E Rohrs. "Impulse response shortening for discrete multitone transceivers." In: *IEEE Transactions on Communications* 44.12 (1996), pp. 1662–1672 (cit. on p. 70).

[NC98] Rohit Negi and John Cioffi. "Pilot tone selection for channel estimation in a mobile OFDM system." In: *IEEE Transactions on Consumer Electronics* 44.3 (1998), pp. 1122–1128 (cit. on p. 38).

[NLS12] Gaëtan Ndo, Hao Lin, and Pierre Siohan. "FBMC/OQAM equalization: Exploiting the imaginary interference." In: *2012 IEEE 23rd International Symposium on Personal, Indoor and Mobile Radio Communications-(PIMRC)*. IEEE. 2012, pp. 2359–2364 (cit. on p. 36).

[Par+03] Byungjoon Park et al. "A novel timing estimation method for OFDM systems." In: *IEEE Communications letters* 7.5 (2003), pp. 239–241 (cit. on p. 36).

[PS08] J.G. Proakis and M. Salehi. "Digital Communications, 5th edition." In: McGraw-Hill Higher Education, 2008. Chap. 9.2-1, pp. 605–609 (cit. on pp. 5, 12, 32, 34, 76, 92, 96).

[PS11] Didier Pinchon and Pierre Siohan. "Closed-form expressions of optimal short PR FMT prototype filters." In: *2011 IEEE Global Telecommunications Conference-GLOBECOM 2011*. IEEE. 2011, pp. 1–5 (cit. on pp. 25, 26).

[PSP10] Erdal Panayirci, Habib Senol, and H Vincent Poor. "Joint channel estimation, equalization, and data detection for OFDM systems in the presence of very high mobility." In: *IEEE Transactions on Signal Processing* 58.8 (2010), pp. 4225–4238 (cit. on p. 38).

[RBL05] Luca Rugini, Paolo Banelli, and Geert Leus. "Simple equalization of time-varying channels for OFDM." In: *IEEE communications letters* 9.7 (2005), pp. 619–621 (cit. on p. 69).

[RHS14] Laurent Ros, Hussein Hijazi, and Eric-Pierre Simon. "Complex amplitudes tracking loop for multipath channel estimation in OFDM systems under slow to moderate fading." In: *Signal Processing* 97 (2014), pp. 134–145 (cit. on p. 36).

[Ric51] Stephen O Rice. "Reflection of electromagnetic waves from slightly rough surfaces." In: *Communications on pure and applied mathematics* 4.2-3 (1951), pp. 351–378 (cit. on p. 4).

[RJA01] Laurent Ros, Geneviève Jourdain, and Marylin Arndt. "Interpretations and performances of linear reception in downlink TD-CDMA and multi-sensor extension." In: *Annales des télécommunications* 56.5 (2001), pp. 275–290 (cit. on pp. 35, 135).

[Roq12] Damien Roque. "Modulations multiporteuses WCP-OFDM: évaluation des performances en environnement radiomobile." PhD thesis. Université de Grenoble, 2012 (cit. on p. 20).

[Ros] Laurent Ros. *Communication sans Fil, course of Grenoble-INP, chapter III "Performances sous un canal "flat fading" de Rayleigh, puis avec techniques de diversite", 2022.* URL: `https://chamilo.grenoble-inp.fr/main/document/document.php?cidReq=PHELMA5PMSCSF0` (cit. on p. 139).

[Ros16] Laurent Ros. *Traitement du signal pour les communications numériques au travers de canaux radio-mobiles.* 2016 (cit. on p. 36).

[SA98] Marvin K Simon and Mohamed-Slim Alouini. "A unified approach to the performance analysis of digital communication over generalized fading channels." In: *Proceedings of the IEEE* 86.9 (1998), pp. 1860–1877 (cit. on pp. 76, 92, 96).

[Sch04] Philip Schniter. "Low-complexity equalization of OFDM in doubly selective channels." In: *IEEE Transactions on Signal processing* 52.4 (2004), pp. 1002–1011 (cit. on p. 73).

[Sch82] Robert Scholtz. "The origins of spread-spectrum communications." In: *IEEE transactions on Communications* 30.5 (1982), pp. 822–854 (cit. on p. 15).

[SKJ94] Hikmet Sari, Georges Karam, and I Jeanclaud. "Frequency-domain equalization of mobile radio and terrestrial broadcast channels." In: *1994 IEEE GLOBECOM. Communications: The Global Bridge.* IEEE. 1994, pp. 1–5 (cit. on p. 68).

[SL03] Won-Gyu Song and Jong-Tae Lim. "Pilot-symbol aided channel estimation for OFDM with fast fading channels." In: *IEEE Transactions on Broadcasting* 49.4 (2003), pp. 398–402 (cit. on pp. 36, 108).

[SLK97] Hikmet Sari, Y Levy, and G Karam. "An analysis of orthogonal frequency-division multiple access." In: *GLOBECOM 97. IEEE Global Telecommunications Conference. Conference Record.* Vol. 3. IEEE. 1997, pp. 1635–1639 (cit. on p. 45).

[SPP12] Habib Senol, Erdal Panayirci, and H Vincent Poor. "Nondata-aided joint channel estimation and equalization for OFDM systems in very rapidly varying mobile channels." In: *IEEE transactions on signal processing* 60.8 (2012), pp. 4236–4253 (cit. on p. 38).

[SS00] Cyrille Siclet and Pierre Siohan. "Design of BFDM/OQAM systems based on biorthogonal modulated filter banks." In: *Globecom'00-IEEE. Global Telecommunications Conference. Conference Record (Cat. No. 00CH37137).* Vol. 2. IEEE. 2000, pp. 701–705 (cit. on p. 20).

[SSP02] Cyrille Siclet, Pierre Siohan, and Didier Pinchon. "Oversampled orthogonal and biorthogonal multicarrier modulations with perfect reconstruction." In: *2002 14th International Conference on Digital Signal Processing Proceedings. DSP 2002 (Cat. No. 02TH8628)*. Vol. 2. IEEE. 2002, pp. 647–650 (cit. on p. 20).

[Sti+10] TobiasHidalgo Stitz et al. "Pilot-based synchronization and equalization in filter bank multicarrier communications." In: *EURASIP Journal on Advances in Signal Processing* 2010 (2010), pp. 1–18 (cit. on p. 36).

[SWG97] Jorge Luis Seoane, Sarah Kate Wilson, and Saul Gelfand. "Analysis of intertone and interblock interference in OFDM when the length of the cyclic prefix is shorter than the length of the impulse response of the channel." In: *GLOBECOM 97. IEEE Global Telecommunications Conference. Conference Record*. Vol. 1. IEEE. 1997, pp. 32–36 (cit. on p. 17).

[Tan+07] Zijian Tang et al. "Pilot-assisted time-varying channel estimation for OFDM systems." In: *IEEE Transactions on Signal Processing* 55.5 (2007), pp. 2226–2238 (cit. on p. 38).

[TO05] Kok Ann Donny Teo and Shuichi Ohno. "Optimal MMSE finite parameter model for doubly-selective channels." In: *GLOBECOM'05. IEEE Global Telecommunications Conference, 2005.* Vol. 6. IEEE. 2005, 5–pp (cit. on p. 38).

[Tom+05] Stefano Tomasin et al. "Iterative interference cancellation and channel estimation for mobile OFDM." In: *IEEE Transactions on Wireless Communications* 4.1 (2005), pp. 238–245 (cit. on p. 37).

[Ts1] *5G; NR; Physical channels and modulation (3GPP TS 38.211 version 15.8.0 Release 15)*. Standard. European Telecommunications Standards Institute, Jan. 2020 (cit. on p. 53).

[TS93] ETSI TC-SMG. "European Digital Cellular Telecommunication Systems (Phase 2): Radio Transmission and Reception (GSM 05.05)." In: *Sophia Antipolis, France* (1993) (cit. on p. 8).

[WE71] S Weinstein and Paul Ebert. "Data transmission by frequency-division multiplexing using the discrete Fourier transform." In: *IEEE transactions on Communication Technology* 19.5 (1971), pp. 628–634 (cit. on p. 17).

[Wie+49] Norbert Wiener et al. *Extrapolation, interpolation, and smoothing of stationary time series: with engineering applications*. Vol. 113. 21. MIT press Cambridge, MA, 1949 (cit. on pp. 116, 117).

[Wil12] Virginia Vassilevska Williams. "Multiplying Matrices Faster than Coppersmith-Winograd." In: *Proceedings of the Forty-Fourth Annual ACM Symposium on Theory of Computing*. STOC '12. New York, New York, USA: Association for Computing Machinery, 2012, 887–898 (cit. on p. 75).

[WJ08] Ludong Wang and Brian Jezek. "OFDM modulation schemes for military satellite communications." In: *MILCOM 2008-2008 IEEE Military Communications Conference*. IEEE. 2008, pp. 1–7 (cit. on p. 45).

[Won+99] Cheong Yui Wong et al. "Multiuser OFDM with adaptive subcarrier, bit, and power allocation." In: *IEEE Journal on selected areas in communications* 17.10 (1999), pp. 1747–1758 (cit. on p. 45).

[Zha+09] Jiankang Zhang et al. "Decision-directed channel estimation based on iterative linear minimum mean square error for orthogonal frequency division multiplexing systems." In: *IET communications* 3.7 (2009), pp. 1136–1143 (cit. on p. 38).

[ZM05] Thomas Zemen and Christoph F Mecklenbrauker. "Time-variant channel estimation using discrete prolate spheroidal sequences." In: *IEEE Transactions on signal processing* 53.9 (2005), pp. 3597–3607 (cit. on p. 38).

List of Author's Publications

Journals

[J1] Ahmad Hamdan et al. "On multi-carrier systems robustness to Doppler in fast varying flat fading wireless channel." In: *Digital Signal Processing* 117 (2021), p. 103189

Conferences

[C1] Ahmad Hamdan et al. "Interference Analysis for Multi-Carrier Systems Over Fast-Fading Multipath Channels." In: *2021 IEEE Latin-American Conference on Communications (LATINCOM)*. Santo Domingo, Dominican Republic: IEEE, Nov. 2021, pp. 1–6

[C2] Ahmad Hamdan et al. "Equalization With Time Domain Preprocessing for OFDM and FBMC in Flat Fading Fast Varying Channels." In: *2022 IEEE 6th International Symposium on Telecommunication Technologies (ISTT)*. Johor Bahru, Malaysia: IEEE, Nov. 2022, pp. 1–6

Abstract

In the last few decades, communication technologies and the demand for higher quality services provided by these technologies have developed at an extreme rate. As a result, the field of wireless communications research and development has been very active, targeting to meet the requirements in terms of higher throughput, efficiency, higher reliability, use cases and services. In this field, the most common waveforms in use are multi-carrier waveforms (such as OFDM), which are adopted for many standards mainly due to their robustness to multipath propagation, in addition to several other benefits such as the facilitation of multiple access. However, multi-carrier systems are vulnerable to channel variations caused by receiver motion, which, due to the Doppler effect, is a more critical problem at the high carrier frequencies expected to be used in the coming years. Therefore, in this work, the problem of using multicarrier systems in rapidly changing environments is studied in depth, quantified, and solutions are proposed to counteract this vulnerability.

Our first contribution is a pedagogical analysis of the interference caused by high Doppler spread, initially when using a conventional correlator-based receiver. We then derive relative statistical-based analytical expressions to calculate the levels of such interference for oversampled pulse-shaped frequency division multiplexing systems. These are then verified by Monte Carlo simulations. In addition, these formulas have been used to help analyze the characteristics of such interference, its distribution among different neighboring symbols in both time and frequency domains, and the effect of the pulse shape configuration. These observations motivated the need for a more sophisticated receiver, which was discussed later.

To analyze which type of filter performs better under such conditions, we then performed a bit error rate (BER)-based performance analysis. A significant degradation in performance has been observed at high values of the Doppler spread for the existing common frequency domain equalization, so we have proposed to assist the equalization by applying time domain preprocessing. This preprocessing proved to have the ability to achieve diversity from high Doppler spread instead of being negatively affected. Using the proposed techniques with root-raised-cosine (RRC) pulse shape proved to have a significant improvement compared to the state-of-the-art cyclic prefix orthogonal frequency division multiplexing with matrix-form least squares equalization ($\sim$7.5 dB gain observed in the tested scenario).

Since the proposed techniques require knowledge of the channel taps in the time domain, we also proposed a time domain pilot-aided channel estimation that is adapted to operate when used with frequency-limited pulse shapes such as the RRC. The estimation technique was shown to have high accuracy with low mean square error (MSE). A complete implementation was then provided, including the proposed estimation and equalization. Performance in terms of BER was also provided, and it appeared to have only $\sim$1 dB degradation under realistic channel conditions compared to perfect channel knowledge.

Résumé

Les technologies de communication et services associés ont progressé à un rythme fulgurant au cours des dernières décennies. Notamment, dans le domaine des communications sans fil, les travaux de recherche et développement doivent faire face à des demandes de débit, d'efficacité et de fiabilité, mais aussi à de nouveaux usages. Dans ce domaine, les formes d'onde les plus couramment utilisées sont les formes d'onde multiporteuses (comme l'OFDM). Elles sont adoptées dans de nombreuses normes, principalement en raison de leur robustesse à la propagation par trajets multiples, en plus d'autres avantages comme la facilitation de l'accès multiple. Cependant, les systèmes multi-porteuses sont vulnérables à la variation du canal causée par le mouvement du récepteur, qui est, en raison de l'effet Doppler, un problème plus critique pour les hautes fréquences porteuses attendues dans les années à venir. Par conséquent, ce travail examine en profondeur le problème de l'utilisation de systèmes multi-porteuses dans des environnements à variation rapide, le quantifie et propose des solutions d'amélioration.

Notre première contribution est de fournir une analyse pédagogique de l'interférence causée par un étalement Doppler élevé, en présence d'abord d'un récepteur conventionnel à corrélation. Nous dérivons ainsi, à partir d'une analyse statistique, des expressions analytiques de la puissance d'interférence pour les systèmes multiporteuses suréchantillonnées avancées. Ces formules sont validées par des simulations Monte Carlo. En outre, ces formules sont très utiles pour analyser les propriétés de l'interférence, sa distribution dans les différents symboles voisins en temps ou en fréquence, ainsi que l'impact du choix des impulsions utilisées. Ces observations ont aussi motivé le besoin d'utiliser des récepteurs plus sophistiqués.

Afin d'analyser quel type de filtre de mise en forme est le plus performant dans de telles conditions, nous avons ensuite effectué une analyse des performances basée sur le taux d'erreur binaire (TEB). Une dégradation significative des performances a été observée avec l'augmentation de l'étalement Doppler, en présence d'un récepteur à égalisation fréquentielle standard. Nous avons donc proposé d'assister l'égalisation par un prétraitement opérant dans le domaine temporel. Ce prétraitement s'est avéré capable de capter de la diversité avec l'augmentation de l'étalement Doppler, au lieu d'être affecté négativement. L'utilisation des techniques proposées avec des impulsions en racine de cosinus surélevé (RRC) démontre une amélioration significative des performances par rapport à un schéma de transmission classique de l'état de l'art, consistant en l'OFDM à préfixe cyclique, assistée en réception d'un égaliseur fréquentiel matriciel des moindres carrés ($\sim 7,5$ dB de gain observé dans le scénario testé).

Comme les techniques proposées nécessitent de connaître le canal dans le domaine temporel, nous avons également proposé une stratégie d'estimation de canal assistée par des pilotes, et adéquate pour fonctionner avec des formes d'impulsions à bande limitée comme la RRC. La technique d'estimation s'est avérée très précise (faible erreur quadratique moyenne, EQM). Une mise en œuvre complète, comprenant l'estimation de canal et l'égalisation proposées, a ensuite été fournie. Les performances obtenues sont très satisfaisantes, puisqu'on observe un recul des courbes de TEB seulement de $\sim$1 dB par rapport à une connaissance parfaite du canal, pour des scénarios réalistes.

Résumé Etendu

Les technologies de communication ont progressé à un rythme extrême ces dernières décennies, mais la demande de services de meilleure qualité fournis par ces technologies augmente à un rythme plus rapide, ce qui a poussé les constructeurs à développer de façon fulgurante des technologies de communication au cours de la dernière décennie. Une des technologies la plus active dans cette industrie, est la communication sans fil, là où les débits de données, l'efficacité et la fiabilité sont plus élevés. Dans cette optique une étude des usages et des services est désormais considérée comme obligatoire. Dans les prochaines années, alors que la 6ème Génération de communication mobile (6G) se prépare activement, une grande amélioration de ces technologies est nécessaire pour satisfaire l'augmentation de la demande et des services. Parmi toutes les complications que ces exigences soulèvent, il est nécessaire de couvrir les scénarios dans lesquels un récepteur doit recevoir un signal de manière efficace et fiable tout en se déplaçant, et éventuellement en mouvement rapide. Ces problèmes rendent les systèmes mobiles sensibles à un important effet Doppler, en particulier pour les fréquences porteuses élevées, telles que celles qui seront adoptées dans la 6G, outre les problèmes déjà existants telle que la propagation par trajets multiples. La plupart des systèmes de communication modernes, y compris 4G et 5G, utilisent des systèmes multiporteuse en raison de leurs divers avantages. On s'attend à ce que la 6ème génération utilise également une modulation multiporteuse, mais ces systèmes sont vulnérables aux forts effets Doppler, qui peuvent (entre autre) briser l'orthogonalité entre les différentes sous-porteuses. L'objectif de ce travail de thèse est l'étude des performances de systèmes modulations porteuses avancées (indépendamment de toute norme) dans un contexte de fort effet Doppler, et d'en déduire les formes d'ondes et les récepteurs les plus adéquats à ce contexte. Ce résumé étendu traitera de l'analyse de l'interférence, puis d'égalisation, et enfin d'estimation de canal, avant de conclure.

1 Analyse des interférences pour les systèmes multiporteuses

Suite aux difficultés évoquées ci-dessus, ce premier travail analyse les propriétés des systèmes multiporteuses suréchantillonnés (indépendamment de toute norme) en présence d'un important effet Doppler, en termes d'interférences, en supposant d'abord un récepteur conventionnel (banc de corrélations aux formes d'ondes). Pour généraliser l'analyse, nous avons adopté une forme généraliste des systèmes de multiplexage par

répartition en fréquence (FDM), le modélisant comme :

$$\begin{aligned}\hat{c}_{m',n'}|_{m,n} = &\sum_{l}\sum_{q}\tilde{g}^*[q-n'N] \\ &\times (h[q,l]g[q-l-nN]c_{m,n}+\omega[q]) \\ &\times e^{-j2\pi\frac{(q-nN)(m'-m)-m'N(n'-n)+lm}{M}},\end{aligned} \tag{1}$$

où $\hat{c}_{m',n'}$ est le symbole reçu sur la sous-porteuse m' du symbole n', $\hat{c}_{m',n'}|_{m,n}$ est la contribution du symbole transmis sur la sous-porteuse m du symbole n à $\hat{c}_{m',n'}$, M est le nombre de sous-porteuses par symbole, N est le décalage en échantillons entre deux symboles consécutifs, g est la forme de l'impulsion d'émission, $\tilde{g}$ est la forme de l'impulsion de réception, $h[q,l]$ est la réponse du canal à l'échantillon q du l-ème trajet (discret) et ω est le bruit additif blanc gaussien circulaire complexe (AWGN). Notez que pour l'analyse des interférences, ω est mis à zéro pour se concentrer sur l'impact de l'interférence. La forme adoptée de FDM est très flexible pour deux raisons : 1) possibilité de configurer le facteur de suréchantillonnage (N/M) du système en configurant M et N (qui sont réglés sur 32 et 40 pour cette section), et 2) possibilité de configurer les propriétés liées aux impulsions (robustesse, étalement, localisation, etc.) en configurant g et $\tilde{g}$. Le modèle fourni calcule la contribution de chaque symbole transmis à chaque symbole reçu pour une réalisation de canal spécifique. Cela permet le calcul de l'interférence à la manière de Monte Carlo, ayant la puissance observée sur la sous-porteuse m' du symbole n' due à la transmission de la sous-porteuse m du symbole n pour une seule réalisation de canal définie par :

$$\mathcal{P}_{m',n'}|_{m,n} = (\hat{c}_{m',n'}|_{m,n})(\hat{c}_{m',n'}|_{m,n})^*. \tag{2}$$

Pour l'analyse statistique, nous avons adopté le modèle de Jakes avec un canal de Rayleigh. Nous avons alors calculé la puissance reçue attendue :

$$\begin{aligned}P_{\Delta} = &\sum_{l}\sigma_l^2\sum_{\gamma}\sum_{\gamma'}\tilde{g}^*[\gamma-\Delta_s N+l]\tilde{g}[\gamma'-\Delta_s N+l] \\ &\times g[\gamma]g^*[\gamma']J_0(2\pi F_d T_{sa}(\gamma-\gamma'))e^{j2\pi\frac{(\gamma'-\gamma)\Delta_c}{M}},\end{aligned} \tag{3}$$

où J_0 est la fonction de Bessel du premier type d'ordre 0, F_d est la fréquence Doppler et T_{sa} est la période d'échantillonnage, de sorte que $T_s = NT_{sa}$ est le temps symbole et $F_d T_s = NF_d T_{sa}$ est l'étalement Doppler normalisé. Notons que l'indice utilisé est $\Delta = [\Delta_c\ \Delta_s]$ tel que $\Delta_c = m' - m$, et $\Delta_s = n' - n$, au lieu de m , m', n et n'. En effet, la puissance attendue s'est avérée ne pas dépendre directement des indices d'émission et de réception, mais de la différence entre eux. Comme on peut le voir à partir de ces équations, les formes d'impulsion g et $\tilde{g}$ affectent de manière significative les niveaux d'interférence. Pour couvrir autant de variétés de formes d'impulsions que possible, nous sélectionnons les formes d'impulsions (orthogonales, exceptées la

Gaussienne) suivantes à des fins de comparaison en raison de la diversité de leurs critères :

- Impulsions rectangulaires (Rect) : utilisées car elles correspondent à l'implémentation du multiplexage par répartition orthogonale de la fréquence (OFDM). Nous supposons également que g et $\tilde{g}$ sont configurés pour refléter l'usage d'un préfixe cyclique (CP).

- Impulsions minimisant l'énergie hors bande (OBE) : minimisent l'énergie en dehors de la bande fréquentielle occupée par une sous-porteuse pour des facteurs M et N donnés, avec la contrainte d'avoir une longueur d'impulsion limitée à N échantillons.

- Impulsions maximisant la localisation temps-fréquence (TFL) : minimisent le produit de moments centrés d'ordre 2 en temps et en fréquence, pour des facteurs M et N donnés, avec la contrainte d'avoir une longueur d'impulsion limitée à N échantillons.

- Impulsions en racine de cosinus surélevé (Root Raised Cosine : RRC$^{\beta}$) : la forme d'impulsion à bande limitée la plus utilisée. Deux valeurs de roll-off β considérées : 1/4 et 1. Cela nécessite que l'impulsion s'étende sur plusieurs symboles (nous adoptons 9), tout en maintenant idéalement l'orthogonalité avec les tranches de temps voisines.

- Impulsions gaussiennes (Gauss) : utilisées bien que non orthogonales, semi-limitées dans les domaines temporel et fréquentiel. Cependant, cela nécessite de couvrir plusieurs symboles (nous adoptons 3) et cause des interférences dans tous les scénarios. Nous configurons l'impulsion (par sa variance) pour répartir les interférences de manière égale dans les domaines temporel et fréquentiel.

Dans la figure 1, le niveau de puissance d'interférence pour le canal de type "véhicule étendu A" (EVA) a) vs $F_d T_s$, b) vs Δ_c, et c) vs Δ_s est affiché. Les lignes pleines représentent les valeurs théoriques et les lignes pointillées représentent les valeurs obtenues par simulations Monte Carlo, qui semblent y correspondre. Une observation simple se trouve dans la figure 1.a), qui fournit les niveaux d'interférence pour différentes formes d'impulsions par rapport à $F_d T_s$. Cependant, un examen plus approfondi de la propagation de ces interférences est fourni par la figure 1.b) et c), ce qui aide à comprendre les propriétés d'interférence et à sélectionner/concevoir des techniques d'égalisation et d'estimation de canal appropriées.

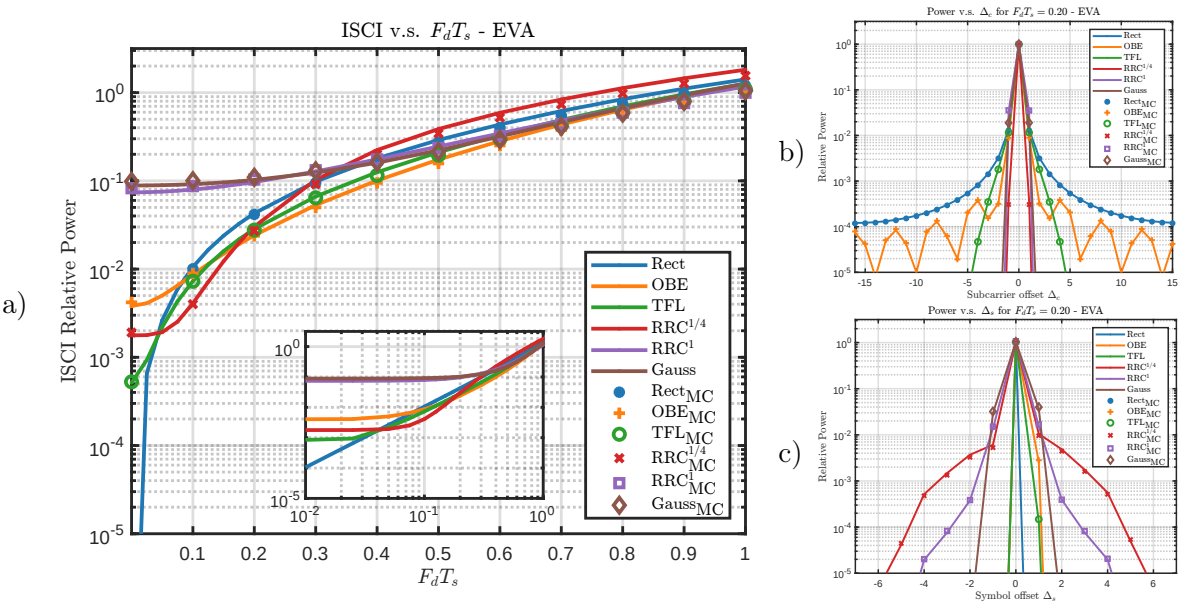

Figure 1: Niveau de puissance d'interférence pour le canal de type "véhicule étendu A" (EVA) a) vs F_dT_s, b) vs Δ_c et c) vs Δ_s, le tout pour $M = 32$ et $N = 40$.

2 Égalisation assistée dans le domaine temporel pour les systèmes multiporteuses

Pour vérifier l'impact de cette interférence sur le taux d'erreur binaire (BER) et analyser quel type de filtre fonctionne le mieux dans de telles conditions, nous avons effectué une analyse des performances basée sur le BER. Puisque 1) nous considérons un système multiporteuse suréchantillonné ($N > M$), et puisqu'une forme d'impulsion peut s'étendre sur plus d'un seul symbole (9 pour RRC et 3 pour Gauss), il est possible que les échantillons dans le domaine temporel contiennent certaines informations (dues à la variation du canal) qui pourraient être manquées en raison de la transition vers le domaine fréquentiel. Par conséquent, nous adoptons une aide à l'égalisation en ajoutant un prétraitement dans le domaine temporel. Nous testons deux prétraitements dans le domaine temporel : 1) Erreur quadratique moyen minimale (MMSE) dans le domaine temporel, et 2) Multiplicateur de canal adapté (MCM) qui applique le filtre adapté au canal dans le domaine temporel. Notez que pour MCM, le filtre n'est pas un filtre classique à gain fixe, mais un filtre à gain variable en raison de la variation du canal. De plus, MMSE$_t$ (indexé par t pour indiquer qu'il s'agit d'une procédure dans le domaine temporel) peut être appliqué sans égaliseur dans le domaine fréquentiel (classique), alors que le MCM en nécessite un. En plus des opérations proposées, nous analysons les égaliseurs suivants :

- MMSE$_f$: l'égaliseur MMSE classique à un coefficient par sous-porteuse (diagonal) dans le domaine fréquentiel.

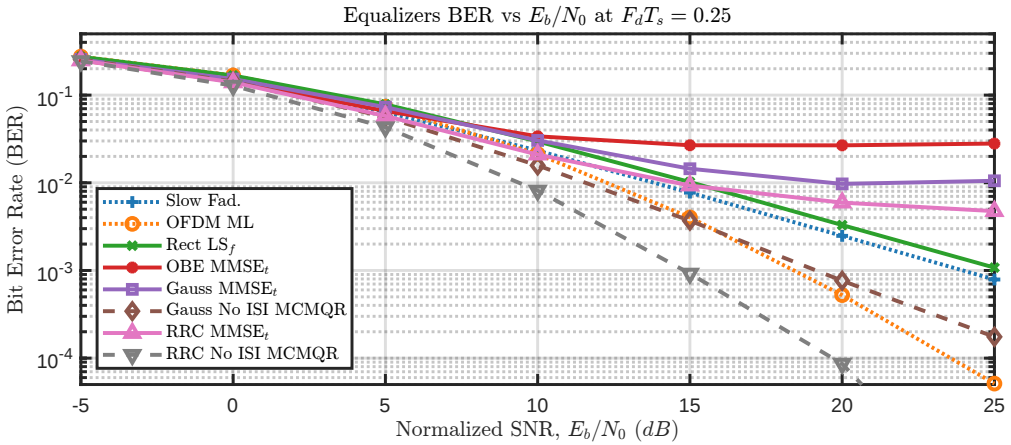

Figure 2: BER vs E_b/N_0 à $F_dT_s = 0,25$ pour le meilleur égaliseur par forme d'impulsion pour un canal à 2 trajets avec un étalement de retard $0,2T_s$.

- LS$_f$: égaliseur MMSE multi-tap (matrice) dans le domaine fréquentiel.
- QR$_f$: égaliseur qui procède par décomposition QR dans le domaine fréquentiel avec annulation successive des interférences.

Nous adoptons l'égalisation QR$_f$ à utiliser avec MCM, ou ce que nous avons nommé MCMQR. Dans la figure 2, nous fournissons les performances du meilleur égaliseur pour chaque forme d'impulsion par rapport au rapport signal sur bruit (SNR) normalisé E_b/N_0 pour $F_dT_s = 0,25$. En plus, nous donnons en référence les performances théoriques en évanouissement lent ($F_dT_s \to 0$) et les performances en OFDM avec récepteur optimal à maximum de vraisemblance (OFDM ML). La légende "No ISI" est utilisée lorsque l'interférence inter-symbole (ISI) est parfaitement supprimée, considérée pour des impulsions ayant un ISI significatif. Nous avons observé que la combinaison égaliseur/impulsion la plus performante est la forme d'impulsion RRC avec MCMQR et annulation d'ISI.

Pour approcher l'annulation de l'ISI pratiquement nous proposons de le faire de manière itérative en détectant les symboles, en reconstruisant l'interférence, puis en l'annulant. Nous avons observé qu'avant d'annuler l'ISI, le meilleur égaliseur pour la forme d'onde RRC est MMSE$_t$. Par conséquent, dans l'annulation itérative de l'ISI, nous effectuons la première itération avec MMSE$_t$, puis MCMQR pour les itérations suivantes. Les performances de cette procédure sont fournies par la figure 3 et comparées aux performances obtenues en OFDM avec égaliseur fréquentiel matriciel performant (Rect LS$_f$). On observe un gain d'environ 5 dB pour un BER $\sim 10^{-2}$, et d'environ 7.5 dB pour un BER $\sim 10^{-3}$. Nous pouvons observer que le gain est plus grand avec l'augmentation de E_b/N_0, ce qui signifie une meilleure "pente" du système proposé réalisant une certaine diversité implicite. Des gains plus élevés ont été observés pour les canaux à trajet unique. Cependant, ce gain de performance nécessite de connaître la réponse du canal dans le domaine temporel, ce qui n'est pas courant

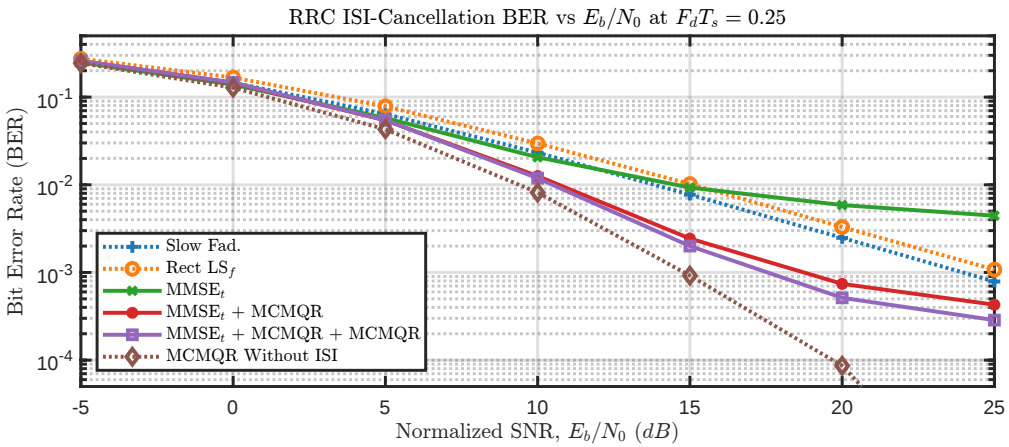

Figure 3: BER vs E_b/N_0 à $F_dT_s = 0,25$ pour le système multiporteuse avec forme d'onde RRC avec différentes itérations d'annulation de l'ISI. Canal supposé être un canal à 2 trajets avec un étalement de retard $\mathcal{T} = 0.2T_s$ et parfaitement connu.

dans la littérature. Dans la section suivante, nous discutons d'une technique proposée pour estimer avec précision la réponse du canal dans le domaine temporel dans des environnements à variation rapide.

3 Estimation de canal dans le domaine temporel pour les systèmes multiporteuses

L'impulsion RRC s'est avérée être la meilleure impulsion lorsqu'elle est combinée avec les techniques proposées, qui nécessitent de connaître la réponse du canal dans le domaine temporel. Par conséquent, nous avons également proposé une estimation de canal assistée par pilote dans le domaine temporel qui est adaptée pour fonctionner lorsqu'elle est utilisée avec des formes d'impulsions limitées en fréquence comme le RRC. La technique est basée sur l'insertion séparée de symboles pilotes complexes de module unitaire dans le domaine temporel. Nous définissons d'abord ce qui suit :

- p_k^W, l'ensemble des sous-porteuses réservées au k-ème pilote avec $k \in [0 \;\; P-1]$, où P est le nombre de pilotes, et W est le nombre de sous-porteuses (ou bande équivalente) réservées pour chaque pilote,
- $p_k^{(i)}$, la i-ème entrée de p_k^W avec $i \in [0 \;\; W-1]$,
- $p_k = \frac{1}{W}\sum_{i=0}^{W-1} p_k^{(i)}$, la fréquence du k-ème pilote normalisée par la fréquence de sous-porteuse (pas nécessairement un nombre entier),
- et $p_{\text{range}} = \left\{p_k^W \;\; \forall \;\; k \in [0 \;\; P-1]\right\}$ l'ensemble de toutes les sous-porteuses réservées pour les P pilotes.

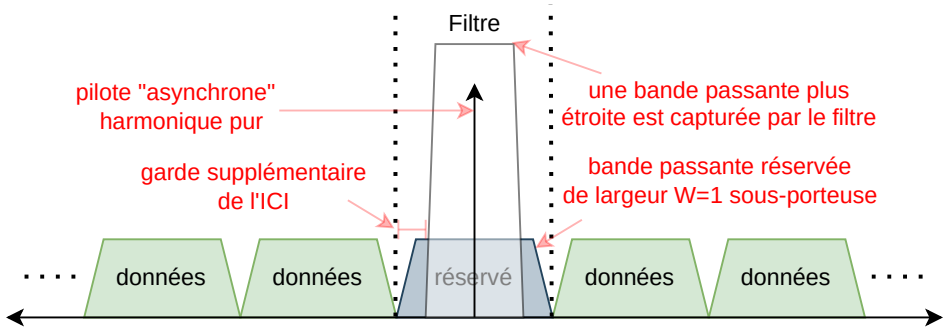

Figure 4: Représentation dans le domaine fréquentiel des symboles de données et du pilote à un seul ton pour un nombre de sous-porteuses réservées à un pilote $W = 1$.

Puisque nous supposons P sous-porteuses pilotes équidistantes (dans le domaine fréquentiel), le premier (0-ème) indice de sous-porteuse des sous-porteuses réservées au k-ème pilote $p_k^{(0)}$ est défini par :

$$p_k^{(0)} = \text{round}\left(k\frac{M}{P}\right). \tag{4}$$

où $k \in [0 \;\; P-1]$. Notez que cela suppose que M/P est un entier. Suivant cette définition, $p_k^{(i)}$, l'ensemble des sous-porteuses réservées au k-ème pilote est défini par :

$$p_k^W = \left\{p_k^{(0)} + i \;\; \forall \;\; i \in [0 \;\; W-1]\right\}. \tag{5}$$

D'autre part, sachant que le nombre total de sous-porteuses est M avec des indices $m \in [0 \;\; M-1]$, l'ensemble des indices de sous-porteuses qui peuvent encore être utilisés pour les données est :

$$d_{\text{range}} = [0 \;\; M-1] \ominus p_{\text{range}}, \tag{6}$$

où $\ominus$ est l'opérateur de différence d'ensemble. Suite à cette allocation de symboles de données et de pilotes, on modifie la définition du signal émis pour supporter la présence des pilotes. Le q-ème échantillon du signal transmis s peut alors être transmis comme :

$$s\left[q\right] = s_{\text{data}}\left[q\right] + s_{\text{pilot}}\left[q\right], \tag{7}$$

où s_{data} représente les échantillons générés du fait de la transmission des symboles de données, et s_{pilot} représente les échantillons générés du fait de la transmission des pilotes. Les échantillons générés du fait de la transmission des symboles de données s_{data} sont alors définis par :

$$s_{\text{data}}\left[q\right] = \sum_n \sum_m g\left[q - nN\right] e^{j2\pi \frac{m(q-nN)}{M}} c_{m,n} \;\; \forall \;\; m \in d_{range}. \tag{8}$$

Puisque nous supposons des pilotes "asynchrones" harmoniques purs (comme présenté dans la figure 4), nous définissons les échantillons générés en raison de la transmission

des pilotes s_{pilot} par :

$$s_{\text{pilot}}[q] = \frac{1}{\sqrt{N}} \sum_{k=0}^{P-1} e^{j2\pi \frac{p_k q}{M}}. \tag{9}$$

Le signal reçu dû à l'émission du signal pilote s_{pilot} est alors :

$$r_{\text{pilot}}[q] = \frac{1}{\sqrt{N}} \sum_{l=0}^{L-1} h[q,l] \sum_{k=0}^{P-1} e^{j2\pi \frac{p_k (q-l)}{M}} + \omega[q], \tag{10}$$

On essaie alors d'« isoler » les symboles pilotes reçus en les filtrant à l'aide d'un filtre $\hat{g}$ adapté pour limiter sa bande passante à la variation du canal. Nous considérons trois filtres pour ce travail :

- FIR1 : généré à l'aide de la fonction Matlab *fir1* avec une bande passante $2(F_d T_s + 0.01)$ (normalisée à la bande passante de la sous-porteuse),
- WNR_n : utilisation d'un filtre de Wiener en supposant que seules les densités spectrales de puissance (PSD) de bruit et de canal sont prises en compte pour la conception du filtre,
- et WNR : utilisation du filtre de Wiener en supposant que les PSD de bruit, de canal et d'interférence sont prises en compte pour la conception du filtre.

Notons que ces filtres de Wiener ne sont pas réalisables en raison d'une réponse infinie dans le domaine temporel, et sont par conséquent tronqués à l'aide de méthodes de fenêtrage. Cela réduit la précision de la sortie du filtre, en raison de la capture imparfaite de la PSD de la réponse du canal. Chaque pilote est filtré séparément et les résultats sont mis en correspondance avec les retards des trajets (supposés connus) en utilisant une méthode des moindres carrés.

Dans la figure 5, les performances de la technique d'estimation de canal proposée sont fournies pour a) $W = 1$ et b) $W = 3$ sous-porteuses réservées par pilote. Les lignes pleines signifient les niveaux théoriques de l'erreur quadratique moyenne (MSE) et les lignes pointillées signifient les valeurs obtenues par simulation. Les tracés Interp reflètent les performances de l'estimation classique basée sur l'interpolation, effectuée trois fois en observant les valeurs des pilotes dans le domaine fréquentiel, puis en les interpolant (à l'aide de spline) pour obtenir les coefficients dans le domaine temporel. La limite '+ICI' signifie le $F_d T_s$ minimum qui produit l'ICI entre les sous-porteuses de données et les sous-porteuses pilotes, qui est $0,25$ pour $W = 1$ et $0,75$ pour $W = 3$. Par conséquent, après avoir dépassé la limite "+ICI", les sous-porteuses de données commencent à interférer avec les sous-porteuses pilotes et augmentent par conséquent l'erreur générée par les interférences. Cependant, l'impact de cette interférence n'est devenu significatif que pour les $F_d T_s$ plus élevés. Tout d'abord, nous pouvons observer

a)

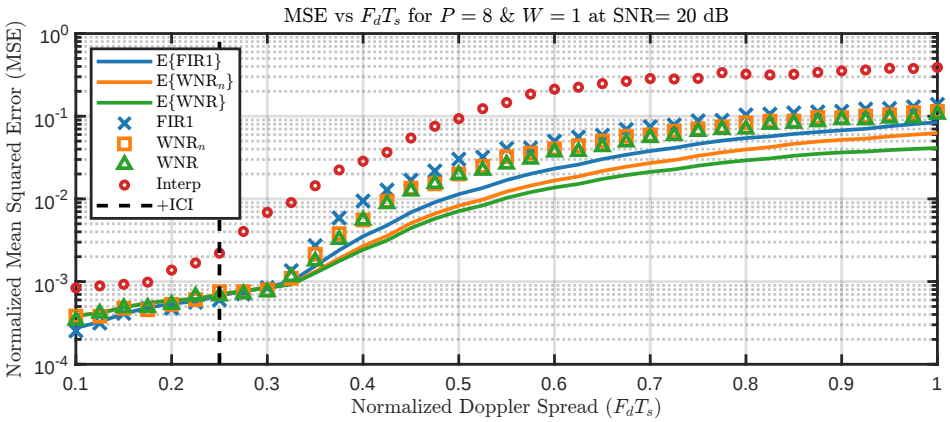

b)

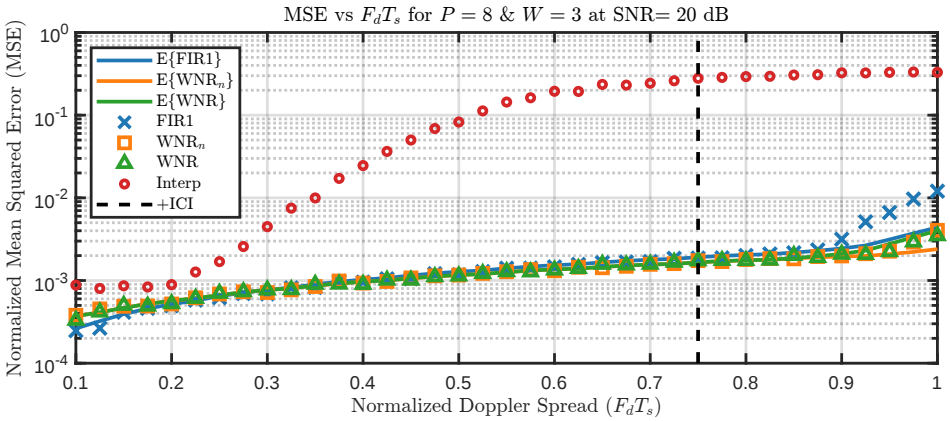

Figure 5: MSE vs F_dT_s à $E_b/N_0 = 20$ dB pour la technique d'estimation de canal proposée. Canal supposé être un canal à 2 trajets avec étalement de retard $\mathcal{T} = T_s/8$ avec une puissance égale par voie. a) pour $W = 1$ et b) pour $W = 3$.

que la méthode proposée est plus performante que la méthode Interp classique pour tous les F_dT_s, mais tous les filtres ont des performances similaires. Deuxièmement, notons que pour la méthode Interp, la dégradation des performances commence à $F_dT_s \approx 0,2$ pour $W = 1$ et $W = 3$, où ces méthodes souffrent non seulement d'interférences, mais de l'incapacité à capturer la variation du canal. Cela montre la validité de notre approche et son amélioration significative par rapport aux méthodes classiques. Étant donné que les performances sont presque similaires pour tous les filtres, nous retenons pour la suite l'utilisation de FIR1 en raison de sa simplicité de conception.

Dans la figure 6, nous avons fourni les simulations en considérant un scénario complet combinant les techniques d'estimation et d'égalisation proposées. Les lignes pleines reflètent les performances lorsque l'on considère notre estimation de canal proposée, et la ligne pointillée reflète les performances lorsque l'on a une connaissance parfaite du canal. Différentes itérations d'égalisation/annulation d'ISI ont été appelées *technique*$^{\text{itération}}$. Notez que la première technique MMSE (dans le domaine temporel) a l'indice d'itération 0 puisqu'elle est considérée comme une pré-estimation. Un graphique supplémentaire 'Rect LS$_f$' est fourni montrant les performances lors de l'utilisation

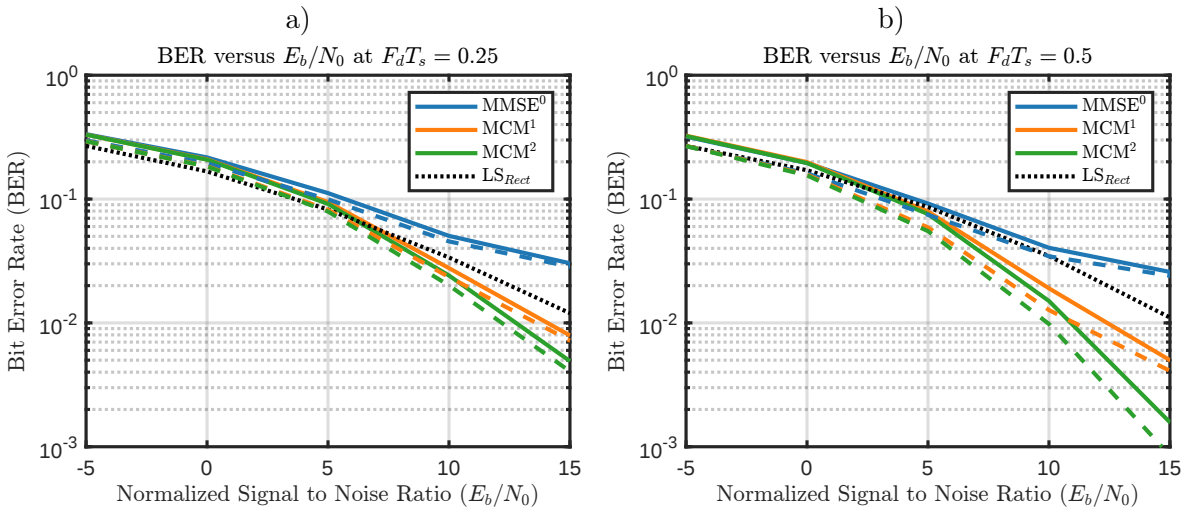

Figure 6: BER vs E_b/N_0 avec la technique d'estimation de canal proposée pour $M = 64$, $N = 80$ et $P = 8$. Canal supposé être un canal à 2 trajets avec étalement de retard $\mathcal{T} = T_s/8$ avec une puissance égale par voie. a) $F_dT_s = 0,25$ et $W = 1$, et b) $F_dT_s = 0,5$ et $W = 3$.

de la technique CP-OFDM avec l'égaliseur des moindres carrés multi-tap (LS) dans le domaine fréquentiel, idéal dans le cas d'une connaissance parfaite du canal. En comparant le BER obtenu en utilisant notre technique d'estimation à celui obtenu en utilisant une connaissance parfaite du canal, nous pouvons observer une dégradation de seulement ∼1 dB. En plus, en comparant les performances de 'Rect LS$_f$', nous observons que notre système global a des performances nettement meilleures, atteignant une amélioration de ∼4 dB à un BER de 10^{-2}, avec une amélioration augmentant avec E_b/N_0, ce qui signifie de nouveau une meilleure « pente » du système proposé réalisant une certaine diversité implicite.

4 Conclusion

Dans ce travail, nous avons fourni des expressions statistiques pour calculer les niveaux d'interférence pour les systèmes de multiplexage par répartition de fréquence en forme d'impulsions suréchantillonnées, en présence du récepteur conventionnel (banc de filtres adaptés aux formes d'ondes). Ces expressions statistiques ont ensuite été vérifiées par des simulations de Monte Carlo. En plus de cela, cette formulation a été utilisée pour aider à analyser les propriétés d'une telle interférence, sa distribution dans différents symboles voisins dans les domaines temporel et fréquentiel, et l'impact de la configuration de la forme de l'impulsion sur une telle interférence et sa distribution. Pour vérifier l'impact de cette interférence sur le taux d'erreur binaire (BER) et analyser quel type de filtre fonctionne le mieux dans de telles conditions, nous avons effectué une analyse des performances basée sur le BER. Une dégradation significative des performances a été observée avec l'augmentation de l'étalement Doppler pour l'égalisation commune

existante, nous avons donc proposé d'assister l'égalisation par un prétraitement dans le domaine temporel. Le prétraitement proposé s'est avéré avoir la capacité d'obtenir un gain en diversité à partir d'un étalement Doppler élevé au lieu d'être affecté négativement. L'utilisation des techniques proposées avec la forme d'impulsion en racine de cosinus surélevé (RRC) s'est avérée amener une amélioration jusqu'à $7,5$ dB par rapport à la technique multiporteuse OFDM à préfixe cyclique, équipée d'un égaliseur matriciel fréquentiel, pour des canaux multi-trajets à variation rapide. Nous avons également observé que le gain augmentait avec E_b/N_0, signifiant la capacité à bénéficier de la diversité temporelle. L'impulsion RRC s'est avérée être la meilleure impulsion lorsqu'elle est combinée avec les techniques proposées. Ces dernières nécessitent de connaître les coefficient du canal dans le domaine temporel. Par conséquent, nous avons également proposé une estimation de canal assistée par pilote dans le domaine temporel qui est adaptée pour fonctionner lorsqu'elle est utilisée avec des formes d'impulsions limitées en fréquence comme le RRC. La technique d'estimation s'est avérée avoir une grande précision avec une faible erreur quadratique moyenne (MSE). Une implémentation complète a ensuite été fournie incluant l'estimation et l'égalisation proposées. Des performances en termes de BER ont également été fournies, et il est apparu, dans des conditions de canal réalistes, une dégradation de seulement $\sim$1 dB par rapport à une connaissance parfaite du canal.